UNIVERSITY OF VIRGINIA

DOCTOR OF PHILOSOPHY'S DISSERTATION

Presented to the Faculty of
the School of Engineering and Applied Science
in the University of Virginia

Heze Chen

August 2023

Bridging Elasticity and Structural Engineering with the Finite Volume Method

A

Dissertation

Presented to

the faculty of the School of Engineering and Applied Science
University of Virginia

in partial fulfillment
of the requirements for the degree

Doctor of Philosophy

by

Heze Chen

August 2023

APPROVAL SHEET

This

Dissertation

is submitted in partial fulfillment of the requirements
for the degree of

Doctor of Philosophy

Author: Heze Chen

This Dissertation has been read and approved by the examing committee:

Advisor: Marek-Jezy Pindera

Advisor: Jose Gomez

Committee Member: Devin Harris

Committee Member: Katie MacDonald

Committee Member: Marcio Cavalcante

Committee Member:

Committee Member:

Committee Member:

Accepted for the School of Engineering and Applied Science:

Jennifer L. West, School of Engineering and Applied Science

August 2023

Acknowledgement

I would like to express my heartfelt gratitude to the individuals who have played a significant role in the completion of my Ph.D. studies.

First and foremost, I am immensely grateful to my co-advisors, **Prof. Marek-Jerzy Pindera** and **Prof. Jose Gomez**, for their exceptional guidance throughout this journey. Our weekly group meetings over the past five years have been invaluable, and I will undoubtedly miss them greatly following my graduation.

I would also like to extend my sincere thanks to my committee chair, **Prof. Devin Harris**, and other committee members who supported me through my Ph.D. qualifying exam, proposal, and final dissertation defense. I am truly appreciative of the feedback and comments provided by **Prof. Marcio Cavalcante**, which significantly contributed to my understanding of FEM and 3D FVM solution in structural engineering. Furthermore, I am grateful for the opportunity to collaborate with **Prof. Katie MacDonald** on the Mass Grass project for four semesters. This experience has broadened my perspective on applying structural engineering principles to architectural design using sustainable materials. I feel fortunate to have worked with architecture and environmental science teams, as well as a talented group of undergraduate engineering students: **Jeyi Lee**, **Chris Le**, **Nicole Piatko**, **Cole Cestaro**, **Caroline Lystash**, **Karthik Eswarapragada**, **Austin Davis**, **Tingyo Tan**, **Samuel Segal**, and **Yechan Kim**.

I also have to express my appreciation to my colleagues **Donald Martin**, **Malik Corum**, **Runze Yan**, **Luwei Zeng**, **Shizhen Yin**, **Zhaoxia Ma**, **Aya Yehia**, **Afrida Raida**, **Abdou Ndong**, **Seth Engel**, **Robin Kim**, **Moeen Mostafavi**, **David Gutierrez**, **Ugur Killc**, **Daniela Quintero**, **Aashutosh Aryal**, **Benjamin Goffin**, **Ziyue Zhu**, and all my other office mates in THN-D221, where I have spent all four years of my Ph.D. Your camaraderie and intellectual peer discussions have enriched my academic experience.

I am thankful for the funding support from the Civil & Environmental Engineering Department (CEE), Applied Mathematics (APMA) Department, and Data Science (DS) School for the teaching assistantships and research assistantships. I am sincerely grateful to **Prof. Monika Abramenko**, **Prof. Stacie Pisano**, and **Prof. Meiqin Li** from the APMA department for their mentorship and working ethics as I worked with them as a teaching assistant. I am honored to have the opportunity to continue collaborating with them and their ongoing support will undoubtedly contribute to my professional growth and research endeavors. I would like to thank all the staff in our CEE department, including lab manager **Ryan Henry**, coordinator **Chantel Gross**, and our custodian **Franko**, for their help and encouragements.

The patience and support of my family, especially my mother and grandparents, are deeply valued. I also appreciate my family financial support and the challenges presented by my father during my Ph.D., which have made me mentally stronger. I would also like to extend my gratitude to my cousin, **Fenghe Chen**, for her meticulous proofreading assistance.

Lastly, I would like to dedicate a special section of this acknowledgment to my beloved wife, **Yiqing Xu**. Her unwavering support throughout my Ph.D. journey has been so cherished. I am indebted to her persistence and encouragement, which played an important role in my decision to pursue my studies abroad after obtaining my bachelor's degree in ZJUT.

I am sincerely grateful to all these individuals, both mentioned and unmentioned, for their support, mentorship, and collaboration throughout my Ph.D. studies. While I may not have listed everyone by name, please know that your contributions have been deeply appreciated. Your encouragement and inspiration have shaped my academic journey and continue to motivate me to keep moving forward!

Abstract

The theory of elasticity serves as a vital mathematical framework for studying deformations and stress distributions in elastic solid bodies and structural members subjected to external loads. However, the analysis of three-dimensional elasticity problems can be intricate and computationally demanding. To simplify the analysis, assumptions are made based on the geometry and boundary conditions, leading to quasi-three-dimensional models. This dissertation presents, for the first time, novel implementations of finite-volume based solutions for important classes of elasticity problems discussed in standard and advanced monographs on the theory of elasticity, namely: plane problems, torsion problems, and flexure problems of structural members.

For plane problems, which pertain to structural members subjected to loads acting solely in the plane of the structure, the dissertation formulates plane stress, plane strain, and generalized plane strain conditions within a parametric finite-volume framework. This framework is extended to analyze orthotropic and monoclinic materials. The developed finite-volume method (FVM) is verified using elasticity solutions for bending of rectangular cantilever beams under plane strain and plane stress assumptions and then applied to investigate deformation and attendant stress fields of multi-layered and heterogeneous beams with inclusions and porosities. Additionally, FVM is employed to assist in accurate shear characterization of advanced unidirectional composites in off-axis tension tests and Iosipescu shear tests.

This dissertation also addresses the study of prismatic bars with arbitrary cross sections bounded by a cylindrical surface and transverse planes with loadings applied solely on their end faces. Solutions to this class of problems play critical roles in structural engineering design of members of practical cross sections whose response to transverse loading is limited to bending, with twisting eliminated or minimized. By utilizing the principle of superposition, the complete equilibrium problem of an elastic bar was solved by decomposing the applied loading into four elementary loadings: extension, bending, torsion, and flexure. FVM-based approach was subsequently developed to analyze torsion of bars with curved boundaries and to assess the flexural response of beams with different cross sections. The accuracy and convergence of the FVM were validated through comparison with analytical solutions for cross sections with convex and concave boundaries.

Overall, FVM was demonstrated to successfully assess torsion-flexure behavior of various beam cross sections of practical interest in structural design. Upon comparison with three-dimensional finite element simulations of a series of cantilever beams, it also verified Saint Venant's principle often invoked in structural design by quantifying the extent to which end effects propagate into the beam.

The developed method fills the gap in the elasticity theory formulation and limited analytical solutions of complex problems, offering a powerful alternative to variational techniques. The findings obtained by the demonstrated accurate FVM analyses of a wide range of structural problems contribute to the design and development of safer and more efficient structures in various engineering fields. Moreover, the method’s transparent framework makes it readily accessible to the structural engineering community, democratizing the analysis and design process. A Graphical User Interface (GUI) developed for torsion problems of common structural engineering members has been employed successfully in the delivery of advanced mechanics of materials courses and made available to structural engineers in the industry and government laboratories.

List of Tables

List of Figures

Table of Contents

Chapter 1

Introduction

1.1 Motivation

Structural engineering, one of the disciplines of civil engineering, aims to design and create forms, shapes, and constructs of man-made structures that meet desired function and safety requirements. It is crucial to calculate stability, strength, stiffness, and even dynamic susceptibility of built structures including buildings and other types of structures. Stability, strength, stiffness, and dynamic susceptibility are potentially involved in the integral structural design, manufacture and building process, and they are calculated based on applied physical laws and empirical knowledge of structural performance of different materials and configurations. Empirical knowledge in structural engineering leads to the application of proven sizes, proportions, materials, and assemblies based on previous engineering practice, and the basis of empirical design is merely accumulated experience without regard to any systematic theory. Previous experience increases our confidence in conventional design; however, it can be insufficient or inaccurate when constructing novel or complex structures. The theory of elasticity provides the underpinning knowledge necessary for the design of durable and safe structures. In particular, as most civil structures are designed to resist loadings and provide long-term service without drastic geometric changes, linear elasticity enables accurate analysis of structural members undergoing small deformations.

Elasticity is the ability of a deformed elastic material body to return to its original shape and size when the forces causing the deformations are removed. The theory of elasticity is concerned with the study of the response of elastic material bodies to the action of applied forces. In linear elasticity, deformations do not exceed certain limits that are determined by the constitutive characteristics of materials represented by mathematical models of linearly elastic solid materials. The linearly elastic properties of any solid material relate forces to deformations, thus providing rigorous mathematical insight into physics. Hooke's law states that the force needed to extend or compress a spring by some distance scales linearly with respect to that change in the spring's length, and the generalization of this principle to continuous elastic materials produces generalized Hook's law that is essentially important in the fundamentals of elasticity. A wide range of real structural engineering problems undergoing small deformation may be solved using this model within the framework of elasticity.

One of the fundamental concepts in mechanics is *continuum*. At the atomistic scale, a medium occupied by a solid or fluid, is made of discrete particles of protons, neutrons, and electrons; macroscopically, the medium is assumed to contain no gaps or voids between material points so that it can be divided indefinitely into smaller and smaller parts without encountering a void. This ideal concept allows to shrink an arbitrarily small region to a point, and all spatial derivatives of various quantities associated with the medium can be properly defined using the tools of calculus.

The governing equations of a continuum are derived using the laws of physics, which are *the principle of conservation of mass, the principle of balance of linear momentum, the principle of balance of angular momentum,* and *the principle of conservation of energy*. However, these principles do not explicitly account for geometric changes or mechanical responses of the continuum. Without these considerations, the equations derived from the conservation and balance laws are insufficient to determine the total response of a continuum. Moreover, to apply these equations in the small or at a point within a body, additional variables need to be introduced that define the internal forces and deformations, how they are allowed to vary and how they are related. These variables describe the statics and kinematics of material points within the body.

The variation of internal forces or statics is described using the concept of traction or force intensity acting across an infinitesimal area of a surface as this area tends to a point (see Figure 1-1),

$$t_i = \sigma_{ij} n_j \tag{1. 1}$$

where n_j is the unit normal vector components. Hence an infinitesimal material element with six orthogonal faces is subjected to three traction vectors on the front faces, and equal but opposite traction vectors on the back faces that ensure equilibrium in each orthogonal axial direction. Traction vectors on each face may be expressed in terms of normal and tangential components, leading to the concept of a stress tensor at a point characterized by nine components that occur in pairs on three faces.

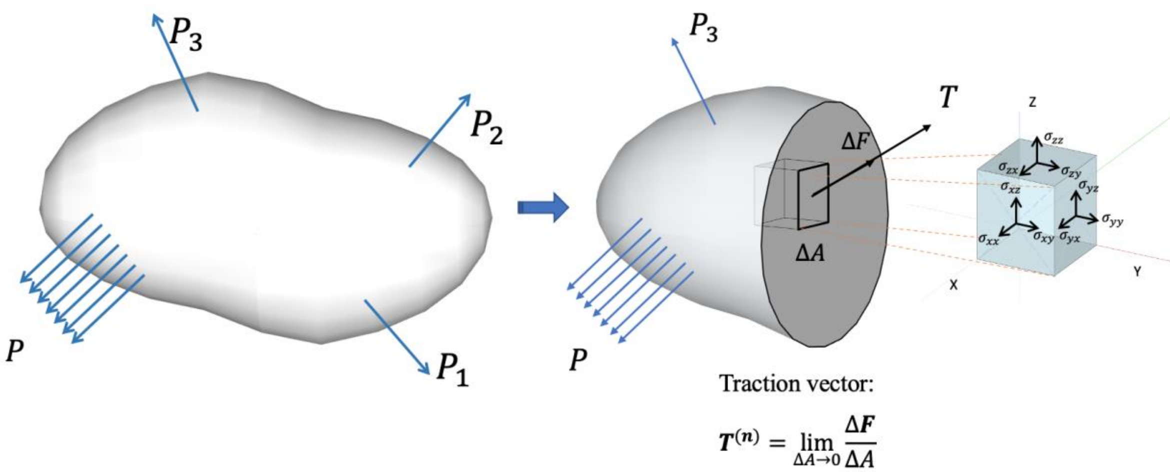

Figure 1-1 Illustration of stress and traction in an infinitesimal cubical element in a body

The moment equilibrium about each of the three orthogonal axes leads to the symmetry of the stress tensor components. Moreover, the force equilibrium consideration of an infinitesimal tetrahedron generated by slicing the infinitesimal material element diagonally leads to the conclusion that the stress components transform as the components of a second-order tensor from one coordinate system to another. If we allow the stress components on opposite faces of an infinitesimal material element to vary, we obtain three partial differential equations of equilibrium that govern the variation of six stress components from material point to material point along three orthogonal axes,

$$\frac{\partial \sigma_{ij}}{\partial x_j} + p_i = 0 \tag{1. 2}$$

The variation of internal deformations or kinematics is described using the concept of strain. Strain is defined in terms of displacements by measuring the change in the distance between any two infinitesimally close adjacent material points. This leads to the expressions for strain components in terms of three displacement components of a material point along the three axes, known as strain-displacement relations. In linear elasticity, strain is assumed to be small so that the strain valid for large deformation is replaced by its first-order approximation,

$$\epsilon_{ij} = \frac{1}{2}\left(\frac{\partial u_i}{\partial x_j} + \frac{\partial u_j}{\partial x_i}\right) + \frac{\partial u_k}{\partial x_i}\frac{\partial u_k}{\partial x_j} \rightarrow \epsilon_{ij} = \frac{1}{2}\left(\frac{\partial u_i}{\partial x_j} + \frac{\partial u_j}{\partial x_i}\right) \tag{1. 3}$$

where u's are the displacement components and x's are the coordinate components in the permutation notation. By definition, the nine strain components are symmetric, and may be shown to obey second-order tensor coordinate transformation laws. Whereas the three continuous displacement components may be varied arbitrarily, the six strain components may not because the integration of the six strain-displacement equations may not produce unique expressions of displacements if strain variation is prescribed arbitrarily. The uniqueness of displacements is ensured by compatibility conditions, which impose constraints on how each strain can vary with spatial coordinates.

$$\delta_{ijk}\delta_{pqr}\frac{\partial^2 \epsilon_{jq}}{\partial x_k \partial x_r} = 0 \tag{1. 4}$$

Three compatibility equations govern the variation of three in-plane strains in each plane, and the remaining three govern the variation of shear strains in each plane. They may be considered analogous to the stress equilibrium equations.

Constitutive equations describe the mechanical behavior of the continuum, and for a linearly elastic solid relate stress components (static variables) to strain components (kinematic variables). The most general way to relate the second-order stress tensor components to the corresponding strain components in a three-dimensional space is through a fourth-order tensor called the stiffness tensor as follows: $\sigma_{ij} = C_{ijkm}\varepsilon_{km}$, ensuring each stress component is a linear combination of all nine strain components. If the material is isotropic (independent of the orientation of the material tested), homogeneous and linearly elastic, the number of coefficients in fourth-order tensor is reduced to two, and the stress-strain relation is simplified as

$$\sigma_{ij} = \lambda\varepsilon_{kk}\delta_{ij} + 2\mu\epsilon_{ij} \tag{1. 5}$$

where λ and μ are known as Lamé's constants, and δ_{ij} is the Kronecker delta.

In general, the governing differential equations in elasticity represent the variation in the dependent variables, such as strain and stress, as a function of position and time. The governing differential equations involve derivatives with respect to spatial coordinates and time, the solution of problems in elasticity depends on the appropriate boundary and initial conditions. For example, an elasticity problem could be simplified as a boundary value problem if it is time-independent, and one can either employ the displacement formulation or stress formulation to solve this problem.

In the displacement formulation, the three stress equilibrium equations are expressed in terms of displacements using stress-strain and strain-displacement equations to yield three Navier's equations,

$$(\lambda + \mu)\frac{\partial^2 u_j}{\partial x_i \partial x_j} + \mu\frac{\partial^2 u_i}{\partial x_j \partial x_j} + p_i = 0 \tag{1. 6}$$

This formulation with continuous displacement fields automatically satisfies the compatibility conditions. Therefore, the displacements, strains and stresses (15 variables) can be solved from the strain-displacement equations, stress-strain relations and stress equilibrium equations (15 equations). Those fifteen equations can be incorporated into three Navier's equations for three displacement components in a homogenous isotropic medium. The other formulation is the stress formulation, which requires the satisfaction of the six strain compatibility equations. Stress formulation expresses strain compatibility equations in terms of six stress components using stress-strain relations and stress equilibrium equations where strain-displacement equations are not actually used. While Navier's equations depict a relationship for the displacements, the stress formulation alternatively develops a relationship for the stresses by incorporating the strain-stress relations into the compatibility equations, which are known as Beltrami-Michell equations.

$$\sigma_{ij,kk} + \frac{1}{1+\upsilon}\sigma_{kk,ij} = -\frac{\upsilon}{1-\upsilon}p_{k,k}\delta_{ij} - (p_{i,j} + p_{j,i}) \tag{1. 7}$$

A summary of the governing equations of elasticity described above is provided in the table below.

Table 1-1 The governing differential equations in elasticity

	Equation expression in index notation	Equation set index	Number of equations in each set
Strain-displacement equations	$\epsilon_{ij} = \frac{1}{2}\left(\frac{\partial u_i}{\partial x_j} + \frac{\partial u_j}{\partial x_i}\right)$	(1.1)	6
Constitutive equations (stress-strain relations)	$\sigma_{ij} = \begin{cases} C_{ijkm}\varepsilon_{km} \text{ (anisotropic)} \\ \lambda\varepsilon_{kk}\delta_{ij} + 2\mu\epsilon_{ij} \text{ (isotropic)} \end{cases}$	(1.2)	6
Stress equilibrium equations	$\frac{\partial \sigma_{ij}}{\partial x_j} + p_i = 0$	(1.3)	3
Strain compatibility equations	$\epsilon_{ijk}\epsilon_{pqr}\frac{\partial^2 e_{jq}}{\partial x_k \partial x_r} = 0$	(1.4)	6
Navier's equations	$(\lambda+\mu)\frac{\partial^2 u_j}{\partial x_i \partial x_j} + \mu\frac{\partial^2 u_i}{\partial x_j \partial x_j} + p_i = 0$	(1.1)+(1.2)+(1.3)	3
Beltrami-Michell equations	$\sigma_{ij,kk} + \frac{1}{1+\upsilon}\sigma_{kk,ij} = -\frac{\upsilon}{1-\upsilon}p_{k,k}\delta_{ij} - (p_{i,j} + p_{j,i})$	(1.2)+(1.3)+(1.4)	6

To solve a set of differential equations for an elasticity problem, boundary conditions are crucial to determine the solution from those governing differential equations with either displacement or stress formulation. Based on prescribed displacements, tractions, or both on the boundary of the analyzed object, there are three types of boundary conditions: displacement boundary conditions, traction boundary conditions and mixed boundary conditions with both prescribed displacements and tractions.

A general analytical solution to the three-dimensional governing differential equations for an arbitrarily shaped body does not exist. Hence elasticity problems are divided into classes of problems which enables simplification of the solution based on specific constraints and boundary conditions with appropriate assumptions made for the geometric shape of the object.

1.2 Categories of Elasticity Problems and Solution Methodologies

The categories of elasticity problems are based on geometry and the manner of boundary condition application that gives rise to specific functional forms of displacements, strains and stresses arising within the elastic body or structure. The extension, torsion and flexure of prismatic bars is directly applicable to structural engineering problems involving beams of arbitrary cross sections loaded on their ends only, with the bounding surface parallel to the axis traction free.

Plane problems is another large category applicable to prismatic bars with rectangular cross sections. Quasi-three-dimensional problems involving axisymmetric geometries and loading is another class that reduces to fields in cylindrical coordinates without longitudinal dependence. The most general class involves fully three-dimensional problems where the displacements, strains and stresses are functions of the three spatial coordinates, and hence require fully numerical formulations and solutions. The specific classes of problems and corresponding analytical solution methodologies that serve as validation tools for established or emerging alternative solution approaches are discussed in the sequel to motivate the approach taken in this dissertation in solving structural engineering problems.

1.2.1 Extension, Torsion and Flexure Problems

One technically important class of problems in the theory of elasticity concerns the study of prismatic bars of arbitrary cross section bounded by a cylindrical surface and by a pair of planes normal to the traction-free surface with loading applied only on its end faces. Suppose the length of such a bar is much longer than its transverse dimensions, the exact details of end face load application would not matter so long as the resultants forces or moments are statically equivalent to the applied ones. Based on Saint-Venant's principle, the effect of actual load distribution decays rapidly with the distance from the ends, leaving the stress or strain field in a central region depending only on the force resultants transmitted along the prismatic bar. The solution to such problems is directly applicable to beams of arbitrary cross section loaded on their end faces.

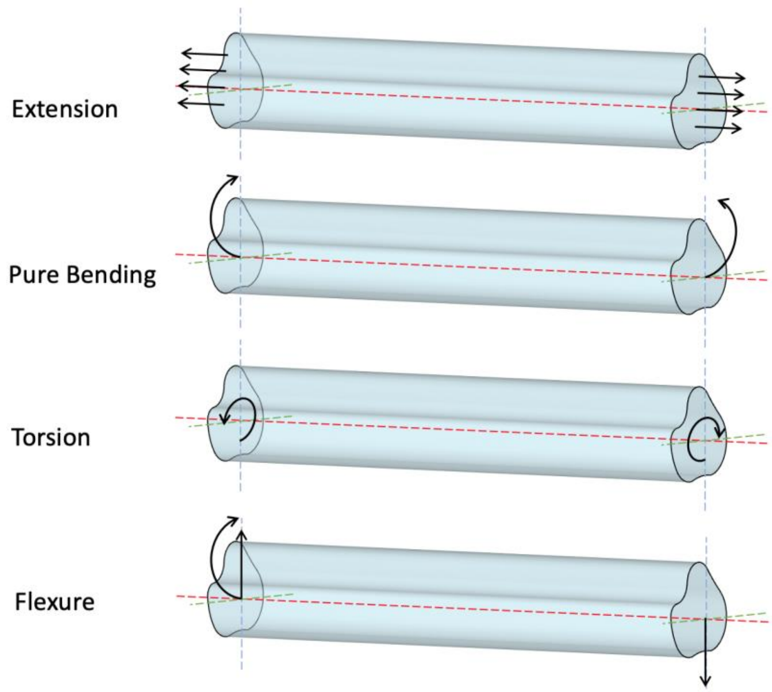

Figure 1-2 Four fundamental elasticity problems for prismatic bars

The complete problem of equilibrium of an elastic bar with a traction-free lateral surface can be solved by utilizing the principle of superposition because loading applied to the end faces may be decomposed into four elementary loadings that produce: extension, bending, torsion, and flexure (illustrated in Figure 1-2). The flexure problem involves loading of the bar's end-face by tangential force that produces not just bending about two axes orthogonal to the bar's longitudinal axis, but also twisting if not applied through a specific point. The identification of this point, as known as the shear center, is a key problem in the design of prismatic bars. The combined problem involving loading by end-face tangential forces that produce both bending and torsion is often known as the torsion-flexure problem.

The general way to solve the four elementary problems (extension, bending, torsion, and flexure) is the Saint-Venant's semi-inverse method. Categorizing a bar problem into any of those four consists of making certain assumptions about the components of stress, strain, or displacement, yet leaving enough freedom in the quantities involved to satisfy equilibrium and compatibility conditions. The extension of homogeneous isotropic beams by longitudinal forces has a straight-forward solution where the non-zero stress is the only normal stress in the direction of extension based on uniform stretch assumption. The stress in a bar subjected to a bending moment that produces constant curvature gives rise to axial normal stress that varies linearly across the bar’s cross section, with the origin set at the centroid. This result is valid for any cross-section’s shape. The remaining problems involving torsion and flexure require more intricate analysis and solution approaches and are discussed below.

Saint-Venant’s Torsion Problem

The solution to torsion problems occupies an important place in the theory of elasticity as it demonstrates an important solution technique that reduces a seemingly three-dimensional elasticity problem involving three unknown displacements to a two-dimensional one involving just one displacement. In this approach, known as Saint Venant's semi-inverse method, explicit expressions for the two in-plane displacements in the bar's cross section are obtained from geometric considerations of the deformation of a prismatic bar subjected to pure torsion by twisting moments directed along the bar's axis applied to the end faces. The out-of-plane displacement, proportional to the so-called warping function, is assumed to depend on the in-plane coordinates. The displacement field satisfies two of the three equilibrium equations of elasticity and produces only shear stresses acting on the bar's cross section that generates the applied twisting moment. The governing differential equation for the unknown warping function is the Laplace equation obtained from the third equilibrium equation, expressed in terms of displacements, that relates the out-of-plane shear stress components. The boundary conditions that the warping function must satisfy are given in terms of the normal derivative of the warping function on the cross-section’s boundary defined by the boundary itself. They are obtained from the traction-free condition on the bar’s lateral boundary. This formulation belongs to one of the boundary-value problems in the potential theory and may be solved in terms of harmonic functions. However, it is more convenient to reformulate the problem in terms of the Prandtl stress function defined to satisfy the third equilibrium equation directly. The Prandtl stress function is governed by the Poisson’s equation subject to simpler boundary conditions that may be used to construct solutions to a number of technologically important cross section using simple polynomials (circular, elliptical and triangular) or Fourier series (rectangular).

A general solution methodology to torsion problems involves the use of a complex potential, with real and imaginary harmonic parts representing the warping function and its complement, that may be expressed in terms of a series or constructed through a mapping of a unit circle onto the actual cross section of the bar, both in complex planes. The mapping function for an arbitrary cross section involves complex series whose coefficients dictate the actual shape. This approach requires the determination of the inverse transformation in the construction of the complex potential function which is typically done numerically. For this reason, numerical techniques based on variational principles or finite-difference approximation of the governing differential equations are prevalent for pure torsion of arbitrarily shaped cross sections.

Flexure Problem

The solution to the flexure problem is also obtained using the Saint-Venant's semi-inverse method, albeit based on the assumption of axial stress field motivated by the bending problem. The governing differential equations for the remaining stress components are obtained from the compatibility equations and reduced to the determination of three harmonic functions that represent bending about two orthogonal axes and twisting. The general torsion-flexure problem may be decoupled into pure torsion and bending problems if a point is found through which a prismatic bar, fixed at one end and loaded at the other, may be loaded to produce just pure bending. This point known as the shear center plays a significant role in the design of cantilever beams. By identifying the location of the shear center, one can minimize the local twisting in the torsion-flexure problem by applying the loading on it.

Analytical solutions have been developed for torsion-flexure problems, but they are limited to cross sections that are typically not of wide-ranging structural engineering interest. Beam cross sections that appear in structural designs, including I-beams, T-beams, and channel beams amongst many others, are not easily amenable to analytical techniques and require either thin-wall approximations when applicable or numerical solutions.

1.2.2 Plane Problems

Plane problems are two-dimensional problems wherein the stress and displacement components in the analysis plane of the structure depend on only two in-plane coordinates and the boundary conditions are imposed in that plane. They are simplified elasticity models that are more manageable than those simulated in real three-dimensions. In these simplified elasticity models, the variation of the specific mechanical response is neglected in the thickness direction.

There are two distinct types of two-dimensional problems: *plane strain* and *plane stress* (see Figure 1-3). Plane strain arises in the study of the deformation of large cylindrical bodies loaded by external forces so that the component of deformation in the direction of the axis of the cylinder vanishes. The remaining components do not vary along the length of the cylinder. Plane stress appears in the study of the deformation of thin plates without any capability to resist the stress in the out-of-plane direction. Therefore, the stress components in the direction of the thickness of the plate vanish. These two physically distinct assumptions can be useful when modeling certain idealized geometries and solving technically important structural problems.

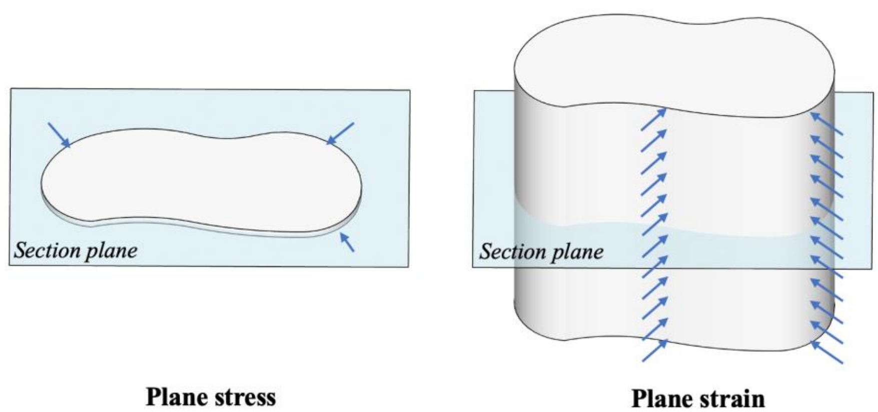

Figure 1-3 Plane stress (left) and plane strain (right) illustration

The solution of a problem under either the plane strain or plane stress assumptions involves finding a two-dimensional stress field, defined in terms of the in-plane stress components which satisfy the equilibrium equations, Eq. (1. 1), and for which the corresponding strains satisfy only one compatibility equation, Eq. (1. 4). Additionally, the relation between the in-plane shear stress and the in-plane shear strain stays the same for both assumptions. In fact, the equilibrium and compatibility equations are the same in both assumptions, with the only difference being in the relation between the stress and strain components.

The general method of solution of two-dimensional boundary value problems in elasticity requires proof of the existence of solutions, the method involving the complex variable is based on a reduction of the problems to the solutions of certain functional equations in a complex domain, thus effectively deduces explicit solutions of many technically important problems. In plane elasticity, Kolossoff (1909) put forward the systematic use of the complex variable theory. The complete conclusion was made forty years later inspired by the work of Muskhelishvili (1953). The boundary value problems in plane elasticity can always be reduced from a set of differential equations to solving a biharmonic equation of the case with the absence of body force. The Airy stress function, which relates to the three in-plane stress components, is specifically used for two-dimensional elasticity problems without any body forces. Therefore, stress fields that are derived from an Airy stress function which also satisfies the biharmonic equation will certainly satisfy equilibrium and correspond to compatible strain fields. Most three-dimensional problems are treated in terms of displacements instead of strains, which satisfies the requirement of compatibility identically. However, in two-dimensional problems, all except one of the compatibility equations degenerate to identities, so that a formulation in terms of stresses or strains is more practical than the displacements. Solving this sort of problem is essentially looking for the solution to the fundamental biharmonic boundary-value problem for a homogeneous isotropic elastic material. Because this boundary-value problem depends on the Airy stress function, two analytical functions of a complex variable rise to be the key to the general solution of the biharmonic solution. Analytical solutions to the biharmonic equation have their limitations in dealing with problems with irregular domains, therefore mapping to a unit circle was introduced to the complex theory method to better approximate the analyzed domains. Methods of the theory of functions of a complex variable and the conformal transformation can give solutions to planes with arbitrary shapes, and have been applied for solving many plane elasticity problems, yet they are not computationally efficient with high accuracy results because the mapping function is based on sufficient finite series of complex functions.

With the rapid development of composites technology, materials employed in beams can be tailored and assembled to achieve the required stiffness and strength of the beam. Composite beams are widely used in civil, mechanical and aerospace engineering to resist end loadings with better performance, for instance, reinforced concrete beams, rotating shafts in advanced motor engines, air-craft wings, etc. They all involve the problem of determining this “central” form of stress or strain distribution associated with various force resultant at the end of beam.

1.3 The Finite Volume Method in the Solution of Elasticity Problems

Numerical methods based on variational principles in mechanics can provide solutions to elasticity problems for which analytical solutions do not exist, in the case of complex geometries and heterogeneous materials for instance. These methods are in wide use because they only require use of standard functions and operations, thereby avoiding complex mathematical manipulation and computation. Variational formulation of boundary value problems may be traced to minimum hypotheses that minimize certain functionals and is based on the continuous development of solutions of differential equations by using variational ideas. Rayleigh (1896), Ritz (1909), and Galerkin (1968) were the major contributors to approximations of solutions based on variational methods in engineering applications at the end of the nineteenth century and in the early years of the twentieth century. Modern variational principles began with the works of Hellinger (1907) and Hu (1955), and Reissner (1950) (1965) (1985) on mixed variational principles for elasticity problems. The finite element method (FEM) then became a popular method for numerically solving differential equations in engineering practice. While solving an elasticity problem, the FEM discretizes a large object into smaller and simpler parts that are called finite elements. This is achieved by a particular space partitioning in the space dimensions, which is implemented by the construction of a mesh of the object: the numerical domain for the solution, which has a finite number of points. The finite element method formulation of a boundary value problem results in a system of algebraic equations rather than differential equations. The FEM approximates a solution at nodes by minimizing an associated error function via the calculus of variations, and finally gives the approximation of the unknown variables over the entire domain.

An attractive alternative to the solution of the elasticity problem is offered by the finite-volume method (FVM) which has gained popularity because of its explicit form and ability to deal with composite structures. FVM is a well-established numerical technique for the solution of boundary-value problems in fluid mechanics, cf. LeVeque (2002), Versteeg and Malalasekera (1965). The entire domain also requires discretization like FEM, but each partition is called “subvolume” as the conventional name of the domain is “volume” inherited from fluid mechanics.

Satisfaction of the governing field equations within subvolumes of the investigated discretized domain in an integral sense is a key feature of FVM which distinguishes it from variational techniques such as the finite-element method. In the context of fluid mechanics applications, this is done upon first expressing the field equations in a finite-difference form, and then extrapolating the grid point field variables to the subvolume surfaces surrounding each point to enable the required surface integration, thereby ensuring local field equation satisfaction in the integral sense. The simplicity and stability of the FVM in fluid mechanics applications have motivated the transition of this technique to solid mechanics problems as an alternative to the finite-element approach. Three versions of the finite-volume technique can be identified in the analysis of solid mechanics problems, as Cavalcante et al. (2012) discussed. These versions are characterized by different subvolume discretization of the investigated domain and different displacement field representations within subvolumes, which lead to a different manner of approximating field variables along subvolume surfaces.

The first two approaches, known as the cell-centered and cell vertex finite-volume techniques originally developed for homogeneous materials and structures, were motivated by the established finite-volume technique for fluid mechanics problems and elements of the finite-element method. The cell-centered FVM is similar to the original fluid mechanics version and employs subvolumes which are centered around grid points at which field variables are defined. In the cell vertex or vertex-based version, the finite-volume approach leverages elements of the finite-element method in domain discretization and displacement field approximation. The third version of FVM evolved independently and nearly in parallel to model materials with heterogeneous microstructures, including periodic and functionally graded materials, cf. Suquet (1985), Charalambakis and Murat (2006), Buryachenko (2007), Birman and Byrd (2007), Chatzigeorgiou et al. (2008), and Paulino et al. (2003). The structural finite-volume theory has its origins in the so-called Higher-Order Theory for Functionally Graded Materials (HOTFGM), developed in a sequence of papers in the 1990s and summarized in Aboudi et al. (1999). This theory provided the main framework for the construction of its homogenized counterpart initially named the Higher-Order Theory for Periodic Multiphase Materials by Aboudi et al. (2003). The structural and homogenized versions of these so-called higher-order theories were subsequently reconstructed in a sequence of papers by Bansal and Pindera (2003) (2005) (2006) and Zhong et al. (2004) by simplifying the discretization of the analysis domain which, in turn, facilitated implementation of the efficient local/global stiffness matrix approach, Bufler (1971), Pindera (1991). The re-constructed theories were further extended by Cavalcante et al. (2007), Gattu et al. (2008) and Khatam and Pindera (2009) by incorporating parametric mapping to enable efficient modeling of complex microstructures using quadrilateral subvolumes. The re-constructed finite-volume theories are similar to the cell-centered techniques that evolved in parallel for homogeneous materials and structures during the same time frame. However, in contrast with the early cell-centered techniques, the re-constructed theories employ explicit displacement field approximation within individual subvolumes, and follow an elasticity-based approach in satisfying interfacial displacement and traction continuity conditions in a surface-averaged sense. This is consistent with the satisfaction of equilibrium equations in a surface-averaged sense and leads to an explicit construction of local stiffness matrices for individual subvolumes which, in turn, substantially reduces the number of unknown variables, and allows direct comparison with the finite-element method. Assembly of local stiffness matrices into the global stiffness matrix is then performed such that the continuity of surface-averaged tractions and displacements is satisfied. The satisfaction of both traction and displacement continuity across subvolume faces produces a robust solution technique that naturally accommodates heterogeneous material microstructures. A review of FVM in solid mechanics applications has been recently provided by Cardiff and Demirdzic (2021).

1.4 Objectives

The overarching objective of this dissertation is to demonstrate the application of the FVM developed at the University of Virginia during the past twenty years to structural engineering problems involving torsion, flexure and plane problems of elasticity theory, thereby building a bridge between the two fields that are often treated separately. This involves further extension of the theory to enable solutions to the above classes of problems, and subsequent application to the solution of specific problems of importance in the design of structural engineering components as well as advanced material testing. Traditional and emerging structural components are considered, including components made up of laminated cross sections, and cross sections reinforced or weakened by cylindrical inclusions or cavities. Application to the testing of orthotropic and monoclinic materials using the off-axis tension test and Iosipescu shear test for the determination of axial and transverse moduli of unidirectional composites, is also provided through appropriate extension of the theory.

The proposed work fills the gap between structural engineering and mechanics on the one hand and elasticity theory formulation and limited solutions of the related problems when they cannot be treated using the analytical approach. It also provides a powerful alternative to the widespread use of variational techniques for the considered classes of structural engineering problems.

1.5 Contribution and Its Significance

While FVM has been used extensively in the solution of plane problems with isotropic materials, including contact and crack problems, there appear to be no reported results that address the use of FVM in the solution of plane problems with materials more complicated than orthotropic, such as monoclinic materials with a single plane of material symmetry. Materials with monoclinic elastic moduli in the coordinate system in which analysis is conducted are obtained by rotating a unidirectional composite through an angle about the out-of-plane axis. Multi-directional laminated plates made up of a number of such plies are employed in numerous structural engineering applications, including the aircraft industry. Off-axis plies are also employed in the determination of the axial shear modulus of advanced unidirectional composites based on the off-axis tension test because of its simplicity. The extended finite-volume theory enables re-examination of the effects of various parameters on the accuracy of the results obtained from this test method.

Selected problems involving laminated constructs with rectangular cross sections within the plane strain elasticity framework are also revisited in the context of microstructural effects introduced by the individual layers. Explicit treatment of such microstructures based on the finite-element method is challenging due to the need for extensive discretization when the elastic moduli contrast between the layers is large in the presence of large number of layers. Such problems are illustrated to be readily solved using FVM.

The major contributions of this dissertation include further extension of the finite-volume theory to the Saint-Venant's torsion problem involving arbitrarily shaped cross sections enabled by newly implemented parametric mapping, and the implementation of displacement-based formulation of the general flexure problem based on the inverse method. The parametric mapping capability is implemented within any structured or non-structured mesh framework. This is complemented by a novel incorporation of arbitrary discretization capability and the corresponding assembly algorithm for the global system of equations that enables efficient modeling of cross sections reinforced or weakened by inclusions or porosities, illustrated through examples from the plant world.

In addition, there is a need for accurate, efficient and easy-to-use computational tools that automatically generate results and provide quick answers to pure torsion and the more general torsion-flexure problems in the analysis and design of structural elements. The final products of this research are computer codes that enable pure torsion and combined torsion-flexure analysis of homogeneous and composite structures with the output given in terms of displacement, strain, and stress fields, as well as the torsion rigidity and shear center location, based on solid elasticity foundations. At present, this may only be achieved by a detailed finite-element analysis based on a variational principle that requires detailed meshing, as well as substantial training. The MATLAB-based computational tool executed through a user-friendly graphical user interface based on the developed finite-volume solution strategy will democratize structural engineering analysis in this area, increasing accessibility, and accelerating the development of novel structural designs.

1.6 Outline

The rest of this dissertation is organized as follows. Chapter 2 describes the parametric finite volume method solving for the solution of structural mechanics problems for orthotropic and monoclinic materials within the plane stress and plane strain frameworks, with application to on-axis and off-axis plies and laminated bars of rectangular cross section under tensile, shear and flexural loading. Chapter 3 illustrates the finite-volume solution of Saint-Venant's torsion problem for homogenous and heterogenous orthotropic prismatic bars of arbitrary cross section that require parametric mapping. Both elasticity and finite-element method results are included for comparison with the results generated by FVM based on displacement formulation. Extension of the theory to the general torsion-flexure of structures constructed with homogenous orthotropic materials is given in Chapter 4. The torsion-flexure performances of beams are both analyzed by FVM and analytical method for simple axis-symmetric geometry cross sections loading going through the centroid of the free end face. Chapter 5 discusses the twisting center of any cross sections subjected to torsion, and also includes the algorithm for finding the shear center of arbitrary homogenous shape cross sections via FVM. With the knowledge of the shear center location determined, FVM is further validated by the flexure for a category of heterogenous cantilever beam. Chapter 6 explores the three-dimensional structural problem of prismatic cantilever beams subjected to torsion-flexure deformation and assesses the constraint-induced effects for specific cross sections between the proposed FVM and three-dimensional finite-element method (3D FEM). Lastly, Chapter 7 summarizes the approach of bridging elasticity and structural engineering with FVM and the contributions to both elasticity and structural engineering communities.

Chapter 2

Plane Problems

2.1 Introduction

Solutions to most three-dimensional problems in structural engineering are typically not feasible to obtain analytically due to their complexity. However, many three-dimensional problems may be reduced to two-dimensional if the variation of specific mechanical response in one direction is negligible. This makes such reduced problems more manageable than those simulated in three dimensions. These types of simplifications produce approximate models which do not capture all the details in three dimensions, often not necessary, and the nature and accuracy of the approximation depend on the problems themselves and their loading conditions. Simplifying a three-dimensional problem greatly reduces the computational cost of structural analysis.

Two fundamental simplifications which are frequently used in solid mechanics are the *plane strain* and *plane stress* conditions, where solutions are developed for dimension-reduced problems with axis of symmetry or two-dimensionality. The problems within the plane stress and plane strain assumptions are categorized as *plane problems*, and plane strain and plane stress conditions simplify particular aspects of the complete problem formulation to a plane. The formulation of plane problems results in boundary value problems cast within a two-dimensional domain in a Cartesian coordinate system. Labeling the direction along which stress and strain quantities do not change as z, the plane problem analysis is reduced to the $x - y$ plane.

The solutions to plane elasticity problems using the finite volume method are well documented for isotropic materials, including those with spatial property variations called functionally graded materials cf., Cavalcante and Pindera (2007). Fewer FVM-based solutions to plane problems are available for orthotropic or monoclinic materials in the plane of analysis, including plates laminated with orthotropic layers subjected to bending by transverse loads. Hence in this chapter, the previously developed FVM is extended to the analysis of structural components composed of orthotropic and monoclinic in a state of plane stress, plane strain or generalized plane strain as appropriate, and applied to several technologically important problems.

2.2 Plane Problems

We consider problems involving structures of arbitrary cross section in the $x - y$ plane that are either very thin or very thick in the direction of the z axis. Moreover, the loading is applied in the $x - y$ plane in a manner that does not vary along the z axis, and the cross-section dimensions do not change along this axis. The material or materials making up the cross section obey generalized Hooke's law whose structure depends on the number of planes of material symmetry relative to the $x - y - z$ coordinate system. For orthotropic materials with three planes of symmetry, the stiffness matrix $[\boldsymbol{C}]$ of the generalized Hooke's law has the form,

$$[\boldsymbol{C}] = \begin{bmatrix} C_{11} & C_{12} & C_{13} & 0 & 0 & 0 \\ C_{12} & C_{22} & C_{23} & 0 & 0 & 0 \\ C_{13} & C_{23} & C_{33} & 0 & 0 & 0 \\ 0 & 0 & 0 & C_{44} & 0 & 0 \\ 0 & 0 & 0 & 0 & C_{55} & 0 \\ 0 & 0 & 0 & 0 & 0 & C_{66} \end{bmatrix} \tag{2. 1}$$

This form is general enough to admit unidirectional composites with the fibers oriented either along the x axis, y axis or z axis, with the corresponding relationships among the various stiffness matrix components. Additional relationships are obtained when the stiffness matrix represents isotropic materials. For monoclinic materials with the $x - y$ plane as the single plane of material symmetry, the stiffness matrix $[\boldsymbol{C}]$ has the form,

$$[\boldsymbol{C}] = \begin{bmatrix} C_{11} & C_{12} & C_{13} & 0 & 0 & C_{16} \\ C_{12} & C_{22} & C_{23} & 0 & 0 & C_{26} \\ C_{13} & C_{23} & C_{33} & 0 & 0 & C_{36} \\ 0 & 0 & 0 & C_{44} & C_{45} & 0 \\ 0 & 0 & 0 & C_{45} & C_{55} & 0 \\ C_{16} & C_{26} & C_{36} & 0 & 0 & C_{66} \end{bmatrix} \tag{2. 2}$$

This form represents a unidirectional composite with fibers rotated through an angle about the z axis, producing a material with just one plane of material symmetry in the fixed $x - y - z$ coordinate system.

Structural components with in-plane dimensions that are large relative to the thickness dimension along the z axis are assumed to be in plane stress condition in the $x - y$ plane, if they are homogeneous and if the lateral surfaces are traction free. In this case, the state of stress is assumed to have the following functional form,

$$\sigma_{xx} = \sigma_{xx}(x, y), \sigma_{yy} = \sigma_{yy}(x, y), \sigma_{xy} = \sigma_{xy}(x, y)$$
$$\sigma_{zz} = \sigma_{xz} = \sigma_{yz} = 0 \tag{2. 3}$$

where potential dependence of in-plane stresses on the z coordinate is neglected, and the out-of-plane stresses vanish given the lateral surface traction-free condition and the small thickness of the structure relative to cross-section dimensions. These assumptions imply that if there is a z dependence on the in-plane stress components, it is small. Additionally, the out-of-plane stresses, if present, are small relative to the in-plane stresses and are typically neglected. These approximations make the concept of plane stress an approximate one. Hence the corresponding strain components are also functions of only the in-plane coordinates x and y in light of Eqs. (2. 1) and (2. 2), with the additional result that the out-of-plane normal and shear strains vanish. With the absence of the stresses σ_{zz}, σ_{xz} and σ_{yz} in the assumption, the derivation of its compliance matrix reduced for monoclinic materials under the plane stress condition is elaborated in Appendix I.

Conversely, when the thickness dimension of the structural component becomes large relative to the in-plane dimensions, the deformation is prevented along the z axis, and the loading applied in the $x - y$ plane on the boundary of the cross section does not vary with the z coordinate, the functional form of the displacement field in the $x - y - z$ coordinate system becomes,

$$u = u(x, y), v = v(x, y), w = 0 \tag{2. 4}$$

Using strain-displacement relations, the corresponding strains have the functional form,

$$\begin{gathered} \epsilon_{xx} = \epsilon_{xx}(x, y), \epsilon_{yy} = \epsilon_{yy}(x, y), \gamma_{xy} = \gamma_{xy}(x, y) \\ \epsilon_{zz} = \gamma_{xz} = \gamma_{yz} = 0 \end{gathered} \tag{2. 5}$$

The above strain field in the plain strain condition produces stress field of the same functional form as that for the plane stress state, with the exception that the normal stress component σ_{zz} is also a function of the in-plane coordinates x and y, which is obtained directly from generalized Hooke's law. With the absence of the strains ϵ_{zz}, ϵ_{xz} and ϵ_{yz} in the assumption, the derivation of its compliance matrix reduced for monoclinic materials under the plane strain condition is also detailed in Appendix II.

The concept of generalized plane strain is similar to that of plane strain except that the constraint on the out-of-plane normal strain is replaced by $\epsilon_{zz} = \epsilon_{zz}^{o} = constant$. The constant is either specified or obtained from the condition that the average stress in the direction of the z axis is known, $\bar{\sigma}_{zz} = \int_A \sigma_{zz} dA$ (where A is the entire cross-sectional area). This average stress includes zero if no total force is acting in z direction.

The above assumptions on the functional form of stresses and displacements reduce the generalized Hooke's law, producing direct relations between the in-plane stresses and strains for plane stress, plane strain and generalized plane strain situations. Below, we list these reduced constitutive equations for the most general case of monoclinic material described by Eq. (2. 2). For plane stress problems, we obtain,

$$\begin{bmatrix} \sigma_{xx} \\ \sigma_{yy} \\ \sigma_{xy} \end{bmatrix} = \begin{bmatrix} \bar{C}_{11} & \bar{C}_{12} & \bar{C}_{16} \\ \bar{C}_{12} & \bar{C}_{22} & \bar{C}_{26} \\ \bar{C}_{16} & \bar{C}_{26} & \bar{C}_{66} \end{bmatrix} \begin{bmatrix} \epsilon_{xx} \\ \epsilon_{yy} \\ \gamma_{xy} \end{bmatrix} \tag{2. 6}$$

where $\bar{C}_{ij} = C_{ij} - \frac{C_{i3}C_{3j}}{C_{33}}$ $(i, j = 1, 2, 6)$ are called reduced stiffness elements. For orthotropic materials, the terms that couple normal stresses to shear strains, and vice versa, vanish, $C_{16} = C_{26} = C_{36} = C_{45} = 0$, which results in $\bar{C}_{16} = \bar{C}_{26} = 0$ and $\bar{C}_{66} = C_{66}$.

Alternatively, for plane strain problems, the relations between in-plane stresses and strains relations reduce directly to,

$$\begin{bmatrix} \sigma_{xx} \\ \sigma_{yy} \\ \sigma_{xy} \end{bmatrix} = \begin{bmatrix} C_{11} & C_{12} & C_{16} \\ C_{12} & C_{22} & C_{26} \\ C_{16} & C_{26} & C_{66} \end{bmatrix} \begin{bmatrix} \epsilon_{xx} \\ \epsilon_{yy} \\ \gamma_{xy} \end{bmatrix} \tag{2. 7}$$

with the out-of-plane normal stress σ_{zz} obtained in terms of the in-plane stresses. For generalized plane strain problems, the above constitutive relations are modified as follows,

$$\begin{bmatrix} \sigma_{xx} \\ \sigma_{yy} \\ \sigma_{xy} \end{bmatrix} = \begin{bmatrix} C_{11} & C_{12} & C_{16} \\ C_{12} & C_{22} & C_{26} \\ C_{16} & C_{26} & C_{66} \end{bmatrix} \begin{bmatrix} \epsilon_{xx} \\ \epsilon_{yy} \\ \gamma_{xy} \end{bmatrix} + \begin{bmatrix} C_{13} \\ C_{23} \\ C_{36} \end{bmatrix} \epsilon_{zz} \tag{2. 8}$$

where the overall out-of-plane strain ϵ_{zz}^{o} is either specified or determined as a part of the solution.

For all the above classes of plane problems, the in-plane stresses and strains are functions of the in-plane coordinates, the out-of-plane shear stresses and strains are zero, and the out-of-plane normal stress and strain are either zero or constant. Therefore, the essential governing differential equations described in Chapter 1, equilibrium reduces as follows,

$$\frac{\partial \sigma_{xx}}{\partial x} + \frac{\partial \sigma_{xy}}{\partial y} = 0$$
$$\frac{\partial \sigma_{xy}}{\partial x} + \frac{\partial \sigma_{yy}}{\partial y} = 0 \tag{2. 9}$$

in the absence of body forces, and compatibility reduces as follows

$$\frac{\partial^2 \epsilon_{xx}}{\partial y^2} + \frac{\partial^2 \epsilon_{yy}}{\partial x^2} = \frac{\partial^2 \gamma_{xy}}{\partial x \partial y} \tag{2. 10}$$

For plane stress problems, the additional compatibility equations that are not identically satisfied

$$\frac{\partial^2 \epsilon_{zz}}{\partial x^2} = \frac{\partial^2 \epsilon_{zz}}{\partial y^2} = \frac{\partial^2 \epsilon_{zz}}{\partial x \partial y} = 0 \tag{2. 11}$$

are simply neglected, which further highlights the approximate nature of the plane stress formulation even though solutions may satisfy exactly the reduced system of governing differential equations and the corresponding boundary conditions.

The above equations are solved subject to boundary conditions on the bounding surface of the structure that may be specified in terms of displacements,

$$u = u_C(x, y) \text{ on } C$$
$$v = v_C(x, y) \text{ on } C \tag{2. 12}$$

tractions,

$$t_x^n = \sigma_{xx}^{(C)} n_x + \sigma_{xy}^{(C)} n_y \text{ on } C$$

$$t_y^n = \sigma_{xy}^{(C)} n_x + \sigma_{yy}^{(C)} n_y \text{ on } C \tag{2. 13}$$

or a combination of the two.

Solutions to the above elasticity equations subject to the specified boundary conditions, dependent on the problem at hand, may be formulated using displacement or stress formulation for the three classes of problems discussed in the foregoing. In the displacement formulation, the stress equilibrium equations are expressed in terms of displacements using strain-displacement and constitutive equations, reducing the problem to two coupled partial differential equations in the unknown displacements $u(x, y)$ and $v(x, y)$ subject to displacement, traction, or mixed boundary conditions. These equations are similar for the three classes of plane problems, with the difference in the constant coefficients multiplying various partial derivatives of the displacements involving elastic moduli that depend on whichever plane stress, plane strain, or generalized plane strain problem is being solved.

In the stress formulation, the governing equations are the two stress equilibrium equations, Eq. (2. 9) and the surviving compatibility equation, Eq. (2. 10), which is then expressed in terms of in-plane stresses using the constitutive equations, and further simplified with the aid of the two stress equilibrium equations. A potential function called Airy's stress function is subsequently introduced from which in-plane stresses are derived such that the stress equilibrium equations are identically satisfied, thereby reducing the three equations to a single compatibility equation in the unknown potential. For isotropic materials, this fourth-order partial differential equation is known as the biharmonic equation which is characterized by the absence of material dependent coefficients associated with the various partial derivatives. Its solution has been described in Chapter 1 for plane problems. For orthotropic or monoclinic materials, the transformed compatibility equation contains material dependent coefficients, different for plane stress and plane strain problems, complicating the solution approaches. The monograph by Ting (1996) is one of the few authoritative books on anisotropic elasticity with applications to composite materials.

2.3 Finite Volume Method for Plane Problems

The finite volume method employs the displacement formulation to solve plane problems involving arbitrary cross sections of investigated structural components that may be homogeneous or heterogeneous. These features motivate the partition of the cross section into quadrilateral subvolumes that are assigned material properties which mimic the cross-section's microstructure and shape. The subvolumes may be isotropic, transversely isotropic in the $x - y$ plane, orthotropic or monoclinic. These quadrilateral subvolumes are the elementary units in the finite volume analysis wherein the local displacement fields are approximated using simple polynomial expressions. Using the displacement formulation ensures that the compatibility equations in each subvolume are identically satisfied, and the use of strain-displacement and constitutive equations leads to direct calculation of the local stress fields through simple differentiation. In addition, the use of simple polynomials precludes point-wise satisfaction of the displacement and traction components across common faces of adjacent subvolumes. Hence a compromise is employed that involves the imposition of interfacial displacement and traction continuity in a surface-average sense. The equilibrium equations are satisfied in a surface-average sense as well. Hence the solution strategy employed in FVM follows the elasticity-based solution strategy, albeit in a surface-average as opposed to a point-wise sense. Thus, it differs fundamentally from the variational-based solution strategies based on energy minimization. Whereas the subvolume equilibrium is always satisfied in a surface-average sense, the point-wise accuracy of the method increases with partition refinement.

The above overview of the method clearly suggests that the finite volume method was originally developed as a semi-analytical tool to account for material heterogeneity with arbitrary geometric shapes and distributions, and avoid intricate mathematical derivations in the presence of complex microstructural details in the solution of plane problems beyond isotropic materials. In this chapter, structures and components with orthotropic and monoclinic materials with the plane of material symmetry lying in the $x - y$ plane are analyzed due to their importance in the composite structural industry. This fills a void in the current literature where the majority of analyses are conducted for cross sections made up of isotropic materials.

The partitioning of the analyzed domain using (i) quadrilateral subvolumes to accommodate cross sections of arbitrary shapes is accomplished using parametric mapping of the actual quadrilateral subvolume in the physical plane, Figure 2-1 (left), onto the square domain in the reference plane, Figure 2-1 (right). The displacement field approximation is also made in the reference plane, and thus the FVM analysis, which entails the development of relations between displacement and traction quantities, is conducted in both planes. The establishment of these relations enables the construction of the local stiffness matrix for each quadrilateral subvolume in the physical plane that relates the surface-averaged in-plane displacements to the corresponding tractions. The local stiffness matrix is constructed such that the quadrilateral subvolume's equilibrium is satisfied in the physical plane, and the assembly of all the local stiffness matrices ensures that traction and displacement continuity, and prescribed boundary conditions are satisfied as well.

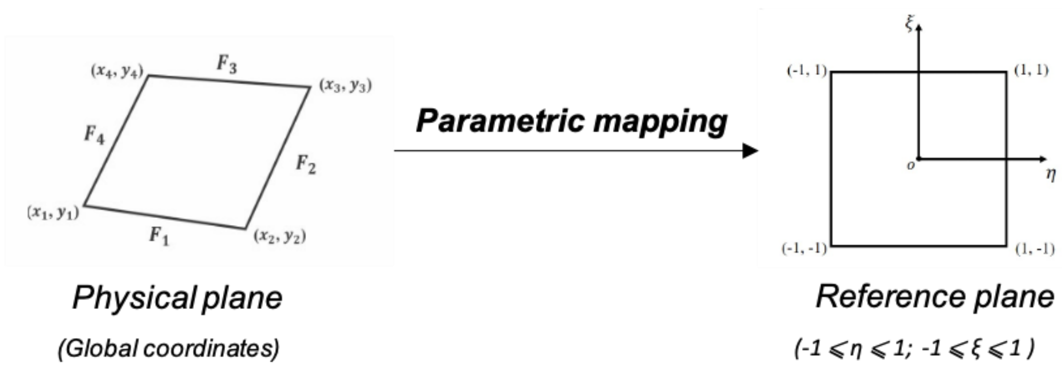

Figure 2-1 Mapping of square reference subvolume onto quadrilateral one used in the construction of meshes for FVM analysis

This section first describes the parametric mapping employed in the theory's construction, followed by subvolume discretization into quadrilateral partitions, displacement field construction, and the solution for these in-plane displacements using the parametric FVM. Towards this end, local coordinate systems $(\bar{x}, \bar{y})^{(i)}$ are set up at the subvolumes' centroids, where the coordinates $(x, y)^{(i)}$ of an arbitrary point within the subvolume (i) are referred to the global coordinate system. The global coordinates are employed in the parametric mapping described in the following subsection, whereas the local coordinates transferred in the reference system are employed in the in-plane displacement, strain, and stress field representation in each subvolume.

2.3.1 Parametric Mapping

The reference subvolume is a square in the $\eta - \xi$ plane bounded by $-1 \leq \eta \leq 1, 1 \leq \xi \leq 1$. The vertices are numbered such that the first set of coordinates is at the lower left corner and the numbering convention increases in a counterclockwise fashion. The faces are numbered similarly such that the face F_p lies between the vertices $\left(\bar{x}_p, \bar{y}_p\right)^{(i)}$ and $\left(\bar{x}_{p+1}, \bar{y}_{p+1}\right)^{(i)}$ with $p+1$ going to 1 when $p = 4$. Thus, the components of the unit normal vector $\boldsymbol{n_p^{(i)}} = \left[n_x, n_y\right]_p^{(i)}$ to the face F_p in each subvolume (i) are given by

$$n_{x|_p} = \frac{\bar{y}_{p+1}^{(i)} - \bar{y}_p^{(i)}}{l_p}, \; n_{y|_p} = \frac{\bar{x}_{p+1}^{(i)} - \bar{x}_p^{(i)}}{l_p} \tag{2. 14}$$

where $l_p = \sqrt{\left(\bar{x}_{p+1}^{(i)} - \bar{x}_p^{(i)}\right)^2 + \left(\bar{y}_{p+1}^{(i)} - \bar{y}_p^{(i)}\right)^2}$. The mapping if the point (η, ξ) in the reference subvolume to the corresponding point $(\bar{x}, \bar{y})^{(i)}$ in the subvolume of the actual discretized cross section is given by Cavalcante et al (2007).

$$\begin{aligned} \bar{x}^{(i)}(\eta, \xi) &= N_1(\eta, \xi)\bar{x}_1^{(i)} + N_2(\eta, \xi)\bar{x}_2^{(i)} + N_3(\eta, \xi)\bar{x}_3^{(i)} + N_4(\eta, \xi)\bar{x}_4^{(i)} \\ \bar{y}^{(i)}(\eta, \xi) &= N_1(\eta, \xi)\bar{y}_1^{(i)} + N_2(\eta, \xi)\bar{y}_2^{(i)} + N_3(\eta, \xi)\bar{y}_3^{(i)} + N_4(\eta, \xi)\bar{y}_4^{(i)} \end{aligned} \tag{2. 15}$$

where $N_1(\eta, \xi) = \frac{1}{4}(1-\eta)(1-\xi)$, $N_2(\eta, \xi) = \frac{1}{4}(1+\eta)(1-\xi)$, $N_3(\eta, \xi) = \frac{1}{4}(1+\eta)(1+\xi)$, $N_4(\eta, \xi) = \frac{1}{4}(1-\eta)(1+\xi)$.

The determination of the strains and stresses within quadrilateral subvolumes requires the relationship between first partial derivatives of the subvolume displacements (general expression: φ) in the two planes $\eta - \xi$ and $x - y$. These are related through the Jacobian $\boldsymbol{J}$ and its inverse $\boldsymbol{J}^{-1}$,

$$\begin{bmatrix} \dfrac{\partial \varphi}{\partial \eta} \\ \dfrac{\partial \varphi}{\partial \xi} \end{bmatrix}^{(i)} = \boldsymbol{J} \begin{bmatrix} \dfrac{\partial \varphi}{\partial x} \\ \dfrac{\partial \varphi}{\partial y} \end{bmatrix}^{(i)} \leftrightarrow \begin{bmatrix} \dfrac{\partial \varphi}{\partial x} \\ \dfrac{\partial \varphi}{\partial y} \end{bmatrix}^{(i)} = \boldsymbol{J}^{-1} \begin{bmatrix} \dfrac{\partial \varphi}{\partial \eta} \\ \dfrac{\partial \varphi}{\partial \xi} \end{bmatrix}^{(i)} \tag{2. 16}$$

where the Jacobian $\boldsymbol{J}$ is obtained from the transformation equations in the form

$$\boldsymbol{J} = \begin{bmatrix} \dfrac{\partial \bar{x}^{(i)}}{\partial \eta} & \dfrac{\partial \bar{y}^{(i)}}{\partial \eta} \\ \dfrac{\partial \bar{x}^{(i)}}{\partial \xi} & \dfrac{\partial \bar{y}^{(i)}}{\partial \xi} \end{bmatrix} = \begin{bmatrix} A_1^{(i)} + A_2^{(i)}\xi & A_4^{(i)} + A_5^{(i)}\xi \\ A_3^{(i)} + A_2^{(i)}\eta & A_6^{(i)} + A_5^{(i)}\eta \end{bmatrix} \tag{2. 17}$$

with $A_1, \ldots, A_6$ are given in terms of the vertex coordinates $\left(\bar{x}_p, \bar{y}_p\right)^{(i)}$

$A_1^{(i)} = \frac{1}{4}(-\bar{x}_1 + \bar{x}_2 + \bar{x}_3 - \bar{x}_4)^{(i)}$, $A_2^{(i)} = \frac{1}{4}(\bar{x}_1 - \bar{x}_2 + \bar{x}_3 - \bar{x}_4)^{(i)}$

$A_3^{(i)} = \frac{1}{4}(-\bar{x}_1 - \bar{x}_2 + \bar{x}_3 + \bar{x}_4)^{(i)}$, $A_4^{(i)} = \frac{1}{4}(-\bar{y}_1 + \bar{y}_2 + \bar{y}_3 - \bar{y}_4)^{(i)}$

$A_5^{(i)} = \frac{1}{4}(\bar{y}_1 - \ y_2 + \bar{y}_3 - \bar{y}_4)^{(i)}$, $A_6^{(i)} = \frac{1}{4}(-\bar{y}_1 - \ y_2 + \bar{y}_3 + \bar{y}_4)^{(i)}$

For consistency with the surface-averaging framework of the finite-volume theory, the two sets of partial derivatives are connected through the volume-averaged Jacobian $\bar{\boldsymbol{J}}$,

$$\bar{\boldsymbol{J}} = \frac{1}{4}\int_{-1}^{+1}\int_{-1}^{+1} \boldsymbol{J} d\eta d\xi = \begin{bmatrix} A_1 & A_4 \\ A_3 & A_6 \end{bmatrix}^{(i)} \tag{2. 18}$$

with the inverse $\bar{\boldsymbol{J}}^{-1}$

$$\bar{\boldsymbol{J}}^{-1} = \frac{1}{|\bar{\boldsymbol{J}}|}\begin{bmatrix} A_6 & -A_4 \\ -A_3 & A_1 \end{bmatrix}^{(i)} = \frac{1}{A_1^{(i)}A_6^{(i)} - A_3^{(i)}A_4^{(i)}}\begin{bmatrix} A_6^{(i)} & -A_4^{(i)} \\ -A_3^{(i)} & A_1^{(i)} \end{bmatrix} \tag{2. 19}$$

In constructing the local stiffness matrix for each subvolume in terms of the surface-averaged displacements and tractions, $\boldsymbol{J}^{-1}$ is replaced by $\bar{\boldsymbol{J}}^{-1}$ in order to generate the elements of the stiffness matrix in closed form. This replacement avoids costly numerical integrations. For each subvolume (i),

$$\begin{gathered}
\begin{bmatrix} \dfrac{\widehat{\partial\varphi}}{\partial x} \\ \dfrac{\widehat{\partial\varphi}}{\partial y} \end{bmatrix}^{(i)}_{\xi=\mp1} = \bar{\boldsymbol{J}}^{-1(i)} \begin{bmatrix} \dfrac{\widehat{\partial\varphi}}{\partial \eta} \\ \dfrac{\widehat{\partial\varphi}}{\partial \xi} \end{bmatrix}^{(i)}_{\xi=\mp1} = \frac{1}{|\bar{\boldsymbol{J}}|^{(i)}}\begin{bmatrix} A_6 & -A_4 & 0 & \pm3A_4 \\ -A_3 & A_1 & 0 & \mp3A_1 \end{bmatrix}^{(i)} \begin{bmatrix} W_{\varphi(10)} \\ W_{\varphi(01)} \\ W_{\varphi(20)} \\ W_{\varphi(02)} \end{bmatrix}^{(i)} \\
\begin{bmatrix} \dfrac{\widehat{\partial\varphi}}{\partial x} \\ \dfrac{\widehat{\partial\varphi}}{\partial y} \end{bmatrix}^{(i)}_{\eta=\pm1} = \bar{\boldsymbol{J}}^{-1(i)} \begin{bmatrix} \dfrac{\widehat{\partial\varphi}}{\partial \eta} \\ \dfrac{\widehat{\partial\varphi}}{\partial \xi} \end{bmatrix}^{(i)}_{\eta=\pm1} = \frac{1}{|\bar{\boldsymbol{J}}|^{(i)}}\begin{bmatrix} A_6 & -A_4 & \pm3A_6 & 0 \\ -A_3 & A_1 & \mp3A_3 & 0 \end{bmatrix}^{(i)} \begin{bmatrix} W_{\varphi(10)} \\ W_{\varphi(01)} \\ W_{\varphi(20)} \\ W_{\varphi(02)} \end{bmatrix}^{(i)}
\end{gathered} \tag{2. 20}$$

where $\varphi(x, y)$ could be any of the selected field quantities. Some concise notations of the vectors in the expressions above are made for convenience of notation,

$$\boldsymbol{a}_{1,3}^{(i)} = \frac{1}{|\bar{J}|^{(i)}}[A_6 \quad -A_4 \quad 0 \quad \pm3A_4]^{(i)}, \boldsymbol{a}_{2,4}^{(i)} = \frac{1}{|\bar{J}|^{(i)}}[A_6 \quad -A_4 \quad \pm3A_6 \quad 0]^{(i)},$$

$$\boldsymbol{b}_{1,3}^{(i)} = \frac{1}{|\bar{J}|^{(i)}}[-A_3 \quad A_1 \quad 0 \quad \mp3A_1]^{(i)}, \boldsymbol{b}_{2,4}^{(i)} = \frac{1}{|\bar{J}|^{(i)}}[-A_3 \quad A_1 \quad \mp3A_3 \quad 0]^{(i)}$$

And also $\boldsymbol{W}_{\varphi}^{(i)}$ is used to denote the vector of coefficients in the second-order expansion of $\varphi(x, y)$ which will be explained in detail in the following section.

$$
\boldsymbol{W}_{\varphi}^{(i)} = \begin{bmatrix} W_{\varphi(10)} \\ W_{\varphi(01)} \\ W_{\varphi(20)} \\ W_{\varphi(02)} \end{bmatrix}^{(i)}
$$

2.3.2 Displacement and Stress Fields

The two in-plane displacements are approximated in each subvolume using a second-order expansion in the local coordinates as follows,

$$
\begin{aligned}
u^{(i)} &= W_{u(00)}^{(i)} + \eta^{(i)} W_{u(10)}^{(i)} + \xi^{(i)} W_{u(01)}^{(i)} + \frac{1}{2}\left(3\eta^{(i)^2} - 1\right) W_{u(20)}^{(i)} \\
&\quad + \frac{1}{2}\left(3\xi^{(i)^2} - 1\right) W_{u(02)}^{(i)} \\
v^{(i)} &= W_{v(00)}^{(i)} + \eta^{(i)} W_{v(10)}^{(i)} + \xi^{(i)} W_{v(01)}^{(i)} + \frac{1}{2}\left(3\eta^{(i)^2} - 1\right) W_{v(20)}^{(i)} \\
&\quad + \frac{1}{2}\left(3\xi^{(i)^2} - 1\right) W_{v(02)}^{(i)}
\end{aligned}
\tag{2. 21}
$$

$w = \epsilon_{zz} z$ ($\epsilon_{zz} = 0$ if it is plane stress/strain)

where $W_{u(mn)}^{(i)}$ and $W_{v(mn)}^{(i)}$ are unknown coefficients subsequently redefined in terms of the surface-averaged displacements along the four subvolume faces ($p = 1, 2, 3, 4$ following the subvolume faces order convention described in Eq. (2. 14)). The above displacement field representations produce the three in-plane strains and an additional out-of-plane normal strain for the generalized plane strain case,

$$
\hat{\epsilon}_{xx|p}^{(i)} = \frac{\widehat{\partial u}^{(i)}}{\partial x_p} = \boldsymbol{a}_p^{(i)} \boldsymbol{W}_u^{(i)} \tag{2. 22}
$$

$$\hat{\epsilon}_{yy|p}^{(i)} = \widehat{\frac{\partial v}{\partial y}}_p^{(i)} = \boldsymbol{b}_p^{(i)} \boldsymbol{W}_v^{(i)}$$

$$\hat{\gamma}_{xy|p}^{(i)} = \widehat{\frac{\partial u}{\partial y}}_p^{(i)} + \widehat{\frac{\partial v}{\partial x}}_p^{(i)} = \boldsymbol{b}_p^{(i)} \boldsymbol{W}_u^{(i)} + \boldsymbol{a}_p^{(i)} \boldsymbol{W}_v^{(i)}$$

$$\hat{\epsilon}_{zz|p}^{(i)} = \widehat{\frac{\partial w}{\partial x}}_p^{(i)} = \epsilon_{zz} \ (\epsilon_{zz} = 0 \text{ if it is classic plane stress/strain})$$

The subvolumes may be occupied by monoclinic materials whose stiffness matrix elements, in the case of unidirectional composites, may be obtained by rotational transformation about the z axis from the principal material coordinate system wherein they are orthotropic. The reduced constitutive equations contain stiffness matrix elements that dependent on the plane case considered, and these elements may vary from subvolume to subvolume as is the case in functionally graded materials within the framework of the specific plane case. The corresponding in-plane stress components (σ_{zz} may be of interest in generalized plane strain condition) in these planes in each subvolume are given, respectively, below after substituting the surface-averaged expressions in Eq. (2. 22):

Plane strain

$$\begin{bmatrix} \hat{\sigma}_{xx} \\ \hat{\sigma}_{yy} \\ \hat{\sigma}_{xy} \end{bmatrix}_p^{(i)} = \begin{bmatrix} C_{11} & C_{12} & C_{16} \\ C_{12} & C_{22} & C_{26} \\ C_{16} & C_{26} & C_{66} \end{bmatrix}^{(i)} \begin{bmatrix} \boldsymbol{a}_p^{(i)} \boldsymbol{W}_u^{(i)} \\ \boldsymbol{b}_p^{(i)} \boldsymbol{W}_v^{(i)} \\ \boldsymbol{b}_p^{(i)} \boldsymbol{W}_u^{(i)} + \boldsymbol{a}_p^{(i)} \boldsymbol{W}_v^{(i)} \end{bmatrix} \qquad (2.\ 23)$$

Generalized plane strain

$$\begin{bmatrix} \hat{\sigma}_{xx} \\ \hat{\sigma}_{yy} \\ \hat{\sigma}_{xy} \end{bmatrix}_p^{(i)} = \begin{bmatrix} C_{11} & C_{12} & C_{16} \\ C_{12} & C_{22} & C_{26} \\ C_{16} & C_{26} & C_{66} \end{bmatrix}^{(i)} \begin{bmatrix} \boldsymbol{a}_p^{(i)} \boldsymbol{W}_u^{(i)} \\ \boldsymbol{b}_p^{(i)} \boldsymbol{W}_v^{(i)} \\ \boldsymbol{b}_p^{(i)} \boldsymbol{W}_u^{(i)} + \boldsymbol{a}_p^{(i)} \boldsymbol{W}_v^{(i)} \end{bmatrix} + \begin{bmatrix} C_{13} \\ C_{23} \\ C_{36} \end{bmatrix} \epsilon_{zz} \tag{2. 24}$$

Plane stress

$$\begin{bmatrix} \hat{\sigma}_{xx} \\ \hat{\sigma}_{yy} \\ \hat{\sigma}_{xy} \end{bmatrix}_p^{(i)} = \begin{bmatrix} \bar{C}_{11} & \bar{C}_{12} & \bar{C}_{16} \\ \bar{C}_{21} & \bar{C}_{22} & \bar{C}_{26} \\ \bar{C}_{16} & \bar{C}_{26} & \bar{C}_{66} \end{bmatrix}^{(i)} \begin{bmatrix} \boldsymbol{a}_p^{(i)} \boldsymbol{W}_u^{(i)} \\ \boldsymbol{b}_p^{(i)} \boldsymbol{W}_v^{(i)} \\ \boldsymbol{b}_p^{(i)} \boldsymbol{W}_u^{(i)} + \boldsymbol{a}_p^{(i)} \boldsymbol{W}_v^{(i)} \end{bmatrix} \tag{2. 25}$$

2.3.3 Local Stiffness Matrix Construction

In order to reduce the number of unknown coefficients in the in-plane displacement approximation when cross sections are discretized into a large number of subvolumes, we re-formulate the plane problem in terms of surface-averaged displacements on the four faces of each subvolume as the primary solution variables. Then we construct a local stiffness matrix for each subvolume by relating the surface-average displacements to the corresponding surface-average tractions. We start by defining the surface-average displacements,

$$\begin{aligned}
\hat{u}_{1,3}^{(i)} &= \frac{1}{2}\int_{-1}^{1} u^{(i)}(\eta, \xi = \mp 1) d\eta = W_{u(00)}^{(i)} \mp W_{u(01)}^{(i)} + W_{u(02)}^{(i)} \\
\hat{u}_{2,4}^{(i)} &= \frac{1}{2}\int_{-1}^{1} u^{(i)}(\eta = \pm 1, \xi) d\xi = W_{u(00)}^{(i)} \pm W_{u(10)}^{(i)} + W_{u(20)}^{(i)} \\
\hat{v}_{1,3}^{(i)} &= \frac{1}{2}\int_{-1}^{1} v^{(i)}(\eta, \xi = \mp 1) d\eta = W_{v(00)}^{(i)} \mp W_{v(01)}^{(i)} + W_{v(02)}^{(i)} \\
\hat{v}_{2,4}^{(i)} &= \frac{1}{2}\int_{-1}^{1} v^{(i)}(\eta = \pm 1, \xi) d\xi = W_{v(00)}^{(i)} \pm W_{v(10)}^{(i)} + W_{v(20)}^{(i)}
\end{aligned} \tag{2. 26}$$

Hence the first and second-order coefficients $W_{u(mn)}^{(i)}$ and $W_{v(mn)}^{(i)}$ may be expressed in terms of the surface-averaged displacements and the zero-order coefficients $W_{u(00)}^{(i)}$ and $W_{v(00)}^{(i)}$,

$$\boldsymbol{W}_u^{(i)} = \begin{bmatrix} W_{u(10)} \\ W_{u(01)} \\ W_{u(20)} \\ W_{u(02)} \end{bmatrix}^{(i)} = \frac{1}{2}\begin{bmatrix} 0 & 1 & 0 & -1 \\ -1 & 0 & 1 & 0 \\ 0 & 1 & 0 & 1 \\ 1 & 0 & 1 & 0 \end{bmatrix}\begin{bmatrix} \hat{u}_1 \\ \hat{u}_2 \\ \hat{u}_3 \\ \hat{u}_4 \end{bmatrix}^{(i)} - \begin{bmatrix} 0 \\ 0 \\ 1 \\ 1 \end{bmatrix} W_{u(00)}^{(i)}$$

$$\boldsymbol{W}_v^{(i)} = \begin{bmatrix} W_{v(10)} \\ W_{v(01)} \\ W_{v(20)} \\ W_{v(02)} \end{bmatrix}^{(i)} = \frac{1}{2}\begin{bmatrix} 0 & 1 & 0 & -1 \\ -1 & 0 & 1 & 0 \\ 0 & 1 & 0 & 1 \\ 1 & 0 & 1 & 0 \end{bmatrix}\begin{bmatrix} \hat{v}_1 \\ \hat{v}_2 \\ \hat{v}_3 \\ \hat{v}_4 \end{bmatrix}^{(i)} - \begin{bmatrix} 0 \\ 0 \\ 1 \\ 1 \end{bmatrix} W_{v(00)}^{(i)} \tag{2. 27}$$

or

$$\boldsymbol{W}_u^{(i)} = \frac{1}{2}\boldsymbol{\alpha}\hat{\boldsymbol{u}}^{(i)} - \boldsymbol{\beta} W_{u(00)}^{(i)}$$

$$\boldsymbol{W}_v^{(i)} = \frac{1}{2}\boldsymbol{\alpha}\hat{\boldsymbol{v}}^{(i)} - \boldsymbol{\beta} W_{v(00)}^{(i)}$$

Similarly, the corresponding surface-averaged interfacial tractions are defined as follows,

$$\hat{t}_{x|1,3}^{(i)} = \frac{1}{2}\int_{-1}^{1} t_x^{(i)}(\eta, \xi = \mp 1)\, d\eta$$

$$\hat{t}_{x|2,4}^{(i)} = \frac{1}{2}\int_{-1}^{1} t_x^{(i)}(\eta = \pm 1, \xi)\, d\xi \tag{2. 28}$$

$$\hat{t}_{y|1,3}^{(i)} = \frac{1}{2}\int_{-1}^{1} t_y^{(i)}(\eta, \xi = \mp 1)\, d\eta$$

$$\hat{t}^{(i)}_{y|2,4} = \frac{1}{2}\int_{-1}^{1} t^{(i)}_{y}(\eta = \pm 1, \xi) d\xi$$

where the traction vector associated with the face p characterized by the unit normal vector $\boldsymbol{n}_p$ is $t^{(i)}_x|_p = \sigma^{(i)}_{ix} n^{(i)}_i|_p \; (i = x, y)$ and $t^{(i)}_y|_p = \sigma^{(i)}_{iy} n^{(i)}_i|_p \; (i = x, y)$. Hence the traction vector components on any of the four subvolume faces become, in terms of the three in-plane stress components,

$$\hat{t}^{(i)}_{x|p} = [\hat{\sigma}^{(i)}_{xx} n^{(i)}_x + \hat{\sigma}^{(i)}_{xy} n^{(i)}_y]_p$$
$$\hat{t}^{(i)}_{y|p} = [\hat{\sigma}^{(i)}_{xy} n^{(i)}_x + \hat{\sigma}^{(i)}_{yy} n^{(i)}_y]_p \tag{2. 29}$$

which are expressed in terms of the corresponding surface-averaged shear strains for the three plane strain cases below.

Plane strain

$$\hat{t}^{(i)}_{x|p} = \left([C_{11} \quad C_{12} \quad C_{16}]^{(i)} n^{(i)}_{x|p} + [C_{16} \quad C_{26} \quad C_{66}]^{(i)} n^{(i)}_{y|p}\right) \begin{bmatrix} \boldsymbol{a}_p \boldsymbol{W}_u \\ \boldsymbol{b}_p \boldsymbol{W}_v \\ \boldsymbol{b}_p \boldsymbol{W}_u + \boldsymbol{a}_p \boldsymbol{W}_v \end{bmatrix}^{(i)}$$
$$\hat{t}^{(i)}_{y|p} = \left([C_{16} \quad C_{26} \quad C_{66}]^{(i)} n^{(i)}_{x|p} + [C_{21} \quad C_{22} \quad C_{26}]^{(i)} n^{(i)}_{y|p}\right) \begin{bmatrix} \boldsymbol{a}_p \boldsymbol{W}_u \\ \boldsymbol{b}_p \boldsymbol{W}_v \\ \boldsymbol{b}_p \boldsymbol{W}_u + \boldsymbol{a}_p \boldsymbol{W}_v \end{bmatrix}^{(i)} \tag{2. 30}$$

Generalized plane strain

$$\hat{t}_{x|p}^{(i)} = \Big([C_{11} \quad C_{12} \quad C_{16}]^{(i)} n_{x|p}^{(i)} + [C_{16} \quad C_{26} \quad C_{66}]^{(i)} n_{y|p}^{(i)} \Big)$$

$$\begin{bmatrix} \boldsymbol{a}_p \boldsymbol{W}_u \\ \boldsymbol{b}_p \boldsymbol{W}_v \\ \boldsymbol{b}_p \boldsymbol{W}_u + \boldsymbol{a}_p \boldsymbol{W}_v \end{bmatrix}^{(i)} + (C_{13} n_{x|p}^{(i)} + C_{36} n_{y|p}^{(i)}) \epsilon_{zz}$$

$$\hat{t}_{y|p}^{(i)} = \Big([C_{16} \quad C_{26} \quad C_{66}]^{(i)} n_{x|p}^{(i)} + [C_{12} \quad C_{22} \quad C_{26}]^{(i)} n_{y|p}^{(i)} \Big) \tag{2. 31}$$

$$\begin{bmatrix} \boldsymbol{a}_p \boldsymbol{W}_u \\ \boldsymbol{b}_p \boldsymbol{W}_v \\ \boldsymbol{b}_p \boldsymbol{W}_u + \boldsymbol{a}_p \boldsymbol{W}_v \end{bmatrix}^{(i)} + (\bar{C}_{36} n_{x|p}^{(i)} + \bar{C}_{23} n_{y|p}^{(i)}) \epsilon_{zz}$$

Plane stress

$$\hat{t}_{x|p}^{(i)} = \Big([\bar{C}_{11} \quad \bar{C}_{12} \quad \bar{C}_{16}]^{(i)} n_{x|p}^{(i)} + [\bar{C}_{16} \quad \bar{C}_{26} \quad \bar{C}_{66}]^{(i)} n_{y|p}^{(i)} \Big)$$

$$\begin{bmatrix} \boldsymbol{a}_p \boldsymbol{W}_u \\ \boldsymbol{b}_p \boldsymbol{W}_v \\ \boldsymbol{b}_p \boldsymbol{W}_u + \boldsymbol{a}_p \boldsymbol{W}_v \end{bmatrix}^{(i)}$$

$$\hat{t}_{y|p}^{(i)} = \Big([\bar{C}_{16} \quad \bar{C}_{26} \quad \bar{C}_{66}]^{(i)} n_{x|p}^{(i)} + [\bar{C}_{21} \quad \bar{C}_{22} \quad \bar{C}_{26}]^{(i)} n_{y|p}^{(i)} \Big) \tag{2. 32}$$

$$\begin{bmatrix} \boldsymbol{a}_p \boldsymbol{W}_u \\ \boldsymbol{b}_p \boldsymbol{W}_v \\ \boldsymbol{b}_p \boldsymbol{W}_u + \boldsymbol{a}_p \boldsymbol{W}_v \end{bmatrix}^{(i)}$$

The last step in the construction of the local stiffness matrix is to express the zero-order coefficients $W_{u(00)}^{(i)}$ and $W_{v(00)}^{(i)}$ in terms of the surface-averaged displacements. This is achieved by satisfying the first two equilibrium equations in the surface-averaged sense. The surface tractions associated with each face of the (i) subvolume are related to each other through the equilibrium equations satisfied in a volume-average sense. Using Gauss Theorem, the equilibrium equations are expressed in terms of surface-averaged traction components,

$$\oint_s \sigma_{jx}^{(i)} n_j^{(i)} ds = \oint_s t_x^{(i)}\ ds = \sum_{p=1}^{4} \hat{t}_x^{(i)} l_p^{(i)} = 0$$

$$\oint_s \sigma_{jy}^{(i)} n_j^{(i)} ds = \oint_s t_y^{(i)}\ ds = \sum_{p=1}^{4} \hat{t}_y^{(i)} l_p^{(i)} = 0 \qquad (2.\ 33)$$

where s is the contour of subvolume (i) boundary.

Expanding the summation equations Eq. (2. 33) for the surface-averaged tractions multiplied with the corresponding length over each subvolume contour, there are two equations for each plane condition describing the stress equilibrium in the surface-averaged sense in x and y directions that may be expressed in the same symbolic form:

$$X\ direction\colon\ \mathcal{A}^{(i)} \boldsymbol{W}_u^{(i)} + \mathcal{B}^{(i)} \boldsymbol{W}_v^{(i)} = \epsilon_{zz} \mathsf{C}_{\mathcal{AB}}$$

$$Y\ direction\colon \mathcal{C}^{(i)} \boldsymbol{W}_u^{(i)} + \mathcal{D}^{(i)} \boldsymbol{W}_v^{(i)} = \epsilon_{zz} \mathsf{C}_{\mathcal{CD}} \qquad (2.\ 34)$$

where the coefficients $\mathcal{A}^{(\mathrm{i})}$, $\mathcal{B}^{(i)}$, $\mathcal{C}^{(i)}$, $\mathcal{D}^{(i)}$, $\mathsf{C}_{\mathcal{AB}}$ and $\mathsf{C}_{\mathcal{CD}}$ for the three plane cases are,

Plane strain and generalized plane strain

$$\mathcal{A}^{(i)} = \sum_{p=1}^{4} \left(C_{11}^{(i)} n_{x|p}^{(i)} + C_{16}^{(i)} n_{y|p}^{(i)} \right) \boldsymbol{a}_p^{(i)} l_p^{(i)} + \sum_{p=1}^{4} \left(C_{16}^{(i)} n_{x|p}^{(i)} + C_{66}^{(i)} n_{y|p}^{(i)} \right) \boldsymbol{b}_p^{(i)} l_p^{(i)}$$

$$\mathcal{B}^{(i)} = \sum_{p=1}^{4} \left(C_{16}^{(i)} n_{x|p}^{(i)} + C_{66}^{(i)} n_{y|p}^{(i)} \right) \boldsymbol{a}_p^{(i)} l_p^{(i)} + \sum_{p=1}^{4} \left(C_{12}^{(i)} n_{x|p}^{(i)} + C_{26}^{(i)} n_{y|p}^{(i)} \right) \boldsymbol{b}_p^{(i)} l_p^{(i)}$$

$$\mathcal{C}^{(i)} = \sum_{p=1}^{4} \left(C_{16}^{(i)} n_{x|p}^{(i)} + C_{12}^{(i)} n_{y|p}^{(i)} \right) \boldsymbol{a}_p^{(i)} l_p^{(i)} + \sum_{p=1}^{4} \left(C_{66}^{(i)} n_{x|p}^{(i)} + C_{26}^{(i)} n_{y|p}^{(i)} \right) \boldsymbol{b}_p^{(i)} l_p^{(i)}$$

$$\mathcal{D}^{(i)} = \sum_{p=1}^{4}\left(C_{66}^{(i)} n_{x|p}^{(i)} + C_{26}^{(i)} n_{y|p}^{(i)}\right) \boldsymbol{a}_p^{(i)} l_p^{(i)} + \sum_{p=1}^{4}\left(C_{26}^{(i)} n_{x|p}^{(i)} + C_{22}^{(i)} n_{y|p}^{(i)}\right) \boldsymbol{b}_p^{(i)} l_p^{(i)}$$

$$\mathsf{C}_{\mathcal{AB}} = \begin{cases} 0 \quad (plane\ strain) \\ -\sum_{p=1}^{4}\left(\bar{C}_{13}^{(i)} n_{x|p}^{(i)} + \bar{C}_{36}^{(i)} n_{y|p}^{(i)}\right) l_p^{(i)} \quad (generalized\ plane\ strain) \end{cases}$$

$$\mathsf{C}_{\mathcal{CD}} = \begin{cases} 0 \quad (plane\ strain) \\ -\sum_{p=1}^{4}(\bar{C}_{36}^{(i)} n_{x|p}^{(i)} + \bar{C}_{23}^{(i)} n_{y|p}^{(i)})\, l_p^{(i)} \quad (generalized\ plane\ strain) \end{cases}$$

Plane stress

$$\mathcal{A}^{(i)} = \sum_{p=1}^{4}\left(\bar{C}_{11}^{(i)} n_{x|p}^{(i)} + \bar{C}_{16}^{(i)} n_{y|p}^{(i)}\right) \boldsymbol{a}_p^{(i)} l_p^{(i)} + \sum_{p=1}^{4}\left(\bar{C}_{16}^{(i)} n_{x|p}^{(i)} + \bar{C}_{66}^{(i)} n_{y|p}^{(i)}\right) \boldsymbol{b}_p^{(i)} l_p^{(i)}$$

$$\mathcal{B}^{(i)} = \sum_{p=1}^{4}\left(\bar{C}_{16}^{(i)} n_{x|p}^{(i)} + \bar{C}_{66}^{(i)} n_{y|p}^{(i)}\right) \boldsymbol{a}_p^{(i)} l_p^{(i)} + \sum_{p=1}^{4}\left(\bar{C}_{12}^{(i)} n_{x|p}^{(i)} + \bar{C}_{26}^{(i)} n_{y|p}^{(i)}\right) \boldsymbol{b}_p^{(i)} l_p^{(i)}$$

$$\mathcal{C}^{(i)} = \sum_{p=1}^{4}\left(\bar{C}_{16}^{(i)} n_{x|p}^{(i)} + \bar{C}_{12}^{(i)} n_{y|p}^{(i)}\right) \boldsymbol{a}_p^{(i)} l_p^{(i)} + \sum_{p=1}^{4}\left(\bar{C}_{66}^{(i)} n_{x|p}^{(i)} + \bar{C}_{26}^{(i)} n_{y|p}^{(i)}\right) \boldsymbol{b}_p^{(i)} l_p^{(i)}$$

$$\mathcal{D}^{(i)} = \sum_{p=1}^{4}\left(\bar{C}_{66}^{(i)} n_{x|p}^{(i)} + \bar{C}_{26}^{(i)} n_{y|p}^{(i)}\right) \boldsymbol{a}_p^{(i)} l_p^{(i)} + \sum_{p=1}^{4}\left(\bar{C}_{26}^{(i)} n_{x|p}^{(i)} + \bar{C}_{22}^{(i)} n_{y|p}^{(i)}\right) \boldsymbol{b}_p^{(i)} l_p^{(i)}$$

$$\mathsf{C}_{\mathcal{AB}} = 0$$

$$\mathsf{C}_{\mathcal{CD}} = 0$$

Solving the set of two linear equations above by Cramer's rule and using the expressions for the surface-averaged tractions in terms of the surface-averaged displacements and the zero-order coefficients, Eq. (2. 30), (2. 31), (2. 32), the above two equilibrium equations yield the zero-order coefficients solely in terms of the surface-averaged displacements for each direction,

$$W_{u(00)}^{(i)} = [(\mathcal{A}^{(i)}\mathcal{D}^{(i)}\boldsymbol{\beta} - \mathcal{C}^{(i)}\mathcal{B}^{(i)}\boldsymbol{\beta})\boldsymbol{\alpha}\widehat{\boldsymbol{u}}^{(i)} + (\mathcal{B}^{(i)}\mathcal{D}^{(i)}\boldsymbol{\beta} - \mathcal{D}^{(i)}\mathcal{B}^{(i)}\boldsymbol{\beta})\boldsymbol{\alpha}\widehat{\boldsymbol{v}}^{(i)} + (\mathsf{C}_{\mathcal{CD}}\mathcal{B}^{(i)}\boldsymbol{\beta} - \mathsf{C}_{\mathcal{AB}}\mathcal{D}^{(i)}\boldsymbol{\beta})\bar{\epsilon}_{zz}]/(2\mathcal{A}^{(i)}\boldsymbol{\beta}\mathcal{D}^{(i)}\boldsymbol{\beta} - 2\mathcal{B}^{(i)}\boldsymbol{\beta}\mathcal{C}^{(i)}\boldsymbol{\beta})$$

$$W_{v(00)}^{(i)} = \left[(\mathcal{C}^{(i)}\mathcal{A}^{(i)}\boldsymbol{\beta} - \mathcal{A}^{(i)}\mathcal{C}^{(i)}\boldsymbol{\beta})\boldsymbol{\alpha}\widehat{\boldsymbol{u}}^{(i)} + \left(\mathcal{D}^{(i)}\mathcal{A}^{(i)}\boldsymbol{\beta} - \mathcal{B}^{(i)}\mathcal{C}^{(i)}\boldsymbol{\beta}\right)\boldsymbol{\alpha}\widehat{\boldsymbol{v}}^{(i)} + (\mathsf{C}_{\mathcal{AB}}\mathcal{C}^{(i)}\boldsymbol{\beta} - \mathsf{C}_{\mathcal{CD}}\mathcal{A}^{(i)}\boldsymbol{\beta})\bar{\epsilon}_{zz}\right]/(2\mathcal{A}^{(i)}\boldsymbol{\beta}\mathcal{D}^{(i)}\boldsymbol{\beta} - 2\mathcal{B}^{(i)}\boldsymbol{\beta}\mathcal{C}^{(i)}\boldsymbol{\beta}) \tag{2. 35}$$

Now the first and second-order coefficients $W_{u(mn)}^{i}$ and $W_{v(mn)}^{i}$ (where $m+n \neq 0$) can be expressed in terms of the surface-averaged displacements and the additional constant ϵ_{zz} strain.

$$\boldsymbol{W}_{u}^{(i)} = \mathcal{E}\widehat{\boldsymbol{u}}^{(i)} + \mathcal{F}\widehat{\boldsymbol{v}}^{(i)} + \vec{\mathsf{C}}_{\mathcal{EF}}\epsilon_{zz}$$

$$\boldsymbol{W}_{v}^{(i)} = \mathcal{G}\widehat{\boldsymbol{v}}^{(i)} + \mathcal{H}\widehat{\boldsymbol{u}}^{(i)} + \vec{\mathsf{C}}_{\mathcal{GH}}\epsilon_{zz} \tag{2. 36}$$

where

$$\mathcal{E} = \frac{1}{2}\boldsymbol{\alpha} - \boldsymbol{\beta}\frac{\mathcal{A}^{(i)}\mathcal{D}^{(i)}\boldsymbol{\beta} - \mathcal{C}^{(i)}\mathcal{B}^{(i)}\boldsymbol{\beta}}{2\mathcal{A}^{(i)}\boldsymbol{\beta}\mathcal{D}^{(i)}\boldsymbol{\beta} - 2\mathcal{B}^{(i)}\boldsymbol{\beta}\mathcal{C}^{(i)}\boldsymbol{\beta}}\boldsymbol{\alpha}, \qquad \mathcal{F} = -\boldsymbol{\beta}\frac{\mathcal{B}^{(i)}\mathcal{D}^{(i)}\boldsymbol{\beta} - \mathcal{D}^{(i)}\mathcal{B}^{(i)}\boldsymbol{\beta}}{2\mathcal{A}^{(i)}\boldsymbol{\beta}\mathcal{D}^{(i)}\boldsymbol{\beta} - 2\mathcal{B}^{(i)}\boldsymbol{\beta}\mathcal{C}^{(i)}\boldsymbol{\beta}}\boldsymbol{\alpha},$$

$$\vec{\mathsf{C}}_{\mathcal{EF}} = -\boldsymbol{\beta}\frac{\mathsf{C}_{\mathcal{CD}}\mathcal{B}^{(i)}\boldsymbol{\beta} - \mathsf{C}_{\mathcal{AB}}\mathcal{D}^{(i)}\boldsymbol{\beta}}{2\mathcal{A}^{(i)}\boldsymbol{\beta}\mathcal{D}^{(i)}\boldsymbol{\beta} - 2\mathcal{B}^{(i)}\boldsymbol{\beta}\mathcal{C}^{(i)}\boldsymbol{\beta}},$$

$$\mathcal{G} = \frac{1}{2}\boldsymbol{\alpha} - \boldsymbol{\beta}\frac{\mathcal{D}^{(i)}\mathcal{A}^{(i)}\boldsymbol{\beta} - \mathcal{B}^{(i)}\mathcal{C}^{(i)}\boldsymbol{\beta}}{2\mathcal{A}^{(i)}\boldsymbol{\beta}\mathcal{D}^{(i)}\boldsymbol{\beta} - 2\mathcal{B}^{(i)}\boldsymbol{\beta}\mathcal{C}^{(i)}\boldsymbol{\beta}}\boldsymbol{\alpha}, \qquad \mathcal{H} = -\boldsymbol{\beta}\frac{\mathcal{C}^{(i)}\mathcal{A}^{(i)}\boldsymbol{\beta} - \mathcal{A}^{(i)}\mathcal{C}^{(i)}\boldsymbol{\beta}}{2\mathcal{A}^{(i)}\boldsymbol{\beta}\mathcal{D}^{(i)}\boldsymbol{\beta} - 2\mathcal{B}^{(i)}\boldsymbol{\beta}\mathcal{C}^{(i)}\boldsymbol{\beta}}\boldsymbol{\alpha},$$

$$\vec{\mathsf{C}}_{\mathcal{GH}} - \boldsymbol{\beta}\frac{\mathsf{C}_{\mathcal{AB}}\mathcal{C}^{(i)}\boldsymbol{\beta} - \mathsf{C}_{\mathcal{CD}}\mathcal{A}^{(i)}\boldsymbol{\beta}}{2\mathcal{A}^{(i)}\boldsymbol{\beta}\mathcal{D}^{(i)}\boldsymbol{\beta} - 2\mathcal{B}^{(i)}\boldsymbol{\beta}\mathcal{C}^{(i)}\boldsymbol{\beta}},$$

For the generalized plane strain problem, the out-of-plane normal stress is obtained after substituting the coefficients in the expressions of Eq. (2. 36), and is given below.

$$\sigma_{zz}^{(i)} = [C_{13} \quad C_{23} \quad C_{36}]\begin{bmatrix} \boldsymbol{a}_p\boldsymbol{W}_u \\ \boldsymbol{b}_p\boldsymbol{W}_v \\ \boldsymbol{b}_p\boldsymbol{W}_u + \boldsymbol{a}_p\boldsymbol{W}_v \end{bmatrix}^{(i)} + C_{33}\epsilon_{zz} =$$

$$\begin{aligned} &= \left(C_{13}\boldsymbol{a}_p\mathcal{E} + C_{36}\boldsymbol{b}_p\mathcal{E} + C_{23}\boldsymbol{b}_p\mathcal{H} + C_{36}\boldsymbol{a}_p\mathcal{H}\right)\widehat{\boldsymbol{u}}^{(i)} \\ &+ \left(C_{13}\boldsymbol{a}_p\mathcal{F} + C_{36}\boldsymbol{b}_p\mathcal{F} + C_{23}\boldsymbol{b}_p\mathcal{G} + C_{36}\boldsymbol{a}_p\mathcal{G}\right)\widehat{\boldsymbol{v}}^{(i)} + (C_{13}\boldsymbol{a}_p\vec{\mathsf{C}}_{\mathcal{E}\mathcal{F}} \\ &+ C_{36}\boldsymbol{b}_p\vec{\mathsf{C}}_{\mathcal{E}\mathcal{F}} + C_{23}\boldsymbol{b}_p\vec{\mathsf{C}}_{\mathcal{G}\mathcal{H}} + C_{36}\boldsymbol{a}_p\vec{\mathsf{C}}_{\mathcal{G}\mathcal{H}} + C_{33})\epsilon_{zz} \end{aligned} \tag{2. 37}$$

Also, substituting the first and second-order coefficient expressions Eq. (2. 36) into the surface-averaged traction components in the x and y direction acting on the four edges of the subvolume Eq. (2. 29), (2. 30), (2. 31), the surface-averaged traction components are obtained solely in terms of the corresponding surface-averaged displacements, related through the local stiffness matrix,

$$\begin{bmatrix} \hat{t}_{x|1} \\ \hat{t}_{y|1} \\ \hat{t}_{x|2} \\ \hat{t}_{y|2} \\ \hat{t}_{x|3} \\ \hat{t}_{y|3} \\ \hat{t}_{x|4} \\ \hat{t}_{y|4} \end{bmatrix}^{(i)} = \boldsymbol{K}^{(i)} \begin{bmatrix} \hat{u}_1 \\ \hat{v}_1 \\ \hat{u}_2 \\ \hat{v}_2 \\ \hat{u}_3 \\ \hat{v}_3 \\ \hat{u}_4 \\ \hat{v}_4 \end{bmatrix}^{(i)} + \boldsymbol{K}_{ezz}^{(i)}\epsilon_{zz} \tag{2. 38}$$

where $\boldsymbol{K}^{(i)} = \begin{bmatrix} k_{11} & k_{12} & k_{13} & k_{14} & k_{15} & k_{16} & k_{17} & k_{18} \\ k_{21} & k_{22} & k_{23} & k_{24} & k_{25} & k_{26} & k_{27} & k_{28} \\ k_{31} & k_{32} & k_{33} & k_{34} & k_{35} & k_{36} & k_{37} & k_{38} \\ k_{41} & k_{42} & k_{43} & k_{44} & k_{45} & k_{46} & k_{47} & k_{48} \\ k_{51} & k_{52} & k_{53} & k_{54} & k_{55} & k_{56} & k_{57} & k_{58} \\ k_{61} & k_{62} & k_{63} & k_{64} & k_{65} & k_{66} & k_{67} & k_{68} \\ k_{71} & k_{72} & k_{73} & k_{74} & k_{75} & k_{76} & k_{77} & k_{78} \\ k_{81} & k_{82} & k_{83} & k_{84} & k_{85} & k_{86} & k_{87} & k_{88} \end{bmatrix}^{(i)}$ and $\boldsymbol{K}_{ezz}^{(i)} = \begin{bmatrix} k_1^{ezz} \\ k_2^{ezz} \\ k_3^{ezz} \\ k_4^{ezz} \\ k_5^{ezz} \\ k_6^{ezz} \\ k_7^{ezz} \\ k_8^{ezz} \end{bmatrix}^{(i)}$

The distinct elements $k_{rc}^{(i)}$ in the local stiffness matrix $\boldsymbol{K}^{(i)}$ and the local vector $\boldsymbol{K}_{ezz}^{(i)}$ are given explicitly in terms of subvolume moduli and geometry in the Appendix III (plane stress) and

Appendix IV (plane strain and generalized plane strain) for a general monoclinic material. The vector $\boldsymbol{K}_{ezz}^{(i)}$ is zero unless the generalized plane strain problem is considered.

2.3.4 Global Stiffness Matrix Assembly

The solution for the unknown surface-averaged displacements is obtained by constructing a system of equations such that the interfacial displacement and traction continuity conditions are satisfied together with the traction and/or displacement boundary condition. To maintain the order of the subvolume edges for general unstructured meshing pattern, each subvolume has four identical surface-averaged displacements and tractions allocated in the system of equations. The system of equations for the solution of the unknown surface-averaged displacements, which is comprised of displacement and traction continuity, boundary and constraint conditions, is called the global system.

The index (i) that represents a subvolume in the discretized cross section is employed in the numbering system for all subvolumes in the assembly of the global system of equations. To facilitate the assembly of the global stiffness matrix when unstructured meshing is employed, an adjacency matrix is introduced to relate two common edges of adjacent subvolumes. The dimension of this matrix is equal to the number of all edges, i.e., four times the number of all subvolumes. This adjacency matrix has all "1" s along the diagonal as well as other locations which indicate commonality of any two edges of adjacent subvolumes. Thus, the adjacency matrix is symmetric since the contact of two adjacent edges is in a mutually connected relationship. Figure 2-2 demonstrates a simple example of the adjacency matrix when there are eight edges arising from two subvolumes, where only Edge #2 from Subvolume #1 and Edge #8 from Subvolume #2 are connected.

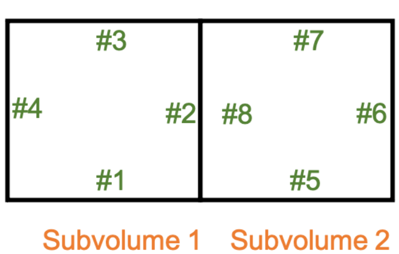

$$\boldsymbol{M}_{adjacency} = \begin{array}{c c} \begin{array}{cccccccc} \#1 & \#2 & \#3 & \#4 & \#5 & \#6 & \#7 & \#8 \end{array} & \\ \begin{bmatrix} 1 & 0 & 0 & 0 & 0 & 0 & 0 & 0 \\ 0 & 1 & 0 & 0 & 0 & 0 & 0 & 1 \\ 0 & 0 & 1 & 0 & 0 & 0 & 0 & 0 \\ 0 & 0 & 0 & 1 & 0 & 0 & 0 & 0 \\ 0 & 0 & 0 & 0 & 1 & 0 & 0 & 0 \\ 0 & 0 & 0 & 0 & 0 & 1 & 0 & 0 \\ 0 & 0 & 0 & 0 & 0 & 0 & 1 & 0 \\ 0 & 1 & 0 & 0 & 0 & 0 & 0 & 1 \end{bmatrix} & \begin{array}{c} \#1 \\ \#2 \\ \#3 \\ \#4 \\ \#5 \\ \#6 \\ \#7 \\ \#8 \end{array} \end{array}$$

Figure 2-2 A simple system of two subvolumes analyzed in FVM and its 8×8 adjacency matrix

We first denote the number of connected edges by N_{con} and the number of unconnected edges by N_{uncon} from the discretized grid. To solve the global system of equations for the surface-averaged displacements, the global stiffness matrix is allocated $(4N_{con} + 2N_{uncon}) + 1$ columns and $4N_{con} + 2N_{uncon}$ rows. Each subvolume has four edges that has x and y displacements and contributes eight equations to the global system. To admit the generalized plane strain problem, there is an additional relationship for surface-averaged tractions with ϵ_{zz} as an unknown besides the unknown surface-averaged displacements, therefore there are $(4N_{con} + 2N_{uncon}) + 1$ unknowns that need to be determined for plane problems. Also, each two connected edges have the same surface-averaged displacements and equal and opposite tractions, which results in $4N_{con}$ equations for traction and displacement continuity conditions in both x and y directions, whereas the unconnected edges only need to satisfy the boundary or constraint conditions also in both x and y directions, producing $2N_{uncon}$ equations. The breakdown of the $4N_{con} + 2N_{uncon}$ rows in the global system is given below:

Displacement continuity condition equations

For a pair of connected edges from adjacent subvolumes, the displacement continuity conditions contribute one equation in the x and y direction each to the global stiffness matrix. p is the edge index from the first subvolume and p' is the edge index from the second subvolume.

$$\begin{gathered} \hat{u}_p^{(i)} - \hat{u}_{p'}^{(i')} = 0 \\ \hat{v}_p^{(i)} - \hat{v}_{p'}^{(i')} = 0 \end{gathered} \tag{2. 39}$$

Traction continuity condition equations

For a pair of connected edges from adjacent subvolumes, the traction continuity conditions contribute one equation each in the x and y direction to the global stiffness matrix. p is the edge index from the first subvolume and p' is the edge index from the second subvolume.

$$t_{x|p}^{(i)} + t_{x|p'}^{(i')} = 0$$
$$t_{y|p}^{(i)} + t_{y|p'}^{(i')} = 0 \tag{2. 40}$$

$t_{x|p}^{(i)}$ and $t_{y|p}^{(i)}$ are expressed as linear combinations of surface-averaged displacements in the global system.

<u>Boundary condition equations</u>

For a pair of connected edges from adjacent subvolumes, the traction boundary conditions contribute one equation each in the x and y direction to the global stiffness matrix,

$$\hat{t}_{x|p}^{(i)} = B_x$$
$$\hat{t}_{y|p}^{(i)} = B_y \tag{2. 41}$$

where B_x and B_y are the exterior tractions applied on the boundary of the domain.

<u>Constraint condition equations</u>

The penalty method is employed to enforce constraints which cannot be easily incorporated into the unstructured subvolumes computation. It works by adding a penalty term to the global stiffness matrix and the restoring-force vectors to impose a prescribed zero. This penalty term imposes a cost on any deviation from the desired constraint, effectively forcing the system to behave as though the constraint is being enforced. This method is applied to those subvolumes next to the constraints based on the zero-displacement conditions in x and y directions. If the subvolume edge is on one of the constraints, e.g., if the first edge ($p = 1$) of subvolume (i) is fixed, the penalty term in the surface-averaged traction expression $k_{11}^{(i)}, k_{12}^{(i)}, k_{21}^{(i)}, k_{22}^{(i)}$ turned to outstanding numbers

$1e7$ to ensure little displacements for fixed end condition in both x and y directions. Thus, the traction expressions at the constraints become

$$\begin{bmatrix} \hat{t}_{x|1}^{(i)} \\ \hat{t}_{y|1}^{(i)} \end{bmatrix}^{(i)} = \begin{bmatrix} 1e7 & 1e7 & k_{13} & k_{14} & k_{15} & k_{16} & k_{17} & k_{18} \\ 1e7 & 1e7 & k_{23} & k_{24} & k_{25} & k_{26} & k_{27} & k_{28} \end{bmatrix}^{(i)} \begin{bmatrix} \hat{u}_1 \\ \hat{v}_1 \end{bmatrix}^{(i)} = 0 \qquad (2.42)$$

in the global system of equations.

<u>Additional equation for the generalized plane strain problem</u>

The out-of-plane strain is constant over the analyzed domain for the generalized plane strain problem, such that the resultant out-of-plane stress is zero.

$$F_z = \sum_{i=1}^{n} \sigma_{zz}^{(i)} \Delta A = 0 \qquad (2.43)$$

where

$$\begin{aligned} \sigma_{zz}^{(i)} = \Big[& C_{13}\Big(\bar{J}_{11}^{(i)}\mathcal{E}_{(1,:)} + \bar{J}_{12}^{(i)}\mathcal{E}_{(2,:)}\Big) + C_{23}\Big(\bar{J}_{21}^{(i)}\mathcal{H}_{(1,:)} + \bar{J}_{22}^{(i)}\mathcal{H}_{(2,:)}\Big) \\ & + C_{36}\Big(\bar{J}_{21}^{(i)}\mathcal{E}_{(1,:)} + \bar{J}_{22}^{(i)}\mathcal{E}_{(2,:)} + \bar{J}_{11}^{(i)}\mathcal{H}_{(1,:)} + \bar{J}_{12}^{(i)}\mathcal{H}_{(2,:)}\Big)\Big] \hat{\boldsymbol{u}}^{(i)} \\ & + \Big[C_{13}\Big(\bar{J}_{11}^{(i)}\mathcal{F}_{(1,:)} + \bar{J}_{12}^{(i)}\mathcal{F}_{(2,:)}\Big) + C_{23}\Big(\bar{J}_{21}^{(i)}\mathcal{G}_{(1,:)} + \bar{J}_{22}^{(i)}\mathcal{G}_{(2,:)}\Big) \\ & + C_{36}\Big(\bar{J}_{21}^{(i)}\mathcal{F}_{(1,:)} + \bar{J}_{22}^{(i)}\mathcal{F}_{(2,:)} + \bar{J}_{11}^{(i)}\mathcal{G}_{(1,:)} + \bar{J}_{12}^{(i)}\mathcal{G}_{(2,:)}\Big)\Big] \hat{\boldsymbol{v}}^{(i)} + [(C_{13}\bar{J}_{11}^{(i)} \\ & + C_{36}\bar{J}_{21}^{(i)})\vec{\complement}_{\mathcal{EF}(1)} + (C_{13}\bar{J}_{12}^{(i)} + C_{36}\bar{J}_{22}^{(i)})\vec{\complement}_{\mathcal{EF}(2)} + (C_{23}\bar{J}_{21}^{(i)} + C_{36}\bar{J}_{11}^{(i)})\vec{\complement}_{\mathcal{GH}(1)} \\ & + (C_{23}\bar{J}_{22}^{(i)} + C_{36}\bar{J}_{12}^{(i)})\vec{\complement}_{\mathcal{GH}(2)} + C_{33}]\epsilon_{zz} \end{aligned}$$

The solution of the above augmented global system of equations yields the unknown surface-averaged displacements, which, in turn, yield the corresponding surface-averaged tractions and pointwise displacements, strains, and stresses in each subvolume.

2.4 Structural Applications

The developed finite-volume solution methodology for plane problems is verified by comparison with several elasticity solutions to structural problems, as well as experimental results for determining mechanical properties of unidirectional composites. Analytical approaches that generate exact elasticity solutions for the flexure of a homogeneous isotropic beam is the first application of FVM within the plane elasticity framework. FVM for plane strain problems is used as an efficient simulation tool to study microstructural effects in deep composite layered plates subjected to flexure using a replacement scheme based on the Postma model (1957). In addition, the parametric mapping capability that facilitates the use of arbitrary quadrilateral subvolumes in mesh discretization levered to investigate the flexure of deep heterogeneous plates reinforced or weakened by circular inclusions and voids, respectively. The increasing use of composites as high-performance structural materials in modern aircraft requires accurate determination of the composite material's response to mechanical loads. Testing provides the means to determine these characteristics of composite materials under controlled conditions. FVM is used to simulate the plane stress response of monoclinic and orthotropic composite test specimens under off-axis tensile and pure shear loading based on the Iosipescu test fixture, and validates key assumptions made in these experiments in the determination of the axial shear modulus.

2.4.1 Flexure of a Cantilever Beam by an End Vertical Load

We consider a homogenous isotropic beam with a rectangular cross section of height h and thickness b subjected to a vertical end load shown in Figure 2-3. If the thickness b is small relative to the height h, the state of stress may be modeled as plane stress. Suppose the left end of the beam is fixed to a rigid wall and loaded on its right end with a resultant force P.

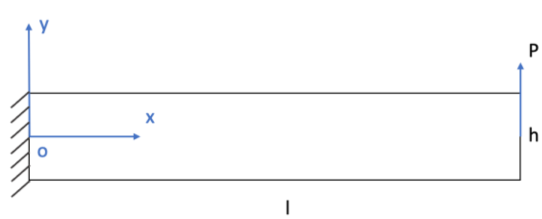

Figure 2-3 Cantilever beam with an end load

Figure 2-3 shows a rectangular beam configuration ($0 \leq x \leq l, -\frac{h}{2} \leq y \leq \frac{h}{2}$), subjected to a transverse force, P at the end $x = l$, with the horizontal boundaries $y = \pm\frac{h}{2}$ being traction-free. Accordingly, the boundary conditions for this problem are prescribed on its three edges as follows:

$$@y = \pm\frac{h}{2} : \begin{cases} \sigma_{xy} = 0 \\ \sigma_{yy} = 0 \end{cases}$$

$$@x = l : \begin{cases} \sigma_{xx} = 0 \\ \int_{-\frac{h}{2}}^{\frac{h}{2}} \sigma_{xy}(x = l, y) dy = P \end{cases} \tag{2. 44}$$

Elasticity solution

The boundary conditions above are imposed in an integral or weak form on the right end face, which means that the actual traction distribution at each point is replaced by the equivalent force resultant. Elasticity problems on rectangular domains, including rectangular beams, may be solved using a polynomial stress function approach when the boundary conditions are expressible as a superposition of polynomials of different orders satisfying the biharmonic equation, or stated in a weak form. Infinite series or transform based solutions are employed when point-wise boundary condition satisfaction is required, such as discontinuous tractions that cannot be expressed as a superposition of polynomials. In the present case, the weak form of boundary conditions on the right end is employed in the elasticity solution below based on the polynomial stress function superposition.

The bending moment in this problem varies linearly with x, and hence that the stress component σ_{xx} will have a leading term proportional to xy. This in turn suggests a fourth-degree polynomial term xy^3 in the stress function φ with the additional stress function terms C_2xy and C_3y^3 that ensure satisfaction of the traction-free boundary conditions on the upper and lower surfaces. The stress-based procedure is therefore to start with the Airy stress function $\varphi = C_1xy^3 + C_2xy + C_3y^3$, and determine the unknown constants such that all the boundary conditions are satisfied. This yields the solution in terms of the following stresses,

$$\sigma_{xx} = -\frac{Py}{I_{zz}}(l - x)$$

$$\sigma_{xy} = -\frac{P(y^2 - \frac{h^2}{4})}{2I_{zz}} \tag{2. 45}$$

$$\sigma_{yy} = 0$$

where $I_{zz} = \frac{bh^3}{12}$ is the moment of inertia about the z axis. These stresses satisfy the boundary conditions on all four faces that maintain the beam in static equilibrium in both plane stress and plane strain.

To determine how the beam is fixed at the wall, the strain-displacement equations are integrated, using Hooke's law, to obtain the corresponding displacement field. Displacement boundary conditions are then employed to determine the unknown integration constants, based on zero rotation of the neutral axis intersecting at the middle point on the fixed end,

$$@(x = 0, y = 0)\begin{cases} \frac{\partial v}{\partial x} = 0 \\ u = 0 \\ v = 0 \end{cases} \tag{2. 46}$$

If the beam is relatively thin, it may be assumed to be in plane stress, yielding the following displacements,

$$u(x, y) = \frac{P}{EI_{zz}}[-\left(l - \frac{x}{2}\right)xy - \frac{2 + v}{6}y^3 + \frac{1 - v}{4}h^2 y]$$

$$v(x, y) = \frac{P}{EI_{zz}}[\frac{v(l - x)}{2}y^2 + \frac{lx^2}{2} - \frac{x^3}{6}] \tag{2. 47}$$

If the beam is relatively thick, it may be assumed to be in plane strain, yielding the following displacements from the conversion table below that relates plane stress and plane strain problems. Replacing the engineering constants in Eq. (2. 47) by the corresponding constants in Table 2-1, the displacements for a thick beam in flexure are

$$u(x,y) = \frac{P(1-\upsilon^2)}{EI_{zz}}[-\left(l-\frac{x}{2}\right)xy - \frac{2-\upsilon}{6(1-\upsilon)}y^3 + \frac{1-2\upsilon}{4(1-\upsilon)}h^2y]$$
$$v(x,y) = \frac{P(1-\upsilon^2)}{EI_{zz}}[\frac{\upsilon(l-x)}{2(1-\upsilon)}y^2 + \frac{lx^2}{2} - \frac{x^3}{6}] \tag{2. 48}$$

Table 2-1 Conversion table of the plane problems for isotropic materials

Plane condition switch	Young's modulus	Poisson's ratio
Plane stress ⇒ Plane strain	$\frac{E}{1-\upsilon^2}$	$\frac{\upsilon}{1-\upsilon}$
Plane strain ⇒ Plane stress	$\frac{E(1+2\upsilon)}{(1+\upsilon)^2}$	$\frac{\upsilon}{1+\upsilon}$

FVM Simulation and Comparison

The elasticity solution to the cantilever beam in plane stress and strain is compared with FVM based simulation. The beam is made of steel ($E = 30{,}000\ ksi$, $\nu = 0.30$) with a length of 80 inches and a height of 10 inches and subjected to a vertical end load of 8,000 lbs. on its right face, parabolically distributed such that it mimics the elasticity solution. This is accomplished by assigning parabolic distribution of surface-averaged tractions to the subvolume faces along the right boundary. In contrast with the elasticity solution, the vertical and horizontal displacement components along the entire left face of the beam are set to zero in a surface-average sense to simulate true built-in boundary conditions. The displacement and stress fields were generated using 100×10 square subvolume discretization of the analyzed rectangular domain, and then plotted based on vertex quantities of each subvolume, which were then interpolated inside each subvolume using a color map. FVM utilizes an averaging scheme at shared nodes, whereas FEM directly enforces nodal continuity. Both methods rely on common grids to determine vertex quantities, enabling a comparison between exact elements in FEM and subvolumes in FVM. Unless explicitly stated otherwise, this dissertation will utilize the aforementioned plotting and comparison methodology throughout the remaining sections.

Figure 2-4 presents comparison of the displacement and stress fields generated by the elasticity and FVM solutions under plane stress conditions. The differences in the displacement fields are very small throughout the beam's cross section, including the immediate vicinity of the left face where the displacement boundary conditions differ in the two solutions. Further, the neutral axis deflections are also comparable. In contrast, the manner of fixing the beam to the wall produces more substantial differences in the stress fields generated by the two solutions both in the immediate vicinity of the fixed wall and in the beam's interior.

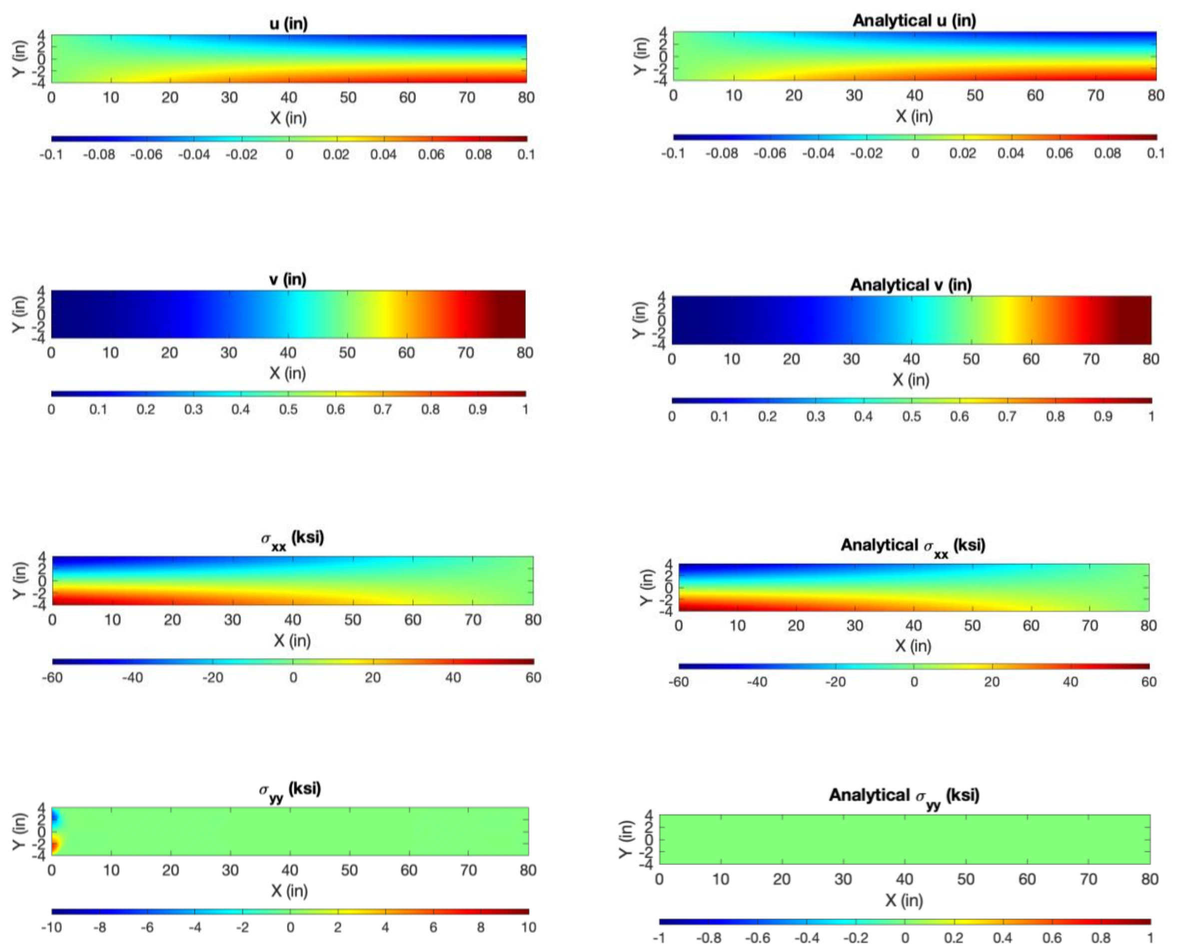

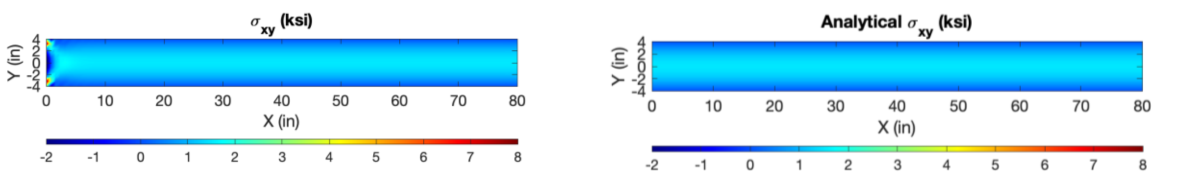

Figure 2-4 Comparison of displacement and stress fields in a cantilever beam with an end load obtained from FVM (left) and elasticity (right) plane stress solutions

This can be barely observed in the axial stress field $\sigma_{xx}(x,y)$ upon plotting the differences in the two solutions in Figure 2-5 for the three stress components. Whereas the differences in the $\sigma_{xy}(x,y)$ and $\sigma_{yy}(x,y)$ stress components are limited to the left face of the beam, and become negligible elsewhere, these differences propagate into the beam much further for the axial stress.

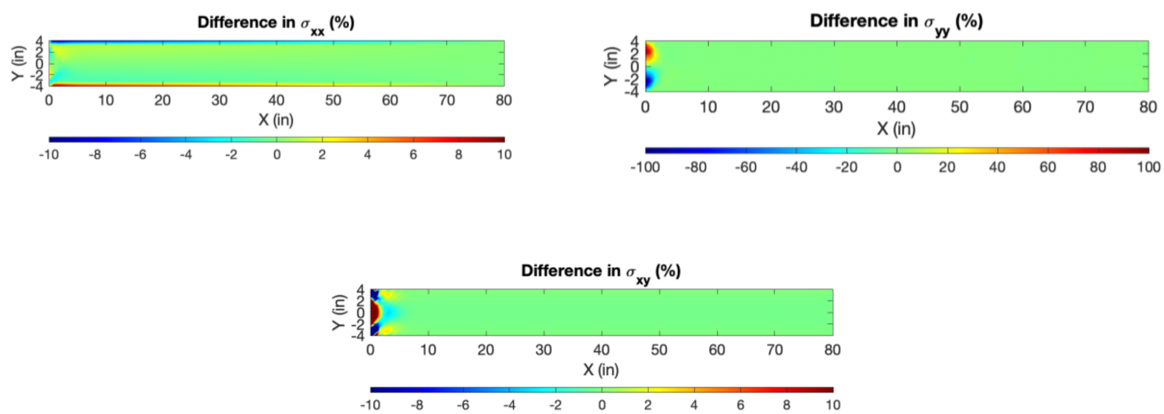

Figure 2-5 Differences in the stress components in a cantilever beam with an end load obtained from FVM and elasticity plane stress solutions

The elasticity solution produces the same in-plane stress distributions under both plane stress and plane strain boundary conditions. In contrast, the FVM solution produces somewhat different stress distributions because of the manner of fixing the left face of the beam. These differences in the plane strain situation mimic the differences between the two solutions observed in the plane stress situation and hence are not illustrated. Conversely, the displacement fields differ under plane stress and plane strain conditions. The differences in the neutral axis deflections predicted by the elasticity and FVM solutions under plane stress and plane strain conditions are presented in Figure 2-6, illustrating the effect of boundary conditions.

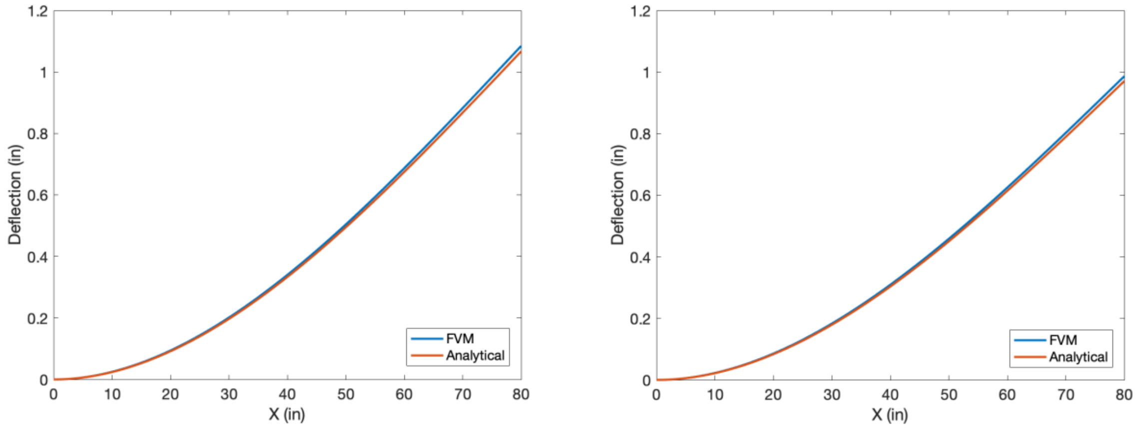

Figure 2-6 Comparison of neutral axis deflections of a cantilever beam with an end load obtained from elasticity and FVM plane stress (left) and plane strain (right) solutions

2.4.2 Bending of a Multi-layered Beam by an End Load

Layered constructions are employed not just in advanced aircraft applications which utilize laminated composite plates, but also in structural engineering components. The lamination plate theory has been employed in the analysis of the response of laminated plates wherein a specific type of a homogenization process based on an assumed deformation field is implemented to replace the layered microstructure with equivalent extension, stretching-bending and bending stiffness matrices. Herein we employ the developed FVM for plane strain applications to investigate the bending of layered constructs accounting for the layered microstructure for comparison with the equivalent homogenized construct. The question that we pose is how many layers are required to obtained the same deflection response that approaches that of the response of an equivalent homogeneous construct with homogenized moduli. Another way of posing this question is to ask when homogenization is valid and when actual layered microstructure needs to be considered.

Postma developed an exact elasticity solution for the overall transversely isotropic properties of periodically layered structures composed of alternating isotropic layers with different elastic moduli, with the direction of anisotropy orthogonal to the plane of alternating layers. This periodic structure consisting of alternating plane, parallel, isotropic, and homogeneous elastic layers can be replaced by a homogeneous, transversely isotropic material as far as its gross-scale elastic behavior is concerned. For such laminations stacking along the direction of the y axis, exact expressions for the homogenized moduli are obtained in the form below, where the five elastic moduli of the equivalent transversely isotropic medium are accordingly expressed in terms of the elastic properties and the ratio of the thicknesses of the individual isotropic layers.

$$\begin{gathered}
C_{11}=\frac{1}{D}\{(d_1+d_2)^2(\lambda_1+2\mu_1)(\lambda_2+2\mu_2) \\
+4d_1d_2(\mu_1-\mu_2)[(\lambda_1+\mu_1)-(\lambda_2+\mu_2)]\} \\
C_{12}=\frac{1}{D}\{(d_1+d_2)[\lambda_1 d_1(\lambda_2+2\mu_2)+\lambda_2 d_2(\lambda_1+2\mu_1)]\} \\
C_{16}=0 \\
C_{22}=\frac{1}{D}\{(d_1+d_2)^2(\lambda_1+2\mu_1)(\lambda_2+2\mu_2)\} \\
C_{26}=0 \\
C_{66}=\frac{(d_1+d_2)\mu_1 u_2}{d_1\mu_2+d_2\mu_1}
\end{gathered} \tag{2. 49}$$

where $D=(d_1+d_2)[d_1(\lambda_2+2\mu_2)+d_2(\lambda_1+2\mu_1)]$, and μ_i are the shear moduli of the individual isotropic layers ($i=1,2$), and d_i are the respective thickness.

A sequence of horizontally layered rectangular cross sections comprised of alternating isotropic layers made of glass and epoxy (glass: $E=10{,}000\ ksi$, $\nu=0.30$; epoxy: $E=500\ ksi$, $\nu=0.30$) were constructed with progressively finer microstructures for the FVM analysis. Specifically, five laminated beams comprised of 2, 4, 8, 16, and 32 alternating glass/epoxy layers with an overall length of 80 inches and height of 10 inches were constructed for comparison with the response of an equivalent Postma-homogenized beam. The layered and homogenized beams were discretized into 320×32 subvolumes for the FVM analysis under the plane strain assumption. The beams were cantilevered at the left end and subjected to a vertical end load of 8,000 lbs. applied on the top right corner of the beam, with the right face traction free.

The results given in the following figures illustrate the displacement and stress fields in the five laminated constructs relative to a homogeneous beam with equivalent homogenized transversely isotropic moduli. The distributions were generated from displacement and stress quantities at subvolume vertices and then interpolated inside each subvolume using a colormap. Figure 2-7 and Figure 2-8 illustrate the horizontal and vertical displacement fields for the layered and homogenized beams, suggesting that 16 layers produce displacement fields that are comparable to the homogenized results.

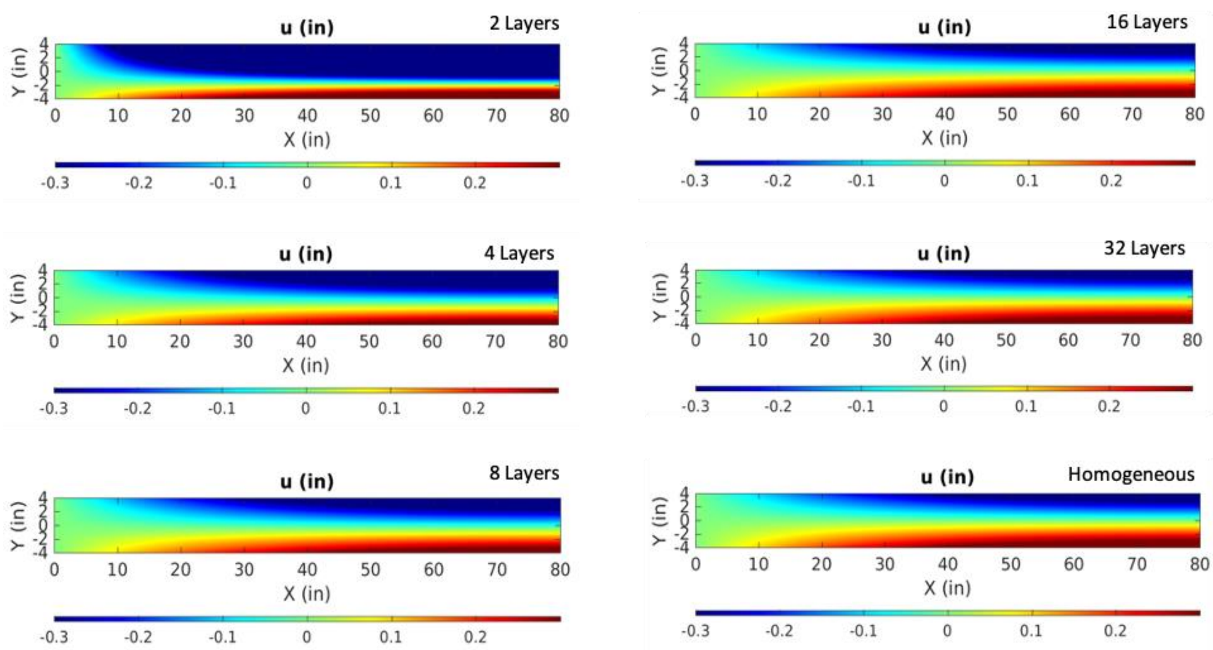

Figure 2-7 Displacement u in cases with 2, 4, 8, 16 and 32 layers and homogenized beam

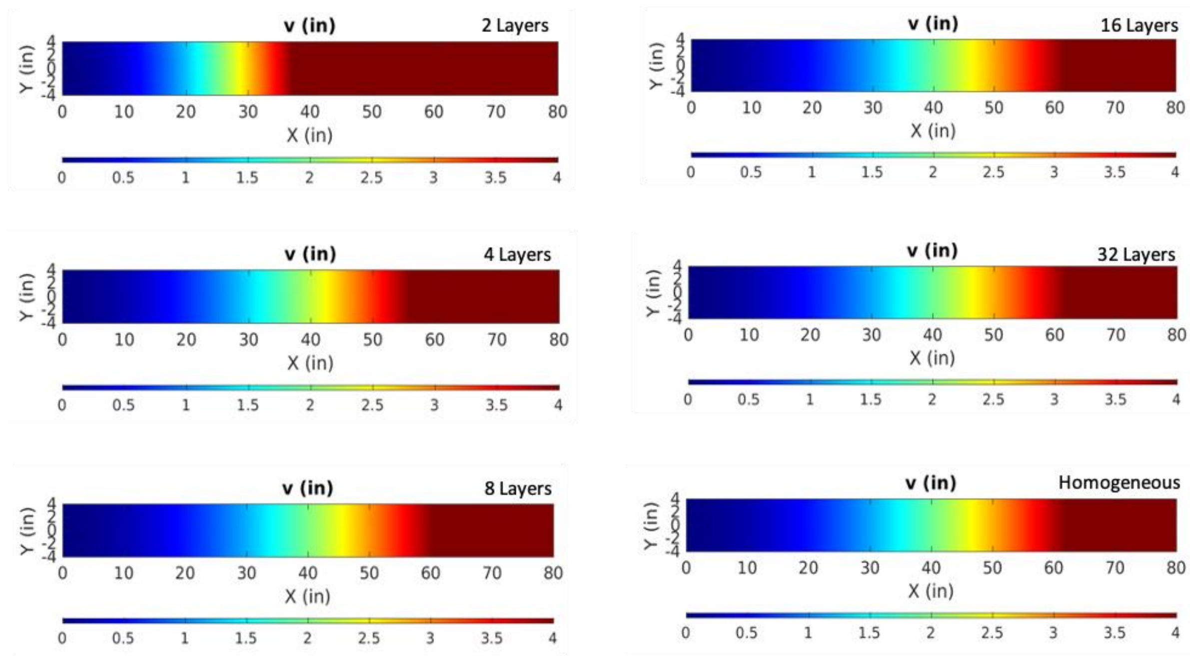

Figure 2-8 Displacement v in cases with 2, 4, 8, 16 and 32 layers and homogenized beam

In contrast, 32 layers are required to produce a comparable axial stress field as observed in Figure 2-9, where the effect of the layered microstructure is clearly visible for the 16-layer configuration. Although not visible at this resolution, this effect is present to a smaller extent in the 32-layer configuration because the axial stress is discontinuous across vertical cross sections due to the discontinuous elastic moduli variation. In the case of the shear stress shown in Figure 2-10, however, 16-layer one is sufficient to approach the stress distribution of the homogenized beam because the shear stress is a traction component along the x and y axes, and hence is continuous in both directions regardless of the material discontinuities. This is one of the strengths of FVM in handling composite materials consisting of multiple layers, even with asymmetric layouts, wherein both displacement and traction continuity is enforced, albeit in a surface-averaged sense.

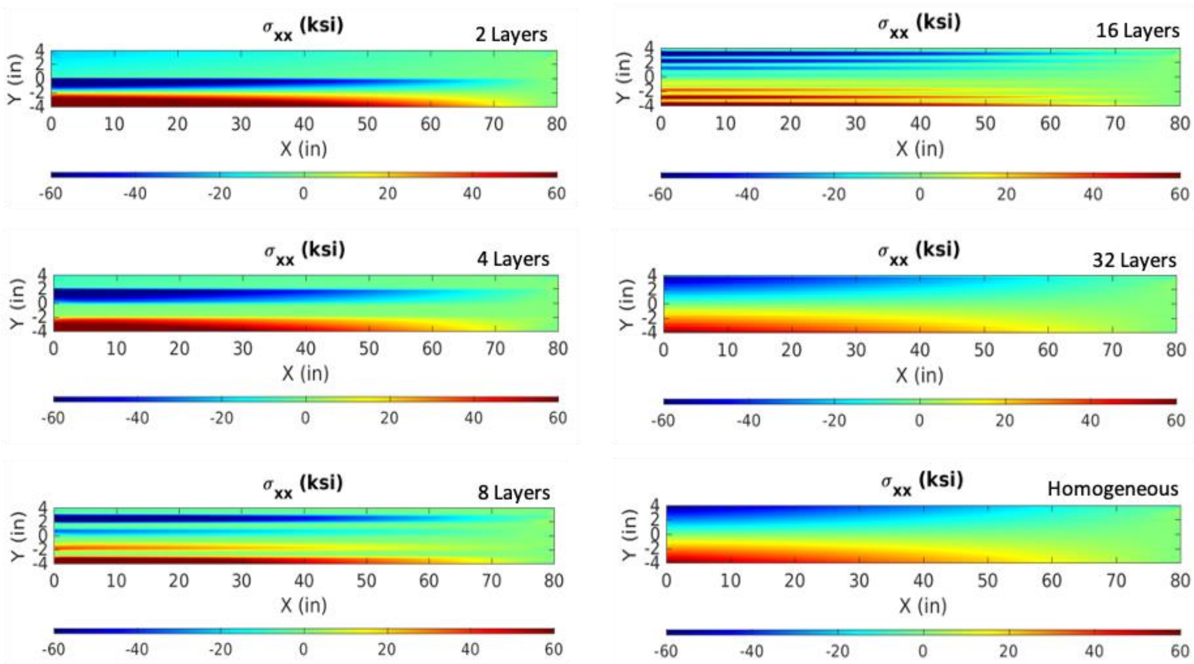

Figure 2-9 Stress σ_{xx} in cases with 2, 4, 8, 16 and 32 layers and homogenized beam

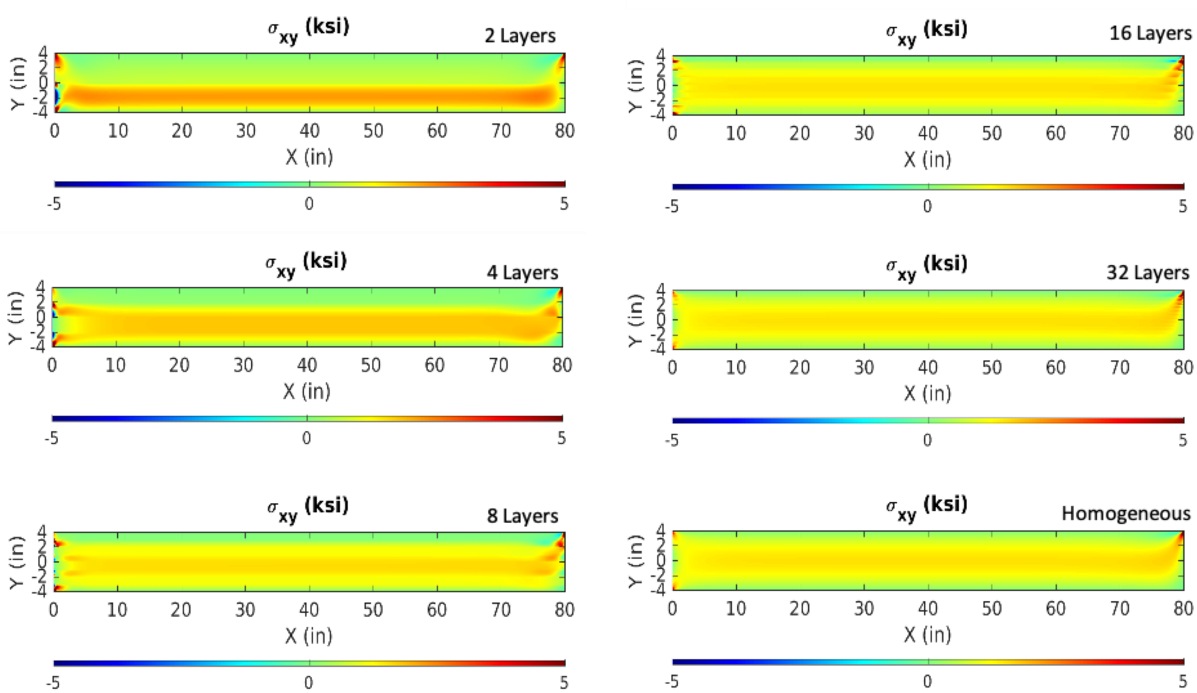

Figure 2-10 Stress σ_{xy} in cases with 2, 4, 8, 16 and 32 layers and homogenized beam

A more quantitative comparison between the stress distributions of layered and homogenized configurations is presented in Figure 2-11, which illustrates cross section graphs of axial and shear stresses half-way along the beams' spans.

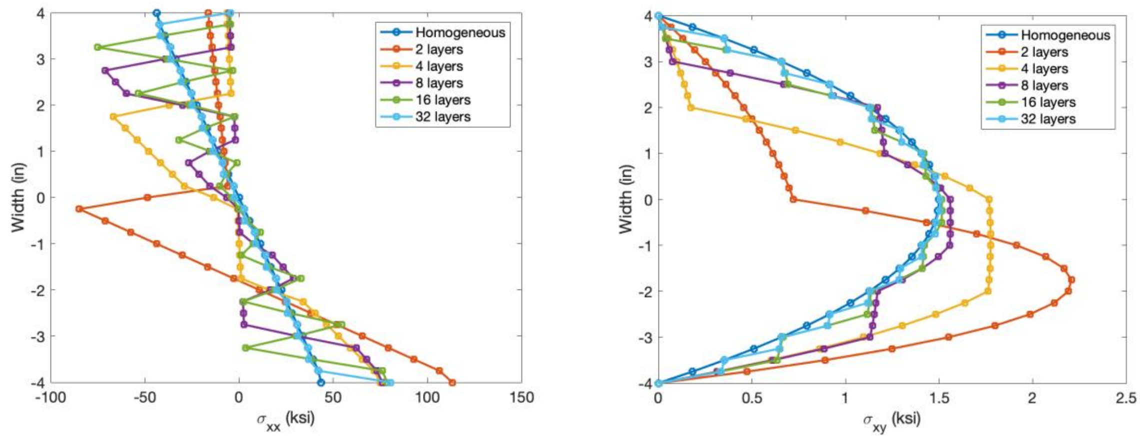

Figure 2-11 Cross section distributions of σ_{xx} (left) and σ_{xy} (right) stresses for the layered and homogenized configurations halfway along the beams' spans

2.4.3 Heterogenous Cantilever Beams with Inclusions and Porosities

Many composite problems are generalized plane strain in nature because of the reinforcement presence. They are often solved using three-dimensional finite element analyses. The FVM technique may be implemented to solve these problems using the developed generalized plane strain formulation, which is achieved by introducing an out-of-plane strain into the two-dimensional finite volume analysis, reducing the computational effort. This strain may be either specified or determined as part of the solution for a given out-of-plane force or average stress.

Herein, the generalized plane strain feature of FVM is illustrated by analyzing the bending of a fiber reinforced and porosity wakened beams subjected to end loads and compared with the plane strain results. These problems mimic the previously analyzed cantilever beam problems. The beams are reinforced by boron fibers in an aluminum matrix containing a 0.3 fiber volume fraction. Aluminum beams weakened by porosities are obtained by removing the fibers, yielding a 0.3 void volume fraction. Unlike the previous studies, in this section, we employ a disordered mesh generated by a commercial software (ANSYS) and adopted for FVM analysis to efficiently model the circular boundaries of both boron fibers and porosities. At present, ANSYS does not provide support for the generalized plane strain condition. As a result, the plane strain condition is chosen as an alternative in FEM simulations. The stress fields for the boron/aluminum beams with a single row of fibers obtained under plane strain modeled in FEM and generalized plane strain modeled in FVM conditions are compared in Figure 2-12, with the corresponding comparison for the voided beams in Figure 2-13.

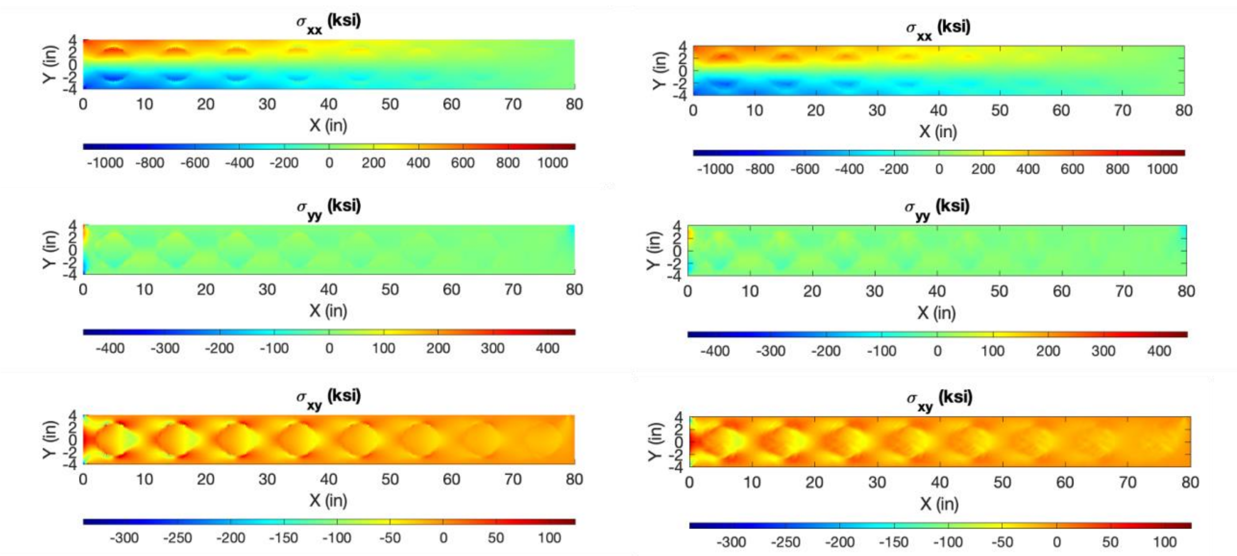

Figure 2-12 Stress components in composite beams in plane strain (FEM results, left) and generalized plane strain (FVM results, right)

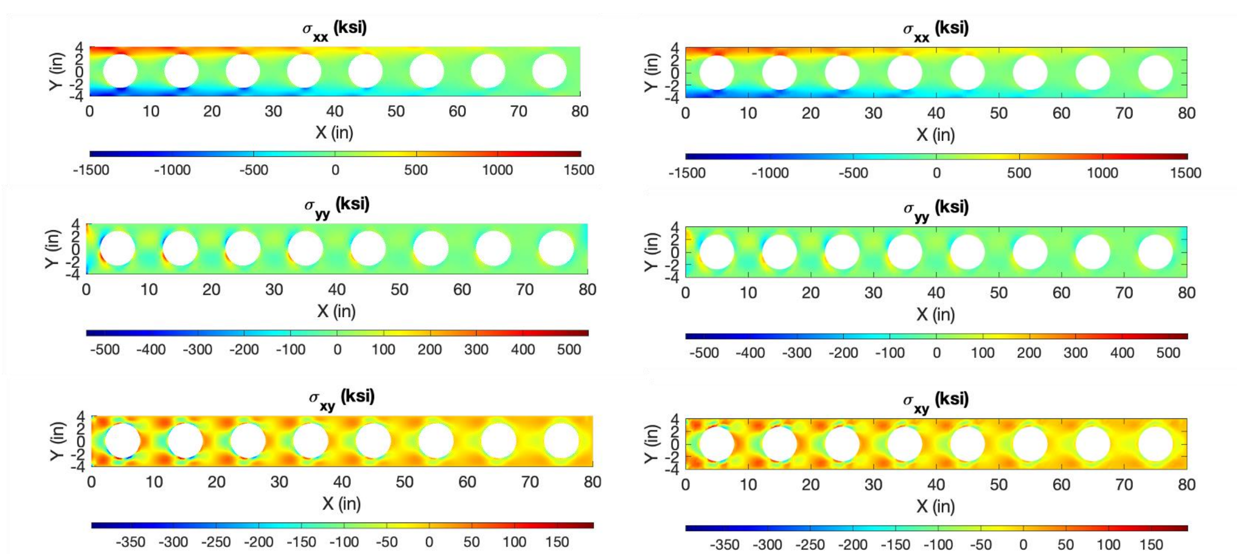

Figure 2-13 Stress components in porous beams in plane strain (FEM results, left) and generalized plane strain (FVM results, right)

2.5 Shear Characterization of Unidirectional Composites

Tensile, compressive, and shear properties of traditional structural materials are most often determined by materials testing and not from complex theoretical analysis. Current test methods are largely based upon technology developed for wood, metals, and adhesives. Yet, composite material test techniques are limited due to their heterogeneity and anisotropy. While the conventional test techniques may be applicable to tensile and compressive tests of composites, it does not appear that a test method which induces a state of pure shear in metals or adhesives will induce a state of pure shear in a composite material. Coupling effects and laminate geometry make the process of determining the shear modulus even more difficult. Accurate characterization of unidirectional composites requires analysis of stress distribution in the test section, proper specimen selection and optimization as well as fixture, and reliable analysis of measurement techniques and associated errors.

Unidirectional lamina with fibers oriented along a specific direction are the basic building blocks of laminated composites. Unidirectional lamina are typically transversely isotropic and are characterized by five elastic constants relative to the principal material coordinate system formed by the intersection of planes of material symmetry. However, at least four of them are required for in-plane stress analysis ($E_{11}, E_{22}, \nu_{12}, G_{12}$). The first three elastic moduli (E_{11}, E_{22}, ν_{12}) are easily and accurately obtained from tensile tests on 0^{o} and 90^{o} specimens with fibers oriented along and transverse to the specimen test axis, respectively. For these specimens, the perturbation in the stress state produced by grips decays relatively rapidly and a uniform state of stress in the specimen's test section is obtained. Specimens with aspect ratios of 5 are sufficiently long to obtain uniform strain and stress fields in the test section, enabling accurate measurement of local strains using a strain gage and calculation of the axial stress from applied load and knowledge of specimen's cross-sectional area, yielding E_{11}, E_{22}, ν_{12}.

Determining the axial shear modulus G_{12} for an anisotropic composite material is the last and also most challenging step in the characterization of in-plane shear response of unidirectional composites, and several different test methods for G_{12} have been proposed since 1960s. Among them, torsion of thin-walled tubes and rail shear tests are well suited for metals but are expensive to conduct. Lee and Munro (1986) have reviewed and evaluated the existing test methods for shear characterization and they found that the most promising test methods are the 10° off-axis tensile test, the $\pm 45°$ laminate test, and the Iosipescu test, based on a set of eleven criteria ranging from accuracy of stiffness and strength parameter determination to ease of specimen preparation and testing. Symmetric $+45°$ and $-45°$ alternating laminates have also been used in shear testing but those samples require expertise in manufacturing. The shear-coupling factors cannot be directly observed in off-angle tension for alternating laminates, and the boundary layer effects near the free edges do not have exact analytical description of the experiments. As a result, the off-axis tension test and Iosipescu shear test are the most common methods utilized to characterize composite materials.

However, a number of problems need to be resolved before these two methods can be used for accurate shear characterization of unidirectional composites, because of discrepancies between the actual stress state and the apparently measured quantities in the respective specimens' test sections. With the correct interpretation of the experiment results, different test methods can yield the same in-plane shear modulus. Herein, FVM serves as a simulation tool to characterize displacement, strain, and stress fields in the test sections of off-axis tension and Iosipescu shear test specimens with the aim of further improving correction procedures for accurate characterization of the axial shear modulus.

2.5.1 Off-axis Tension Test

One of the common test methods for the determination of axial shear modulus of unidirectional composites is the off-axis tension test conducted on specimens whose fiber orientation is neither parallel nor perpendicular to the direction of the applied tensile force. The simplicity of employing the off-axis geometry to characterize the shear response of a unidirectional lamina has resulted in a proposal to employ the 10° off-axis configuration, Chamis (1977). This configuration was chosen because it yields a high value of the shear strain at failure with the corresponding shear stress being the major stress contribution to fracture as determined from a combined-stress failure criterion. However, the off-axis fiber orientation produces a monoclinic material in the coordinate system of the test specimen that also results in shearing in addition to axial and transverse deformations. If the shearing is prevented by the specimen grips, then a highly nonuniform deformation occurs in the test section of the off-axis specimen, Figure 2-14, introducing errors in the measured quantities based on the assumption of uniform states of stress and strain at the gage location. The extent of the introduced error depends not only on the off-axis angle, specimen geometry, end constraint and degree of material anisotropy, but is also different for material parameters.

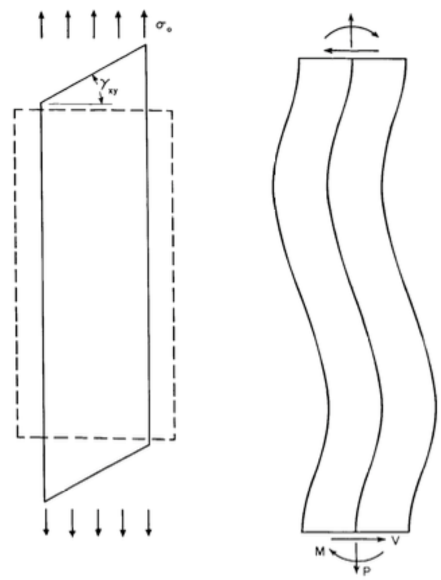

Figure 2-14 Illustrations of influence of end constraints in testing of anisotropic bodies (left: uniform state of stress, right: effect of clamped ends) – Pagano & Halpin (1968)

In practice, the ideal uniform states of stress and strain are extremely hard to achieve due to the end-constraint effect in off-axis specimens. The end-constraint effect produces an additional shear stress, besides axial stress, that leads to inaccurate shear stress evaluation at the strain gage location. To estimate the extent of the stress nonuniformity in off-axis test specimens caused by the end constraints, Pagano and Halpin (1968) developed an approximate stress-based analytical solution for an off-axis specimen with length of l and width of $2h$ that yields the following stresses,

$$\sigma_{xx}(x,y) = -2C_0xy - 2\frac{S_{16}}{S_{11}}C_0y^2 + C_1y + C_2$$

$$\sigma_{yy}(x,y) = 0 \qquad (2.50)$$

$$\tau_{xy}(y) = C_0(y^2 - h^2)$$

where $C_0 = \frac{6S_{16}\epsilon_0}{6h^2(S_{11}S_{66}-S_{16}^2)+S_{11}^2l^2}$, $C_1 = C_0 l$, $C_2 = \frac{C_0}{6S_{16}}(6S_{66}h^2 + S_{11}l^2)$ and ϵ_0 is the applied longitudinal strain. They then calculated errors in the measurement of the off-axis Young's modulus based on the assumption that the axial stress in the test section is uniform and assumed equal to the average axial stress calculated by dividing the applied load by the cross-sectional area of the specimen. These errors were small for off-axis specimens with different orientations and aspect ratios above 6. To eliminate this error in determining the axial Young's modulus, a correction factor η was introduced to compensate for the end-constraint effect.

Pindera and Herakovich (1986) subsequently employed the above analytical solution to estimate errors in the calculation of both the axial shear modulus and the Poisson's ratio as a function of off-axis orientation and geometric and material parameters. In particular, the authors derived correction factors that relate the apparent and true axial shear moduli when the end constraint effects are neglected,

$$\frac{G_{12}}{G_{12}^*} = \frac{\sigma_{12}}{\sigma_{12}^*} \rightarrow G_{12}^* = G_{12}\frac{\sigma_{12}^*}{\sigma_{12}} \qquad (2.51)$$

and have shown that the error in the calculation of the apparent axial shear modulus G_{12}^* may be substantially larger than the error in the apparent off-axis Young's modulus obtained from the Pagano and Halpin's model.

The solution by Halpin and Pagano is based on the application of boundary conditions on the specimen's end faces at one point on opposite faces. These boundary conditions prevent rotation of the end faces in the middle, eliminate rigid body displacement by pinning the central axis on one face, and subjecting it to the axial strain ϵ_0 at the opposite face. This approximation of the actual boundary conditions mimics the action of rigid grips which prevent rotation of the opposite faces and displace one face relative to another by a uniform amount. Herein, we employ the extended FVM methodology to simulate the response of off-axis specimens with different boundary conditions to determine the accuracy of the Halpin-Pagano approximate solution.

The FVM simulations were performed on two 10° off-axis specimen configurations with the dimensions of 80×8 inches discretized into 200×20 square subvolumes, and 40×8 inches discretized into 100×20 square subvolumes. These specimen configurations yield aspect ratios of 10 and 5, respectively, for which the end constraint effect is substantial. The material is graphite/polyimide with the following elastic moduli in the principal material coordinate system: $E_{11} = 19.81\ ksi$, $E_{22} = 1.42\ ksi$, $\nu_{12} = 0.35$, $G_{12} = 0.725\ ksi$. The action of rigid grips is simulated by assigning zero transverse displacement on both faces. The center of one face is set to zero, whereas the center of the opposite face is assigned $\epsilon_{xx}^{o} = 0.01$. In the present study, we investigate the effect of end-face rotation on the resulting stress fields and the ensuing calculation of the apparent axial shear modulus based on the assumption of uniform strain field unaffected by the rigid grips. The investigated end-face rotation cases are described below.

Fully rotating clamped ends

The rotation of the specimens' end faces is simulated by assigning axial displacements that produce uniform rotation which would be obtained by subjecting an off-axis specimen to a uniform axial stress without constraining the ends. The strains produced by uniaxial stress loading are obtained from Hooke's law in the rotated coordinate system that reads,

$$\begin{bmatrix} \epsilon_{xx} \\ \epsilon_{yy} \\ \gamma_{xy} \end{bmatrix} = \begin{bmatrix} \bar{S}_{11} & \bar{S}_{12} & \bar{S}_{16} \\ \bar{S}_{21} & \bar{S}_{22} & \bar{S}_{26} \\ \bar{S}_{16} & \bar{S}_{26} & \bar{S}_{66} \end{bmatrix} \begin{bmatrix} \sigma_{xx} \\ \sigma_{yy} \\ \sigma_{xy} \end{bmatrix} = \begin{bmatrix} \bar{S}_{11} & \bar{S}_{12} & \bar{S}_{16} \\ \bar{S}_{21} & \bar{S}_{22} & \bar{S}_{26} \\ \bar{S}_{16} & \bar{S}_{26} & \bar{S}_{66} \end{bmatrix} \begin{bmatrix} \sigma_{xx}^{o} \\ 0 \\ 0 \end{bmatrix} \tag{2. 52}$$

Therefore, the strain components are expressed in terms of the applied axial tensile stress,

$$\epsilon_{xx}^{o} = \bar{S}_{11}\sigma_{xx}^{o}$$

$$\epsilon_{yy}^{o} = \bar{S}_{12}\sigma_{xx}^{o} \tag{2. 53}$$

$$\gamma_{xy}^{o} = \bar{S}_{16}\sigma_{xx}^{o} = \bar{S}_{16}\epsilon_{xx}^{o}/\bar{S}_{11}$$

From the strain-displacement relation for the in-plane shear strain, we have

$$\gamma_{xy}^{o} = \frac{\partial u}{\partial y} + \frac{\partial v}{\partial x} = \frac{\partial u}{\partial y} \tag{2. 54}$$

Integrating with respect to y, the axial displacement reads,

$$u(x, y) = \gamma_{xy}^{o} y + f(x) \tag{2. 55}$$

Therefore $f(x)$ is obtained by evaluating the axial displacement at $y = 0$, $u(x, y = 0) = f(x) = \epsilon_{xx}^{o} x$. Hence the horizontal displacement $u(x, y)$ at $x = l$, which is the exact displacement boundary condition in the presence of unconstrained rotation, becomes,

$$u(x = l, y) = \gamma_{xy}^{o} y + \epsilon_{xx}^{o} l = \frac{\bar{S}_{16}\epsilon_{xx}^{o} y}{\bar{S}_{11}} + \epsilon_{xx}^{o} l = (\frac{\bar{S}_{16} y}{\bar{S}_{11}} + l)\epsilon_{xx}^{o} \tag{2. 56}$$

whereas at the left end we have,

$$u(x = 0, y) = \gamma_{xy}^{o} y = \frac{\bar{S}_{16} y}{\bar{S}_{11}} \epsilon_{xx}^{o} \tag{2. 57}$$

Partially rotating clamped ends (positive half rotation)

In this simulation, the rigidly clamped ends are allowed to rotate in the same direction half as much as the specimen would shear in the absence of rigid clamps. The corresponding displacement boundary conditions at the left and right ends of the specimen are,

$$u(x=0,y)=\frac{\gamma_{xy}^{o}y}{2}=\frac{\bar{S}_{16}y}{2\bar{S}_{11}}\epsilon_{xx}^{o} \tag{2. 58}$$

$$u(x=l,y)=(\frac{\bar{S}_{16}y}{2\bar{S}_{11}}+l)\epsilon_{xx}^{o} \tag{2. 59}$$

Partially rotating clamped ends (negative half rotation)

In this simulation, the rigidly clamped ends are allowed to rotate in the opposite direction half as much as the specimen would shear in the absence of rigid clamps. The corresponding displacement boundary conditions at the left and right ends of the specimen are,

$$u(x=0,y)=-\frac{\gamma_{xy}^{o}y}{2}=-\frac{\bar{S}_{16}y}{2\bar{S}_{11}}\epsilon_{xx}^{o} \tag{2. 60}$$

$$u(x=l,y)=(-\frac{\bar{S}_{16}y}{2\bar{S}_{11}}+l)\epsilon_{xx}^{o} \tag{2. 61}$$

In the sequel, we first compare the stress fields generated under fully clamped displacement boundary conditions with the Halpin-Pagano model predictions for the 10° off-axis specimen proposed by Chamis for the determination of the axial shear modulus. Subsequently, we employed the FVM solutions for the response of a sequence of off-axis specimens with increasing off-axis angles, and calculated the error in the determination of the axial shear modulus if the effect of end constraints is neglected. The following cases are considered,

(1) Halpin-Pagano solution: end mid points fixed without rotation as elasticity assumptions

(2) FVM simulation #1: with both ends fully fixed

(3) FVM simulation #2: with both ends point fixed but fully free to rotate

(4) FVM simulation #3: with both ends point fixed but half free to rotate

(5) FVM simulation #4: with both ends point fixed but half free to rotate in opposite

Figure 2-15 and Figure 2-16 present comparison of the stress fields generated by the Halpin-Pagano model and FVM simulations #1 (both ends fully fixed) for the specimens with 5 and 10 aspect rations, respectively. The left column of figures are the stress field plots from Halpin-Pagano mode, and the right column of figures are the stress field plots generated from FVM simulations #1.

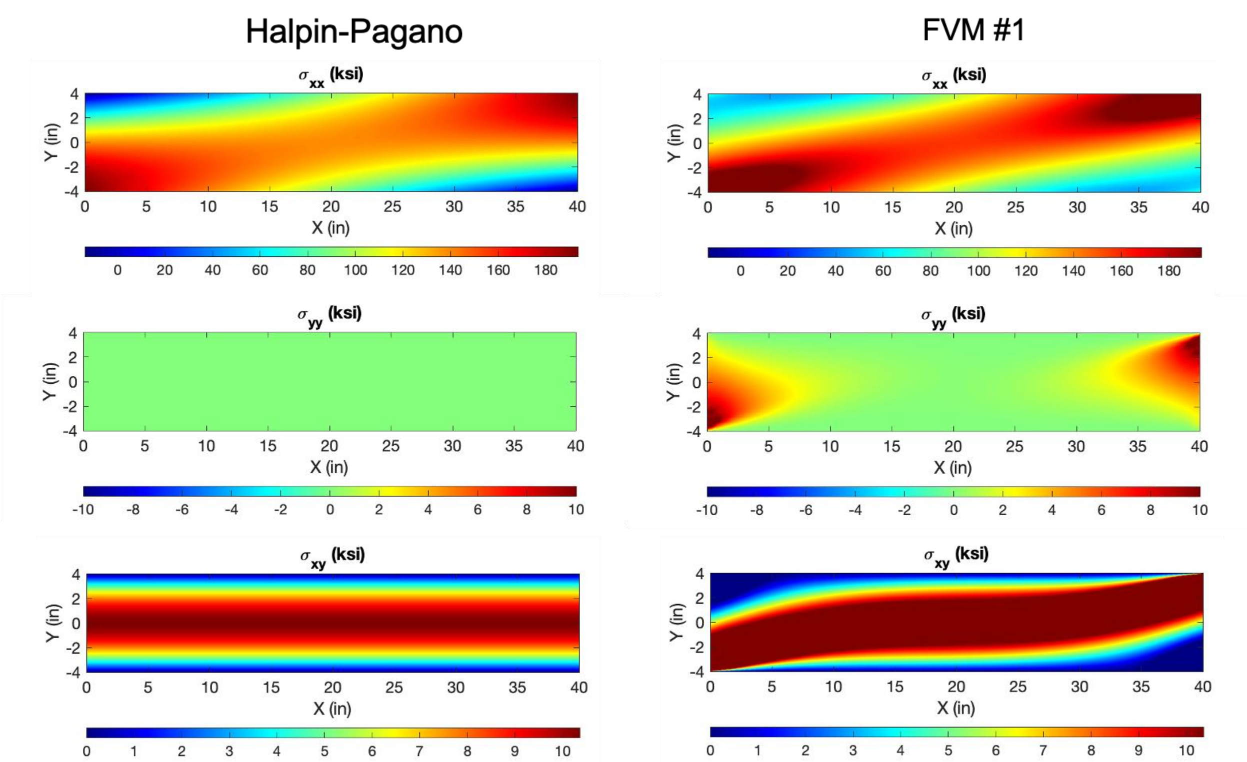

Figure 2-15 Stress fields generated by the Halpin-Pagano model and FVM simulations for the specimens with aspect ratio of 5

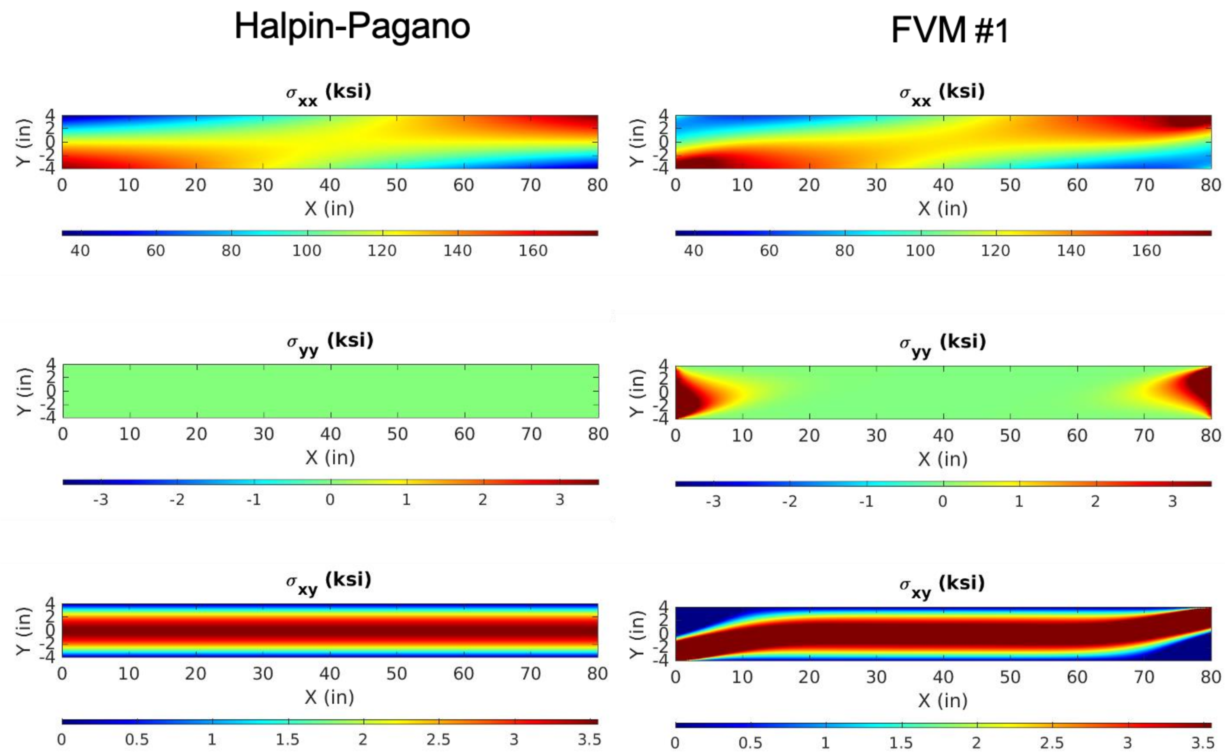

Figure 2-16 Stress fields generated by the Halpin-Pagano model and FVM simulations for the specimens with aspect ratio of 10

Figure 2-17 illustrates the error introduced into the calculation of the axial shear modulus as a function of the off-axis angle predicted by the Halpin-Pagano model and FVM simulations based on the four displacement boundary conditions discussed in the foregoing. Figure 2-17 (right) includes the experimental results generated by Pindera and Herakovich (1986) using a special test fixture that employs rigid clamps but allows some rotation of the specimen ends. All predicted or tested samples that have off-axis angles greater than 30 degrees have nearly prefect agreements with the apparent shear modulus. With experimental results available for some off-axis samples with an aspect ratio of 10, FVM simulations with different end conditions can be compared to Pagano-Halpin's solutions both against the experimental data. The FVM simulation with fixed end exhibits an accurate prediction against the corrected experimental results, and the apparent experimental shear modulus curve lies in between those from FVM simulations with fixed ends and half free rotation ends. This might provide insight into understanding the mechanism of how the grips work in off-axis tension tests and reevaluating the correctness factor for experimental data obtained.

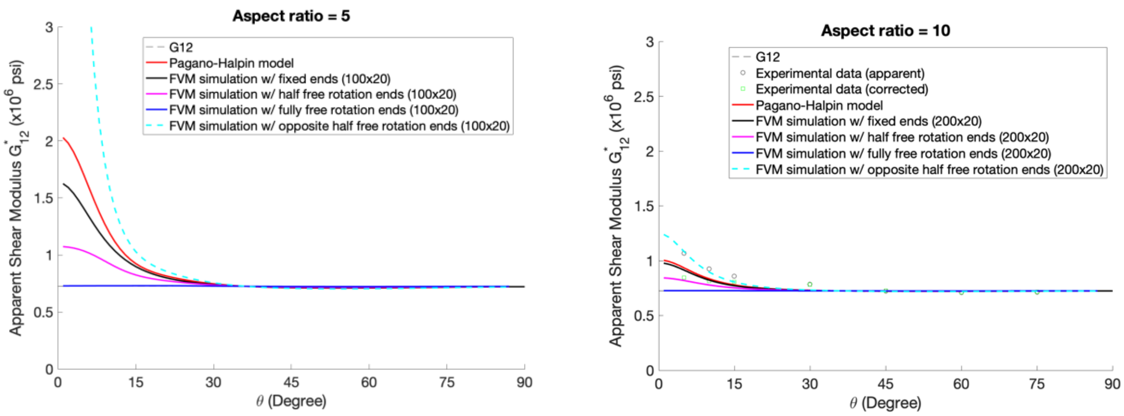

Figure 2-17 The shear modulus obtained from different approaches in a series of off-axis angles for samples with aspect ratios of 5 (left) and 10 (right)

2.5.2 Iosipescu Shear Test

An attractive alternative to the off-axis tension test for the determination of both the initial shear modulus and ultimate shear strength is the Iosipescu test. The Iosipescu shear test was originally designed for measuring shear properties of isotropic and homogenous materials such as metals. The Iosipescu shear test is designed to characterize a material’s response under shear loading based on ASTM D5379 (Standard Test Method for Shear Properties of Composite Materials by the V-Notched Beam Method). A rectangular specimen with opposing “v” shaped notches is placed in the test fixture. One side of the specimen is constrained while the other side is displaced down during this test. Deformation is concentrated along a thin line connecting the opposing “v” notches, thereby producing a predominantly shear state of deformation. The shear load controlled by the hydraulic force system is applied forcing the right part to displace, and the displacement of the right part are measured as well until specimen failure. Pindera et al. (1987) adopted Iosipescu specimens with ASTM-specify overall dimensions but with wider “v” notches as actually measured from their aramid/epoxy and graphite/polyimide testing samples, shown in Figure 2-18. The specimens were cut into 0.08-inch-thick ones in the experiments conducted by

Pindera et al. (1987) and He. et al. (2002) for both 0° and 90° specimens before test performing at a nominal strain rate of 1% per minute.

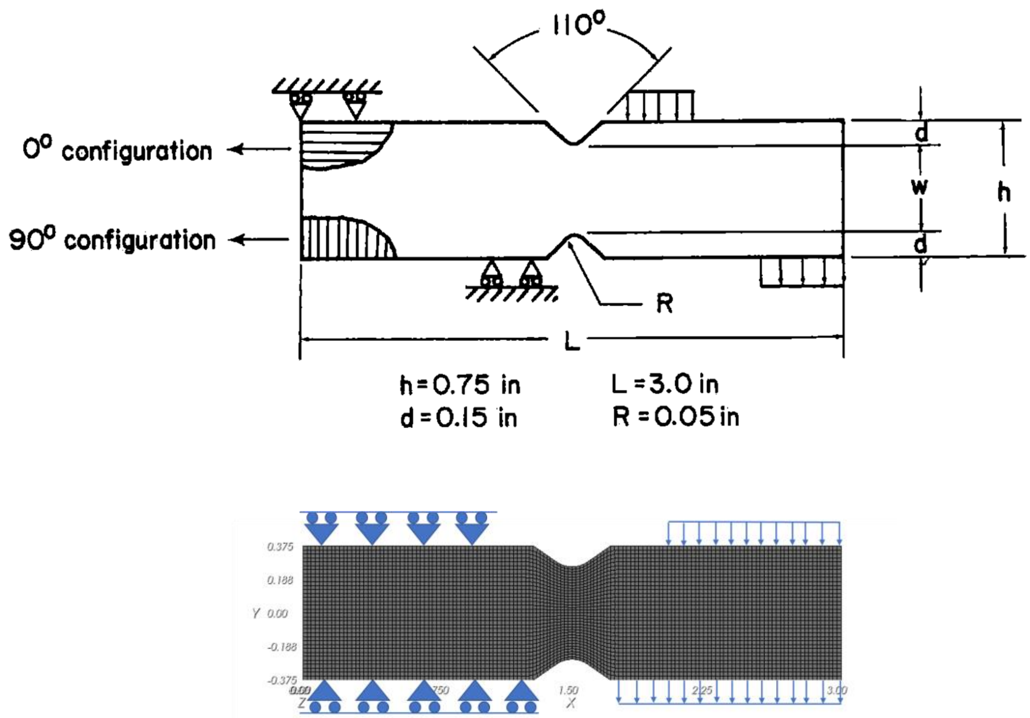

Figure 2-18 Configuration with its boundary conditions for a Iosipescu specimen (top) and its model in FVM with meshing and applied boundary condition (bottom)

Iosipescu shear test can be used for evaluating the in-plane shear modulus G_{12} for 0° and 90° specimens and out-of-plane shear modulus G_{23} for specimens with fibers perpendicular to specimen's plane. Compared with other test methods, such as the thin-walled tube test and the rail shear test, the Iosipescu shear test uses a flat specimen that is easier to fabricate while achieving a nearly pure and uniform shear strain-stress state over the test region. Consequently, more reliable results can be obtained, and the test has become well-accepted among researchers in the field. Therefore, it is investigated theoretically as a mean for determining the in-plane shear modulus and strength of unidirectional composites. However, when employing this test method, care needs to be taken in interpreting the experimental results, because the shear stress distribution along the test section of highly anisotropic Iosipescu specimens is not uniform. Consequently, the average shear stress, commonly calculated by dividing the applied load by the cross-sectional area, is in general not the same as the shear stress at the point where the strain gage is located. FVM simulation is employed herein to analyze the stress distribution in an Iosipescu specimen to determine errors in the calculation of the shear modulus based on shear stress uniformity.

Figure 2-19 and Figure 2-20 compare the in-plane stress fields in the 0º and 90º Iosipescu specimens subjected to the same displacements applied on the top and bottom surfaces of the right-hand side of the specimens.

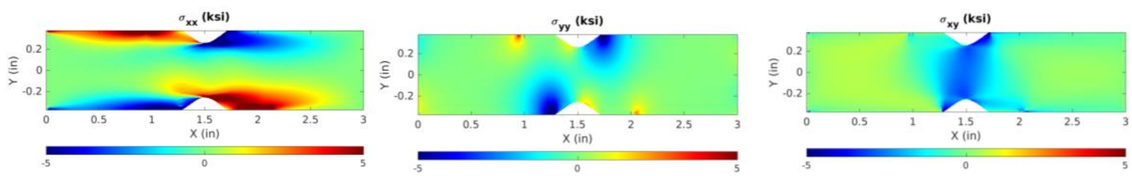

Figure 2-19 Stress fields in 0° aramid/epoxy Iosipescu specimens

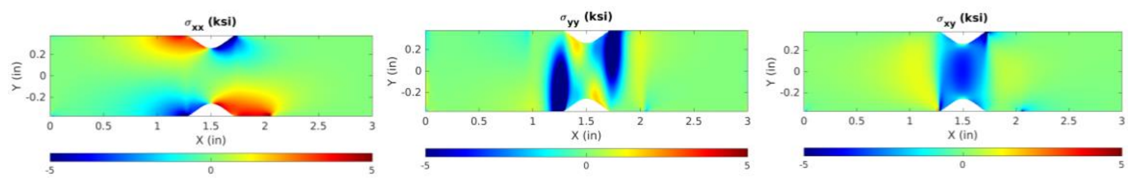

Figure 2-20 *Stress fields in 90° aramid/epoxy Iosipescu specimens*

As observed, in addition to shear stress across the specimens' test section spanning the V-notches, not insignificant axial and transverse normal stresses are also present. These do not influence the axial shear modulus determination for orthotropic or transversely isotropic materials, as is the case of the aramid/epoxy composite analyzed here. Differences in the two normal and one shear stress fields between the "v" notches are observed in the two specimen configurations whose detailed distributions are illustrated in Figure 2-21. The 0° aramid/epoxy Iosipescu specimen has a large variation in stress σ_{xx} through the middle cut in the test section than 90° aramid/epoxy Iosipescu specimen does, but both with relatively small variation in the stress σ_{yy}. Except near the very top and bottom of the middle cut in each test section, 0° aramid/epoxy Iosipescu specimen has a right-facing curve plotting the normalized shear stress along the middle cut of test section, and 90° aramid/epoxy Iosipescu specimen in the opposite possesses a left-facing normalized shear stress curve, both of which match with the tendency reflected in the normalized shear stress distribution plots for aramid/epoxy samples.

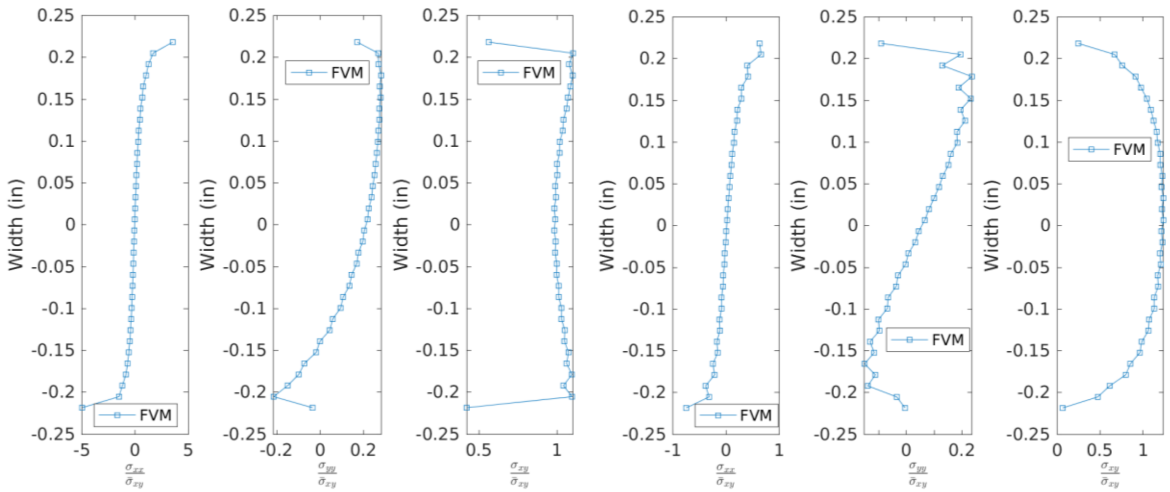

Figure 2-21 Stress distributions across test sections of 0° (left three) and 90° (right three) aramid/epoxy Iosipescu specimens

These differences introduce errors in the determination of the axial shear modulus based on the uniform shear stress assumption. Because the 0° configuration produces a lower magnitude of the shear stress in the middle of the test section, where the strain gage is placed, relative to the uniform shear stress, a higher apparent shear modulus will be calculated. The converse is true for the 90° configuration, thereby underestimating the actual shear modulus. These discrepancies are observed in the experimental data generated by Pindera et al. (1987) on the aramid/epoxy composite.

Similar results are observed in Iosipescu specimens made of graphite/polyimide with different moduli ratios, Figure 2-22 and Figure 2-23, as well as the normalized shear stress distributions in the middle of the test section, Figure 2-24.

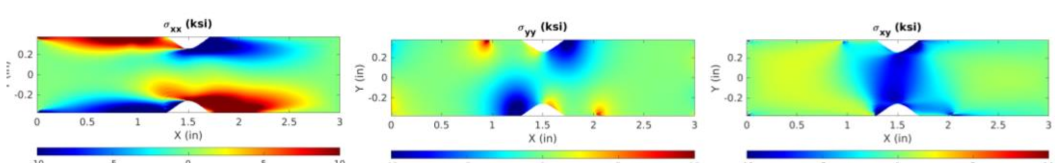

Figure 2-22 Stress fields in 0° graphite/polyimide Iosipescu specimens

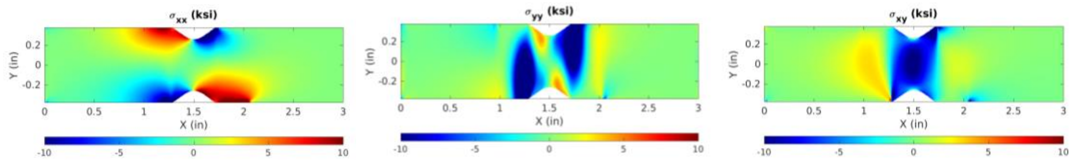

Figure 2-23 Stress fields in 90° graphite/polyimide Iosipescu specimens

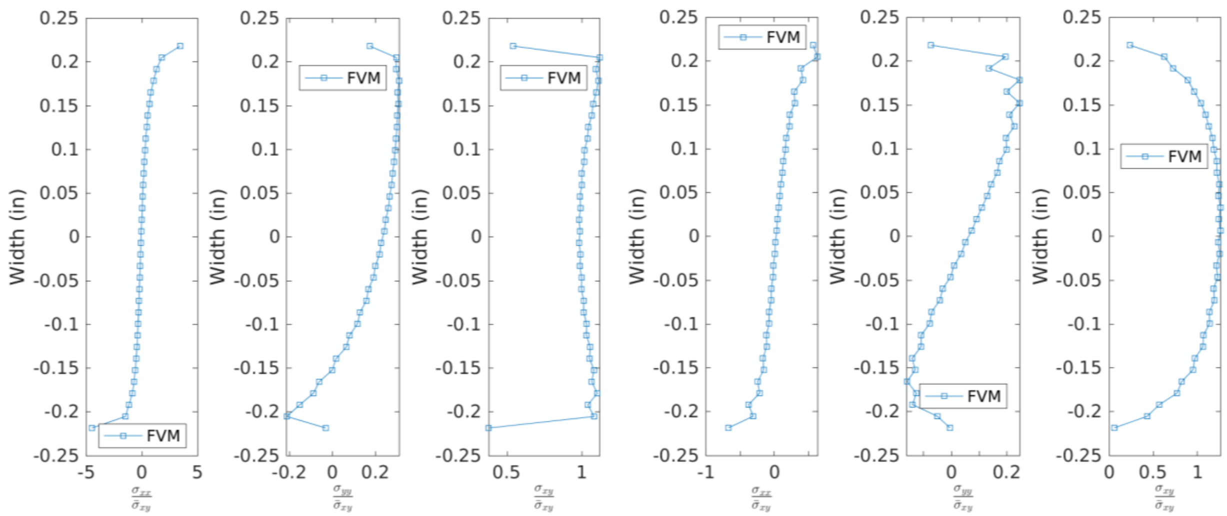

Figure 2-24 Stress distributions across test sections of 0° (left) and 90° (right) graphite/polyimide Iosipescu specimens

2.6 Summary

Plane problems, including plane stress, plane strain, and generalized plane strain conditions have been formulated within the finite-volume framework for numerical solution implementation. The method has been extended to accommodate the analysis of structural components composed of monoclinic and orthotropic materials with one and three planes of symmetry. The extended framework has been verified using elasticity solutions, and subsequently employed to investigate technologically significant problems as well as problems of fundamental interest. These include questions regarding the applicability of homogenization when analyzing the response of multilayered beam or plate-like structures, and analysis errors in the common test methods employed for the determination of the axial shear modulus of advanced unidirectional composites such as off-axis tension tests and Iosipescu shear tests. By visualizing the stress distribution and identifying the effects of end conditions, FVM demonstrates its ability to perform full-field analysis and highlight any differences from Pagano-Halpin's analytical solution. Comparing FVM results and Pagano-Halpin's solutions against experimental data for off-axis samples with an aspect ratio of 10, reveals that the FVM simulation with fixed end accurately predicted the corrected experimental results. FVM also provides an alternative to analyze the full-field behavior of Iosipescu test specimens by validating the correction of the shear stress distribution at the location of the strain gauges for the purpose of minimizing the error in the intralaminar shear modulus.

Chapter 3

Saint Venant's Torsion Problems

3.1 Introduction

Twisting of prismatic bars due to pure torsion along the bar's axis is a fundamental deformation mode in structural analysis and hence plays an important role in the design of structural members of various cross sections, e.g., beams subjected to transverse loading, shafts in power trains, cf., Timoshenko and Goodier (1970), Boresi et al. (1985), Ugural and Fenster (2003), Sadd (2009). This deformation mode is also one of the earliest elasticity problems studied by several scientists, most notably Saint Venant who had proposed the first successful solution to this class of problems using what is now called the Saint Venant's semi-inverse method since 1855. In his approach, the functional form of two of the three displacement components is obtained from the deformation analysis of a bar's cross section perpendicular to the generator axis. The remaining displacement component is then determined such that the governing differential equations of elasticity and boundary conditions are satisfied.

The developed semi-inverse method to the elasticity theory of bars with general cross sections subjected to torsion yields solutions formulated either in terms of displacements or stresses. Analytical solutions to torsion problems are obtained only for a small class of cross sections bounded by surfaces that can be expressed by simple equations, Fourier series expansions, or that can be generated by conformal mapping. Even fewer are available for cross sections that are orthotropic. Moreover, analytical solutions for complicated cross sections do not generally exist, especially cross sections made of heterogeneous materials. Hence numerical solutions are typically employed, as discussed by Chen et al. (2020), with FEM most prevalent due to their ability to efficiently capture arbitrarily shaped cross sections. An attractive alternative to the solution of the Saint Venant's torsion problem is offered by the FVM. Chen et al. (2020) were the first to employ FVM in the solution of Saint Venant's torsion problems of prismatic homogeneous and heterogeneous bars of cross sections made up of rectangular elements, including I, T, box and channel beams. The solution was carried out using the Saint Venant's semi-inverse method within the finite-volume framework developed by Bansal and Pindera (2003) based on the discretization of the analyzed domain into rectangular subvolumes. This framework was developed explicitly for the analysis of heterogeneous materials and enforces continuity of both surface averaged tractions and displacements across adjacent subvolumes. However, the discretization of a prismatic bar's cross section into rectangular subvolumes limits its applicability to domains with linear interfaces and boundaries aligned with the coordinate system in which the analysis takes place. This limitation was overcome by parametric mapping introduced into the finite-volume framework of Bansal and Pindera (2003) in a sequence of contributions dealing with functionally graded and periodic materials by Cavalcante et al. (2007), Gattu et al. (2008), Khatam and Pindera (2009), Cavalcante and Pindera (2012, 2016). In this approach, the analysis domain is discretized into quadrilateral subvolumes using a parametric mapping of a square subvolume from a reference plane to the physical plane that facilitates simulation of curved boundaries and interfaces between subdomains of a cross section containing distinct materials.

In this chapter, parametric mapping is incorporated into the previously developed finite-volume based solution approach to torsion problems. It is then applied to several structural problems involving composite cross sections of non-rectangular shape.

3.2 Saint Venant's Torsion

Within the class of elasticity problems called torsion, a prismatic bar of arbitrary cross section in the $x - y$ plane is shown in Figure 3-1. The bar is loaded by a distribution of forces tangent to the plane transverse to the cylinder's axis that produce a zero net force resultant but is statically equivalent to a moment $(0,0,M_z)$ directed along the z axis. For such bars, the problem reduces to that of pure torsion named after Saint Venant.

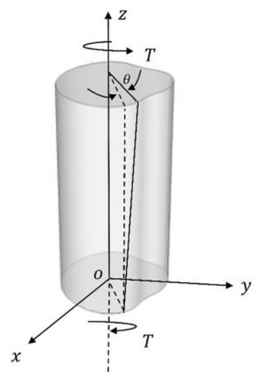

Figure 3-1 Saint Venant's torsion problem showing the deformation of planes passing through the prismatic bar's centroidal axis due to twisting moment applied to the end faces

The solution to torsion problems occupies a vital place in the theory of elasticity as it demonstrates an important solution technique that reduces a seemingly three-dimensional elasticity problem involving three unknown displacements to a two-dimensional one involving just one displacement. In this approach, known as the Saint Venant's semi-inverse method, explicit expressions for the two in-plane displacements in the bar's cross section are obtained from geometric considerations of the deformation of a prismatic bar subjected to pure torsion by twisting moments directed along the bar's axis applied to the end faces. The remaining out-of-plane displacement, proportional to the so-called warping function, is assumed to depend on the in-plane coordinates. The above displacement field satisfies two of the three equilibrium equations of elasticity and produces only shear stresses acting on the bar's cross section that generates the applied twisting moment. Chen et al. (2020, 2021) addressed this problem using the finite-volume technique and provided a summary of methods employed by others. The most recent contribution to the development of new methods for the Saint Venant's torsion problem includes a radial basis meshless method that may also be used for orthotropic and functionally graded cross sections.

It is noted that the Saint-Venant semi-inverse method is valid for regions away from fixed ends according to the Saint-Venant's principle. Consider a long beam whose one end is fixed to a rigid wall, while the other is acted upon by a distribution of forces that produce a resultant force F and/or a couple moment M. While the distributions of strains and stresses near the region of force application may differ, the difference in the local force distribution will have no significant effect on the stress state far enough from the region of application, as long as the systems of applied forces and moments are statically equivalent. In this chapter, it is assumed that the analyzed cross section is sufficiently far away from both ends thus eliminating the end effects.

The torsion problem will be formulated in terms of in-plane displacements or the warping function, then re-formulated in terms of the Prandtl stress function in the preceding sections. The stress formulation facilitates the development of closed-form solutions to several important cross sections of homogeneous bars.

3.2.1 Displacement Formulation and Warping Function

Analysis of the deformation of a prismatic bar subjected to pure twisting moments along the z axis in the $x - y$ plane situated at an arbitrary elevation in z direction from the face relative to which the rotation angle of the cross section is measured, Figure 3-2 based on the kinematic assumptions produces the in-plane displacements in the x and y direction, u and v of the form,

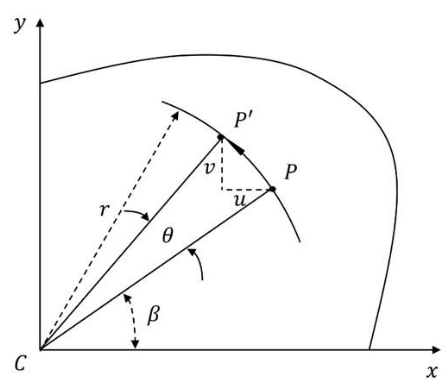

Figure 3-2 Saint Venant's torsion problem with u and v displacement components from kinematic assumptions

$$u(y,z) = -\theta yz\,, v(x,z) = \theta xz \tag{3. 1}$$

where θ is the angle of twist of the cross section per unit length along the bar's axis. The out-of-plane displacement w in the z direction is then assumed to depend only on the in-plane coordinates

(x, y) because the twisting moment does not vary along the bar's axis. It is expressed in terms of the warping function $\psi(x, y)$ as follows

$$w(x, y) = \theta\psi(x, y) \tag{3. 2}$$

for consistency with the in-plane displacement field.

The above displacement fields produce vanishing normal strains, and engineering shear strains only in the planes that contain the z axis, namely $x - z$ plane and $y - z$ plane.

$$\epsilon_{xx} = \epsilon_{yy} = \epsilon_{zz} = \gamma_{xy} = 0$$

$$\gamma_{zx} = \frac{\partial w}{\partial x} - y\theta \tag{3. 3}$$

$$\gamma_{zy} = \frac{\partial w}{\partial y} + x\theta$$

Consequently, the only stresses that result are the shear stresses in the above two planes,

$$\sigma_{zx} = G_{zx}\theta\left(\frac{\partial\psi}{\partial x} - y\right), \sigma_{zy} = G_{zy}\theta\left(\frac{\partial\psi}{\partial y} + x\right) \tag{3. 4}$$

This stress field satisfied exactly the first two equilibrium equations with the third equation

$$\frac{\partial\sigma_{zx}}{\partial x} + \frac{\partial\sigma_{zy}}{\partial y} = 0 \tag{3. 5}$$

producing a condition on $\psi(x, y)$

$$G_{zx}\frac{\partial^2\psi}{\partial x^2}+G_{zy}\frac{\partial^2\psi}{\partial y^2}=0 \tag{3. 6}$$

The above equation is solved subject to the traction-free boundary condition on the prismatic bar's lateral surface

$$t_z=\sigma_{zx}cos(n,x)+\sigma_{zy}cos(n,y)=0 \tag{3. 7}$$

which becomes

$$G_{zx}\frac{\partial\psi}{\partial x}\frac{dx}{dn}+G_{zy}\frac{\partial\psi}{\partial y}\frac{dy}{dn}=G_{zx}y\frac{dx}{dn}-G_{zy}x\frac{dy}{dn} \tag{3. 8}$$

3.2.2 Stress Formulation and Prandtl Potential Function

The torsion problem may be re-formulated in terms of stresses by noting that the surviving third equilibrium equation is satisfied by the potential function $\phi(x,y)$ called Prandtl stress function such that

$$\sigma_{zx}=\frac{\partial\phi}{\partial y},\ \sigma_{zy}=-\frac{\partial\phi}{\partial x} \tag{3. 9}$$

Using these definitions in the expressions for the two stress components given in terms of $\psi(x,y)$, differentiating appropriately and adding the two equations give the governing differential equation for $\phi(x,y)$

$$\frac{1}{G_{zy}}\frac{\partial^2\phi}{\partial x^2}+\frac{1}{G_{zx}}\frac{\partial^2\phi}{\partial y^2}=-2\theta \tag{3. 10}$$

The traction-free boundary condition on the prismatic bar's lateral surface then becomes,

$$t_z = \sigma_{zx}\frac{dx}{dn} + \sigma_{zy}\frac{dy}{dn} = \frac{\partial\phi}{\partial y}\frac{dy}{ds} + \frac{\partial\phi}{\partial x}\frac{dx}{ds} = \frac{d\phi}{ds} = 0 \tag{3. 11}$$

with the corresponding traction-free boundary condition on ϕ

$$\phi(x, y) = constant \ (x, y \in S) \tag{3. 12}$$

Because the shear stress resultant is tangent to the family of lines $\phi = constant$, the traction-free boundary condition may be used to construct the potential function $\phi(x, y)$ for certain cross sections through appropriate choice of the constant that defines the boundary.

Once the solution for either $\psi(x, y)$ or $\phi(x, y)$ is obtained for a given cross section, the angle of twist per unit length θ may be related to the resulting torque produced by the shear stresses σ_{xz} and σ_{yz} through the torsional rigidity D.

$$M = \iint_R \left(x\sigma_{zy} - y\sigma_{zx}\right) dxdy = \theta D \tag{3. 13}$$

3.3 Finite Volume Method for Saint-Venant's Torsion Problems

The finite volume method employs the displacement formulation in the solution of Saint Venant's torsion problems involving arbitrary cross sections that may be homogeneous or heterogeneous. These features motivate partition of the cross section into quadrilateral subvolumes that are assigned material properties which mimic the cross-section's microstructure and shape. The subvolumes may be isotropic or orthotropic as only two shear moduli participate in the problem formulation. These quadrilateral subvolumes are the elementary units in the finite volume analysis wherein the local displacement fields are approximated using simple polynomial expressions. Using the displacement formulation ensures that the compatibility equations in each subvolume are identically satisfied, and the use of strain-displacement and constitutive equations leads to direct calculation of the local stress fields through simple differentiation. The use of simple polynomials precludes point-wise satisfaction of the displacement and traction components across common faces of adjacent subvolumes. Hence a compromise is employed that involves the imposition of interfacial displacement and traction continuity in a surface-average sense. The equilibrium equations are satisfied in a surface-average sense as well. Hence the solution strategy employed in FVM follows the elasticity-based solution strategy, albeit in a surface-average as opposed to point-wise sense. Thus, it differs fundamentally from the variational-based solution strategies based on energy minimization. Whereas the subvolume equilibrium is always satisfied in a surface-average sense, the point-wise accuracy of the method increases with partition refinement.

The above overview of the method again clearly suggests that the finite volume method was originally developed as a semi-analytical tool to account for material heterogeneity with arbitrary geometric shapes and distributions, and to avoid intricate mathematical derivations in the presence of complex microstructural details in the solution of Saint Venant's torsion problems beyond isotropic materials.

The partitioning of the analyzed domain using (i) quadrilateral subvolumes to accommodate cross sections of arbitrary shapes is accomplished using parametric mapping of the reference square domain in the reference plane onto the actual quadrilateral subvolume in the physical plane. The displacement field approximation is also made in the reference plane, and thus the FVM analysis which entails the development of relations between displacement and traction quantities is conducted in both planes. The establishment of these relations enables the construction of the local stiffness matrix for each quadrilateral subvolume in the physical plane that relates the surface-averaged in-plane displacements to the corresponding tractions. The local stiffness matrix is constructed such that the quadrilateral subvolume's equilibrium is satisfied in the physical plane, and the assembly of all the local stiffness matrices ensures that traction and displacement continuity and prescribed boundary conditions are also satisfied.

This section first describes the parametric mapping employed in the theory's construction, followed by subvolume discretization into quadrilateral partitions, displacement field construction, and the solution for these in-plane displacements using the parametric FVM. Towards this end, local coordinate systems $(\bar{x}, \bar{y})^{(i)}$ are set up at the subvolumes' centroids, where the coordinates $(x, y)^{(i)}$ of an arbitrary point within the subvolume (i) are referred in the global coordinate system. The global coordinates are employed in the parametric mapping described in the following subsection, whereas the local coordinates transferred in the reference system are employed in the in-plane displacement, strain and stress field representation in each subvolume.

3.3.1 Transfinite Interpolation

Numerical grid generation arose from the need to compute solutions to partial differential equations in fluid dynamics on physical regions with complex geometry. The accuracy of the solution to partial differential equations depends on how fine and sensitive the grid is for the problem domain. Transfinite interpolation (TFI) is a means to construct functions over a planar domain in such a way that they match a given function on the boundary. The transfinite interpolation method, first introduced by Gordon and Hall (1973), receives its name due to how a function belonging to this class is able to match the primitive function at a nondenumerable number of points. Unlike rectangular discretization which may not conform well to physical regions even with a great number of partitions, the present parametric mapping employs transfinite grid generation that defines the subvolume vertices in the physical domain, introduced by Gordon and Thiel (1982) for constructing meshes originally developed for grid construction in finite-difference and finite-element solutions of boundary-value problems.

All of the subvolume vertex coordinates $\left(x_p, y_p\right)^{(i)}$, where p is the numbering index of the vertices, are generated in the physical domain using transfinite mapping. By transforming a physical region to a simpler region, one removes the complication of the shape of the physical region from the problem. An advantage of this technique is that the boundary conditions become easier to approximate accurately, albeit at the cost of an increase in the complexity of the transformed equations.

To determine the subvolume vertex coordinates, one first maps the physical boundary of the analyzed cross section onto a unit square in the $s - t$ plane. This mapping is defined by equations of the form,

$$\boldsymbol{X}_b(s), \boldsymbol{X}_t(s) \text{ for } 0 \le s \le 1$$
$$\boldsymbol{X}_t(s), \boldsymbol{X}_r(s) \text{ for } 0 \le t \le 1 \tag{3.14}$$

where, for instance, the arbitrary boundary point $\boldsymbol{X}_b(s) = (x_b(s), y_b(s))$ describes parametrically the portion of the boundary in the physical plane that maps onto the bottom unit square in the reference plane. As an example, the identity map that maps a unit square in the physical plane onto unit square in the reference plane is given by,

$$\boldsymbol{X}_b(s) = (s, 0), \boldsymbol{X}_t(s) = (s, 1) \text{ for } 0 \le s \le 1$$
$$\boldsymbol{X}_t(s) = (0, t), \boldsymbol{X}_r(s) = (1, t) \text{ for } 0 \le t \le 1 \tag{3.15}$$

The first-degree Lagrange polynomials $1 - s$, s, $1 - t$ and t are used as blending functions in the basic transfinite interpolation formula to generate the point $x(s,t)$, $y(s,t)$ in the interior of the cross section,

$$x(s,t) = (1-t)x_b(s) + tx_t(s) + (1-s)x_l(t) + sx_r(t) - [stx_t(1) + s(1 - t)x_b(1) + t(1-s)x_t(0) + (1-s)(1-t)x_b(0)]$$
$$y(s,t) = (1-t)y_b(s) + ty_t(s) + (1-s)y_l(t) + sy_r(t) - [sty_t(1) + s(1 - t)y_b(1) + t(1-s)y_t(0) + (1-s)(1-t)y_b(0)] \tag{3.16}$$

Herein, it is natural to divide the entire square domain in the reference plane into the same number of equally spaced horizontal and vertical lines whose intersections determined from the above linear interpolation equations for the given cross section define the subvolume vertex coordinates. Hence a single parameter is required in the parametric boundary representation and the linear interpolation equations for the interior points.

This grid generation using transfinite interpolation is the most widely used algebraic grid generation procedure and also has many possible variations. It is the most often-used procedure to start a structured grid generation project. The advantage of using TFI is that it is an interpolation procedure that can generate grids conforming to specified boundaries. Grid spacing is under direct control. Therefore, TFI is easily programmed and is very computationally efficient. These advantages are offset by the fact that interpolation methods may not generate smooth grids, in particular, when the problem domain has steep curves or bends. In these cases, the grid becomes folded across the bends of the domain. The grid generation procedure will be illustrated using the cross sections in the sequel, which are employed in the verification and assessment of the FVM in Section 3.4.1.

3.3.2 Parametric Mapping

The reference subvolume is a square in the $\eta - \xi$ plane bounded by $-1 \leq \eta \leq 1, 1 \leq \xi \leq 1$. The vertices are numbered such that the first set of coordinates is at the lower left corner and the numbering convention increases in a counterclockwise fashion. The faces are numbered similarly such that the face F_p lies between the vertices $\left(\bar{x}_p, \bar{y}_p\right)^{(i)}$and $\left(\bar{x}_{p+1}, \bar{y}_{p+1}\right)^{(i)}$ with $p+1$ going to 1 when $p = 4$. Thus, the components of the unit normal vector $\boldsymbol{n}_{\boldsymbol{p}}^{(\boldsymbol{i})} = \left[n_x, n_y\right]_p^{(i)}$ to the face F_p in each subvolume (i) are given by

$$n_{x|_p} = \frac{\bar{y}_{p+1}^{(i)} - \bar{y}_p^{(i)}}{l_p}, \; n_{y|_p} = \frac{\bar{x}_{p+1}^{(i)} - \bar{x}_p^{(i)}}{l_p} \tag{3. 17}$$

where $l_p = \sqrt{\left(\bar{x}_{p+1}^{(i)} - \bar{x}_p^{(i)}\right)^2 + \left(\bar{y}_{p+1}^{(i)} - \bar{y}_p^{(i)}\right)^2}$. The mapping if the point (η, ξ) in the reference subvolume to the corresponding point $(\bar{x}, \bar{y})^{(i)}$ in the subvolume of the actual discretized cross section follows that of Cavalcante et al. (2007).

$$\bar{x}^{(i)}(\eta, \xi) = N_1(\eta, \xi)\bar{x}_1^{(i)} + N_2(\eta, \xi)\bar{x}_2^{(i)} + N_3(\eta, \xi)\bar{x}_3^{(i)} + N_4(\eta, \xi)\bar{x}_4^{(i)} \tag{3. 18}$$

$$\bar{y}^{(i)}(\eta,\xi) = N_1(\eta,\xi)\bar{y}_1^{(i)} + N_2(\eta,\xi)\bar{y}_2^{(i)} + N_3(\eta,\xi)\bar{y}_3^{(i)} + N_4(\eta,\xi)\bar{y}_4^{(i)}$$

where $N_1(\eta,\xi) = \frac{1}{4}(1-\eta)(1-\xi)$, $N_2(\eta,\xi) = \frac{1}{4}(1+\eta)(1-\xi)$, $N_3(\eta,\xi) = \frac{1}{4}(1+\eta)(1+\xi)$, $N_4(\eta,\xi) = \frac{1}{4}(1-\eta)(1+\xi)$.

The determination of strains and stresses within quadrilateral subvolumes requires the relationship between first partial derivatives of the warping function ψ in the two planes $\eta - \xi$ and $x - y$. These are related through the Jacobian $\boldsymbol{J}$ and its inverse $\boldsymbol{J}^{-1}$,

$$\begin{bmatrix} \frac{\partial\psi}{\partial\eta} \\ \frac{\partial\varphi}{\partial\xi} \end{bmatrix}^{(i)} = \boldsymbol{J} \begin{bmatrix} \frac{\partial\psi}{\partial x} \\ \frac{\partial\varphi}{\partial y} \end{bmatrix}^{(i)} \leftrightarrow \begin{bmatrix} \frac{\partial\psi}{\partial x} \\ \frac{\partial\varphi}{\partial y} \end{bmatrix}^{(i)} = \boldsymbol{J}^{-1} \begin{bmatrix} \frac{\partial\psi}{\partial\eta} \\ \frac{\partial\varphi}{\partial\xi} \end{bmatrix}^{(i)} \tag{3. 19}$$

where the Jacobian $\boldsymbol{J}$ is obtained from the transformation equations in the form

$$\boldsymbol{J} = \begin{bmatrix} \frac{\partial\bar{x}^{(i)}}{\partial\eta} & \frac{\partial\bar{y}^{(i)}}{\partial\eta} \\ \frac{\partial\bar{x}^{(i)}}{\partial\xi} & \frac{\partial\bar{y}^{(i)}}{\partial\xi} \end{bmatrix} = \begin{bmatrix} A_1^{(i)} + A_2^{(i)}\xi & A_4^{(i)} + A_5^{(i)}\xi \\ A_3^{(i)} + A_2^{(i)}\eta & A_6^{(i)} + A_5^{(i)}\eta \end{bmatrix} \tag{3. 20}$$

with $A_1, \ldots, A_6$ are given in terms of the vertex coordinates $\left(\bar{x}_p, \bar{y}_p\right)^{(i)}$

$$A_1^{(i)} = \frac{1}{4}(-\bar{x}_1 + \bar{x}_2 + \bar{x}_3 - \bar{x}_4)^{(i)}, A_2^{(i)} = \frac{1}{4}(\bar{x}_1 - \bar{x}_2 + \bar{x}_3 - \bar{x}_4)^{(i)}$$

$$A_3^{(i)} = \frac{1}{4}(-\bar{x}_1 - \bar{x}_2 + \bar{x}_3 + \bar{x}_4)^{(i)}, A_4^{(i)} = \frac{1}{4}(-\bar{y}_1 + \bar{y}_2 + \bar{y}_3 - \bar{y}_4)^{(i)}$$

$$A_5^{(i)} = \frac{1}{4}(\bar{y}_1 - y_2 + \bar{y}_3 - \bar{y}_4)^{(i)}, A_6^{(i)} = \frac{1}{4}(-\bar{y}_1 - y_2 + \bar{y}_3 + \bar{y}_4)^{(i)}$$

For consistency with the surface-averaging framework of the finite-volume theory, the two sets of partial derivatives are connected through the volume-averaged Jacobian $\bar{\boldsymbol{J}}$,

$$\bar{\boldsymbol{J}} = \frac{1}{4}\int_{-1}^{+1}\int_{-1}^{+1}\boldsymbol{J}d\eta d\xi = \begin{bmatrix} A_1 & A_4 \\ A_3 & A_6 \end{bmatrix}^{(i)} \tag{3. 21}$$

with the inverse $\bar{\boldsymbol{J}}^{-1}$

$$\bar{\boldsymbol{J}}^{-1} = \frac{1}{|\bar{\boldsymbol{J}}|}\begin{bmatrix} A_6 & -A_4 \\ -A_3 & A_1 \end{bmatrix}^{(i)} = \frac{1}{A_1^{(i)}A_6^{(i)} - A_3^{(i)}A_4^{(i)}}\begin{bmatrix} A_6^{(i)} & -A_4^{(i)} \\ -A_3^{(i)} & A_1^{(i)} \end{bmatrix} \tag{3. 22}$$

In constructing the local stiffness matrix for each subvolume in terms of the surface-averaged displacements and tractions, $\boldsymbol{J}^{-1}$ is replaced by $\bar{\boldsymbol{J}}^{-1}$ in order to generate the elements of the stiffness matrix in closed form. This replacement avoids costly numerical integrations. For each subvolume (i),

$$\begin{aligned}
\begin{bmatrix} \dfrac{\widehat{\partial\psi}}{\partial x} \\ \dfrac{\widehat{\partial\psi}}{\partial y} \end{bmatrix}_{\xi=\mp1}^{(i)} &= \bar{\boldsymbol{J}}^{-1(i)}\begin{bmatrix} \dfrac{\widehat{\partial\psi}}{\partial \eta} \\ \dfrac{\widehat{\partial\psi}}{\partial \xi} \end{bmatrix}_{\xi=\mp1}^{(i)} = \frac{1}{|\bar{\boldsymbol{J}}|^{(i)}}\begin{bmatrix} A_6 & -A_4 & 0 & \pm3A_4 \\ -A_3 & A_1 & 0 & \mp3A_1 \end{bmatrix}^{(i)}\begin{bmatrix} W_{\psi(10)} \\ W_{\psi(01)} \\ W_{\psi(20)} \\ W_{\psi(02)} \end{bmatrix}^{(i)} \\
\begin{bmatrix} \dfrac{\widehat{\partial\psi}}{\partial x} \\ \dfrac{\widehat{\partial\psi}}{\partial y} \end{bmatrix}_{\eta=\pm1}^{(i)} &= \bar{\boldsymbol{J}}^{-1(i)}\begin{bmatrix} \dfrac{\widehat{\partial\psi}}{\partial \eta} \\ \dfrac{\widehat{\partial\psi}}{\partial \xi} \end{bmatrix}_{\eta=\pm1}^{(i)} = \frac{1}{|\bar{\boldsymbol{J}}|^{(i)}}\begin{bmatrix} A_6 & -A_4 & \pm3A_6 & 0 \\ -A_3 & A_1 & \mp3A_3 & 0 \end{bmatrix}^{(i)}\begin{bmatrix} W_{\psi(10)} \\ W_{\psi(01)} \\ W_{\psi(20)} \\ W_{\psi(02)} \end{bmatrix}^{(i)}
\end{aligned} \tag{3. 23}$$

The following concise vector notation is introduced in the expressions above for notational convenience,

$$\boldsymbol{a}_{1,3}^{(i)} = \frac{1}{|\bar{\boldsymbol{J}}|^{(i)}}[A_6 \quad -A_4 \quad 0 \quad \pm 3A_4]^{(i)}, \boldsymbol{a}_{2,4}^{(i)} = \frac{1}{|\bar{\boldsymbol{J}}|^{(i)}}[A_6 \quad -A_4 \quad \pm 3A_6 \quad 0]^{(i)},$$

$$\boldsymbol{b}_{1,3}^{(i)} = \frac{1}{|\bar{\boldsymbol{J}}|^{(i)}}[-A_3 \quad A_1 \quad 0 \quad \mp 3A_1]^{(i)}, \boldsymbol{b}_{2,4}^{(i)} = \frac{1}{|\bar{\boldsymbol{J}}|^{(i)}}[-A_3 \quad A_1 \quad \mp 3A_3 \quad 0]^{(i)}$$

Moreover, the symbol $W_{\psi}^{(i)}$ is used to denote the vector of coefficients in the second-order expansion of $\psi(x, y)$, which will be explained in detail in the following section.

$$\boldsymbol{W}_{\psi}^{(i)} = \begin{bmatrix} W_{\psi(10)} \\ W_{\psi(01)} \\ W_{\psi(20)} \\ W_{\psi(02)} \end{bmatrix}^{(i)}$$

3.3.3 Warping Functions and Stress Fields

The out-of-plane warping function is approximated in each subvolume using a second-order expansion in the local coordinates as follows,

$$\begin{aligned} \psi^{(i)} = W_{\psi(00)}^{(i)} + \eta W_{\psi(01)}^{(i)} + \xi W_{\psi(10)}^{(i)} + \frac{1}{2}(3\eta^2 - 1)W_{\psi(20)}^{(i)} \\ + \frac{1}{2}(3\xi^2 - 1)W_{\psi(02)}^{(i)} \end{aligned} \tag{3. 24}$$

where $W_{\psi(mn)}^{(i)}$ are unknown coefficients subsequently redefined in terms of the surface-averaged warping functions (proportional to the corresponding out-of-plane displacements w) along the four subvolume faces ($p = 1, 2, 3, 4$) following the subvolume-face order convention described in Chapter 2. The above displacement field representations produce the shear strains

$$\hat{\gamma}_{xz|p}^{(i)} = \frac{\widehat{\partial u}}{\partial z_p}^{(i)} + \frac{\widehat{\partial w}}{\partial x_p}^{(i)} = -\theta \hat{y} + \theta \boldsymbol{a}_p^{(i)} \boldsymbol{W}_{\psi}^{(i)} \tag{3. 25}$$

$$\hat{\gamma}_{yz|p}^{(i)} = \widehat{\frac{\partial v}{\partial z}}_p^{(i)} + \widehat{\frac{\partial w}{\partial y}}_p^{(i)} = \theta\hat{x} + \theta \boldsymbol{b}_p^{(i)} \boldsymbol{W}_\psi^{(i)}$$

The subvolumes may be occupied by monoclinic materials whose stiffness matrix elements in the case of unidirectional composites are obtained by rotational transformation about the z axis from the principal material coordinate system wherein they are orthotropic. The reduced constitutive equations contain stiffness matrix elements dependent on the torsion case considered, and these elements may vary from subvolume to subvolume as is the case in functionally graded materials within the framework of the specific plane case. The corresponding shear stress components in these planes in each subvolume are given, respectively, below after substituting the surface-averaged expressions in Eq. (3. 25):

$$\begin{bmatrix} \hat{\sigma}_{yz} \\ \hat{\sigma}_{xz} \end{bmatrix}_p^{(i)} = \begin{bmatrix} C_{44} & C_{45} \\ C_{45} & C_{55} \end{bmatrix}^{(i)} \begin{bmatrix} \theta\hat{x} + \theta \boldsymbol{b}_p^{(i)} \boldsymbol{W}_\psi^{(i)} \\ -\theta\hat{y} + \theta \boldsymbol{a}_p^{(i)} \boldsymbol{W}_\psi^{(i)} \end{bmatrix} \tag{3. 26}$$

3.3.4 Local Stiffness Matrix Construction

In order to reduce the number of unknown coefficients in the out-of-plane displacement approximation when cross sections are discretized into a large number of subvolumes, one shall reformulate the torsion problem in terms of surface-averaged out-of-plane displacements on the four faces of each subvolume as the primary solution variables. Then one constructs a local stiffness matrix for each subvolume by relating the surface-average out-of-plane displacements to the corresponding surface-average tractions. It is common to start by defining the surface-average warping functions, which are the out-of-plane displacements divided by the angle of twist per unit length θ,

$$\hat{\psi}^{(i)}|_{1,3} = \frac{1}{2}\int_{-1}^{1} \hat{\psi}^{(i)}(\eta, \xi = \mp 1)\, d\eta = W_{\psi(00)}^{(i)} \mp W_{\psi(01)}^{(i)} + W_{\psi(02)}^{(i)} \tag{3. 27}$$

$$\hat{\psi}^{(i)}|_{2,4} = \frac{1}{2}\int_{-1}^{1} \hat{\psi}^{(i)}(\eta = \pm 1, \xi)\ d\xi = W_{\psi(00)}^{(i)} \mp W_{\psi(10)}^{(i)} + W_{\psi(20)}^{(i)}$$

Hence, the first and second-order coefficients $W_{\psi(mn)}^{(i)}$ may be expressed in terms of the surface-averaged warping functions and the zero-order coefficient $W_{\psi(00)}^{(i)}$

$$\boldsymbol{W}_{\psi}^{(i)} = \begin{bmatrix} W_{\psi(10)} \\ W_{\psi(01)} \\ W_{\psi(20)} \\ W_{\psi(02)} \end{bmatrix}^{(i)} = \frac{1}{2}\begin{bmatrix} 0 & 1 & 0 & -1 \\ -1 & 0 & 1 & 0 \\ 0 & 1 & 0 & 1 \\ 1 & 0 & 1 & 0 \end{bmatrix}\begin{bmatrix} \hat{\psi}_1 \\ \hat{\psi}_2 \\ \hat{\psi}_3 \\ \hat{\psi}_4 \end{bmatrix}^{(i)} - \begin{bmatrix} 0 \\ 0 \\ 1 \\ 1 \end{bmatrix} W_{\psi(00)}^{(i)} \tag{3. 28}$$

or

$$\boldsymbol{W}_{\psi}^{(i)} = \frac{1}{2}\boldsymbol{\alpha}\widehat{\boldsymbol{\psi}}^{(i)} - \boldsymbol{\beta} W_{\psi(00)}^{(i)}$$

Similarly, the corresponding surface-averaged interfacial tractions are defined as follows,

$$\hat{t}_z^{(i)}|_{1,3} = \frac{1}{2}\int_{-1}^{1} \hat{t}^{(i)}(\eta, \xi = \mp 1)\ d\eta$$
$$\hat{t}_z^{(i)}|_{2,4} = \frac{1}{2}\int_{-1}^{1} \hat{t}^{(i)}(\eta = \pm 1, \xi)\ d\xi \tag{3. 29}$$

where the traction vector associated with the face p characterized by the unit normal vector $\boldsymbol{n}_p$ is $t_z^{(i)}|_p = \sigma_{iz}^{(i)} n_i^{(i)}|_p$ $(i = x, y)$. Hence the traction vector components on any of the four subvolume faces become, in terms of the two shear stress components,

$$\hat{t}_{z|p}^{(i)} = \left[\hat{\sigma}_{xz}^{(i)} n_x^{(i)} + \hat{\sigma}_{yz}^{(i)} n_y^{(i)}\right]_p \tag{3. 30}$$

which are expressed in terms of the corresponding surface-averaged shear strains respectively for general anisotropic materials,

$$\hat{t}_{z|p}^{(i)} = \left([C_{45} \quad C_{55}]^{(i)} n_{x|p}^{(i)} + [C_{44} \quad C_{45}]^{(i)} n_{y|p}^{(i)}\right) \begin{bmatrix} -\theta\hat{y} + \theta \boldsymbol{a}_p^{(i)} \boldsymbol{W}_\psi^{(i)} \\ \theta\hat{x} + \theta \boldsymbol{b}_p^{(i)} \boldsymbol{W}_\psi^{(i)} \end{bmatrix} \tag{3. 31}$$

or more specifically for orthotropic materials,

$$\hat{t}_{z|p}^{(i)} = \left([0 \quad G_{zx}]^{(i)} n_{x|p}^{(i)} + [G_{zy} \quad 0]^{(i)} n_{y|p}^{(i)}\right) \begin{bmatrix} -\theta\hat{y} + \theta \boldsymbol{a}_p^{(i)} \boldsymbol{W}_\psi^{(i)} \\ \theta\hat{x} + \theta \boldsymbol{b}_p^{(i)} \boldsymbol{W}_\psi^{(i)} \end{bmatrix} \tag{3. 32}$$

i.e.,

$$\hat{t}_{z|1,3}^{(i)} = G_{zx}\theta(\boldsymbol{a}_{1,3}^{(i)} \boldsymbol{W}_\psi^{(i)} - \frac{1}{2}\int_{-1}^{1} y|_{\eta,\xi=\mp 1}^{(i)} \, d\eta) n_{x|1,3}^{(i)} + G_{zy}\theta(\boldsymbol{b}_{1,3}^{(i)} \boldsymbol{W}_\psi^{(i)} + \frac{1}{2}\int_{-1}^{1} x|_{\eta,\xi=\mp 1}^{(i)} \, d\eta) n_{y|1,3}^{(i)}$$

$$\hat{t}_{z|2,4}^{(i)} = G_{zx}\theta(\boldsymbol{a}_{2,4}^{(i)} \boldsymbol{W}_\psi^{(i)} - \frac{1}{2}\int_{-1}^{1} y|_{\eta=\pm 1,\xi}^{(i)} \, d\xi) n_{x|2,4}^{(i)} + G_{zy}\theta(\boldsymbol{b}_{2,4}^{(i)} \boldsymbol{W}_\psi^{(i)} + \frac{1}{2}\int_{-1}^{1} x|_{\eta=\pm 1,\xi}^{(i)} \, d\xi) n_{y|2,4}^{(i)}$$

The last step in the construction of the local stiffness matrix is to express the zero-order coefficients $W_{\psi(00)}^{(i)}$ in terms of the surface-averaged warping functions. This is achieved by satisfying the third equilibrium equation in the surface-averaged sense. The surface tractions associated with each face of the (i) subvolume are related to each other through the equilibrium equation satisfied in a volume-average sense. Using Gauss Theorem, the equilibrium equation is expressed in terms of surface-averaged traction components,

$$\oint_s \sigma_{jz}^{(i)} n_j^{(i)} ds = \oint_s t_z^{(i)} \, ds = \sum_{p=1}^{4} \hat{t}_{z|p}^{(i)} l_p^{(i)} = 0 \tag{3. 33}$$

where s is the contour of subvolume (i) boundary.

Expanding the summation equations Eq. (3. 33) for the surface-averaged tractions multiplied by the corresponding length over each subvolume contour, the following relation is obtained between the surface-averaged warping functions on each of the four subvolume faces and the zero-order coefficient $W_{\psi(00)}^{(i)}$,

$$W_{\psi(00)}^{(i)} = \frac{\boldsymbol{A}_h^{(i)}\boldsymbol{\alpha}\widehat{\boldsymbol{\psi}}^{(i)}}{2A_h^{(i)}\boldsymbol{\beta}} \tag{3. 34}$$

where $\boldsymbol{A}_h^{(i)} = \sum_{p=1}^{4} G_{zx}\, l_p^{(i)} n_{x|p}^{(i)} \boldsymbol{a}_p^{(i)} + \sum_{p=1}^{4} G_{zy}\, l_p^{(i)} n_{y|p}^{(i)} \boldsymbol{b}_p^{(i)}$

Substituting the first and second-order coefficient expressions Eq. (3. 28) into the surface-averaged traction components in the z direction acting on the four edges of the subvolume Eq. (3. 31) or (3. 32), the surface-averaged traction components are obtained solely in terms of the corresponding surface-averaged displacements, related through the local stiffness matrix,

$$\begin{bmatrix} \hat{t}_{z|1} \\ \hat{t}_{z|2} \\ \hat{t}_{z|3} \\ \hat{t}_{z|4} \end{bmatrix}^{(i)} \hat{t}_{z|1} = \begin{bmatrix} L_{11} & L_{12} & L_{13} & L_{14} \\ L_{21} & L_{22} & L_{23} & L_{24} \\ L_{31} & L_{32} & L_{33} & L_{34} \\ L_{41} & L_{42} & L_{43} & L_{44} \end{bmatrix}^{(i)} \begin{bmatrix} \hat{\psi}_1 \\ \hat{\psi}_2 \\ \hat{\psi}_3 \\ \hat{\psi}_4 \end{bmatrix}^{(i)} + \begin{bmatrix} C_{T1} \\ C_{T2} \\ C_{T3} \\ C_{T4} \end{bmatrix}^{(i)} \tag{3. 35}$$

where

$\boldsymbol{L}_{p:} = \frac{\theta}{2}\left(G_{zx}\boldsymbol{a}_{\boldsymbol{p}} n_{x|_p} + G_{zy}\boldsymbol{b}_{\boldsymbol{p}} n_{y|_p}\right)\left(\boldsymbol{\alpha} - \frac{\boldsymbol{\beta}\boldsymbol{A}_h\boldsymbol{\alpha}}{\boldsymbol{A}_h\boldsymbol{\beta}}\right)$, **(**$\boldsymbol{L}_{p:}$ stands for the pth row vector in $[\boldsymbol{L}]$**)**

and $C_{Tp} = -G_{zx}\theta I_{T2p} n_{x|_p} + G_{zy}\theta I_{T1p} n_{y|_p}$

$I_{T11}^{(i)} = \frac{1}{2}\int_{-1}^{1} x|_{\eta,\xi=-1}^{(i)}\, d\eta = \frac{x_1+x_2}{2}$, $I_{T21}^{(i)} = \frac{1}{2}\int_{-1}^{1} y|_{\eta,\xi=-1}^{(i)}\, d\eta = \frac{y_1+y_2}{2}$

$I_{T12}^{(i)} = \frac{1}{2}\int_{-1}^{1} x|_{\eta=1,\xi}^{(i)}\ d\xi = \frac{x_2+x_3}{2},\ I_{T22}^{(i)} = \frac{1}{2}\int_{-1}^{1} y|_{\eta=1,\xi}^{(i)}\ d\xi = \frac{y_2+y_3}{2}$

$I_{T13}^{(i)} = \frac{1}{2}\int_{-1}^{1} x|_{\eta,\xi=1}^{(i)}\ d\eta = \frac{x_3+x_4}{2},\ I_{T23}^{(i)} = \frac{1}{2}\int_{-1}^{1} y|_{\eta,\xi=1}^{(i)}\ d\eta = \frac{y_3+y_4}{2}$

$I_{T14}^{(i)} = \frac{1}{2}\int_{-1}^{1} x|_{\eta=-1,\xi}^{(i)}\ d\xi = \frac{x_1+x_4}{2},\ I_{T24}^{(i)} = \frac{1}{2}\int_{-1}^{1} y|_{\eta=-1,\xi}^{(i)}\ d\xi = \frac{y_1+y_4}{2}$

3.3.5 Global Stiffness Matrix Assembly

The solution for the unknown surface-averaged displacements is obtained by constructing a system of equations such that the interfacial displacement and traction continuity conditions are satisfied together with the traction and/or displacement boundary condition. To maintain the order of the subvolume edges for a general unstructured mesh, each subvolume has four identical surface-averaged displacements and tractions allocated in the system of equations. The system of equations for the solution of the unknown surface-averaged displacements, which is comprised of displacement and traction continuity, boundary and constraint conditions, is called the global system.

First, it is necessary to denote the number of connected edges by N_{con} and the number of unconnected edges by N_{uncon} from the discretized grid. To solve the global system of equations for the surface-averaged displacements, the global stiffness matrix is allocated $2N_{con} + N_{uncon}$ columns and $2N_{con} + N_{uncon} + 1$ rows. Each subvolume has four edges with the corresponding number of z displacements and contributes four equations to the global system. Each pair of two connected edges has the same surface-averaged displacements and equal and opposite tractions, which results in $2N_{con}$ equations for traction and displacement continuity conditions in z directions, whereas the unconnected edges only need to satisfy the boundary conditions also in z directions, producing N_{uncon} equations. The breakdown of the $2N_{con} + N_{uncon} + 1$ rows in the global system is given below:

Displacement continuity condition equations

For a pair of connected edges from adjacent subvolumes, the displacement continuity conditions contribute one equation in the z direction each to the global stiffness matrix. p is the edge index from the first subvolume and p' is the edge index from the second subvolume.

$$\hat{\psi}_{p}^{(i)} - \hat{\psi}_{p'}^{(i')} = 0 \tag{3. 36}$$

Traction continuity condition equations

For a pair of connected edges from adjacent subvolumes, the traction continuity conditions contribute one equation each in the z direction to the global stiffness matrix. p is the edge index from the first subvolume and p' is the edge index from the second subvolume.

$$t_{z|p}^{(i)} + t_{z|p'}^{(i')} = 0 \tag{3. 37}$$

$t_{z|p}^{(i)}$ are expressed as linear combinations of surface-averaged displacements in the global system.

Boundary condition equations

For a pair of connected edges from adjacent subvolumes, the traction-free conditions contribute one equation each in the z direction to the global stiffness matrix.

$$\hat{t}_{z|p}^{(i)} = 0 \tag{3. 38}$$

Constraint condition equations

The global system of equations is singular with the rank of $2N_{con} + N_{uncon}$, thereby requiring an additional constraint that eliminates rigid body motion along the prismatic bar's axis. One approach is to constrain the out-of-plane displacement $\psi(x, y)$ by requiring that $\psi(x, y) = 0$ at the cross section's centroid where the in-plane displacements $u(x, y)$ and $v(x, y)$ vanish. This constraint cannot be employed, however, for hollow cross sections with the centroid located outside the cross section itself. A more general and rigorous fixation condition specifically for the torsion problem requires the integral of the out-of-plane displacement along the contour of the cross section to vanish,

$$\oint \psi(x, y) ds = \sum s_{(i,p)} \hat{\psi}^{(i)}_{boundary|p} = 0 \tag{3. 39}$$

where the $s_{(i,p)}$ is the length of the p th edge in subvolume i. Solution of the above augmented global system of equations yields the unknown interfacial surface-averaged displacements which, in turn, yield the corresponding surface-averaged tractions as well as pointwise displacements, strains and stresses in each subvolume.

3.4 Verification and Assessment

The thus-far developed finite-volume based method for the solution of torsion problems is assessed and verified in this section for torsion of homogeneous and heterogeneous bars of different cross sections. The convergence and accuracy of the developed FVM are assessed and verified upon comparison with solutions for cross sections with different boundaries and material properties. This section is divided into two categories based on the cross-section's make-up, namely homogeneous and heterogeneous bars. The finite-volume solution is verified by comparison with the exact analytical solution of the torsion of an isotropic homogeneous bar, and its performance assessed relative to the solutions obtained using FDM and FEM of the same problem based on the displacement formulation. The two formulations of the torsion problem, namely displacement and stress formulation, may be employed in solutions based on FDM and FEM approaches. However, as FVM has not been formulated using the Prandtl's stress function approach at this stage, only displacement-based FDM and FEM are employed in the chapter for comparison purposes.

TFI cross-line grid and 4-node elements are selected for FDM and FEM solutions respectively, preserving the consistency with quadrilateral subvolumes of FVM. The mesh grid in FDM is generated based on the centers of these elements or subvolumes in FEM or FVM, the corners of the cross sections, as well as the midpoints on the outermost edges for boundary elements or subvolumes. As the only unknown in the torsion problem formulation, the warping function generated from these three numerical methods has been compared with the elasticity solution over the entire cross-sectional area. Convergence studies based on these types of cross sections are conducted with different mesh discretizations. This is accomplished by first examining the FVM global convergence with mesh refinement to the elasticity solution, and then comparing FVM local convergence of the displacement and stress fields to the elasticity solution at a large number of grid points throughout the analyzed cross section. Numerical results obtained from finite-difference and finite-element solutions are employed to explore the convergency rate as well.

Rectangular cross sections, high order boundary polynomial (star-shaped) cross sections and circular cross sections with a circular slot (apple-with-a-bite) are homogenous isotropic cross sections for which elasticity solutions are available. These cross sections are selected and tested in Section 3.4.1. Special heterogenous cross sections for which elasticity solutions are available are also modeled numerically. Cross sections composed of two homogenous isotropic parts, as well as elliptic layered cross sections that are designed with specific materials to eliminate warping, are selected and tested as well.

3.4.1 Finite Difference Method (displacement-based)

The displacement-based FDM requires the determination of nodal displacement values at each node of the mesh grid, which can be achieved by solving a set of equations obtained from the discretized differential equation and boundary conditions. The resultant shear stress for the given angle of twist can then be determined using warping functions. The Laplace equation that the warping function $\psi(s,t)$ must satisfy, Eq. (3. 6) is discretized by approximating the partial derivatives of the warping functions by their values at the given and adjacent nodes. With the implementation of the TFI meshing technique, structured grids are generated with the nodal index of (α,β) for the nodes on the centers of each subvolumes or elements in FVM or FEM. N_α and N_β are the row and column numbers of subvolumes or elements in FVM or FEM. FDM has additional nodes settled on the four boundaries denoted as $(0, \beta)$, $(N_\alpha + 1, \beta)$, $(\alpha, 0)$, $(\alpha, N_\beta + 1)$ for the left, right, top and bottom boundary respectively. Using the Taylor series expansions along the x direction at the $(\alpha - 1, \beta)$ and $(\alpha + 1, \beta)$ nodes in an example of equal-spaced orthogonal grid for an isotropic material media, the second partial derivative of $\psi(s, t)$ with respect to s at the (α, β) node in the finite difference form is obtained in terms of the nodal values of the warping function at the three horizontally adjacent nodes,

$$\frac{\partial^2 \psi}{\partial s^2} = \frac{\psi^{(\alpha+1,\beta)} - 2\psi^{(\alpha,\beta)} + \psi^{(\alpha-1,\beta)}}{d^2} \tag{3. 40}$$

where d is the distance between adjacent nodes. Similarly, the first partial derivative with respect to s employed in the calculation of the shear stress component is

$$\frac{\partial \psi}{\partial s} = \frac{\psi^{(\alpha+1,\beta)} - \psi^{(\alpha,\beta)}}{d} \tag{3. 41}$$

Performing the same Taylor series expansions along the t direction, the following results are obtained for the second and first partial derivatives of $\psi(s, t)$ with respect to t

$$\frac{\partial^2 \psi}{\partial t^2} = \frac{\psi^{(\alpha,\beta+1)} - 2\psi^{(\alpha,\beta)} + \psi^{(\alpha,\beta-1)}}{d^2} \tag{3. 42}$$

$$\frac{\partial \psi}{\partial t} = \frac{\psi^{(\alpha,\beta+1)} - \psi^{(\alpha,\beta)}}{d} \tag{3. 43}$$

Combining Eqs. (3. 42) and (3. 43), the finite difference approximation of the Laplace equation for the warping function involving five inner nodes becomes,

$$\psi^{(\alpha+1,\beta)} + \psi^{(\alpha-1,\beta)} + \psi^{(\alpha,\beta+1)} + \psi^{(\alpha,\beta-1)} - 4\psi^{(\alpha,\beta)} = 0 \tag{3. 44}$$

Special treatment is needed for the boundary nodes owing to the lack of four adjacent nodes required for the satisfaction of both the equilibrium and traction-free conditions on the lateral surface. One way to accomplish this is to use forward or backward differencing at each boundary node to satisfy the above two conditions. Another way is to use the central difference scheme since it produces a second-order error, while forward/backward difference yields a first-order error. However, to accomplish this, imaginary nodes outside of the cross-section's domain are introduced. Using the imaginary boundary nodes, the Laplace's equation for boundary nodes is formulated using the central difference in FDM for better accuracy.

Parametric mapping is a useful tool also for creating a finite difference grid that accurately captures the geometry of any arbitrary cross section. Creating a parametric mapping of any part of a cross section from a cylindrical bar can be done by mapping a unit square to a quadrilateral partition. This mapping process again involves the Jacobian which relates the first partial derivatives of the warping function ψ in the physical system and those in the reference system shown in Eq. (3. 19). The second partial derivatives of the warping function ψ with respect to x and y can be expressed as

$$\begin{aligned} \frac{\partial^2\psi}{\partial x^2} &= \frac{\partial}{\partial x}\left(\frac{\partial\psi}{\partial x}\right) = (J_{11}^{-1})^2\frac{\partial^2\psi}{\partial s^2} + 2J_{11}^{-1}J_{12}^{-1}\frac{\partial^2\psi}{\partial s\partial t} + (J_{12}^{-1})^2\frac{\partial^2\psi}{\partial t^2} \\ \frac{\partial^2\psi}{\partial y^2} &= \frac{\partial}{\partial y}\left(\frac{\partial\psi}{\partial y}\right) = (J_{21}^{-1})^2\frac{\partial^2\psi}{\partial s^2} + 2J_{21}^{-1}J_{22}^{-1}\frac{\partial^2\psi}{\partial s\partial t} + (J_{22}^{-1})^2\frac{\partial^2\psi}{\partial t^2} \end{aligned} \tag{3. 45}$$

in terms of the second partial derivatives with respect to s and t in the reference system, and therefore the Laplace equation Eq. (3. 6) for homogenous isotropic materials becomes

$$[(\boldsymbol{J}_{11}^{-1})^2 + (\boldsymbol{J}_{21}^{-1})^2]\frac{\partial^2\psi}{\partial s^2} + 2(\boldsymbol{J}_{11}^{-1}\boldsymbol{J}_{12}^{-1} + \boldsymbol{J}_{21}^{-1}\boldsymbol{J}_{22}^{-1})\frac{\partial^2\psi}{\partial s\partial t} + [(\boldsymbol{J}_{12}^{-1})^2 + (\boldsymbol{J}_{22}^{-1})^2]\frac{\partial^2\psi}{\partial t^2} = 0 \tag{3. 46}$$

The traction-free boundary condition with respect to s and t in the reference system are obtained by mapping the first partial derivatives of the warping function ψ from that in the physical system Eq. (3. 8),

$$\left(\boldsymbol{J}_{11}^{-1}n_x + \boldsymbol{J}_{21}^{-1}n_y\right)\frac{\partial\psi}{\partial s} + \left(\boldsymbol{J}_{12}^{-1}n_x + \boldsymbol{J}_{22}^{-1}n_y\right)\frac{\partial\psi}{\partial t} = yn_x - xn_y \tag{3. 47}$$

where n_x and n_y are the components of the normal of each boundary section curve. The governing differential equation Eq. (3. 46) with its boundary condition Eq. (3. 47) is reduced to a system of equations in finite difference form and subsequently solved, omitting the details. The shear stress components are then obtained from the finite difference form of the expressions below,

$$\begin{aligned} \sigma_{zx} &= \mu\theta\left(\frac{\partial\psi}{\partial x} - y\right) = \mu\theta\left(\boldsymbol{J}_{11}^{-1}\frac{\partial\psi}{\partial s} + \boldsymbol{J}_{12}^{-1}\frac{\partial\psi}{\partial t} - y\right) \\ \sigma_{zy} &= \mu\theta\left(\frac{\partial\psi}{\partial x} + x\right) = \mu\theta\left(\boldsymbol{J}_{21}^{-1}\frac{\partial\psi}{\partial s} + \boldsymbol{J}_{22}^{-1}\frac{\partial\psi}{\partial t} + x\right) \end{aligned} \tag{3. 48}$$

3.4.2 Finite Element Method (displacement-based)

By discretizing a slice of a bar into a finite number of small elements, the torsion problem can also be solved by finding the out-of-plane displacement field that satisfies the governing equations and the boundary conditions via variational principles. Four-node elements, also known as Q4 elements in the finite element analysis, are employed for the convenience of comparing point-to-point quantities in FEM with those in FVM. Several studies, including Cavalcante et al. (2008), Cavalcante and Marques (2014), Cavalcante and Pindera (2016), and Filho and Cavalcante (2023), have highlighted that the Q4 element demonstrates inferior performance in terms of stress distribution when compared to FVM and FEM employing the Q8 element. The Q8 or Q9 element offers a higher level of displacement field detail in comparison to Q4; however, Q4 produces the same size stiffness matrix as the FVM subvolume, thus remaining computational equivalent. It is undeniable that incorporating Q8 or Q9 elements can produce more accurate results than FVM, albeit at the expense of increased computational demands. Therefore, the utilization of the Q4 element is preferred, considering its reasonable computational requirements, even though it may result in slightly less accurate stress distribution. When formulating the torsion problem for any homogenous cylindrical bar in FEM, the displacement field within each element is approximated using linear shape functions $[\boldsymbol{N}]$, which satisfy continuity conditions at the nodes. The displacement approach employed in the FEM solution is briefly described in the sequel for comparison purposes.

The assumed displacement function is approximated by the matrix of element shape function $[\boldsymbol{N}] = [N_1 \quad N_2 \quad N_3 \quad N_4]$, post-multiplied by the vector of displacement function values at the nodes $[\boldsymbol{q}_\psi] = [\psi_1 \quad \psi_2 \quad \psi_3 \quad \psi_4]^T$. The gradient of the assumed displacement function is

$$[\nabla\psi] = [\boldsymbol{B}][\boldsymbol{q}_\psi] \tag{3. 49}$$

where $[\boldsymbol{B}] = \begin{bmatrix} \frac{\partial N_1}{\partial x} & \frac{\partial N_2}{\partial x} & \frac{\partial N_3}{\partial x} & \frac{\partial N_4}{\partial x} \\ \frac{\partial N_1}{\partial y} & \frac{\partial N_2}{\partial y} & \frac{\partial N_3}{\partial y} & \frac{\partial N_4}{\partial y} \end{bmatrix}$ is known as the strain-displacement transformation matrix. This can be computed for each element by the mapping to a unit square through the parametric mapping based on Eq. (3. 19) as $[\boldsymbol{B}] = \boldsymbol{J}^{-1} \begin{bmatrix} \frac{\partial N_1}{\partial \eta} & \frac{\partial N_2}{\partial \eta} & \frac{\partial N_3}{\partial \eta} & \frac{\partial N_4}{\partial \eta} \\ \frac{\partial N_1}{\partial \xi} & \frac{\partial N_2}{\partial \xi} & \frac{\partial N_3}{\partial \xi} & \frac{\partial N_4}{\partial \xi} \end{bmatrix}$.

From elasticity, the shear stress components are expressed in terms of the warping displacement Eq. (3. 4). Substituting the strain-displacement transformation matrix $[B]$ into Eq. (3. 4) yields,

$$\begin{bmatrix} \sigma_{zx} \\ \sigma_{zy} \end{bmatrix} = \theta[\boldsymbol{B}][\boldsymbol{q}_\psi] + \theta \begin{bmatrix} 0 & -1 \\ 1 & 0 \end{bmatrix} \begin{bmatrix} x \\ y \end{bmatrix} \tag{3. 50}$$

The total potential energy of the bar subjected to torsion can be written as

$$\Pi = \frac{z}{2}\iint_A \begin{bmatrix} \sigma_{zx} \\ \sigma_{zy} \end{bmatrix}^T \begin{bmatrix} C_{44} & C_{45} \\ C_{45} & C_{55} \end{bmatrix} \begin{bmatrix} \sigma_{zx} \\ \sigma_{zy} \end{bmatrix} dA \tag{3. 51}$$

Employing the Rayleigh-Ritz method, the displacement and load are related through each stiffness matrix $[\boldsymbol{K}_\psi]$ of each element,

$$\iint_A [\boldsymbol{B}]^T \begin{bmatrix} C_{44} & C_{45} \\ C_{45} & C_{55} \end{bmatrix} [\boldsymbol{B}] dA\, [\boldsymbol{q}_\psi] = \iint_A [B]^T \begin{bmatrix} C_{44} & C_{45} \\ C_{45} & C_{55} \end{bmatrix} \begin{bmatrix} y \\ -x \end{bmatrix} dA \tag{3. 52}$$

In concise notation, this equation is $[\boldsymbol{K}_\psi][\boldsymbol{q}_\psi] = [\boldsymbol{Q}_\psi]$. Due to the complexity of the analytical integral calculations, the FEM used for this comparison incorporates the Gaussian quadrature method as the numerical integration for the quantities over each elemental area. Both 1×1 and 2×2 Gaussian quadrature are implemented and tested. Notice that dA is the area of each small quadrilateral element, and equals $4det([\boldsymbol{J}])$ as the area of mapping unit square is $2 \times 2 = 4$.

The finite-element solution of the torsion problem involves the assembly of the element stiffness matrices according to global nodal indices, which represent the contribution of each element to the overall stiffness of the analyzed bar. The global stiffness matrix assembly for both FVM and FEM follows the same principles based on the kinematics and static compatibilities. The global stiffness matrix is then formed by combining the element stiffness matrices, and the solution is obtained by solving the resulting system of linear equations. However, there is a fundamental difference in the way compatibilities are enforced in FVM and FEM. While FVM ensures compatibilities between common faces, FEM ensures compatibilities between common nodes. It is crucial to emphasize that FVM achieves local satisfaction of equilibrium conditions at the subvolume level, whereas FEM satisfies equilibrium conditions at the nodal level. The shear stress in each element is then generated from the corresponding warping displacement field,

$$\begin{bmatrix}\sigma_{zx}\\ \sigma_{zy}\end{bmatrix} = \theta\left(\begin{bmatrix}C_{44} & C_{45}\\ C_{45} & C_{55}\end{bmatrix}[\boldsymbol{B}]\{q_\psi\} + \begin{bmatrix}C_{44} & C_{45}\\ C_{45} & C_{55}\end{bmatrix}\begin{bmatrix}0 & -1\\ 1 & 0\end{bmatrix}[\boldsymbol{N}]\begin{bmatrix}x_1 & y_1\\ x_2 & y_2\\ x_3 & y_3\\ x_4 & y_4\end{bmatrix}\right) \tag{3. 53}$$

where $\begin{bmatrix}x_1 & y_1\\ x_2 & y_2\\ x_3 & y_3\\ x_4 & y_4\end{bmatrix}$ is matrix containing physical coordinates of four vertices in each element.

3.4.3 Homogenous Isotropic Cross Section

The developed finite-volume solution is verified by comparison with exact elasticity solutions of the torsion of an isotropic homogeneous bar with rectangular, concave boundaries, and a cross section with boundaries formed by two circles with different radii and horizontally offset centers, Figure 3-3, using the terminology rectangular, star-shaped and apple-with-a-bite for the three cross sections, respectively.

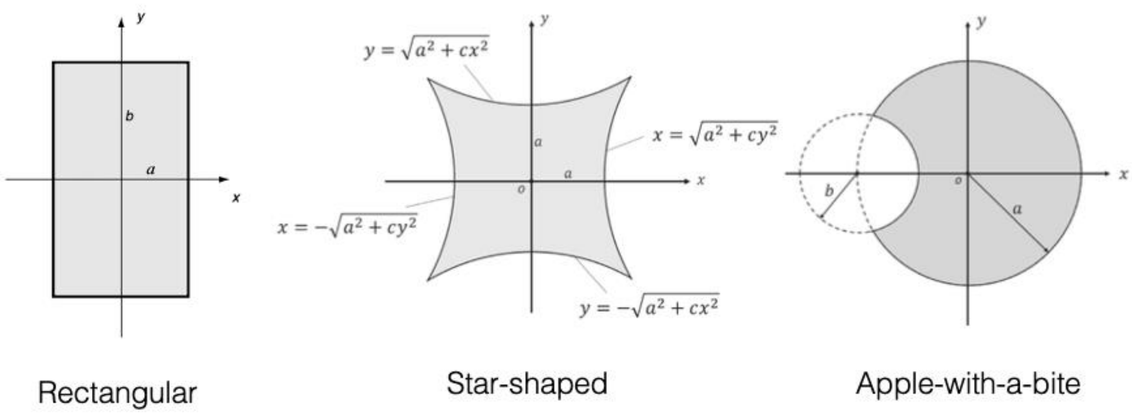

Figure 3-3 Rectangular(left), Star-shaped (middle) and Apple-with-a-bite (right) cross sections

Least-square error difference of the warping function ψ and shear stress resultant τ are calculated at all the mesh grid nodes following the equations below,

$$\Delta\psi_{error} = \sqrt{\frac{\sum_{j=1}^{N_\beta}\sum_{i=1}^{N_\alpha}[\psi^{FVM/FDM/FEM}(x_i,y_i) - \psi^{elast}(x_i,y_i)]^2}{\sum_{j=1}^{N_\beta}\sum_{i=1}^{N_\alpha}[\psi^{elast}(x_i,y_i)]^2}}$$

$$\Delta\tau_{error} = \sqrt{\frac{\sum_{j=1}^{N_\beta}\sum_{i=1}^{N_\alpha}[\tau^{FVM/FDM/FEM}(x_i,y_i) - \tau^{elast}(x_i,y_i)]^2}{\sum_{j=1}^{N_\beta}\sum_{i=1}^{N_\alpha}[\tau^{elast}(x_i,y_i)]^2}} \tag{3. 54}$$

Rectangular cross section

FVM is verified by comparison with exact elasticity, finite-difference and finite-element solutions of the torsion problem of an isotropic homogeneous bar with rectangular $2a \times 2b$ cross sections producing aspect ratios of 1, 5 and 10. Square grids with uniform-size subvolumes or elements are employed to generate solutions. The results shown in Figure 3-4 provide a global picture of the finite-volume, finite-difference and finite-element methods' convergence behavior with mesh refinement to the elasticity solution for the square cross section $(a/b = 1)$. The full-field convergence rates for both the warping function and the shear stress distributions are quadratic, as indicated in Figure 3-4. The three numerical methods (FVM, FDM and FEM) exhibit the same global convergence rates, with slight differences in the local convergence rates in the cross section's corner regions due to the large stress gradients. Similar results are obtained for the remaining cross sections with increasingly greater aspect ratios.

The least-square difference data are log-log plotted versus the mesh discretization in this convergence study. Based on the least square difference data obtained by these three numerical methods, the convergence rate for the warping function ψ and the shear stress resultant τ are shown. Figure 3-4 illustrates the second-order accuracy exhibited by all three solution methods. It is worth noting that FEM employs efficient computation techniques, including 1×1 and 2×2 Gaussian quadrature integration, for warping and shear stress analysis. The implementation of 2×2 Gaussian quadrature integration in FEM is particularly notable, as it offers computational efficiency comparable to that of FVM in terms of the assembly time (includes the construction of the local stiffness matrix for each subvolume and subsequent insertion into the global stiffness matrix), which agrees the corresponding results presented by Cavalcante et al. (2008). FDM has larger error in warping and shear stress resultant in the least square sense. FEM and FVM are comparable in the accuracy of warping function, yet FVM outperforms FEM in the evaluation of the shear stress resultant.

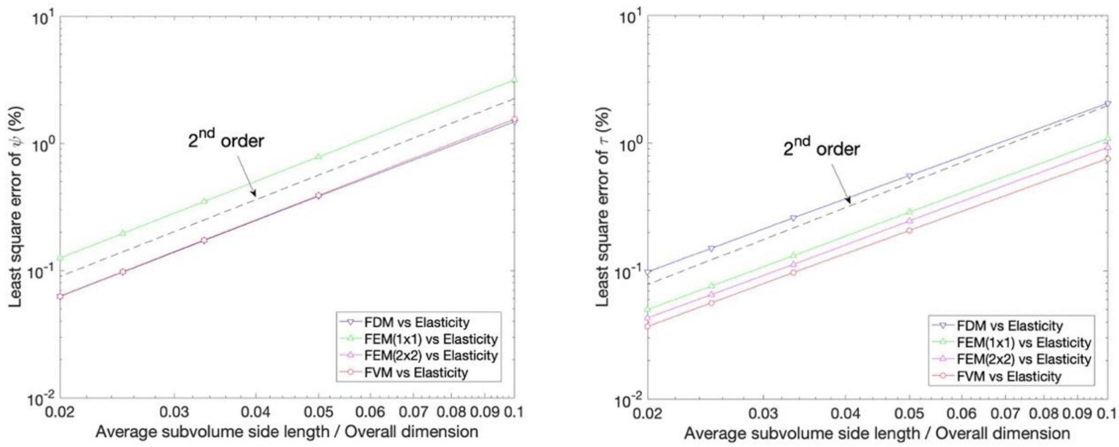

Figure 3-4 Second-order accuracy for all FDM, FVM and FEM with 1×1 and 2×2 Gaussian quadrature integration regarding the warping function (left) and shear stress resultant (right) of square cross sections ($a/b = 1$)

Star-shaped cross section

FVM is also verified by comparison with exact elasticity, finite-difference and finite-element solutions of the torsion problem of an isotropic homogeneous bar with specific concave boundaries that produce a star-shaped cross section. Parametric mapping was employed to generate the grid employed in the cross-section's discretization. The TFI grid for that cross section is shown in the figure to the right of the boundary parametrization.

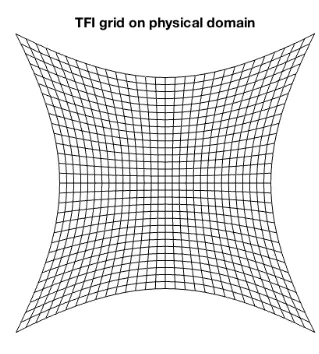

$$\textit{Bottom boundary: } x_b(s) = \frac{(2s-1)a}{\sqrt{1-c}},\ y_b(s) = -\sqrt{a^2 + \frac{c(2s-1)^2a^2}{1-c}}$$

$$\textit{Top boundary: } x_t(s) = \frac{(2s-1)a}{\sqrt{1-c}},\ y_t(s) = \sqrt{a^2 + \frac{c(2s-1)^2a^2}{1-c}}$$

$$\textit{Left boundary: } x_l(s) = -\sqrt{a^2 + \frac{c(2s-1)^2a^2}{1-c}},\ y_l(s) = \frac{(2s-1)a}{\sqrt{1-c}}$$

$$\textit{Right boundary: } x_r(s) = \sqrt{a^2 + \frac{c(2s-1)^2a^2}{1-c}},\ y_r(s) = \frac{(2s-1)a}{\sqrt{1-c}}$$

The analytical solution for the Prandtl stress function $\phi(x, y)$ of an isotropic bar with these concave boundaries is obtained in closed form in terms of the product of two quadratic polynomials of the form,

$$\phi(x, y) = K(a^2 - x^2 + cy^2)(a^2 + cx^2 - y^2) \tag{3. 55}$$

where the vertical and horizontal boundaries are defined by the pairs of curves $x = \pm\sqrt{a^2 + cy^2}$, $y = \pm\sqrt{a^2 + cx^2}$ Hence the stress function vanishes on the boundary, and moreover satisfies the Poisson's equation if $c = 3 - \sqrt{8}$ and $K = -\frac{\mu\theta}{[4a^2(1-\sqrt{2})]}$, where $\mu = G_{zx} = G_{zy}$. The shear stresses σ_{xz} and σ_{yz} are obtained from

$$\begin{aligned} \sigma_{zx}(x, y) &= \frac{\partial\phi}{\partial y} = 2Ky[(a^2(c-1) + (c^2+1)x - 2cy^2) \\ \sigma_{zy}(x, y) &= -\frac{\partial\phi}{\partial x} = -2Kx[(a^2(c-1) + (c^2+1)y - 2cx^2) \end{aligned} \tag{3. 56}$$

and the shear stress resultant field is calculated according to $\tau(x, y) = \sqrt{\sigma_{zx}^2 + \sigma_{zy}^2}$. The warping function is then determined by integrating Eq. (3. 4) using the above equations. This yields,

$$\psi(x, y) = \frac{-2}{4a^2(1-\sqrt{2})} y\left[a^2(c-1)x + \frac{(c^2+1)x^3}{3} - 2cxy^2\right] \tag{3. 57}$$

Figure 3-5 presents the analytical full-field distributions of the warping function $\psi(x, y)$ and shear stress resultant $\tau(x, y)$ obtained from Eqs. (3. 56) and (3. 57) respectively, that were employed in the verification and assessment of the FVM solution for the investigated cross section. The shear stress resultant distribution has been normalized by the product $\mu\theta$.

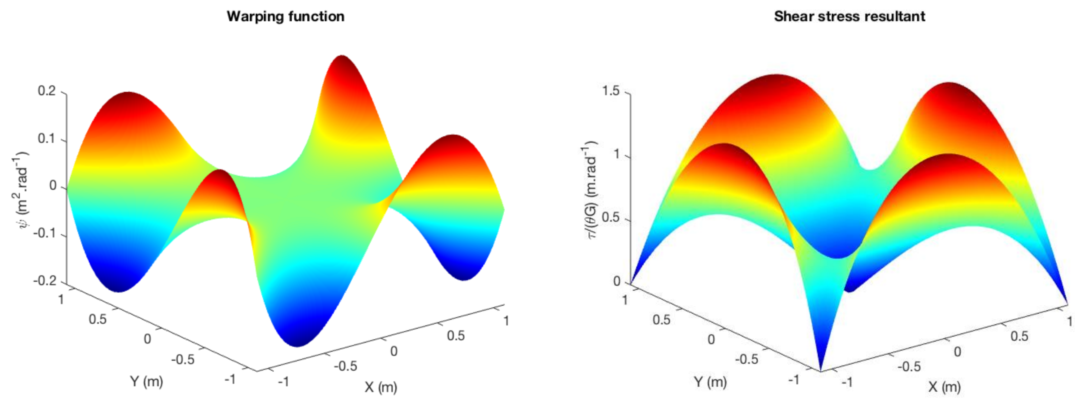

Figure 3-5 Exact elasticity results for the warping function $\psi(x, y)$ and shear stress resultant $\tau(x, y) = \sqrt{\sigma_{zx}^2 + \sigma_{zy}^2}$ distributions employed in the verification and assessment of the parametric FVM predictions for the star-shaped cross section

Since the 2×2 Gaussian quadrature integration exhibits better performance than 1×1 Gaussian quadrature integration, it was selected for comparison and the latter abandoned to avoid greater errors. Figure 3-6 illustrates comparison of the global convergence with mesh refinement of the full-field finite-volume, finite-difference and finite-element solutions for the warping and stress distributions to the elasticity solution in the least-squared sense graphed on a log-log scale. Quadratic convergence is observed for the finite-volume and finite-element solutions with slower convergence exhibited by the finite-difference solution.

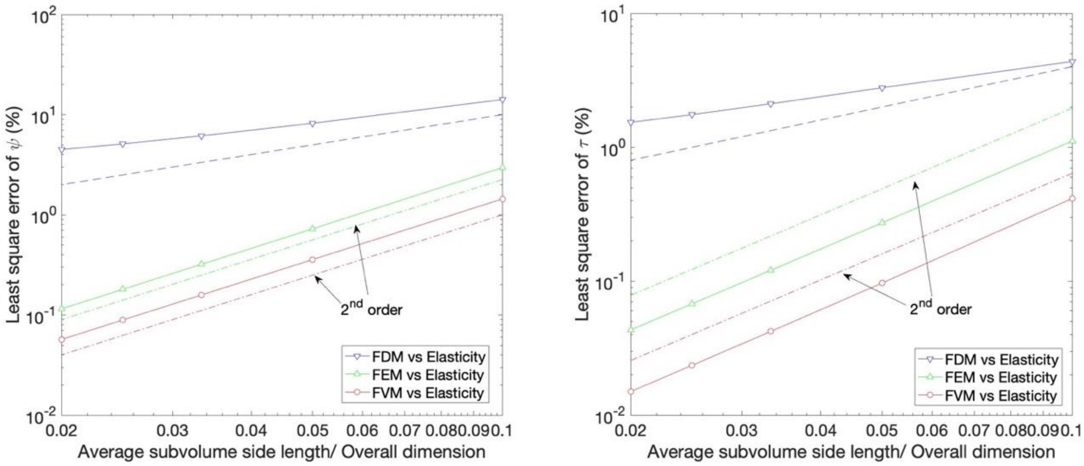

Figure 3-6 Second-order accuracy for all FDM, FVM and FEM (2×2 Gaussian quadrature integration) regarding the warping function (left) and shear stress resultant (right) of the specific star-shape cross sections (curvature constant: $c = 3 - \sqrt{8}$)

Figure 3-6 demonstrate a roughly first-order accuracy of FDM. Specifically, the slope of the FDM in the left figure is 0.7139, and that in the right figure is 0.6502. On the other hand, the second-order accuracy of FVM and FEM with 2×2 Gaussian quadrature integration is evident in the slopes from both figures that are close to 2.

Apple-with-a-bite cross section

FVM is additionally verified by comparison with exact elasticity and finite-element solutions of the torsion problem of an isotropic homogeneous bar with cross-sectional boundaries formed by two circles with different radii and horizontally offset centers that produce an apple-with-a-bite cross section. The TFI grid for that cross section is shown in the figure to the right of the boundary parametrization.

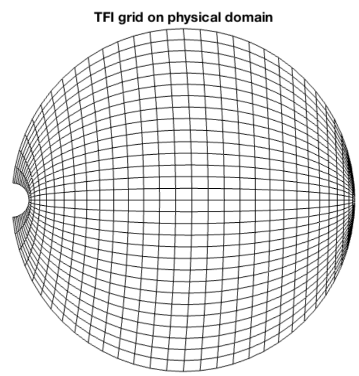

Bottom boundary:

$$x_b(s) = -a\, cos\left[\pi s + (1-2s) arctan(\frac{b\sqrt{4a^2 - b^2}}{2a^2 - b^2})\right]$$

$$y_b(s) = -a\,sin\left[\pi s + (1-2s) arctan(\frac{b\sqrt{4a^2-b^2}}{2a^2-b^2})\right]$$

Top boundary:

$$x_t(s) = -a\,cos\left[\pi s + (1-2s) arctan(\frac{b\sqrt{4a^2-b^2}}{2a^2-b^2})\right]$$

$$y_t(s) = a\,sin\left[\pi s + (1-2s) arctan(\frac{b\sqrt{4a^2-b^2}}{2a^2-b^2})\right]$$

Left boundary:

$$x_l(s) = b\,cos\left[(2s-1) arctan(\frac{\sqrt{4a^2-b^2}}{b})\right] - a$$

$$y_l(s) = \ b\,sin\left[(2s-1) arctan(\frac{\sqrt{4a^2-b^2}}{b})\right]$$

Right boundary:

$$x_r(s) = a\,cos\left[(2s-1)\,arctan\left(\frac{b\sqrt{4a^2-b^2}}{2a^2-b^2}\right)\right]$$

$$y_r(s) = a\,sin\left[(2s-1)\,arctan\left(\frac{b\sqrt{4a^2-b^2}}{2a^2-b^2}\right)\right]$$

The elasticity solution to the problem of the cross section with the boundary formed by these two circles of different radii horizontally offset from each other, is given in terms of the complex potential $\Psi(z), z = x + yi$, cf., Sokolnikoff (1946),

$$\Psi(z) = \Psi(x,y) + i\overline{\Psi}(x,y) = -ia\left(z - \frac{b^2}{z}\right) - \frac{ib^2}{2} \qquad (3.\,58)$$

where Ψ, $\overline{\Psi}$ are related through the Cauchy-Riemann conditions, and a, b are the radii of the larger and smaller circles, respectively. Separating the real and imaginary parts of $\Psi(z)$, one can obtain the warping function $\Psi(x,y)$ in the form,

$$\Psi(x,y) = -\frac{ab^2 y}{x^2+y^2} \tag{3. 59}$$

which yields the shear stress components,

$$\begin{aligned} \sigma_{zx}(x,y) &= \mu\theta\left(\frac{\partial\Psi}{\partial x} - y\right) = \mu\theta(2ab^2\frac{xy}{(x^2+y^2)^2} - y) \\ \sigma_{zy}(x,y) &= \mu\theta\left(-\frac{\partial\Psi}{\partial y} + x\right) = \mu\theta(-a - ab^2\frac{xy}{(x^2+y^2)^2} + x) \end{aligned} \tag{3. 60}$$

Figure 3-7 illustrates the warping function and shear stress resultant fields normalized by the product $\mu\theta$ based on the above equations that were employed in the assessment and verification of the FVM solution to the above problem.

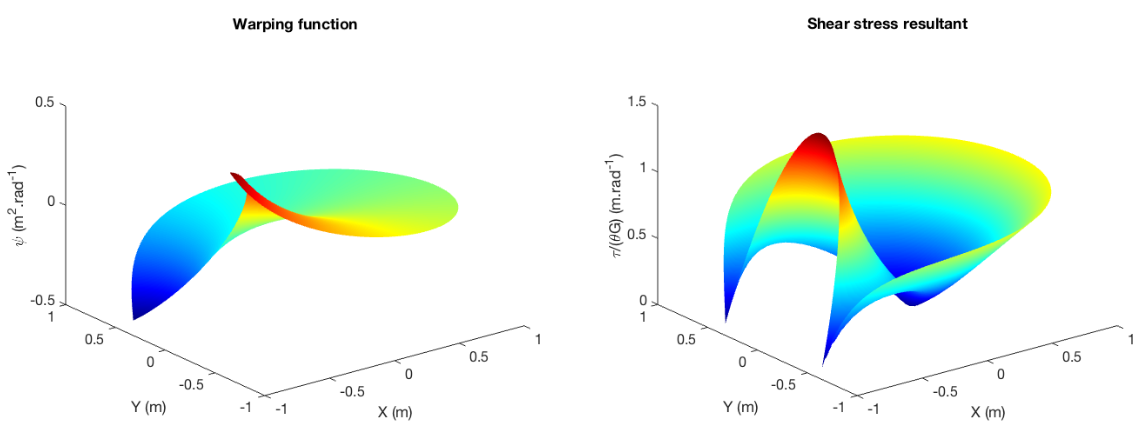

Figure 3-7 Exact elasticity results for the warping function $\psi(x,y)$ and shear stress resultant $\tau(x,y) = \sqrt{\sigma_{zx}^2 + \sigma_{zy}^2}$ distributions employed in the verification and assessment of the parametric FVM predictions for the apple-with-a-bite cross section

It is noted that warping of the cross section only occurs in the vicinity of the concave boundary where the deviation of the shear stress resultant from the linear variation is also pronounced. The maximum shear stress resultant occurs at the bottom of the concave boundary and approaches twice that of the maximum shear stress resultant at the outer boundary of the circular cross section removed from the cutout as the radius of the smaller circle, becomes very small. These distributions were used to calculate the global rates of convergence for the warping function and shear stress resultant fields as a function of the mesh refinement based on the least-squared differences. Figure 3-8 illustrates that the second-order global convergence to the elasticity solution with mesh refinement is also exhibited by the finite-volume and finite-element solutions for this cross section, with small deviations in the local convergence rates in the vicinity of corners. In particular, the FVM global convergence rates are comparable to those of the preceding problem, namely 1.992 and 2.006 for the warping function and the shear stress resultant, respectively, with 2×2 Gaussian quadrature integration.

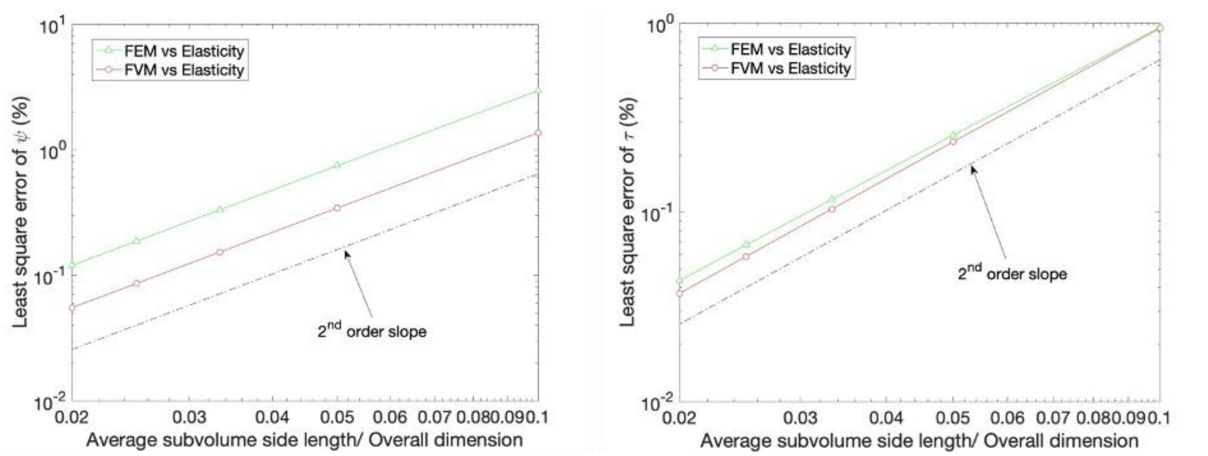

Figure 3-8 Second-order accuracy for FVM and FEM (2×2 Gaussian quadrature integration) regarding the warping function (left) or shear stress of the apple-with-a-bite cross section (right) with the radius ratio of 2

This section ends by pointing out several advantages of the FVM solution strategy relative to the FDM-based or FEM-based one. First, mapping of this particular cross section onto a unit square in the reference plane introduces artificial corners along an otherwise smooth portion of the larger circle's boundary in the physical plane. It is at these corners that the domain discretization becomes distorted as observed. These concentrations increase with mesh refinement due to increasingly grid distortion in the affected regions. In contrast, the FVM approach does not suffer from this problem. However, it must be mentioned that at sufficiently high mesh discretization based on the chosen transfinite mapping, the concomitant subvolumes' distortion becomes high enough to produce an ill-conditioned global system of equations for the determination of the surface-averaged out-of-plane displacements. This can be circumvented through mapping that avoids highly localized subvolume distortions. Nonetheless, the FVM-based solution strategy for the torsion problem is much less sensitive to these localized distortions than FDM or FEM and exhibit higher accuracy as well. This relative insensitivity was also observed in previous studies conducted by the author involving in-plane and anti-plane loading of functionally graded and periodic materials and structures.

3.4.4 Heterogenous Isotropic Cross Section

Heterogenous cross sections are commonly analyzed in torsion due to a great range of engineering applications. FVM has been demonstrated to have the capability to naturally deal with heterogenous cross sections by satisfying continuity of both displacements and tractions across subvolumes' interfaces in a surface-average sense. In contrast, FEM and FDM require dense meshing to account for material differences using material transition zones. Herein, two torsion problems involving heterogeneous cross sections for which exact elasticity solutions are available are selected for comparison with the corresponding FVM results.

Two isotropic rectangular bars with different elastic moduli

The feature of the developed version of the finite-volume theory which makes it especially suitable for torsion problems involving composite cross sections is the explicit satisfaction of both displacement and traction continuity at interfaces that separate regions with different elastic moduli. Comparison is made for the convergence behavior of the FVM with the increasing number of subvolumes relative to the exact elasticity solution of Muskhelishvili (1953) for the torsion problem of a composite cross section comprised of two isotropic rectangular bars with different elastic moduli.

For composite cross sections with the overall aspect ratio of five or less, the following closed-form formula for torsional rigidity may be obtained from the Fourier series solution by approximating the sums accordingly for the above aspect ratio range,

$$D = T/\theta = \frac{8}{3}(G_1 + G_2)ab^3 - 3.361b^4\left(\frac{G_1^2 + G_2^2}{G_1 + G_2}\right) \tag{3. 61}$$

where G_1 and G_2 are the shear moduli of the different rectangular regions in Figure 3-9.

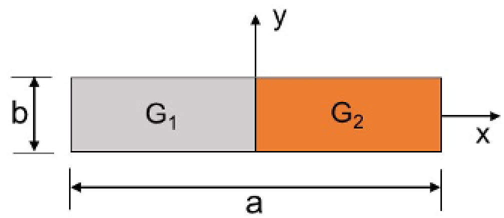

Figure 3-9 Composite cross section comprised of two homogeneous isotropic materials with different shear moduli

For the convergence study, a composite cross section with the overall aspect ratio $a/b = 5$ $(a = 5\ m, b = 1\ m)$ and shear moduli $G_1 = 5862.07\ MPa$ and $G_2 = 279.33\ MPa$ was analyzed. Using these numbers, the torsional rigidity from the elasticity solution was calculated as $63036.3\ MPa.m^4$. Figure 3-10 illustrates convergence of the finite-volume results as a function of the normalized subvolume average width for the torsional rigidity relative to the elasticity solution based on square as well as rectangular subvolumes with aspect ratios (horizontal over vertical dimension) of 0.2, 0.5, 2, 5. The results have been graphed using log-log scales. The convergence of the torsional rigidity with subvolume discretization refinement of a composite cross section comprised of two homogeneous isotropic materials with different shear moduli to the elasticity solution is also quadratic in a large range of subvolume dimensions shown in Figure 3-10.

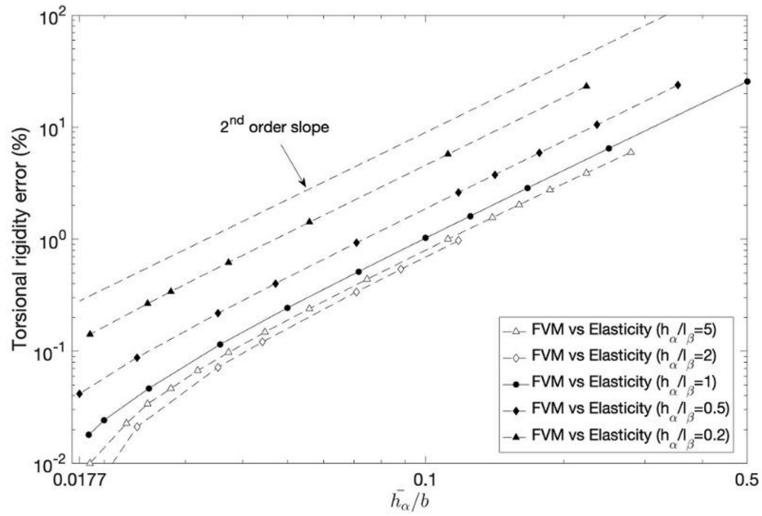

Figure 3-10 Convergence of the composite bar's torsional rigidity with subvolume discretization refinement normalized by the elasticity solution ($\bar{h}_\alpha$ is the edge length of square subvolumes)

3.5 Structural Applications

In this section, FVM's utility is illustrated by analyzing stress fields and resultant torsional rigidity of prismatic bio-inspired constructs with homogeneous and graded cross sections, and then demonstrated how warping of an elliptical cross section may be reduced, and ultimately eliminated, through an appropriate choice of shear modulus orthotropy. Orthotropic shear moduli may be realized through the use of composite materials with directionally dependent elastic moduli, such as fiber reinforced unidirectional composites. By tailoring the fiber and matrix properties in conjunction with the fiber volume fraction, different combinations of shear moduli may be achieved. Hence in the second application, elliptical cross sections made up of homogeneous orthotropic materials with different shear modulus ratios are considered and the results illustrate that no warping occurs with the proper choice of those ratios consistent with theoretical elasticity predictions reported in the literature. They also show that graded cross sections may produce the same result if the orthotropy ratio is preserved at every point of the cross section, also consistent with the elasticity results.

Different shear modulus orthotropy ratios at the homogenized level may also be realized using alternating isotropic layers with different shear moduli. In the third application, based on an exact solution to the layered plane problem, the isotropic shear moduli of the individual layers that produce orthotropy shear modulus ratio at the homogenized level, which yields no warping of elliptical cross sections, are first determined. Then the effect of microstructural refinement on warping of laminated cross sections is investigated as the layer thickness decreases. For other choices of isotropic layer shear moduli ratios, the warping function converges to that of the homogeneous cross section with equivalent orthotropic homogenized moduli ratio with increasing microstructural refinement, which we also demonstrate.

3.5.1 Star-shaped cross sections

The homogeneous star-shaped cross section shown in Figure 3-3 (middle) with increasing values of the parameter c which controls the curvature of the cross section's bounding surfaces has been analyzed. As stated in Section 3.4, exact elasticity solution is available only when $c = 3 - \sqrt{8}$. As c increases, the cross section begins to acquire a pointed star shape. The effect of increasing c on the local stress fields and resulting torsional rigidity is demonstrated using the 50×50 subvolume discretization previously implemented that produces sufficiently converged displacement and stress fields.

Figure 3-11 illustrates the normalized shear stress resultant fields for three homogeneous star-fish cross sections with $c = 0.5, 0.7, 0.9$. As observed, as the cross section's bounding surfaces become more concave, with concomitant shrinkage of the interior region, the regions characterized by the elongated spikes become ineffective in carrying shear stresses. This leads to torsional rigidity reduction. The torsional rigidity of the cross sections, Eq. (3. 13), normalized by the product μA is presented in Table 3-1 for the baseline value $c = 3 - \sqrt{8}$ and five values of c in the interval $0.5 \leq c \leq 0.9$, illustrates that as the bounding surfaces become increasing concave the relative torsional rigidity decreases. This decrease may be mitigated to an extent by grading the cross section in the vicinity of the bounding surfaces. We note that there are just a handful of analytical solutions for the Saint Venant's torsion of graded cross sections that are limited to circular and elliptical boundaries, cf., Horgan and Chan (1999), Horgan (2007).

Table 3-1 Torsional rigidity of the star-shaped cross sections with different curvatures normalized by the shear modulus and corresponding area

$\frac{D}{\mu A}(m^2/rad)$	$c = 0.17$	$c = 0.5$	$c = 0.6$	$c = 0.7$	$c = 0.8$	$c = 0.9$
Homogeneous	5.613	5.398	5.251	5.038	4.722	4.196
Graded	7.469	7.199	6.999	6.709	6.276	5.559

The prevailing approach for arbitrarily shaped orthotropic or graded structural components subjected to torsion is the finite-element method, cf., Darılmaz et al. (2018). Herein the shear modulus, from the value in the isotropic cross section's interior to the bounding surfaces, is graded in increments of 25% within the outermost 4 subvolume layers. That is, the subvolume layer directly adjacent to the bounding surface has the shear modulus of 2.0μ, and the remaining 3 adjacent layers have moduli of 1.75μ, 1.50μ and 1.25μ. The resulting shear stress resultant fields are included in Figure 3-11, as are the corresponding torsional rigidity enhancements in Table 3-1.

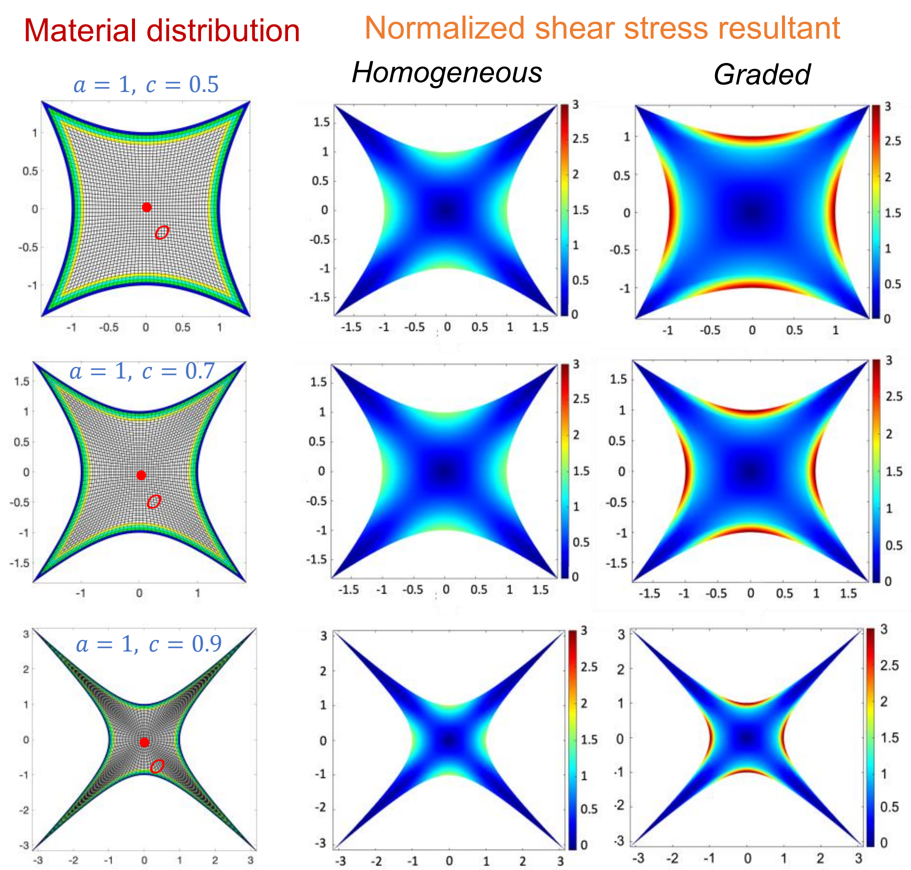

Figure 3-11 Normalized shear stress resultant $\tau(x, y)$ fields in start-shaped cross sections with increasing curvatures defined by the parameter $c =$ 0.5, 0.7, 0.9 (top, middle, bottom). Comparison of the effect of grading the shear modulus in a thin region adjacent to the boundary

As observed in the shear stress resultant fields, grading only affects the interior region of the star-shaped cross section where the shear stress resultant is substantially enhanced in the progressively stiffer region adjacent to the bounding surface, with little effect in the pointed spike regions. As the thickness of the pointed spikes decreases with increasing curvature, the shear stress component that contributes to the torsional rigidity of the construct decreases accordingly as it must vanish along the boundary to satisfy the traction-free boundary condition. Comparison with the corresponding FDM-based results (not included) reveals that when the parameter c becomes sufficiently large ($c = 0.9$) the FDM shear stress fields become inaccurate in the regions of the cross section's pointed spikes.

In summary, analysis of a sequence of star-shaped cross sections with increasingly greater concave boundaries illustrates continuously smooth shear stress fields, and correct behavior at the tips of the elongated spikes. The results also shown that by grading a thin region of the cross section in the immediate vicinity of the bounding surfaces with increasingly larger shear modulus, the loading-bearing capacity of the interior, but not spike, regions may be rendered more effective, thereby enhancing the relative torsional rigidity of the star-shaped construct.

3.5.2 Homogeneous and graded elliptical cross sections

An elliptic cross section is an attractive alternative to traditional cross-sectional shapes, yet it can experience warping and other undesirable effects under torsion. However, the elliptic cross section can be designed without warping, which makes it an even more useful shape for beams subject to torsion in engineering. Thus, in the second illustration of the parametric FVM's extended capability, a prismatic orthotropic bar of an elliptical cross section characterized by distinct shear moduli G_{zx} and G_{zy} is considered. When the orthotropic bar is homogeneous, the warping function for this cross section has been provided by Lekhnitskii (1964) in the form,

$$\psi = \frac{G_{zx}b^2 - G_{zy}a^2}{G_{zx}b^2 + G_{zy}a^2}xy \tag{3. 62}$$

Hence no warping will occur if the shear moduli are related to the minor and major axes of the ellipse, b and a, as follows

$$\sqrt{\frac{G_{zx}}{G_{zy}}} = \frac{a}{b} \tag{3. 63}$$

as also derived more recently by Chen (2004) and Chen and Wei (2005).

The above result has been generalized by Ecsedi (2004), and later by Horgan (2007), to encompass prismatic bars with functionally graded cross sections. In particular, for orthotropic materials with the shear moduli variation in the $x - y$ plane of the form,

$$\begin{aligned} G_{zy} &= \alpha f(x, y) \\ G_{zx} &= \gamma f(x, y) \end{aligned} \tag{3. 64}$$

elliptical cross sections bounded by

$$\alpha x^2 + \gamma y^2 = k^2 \tag{3. 65}$$

will not warp, leading to the relation $\sqrt{\gamma/\alpha} = a/b$ that corresponds to Eq. (3. 63) for the homogeneous cross section.

Herein, it is worth investigating the effect of varying the shear moduli ratio G_{zx}/G_{zy} for an ellipse with the aspect ratio $a/b = 2$ on the cross section's warping for both homogeneous and graded orthotropic cross sections. For the considered a/b ratio, the results below indicate that the ellipse will not warp when $G_{zx}/G_{zy} = 4$ and $\alpha/\gamma = 4$ for homogeneous and graded cross sections, respectively. The corresponding functional forms of the orthotropic shear moduli of the graded cross sections are: $G_{zx} = \alpha(x^2 + 4y^2)$ and $G_{zy} = \gamma(x^2 + 4y^2)$. The extent of warping predicted by the FVM analysis is illustrated for the three ratios $G_{zx}/G_{zy} = 1, 2$ and 4 in Figure 3-12 where decreasing magnitudes of warping are observed with increasing G_{zx}/G_{zy} ratio.

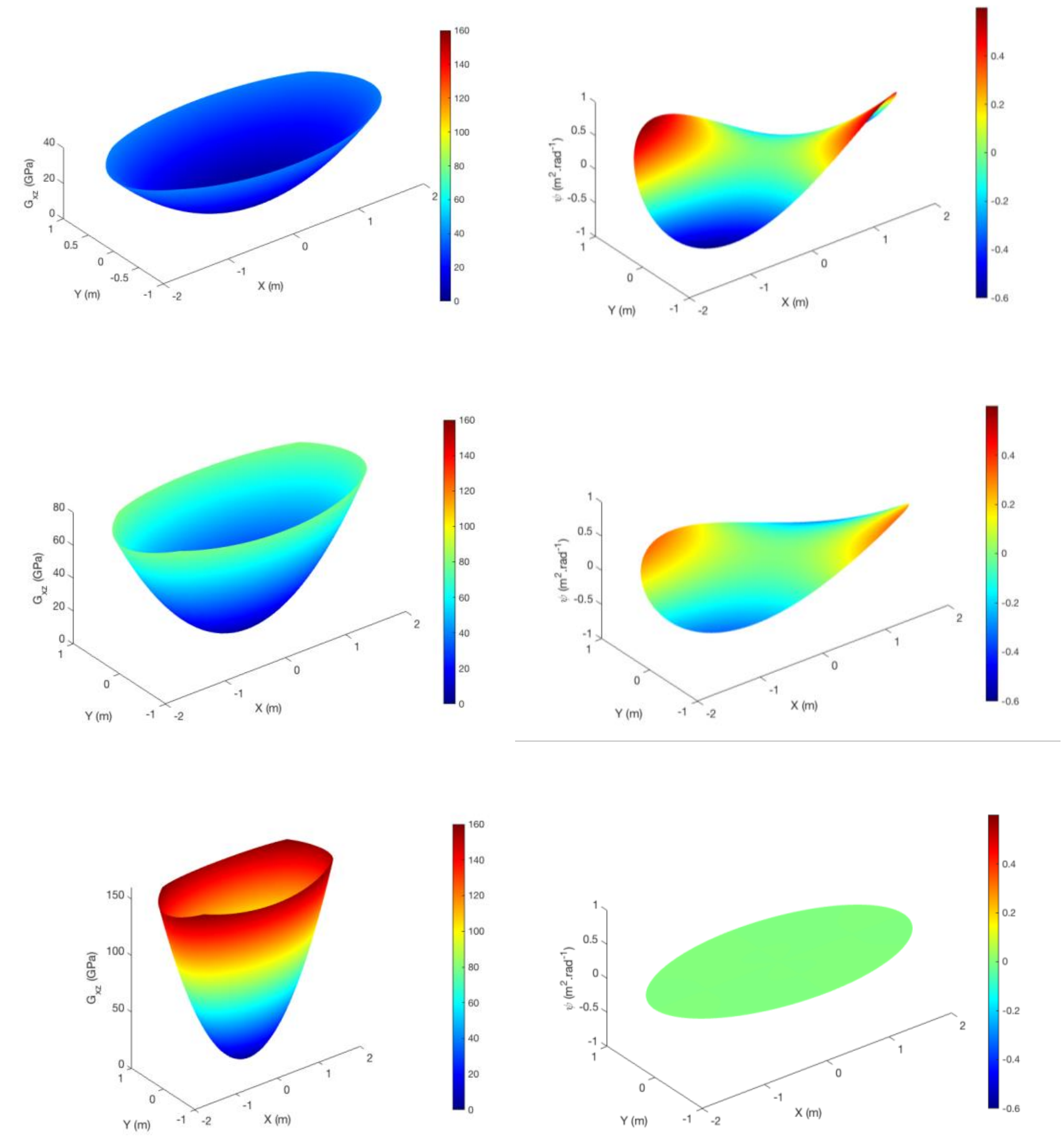

Figure 3-12 Shear modulus G_{xz} distribution (left) and warping (right) of functional graded elliptical cross sections with $a: b = 2: 1$ and different ratios of orthotropic shear moduli: $G_{zx}/G_{zy} = 1$ (top); $G_{zx}/G_{zy} = 2$ (middle); and $G_{zx}/G_{zy} = 4$ (bottom)

The warping functions are identical for homogeneous and graded cross sections with the same shear modulus orthotropy ratio. When the condition $G_{zx}/G_{zy} = 4$ is satisfied for the chosen a/b ratio, the FVM solution does indeed yield the theoretical outcomes for both homogeneous and graded cross sections. There are increasing applications of elliptical cross sections with graded elliptical porosities in the aeronautical industry and structural engineering, which exhibit distinct geometrical features and advanced design. One can also verify that the cross section bounded by two confocal ellipses $\alpha x^2 + \gamma y^2 = k_i^2$ (where $k = 1, 2$) does not warp either, Ecsedi (2004). Using functionally-graded orthotropic cross sections with $G_{zy} = \alpha f(\alpha x^2 + \gamma y^2)$, $G_{zx} = \gamma f(\alpha x^2 + \gamma y^2)$, $\alpha = 1/9, \gamma = 1/4,\ f(p) = p$, the extent of warping can also be seen in the FVM results in Figure 3-13 relative to solid elliptic cross section bounded by the ellipse $\alpha x^2 + \gamma y^2 = k^2$. By combining FVM analysis with an optimization algorithm, other shear moduli orthotropy ratios may be identified for cross sections other than elliptical wherein warping is minimized and perhaps eliminated.

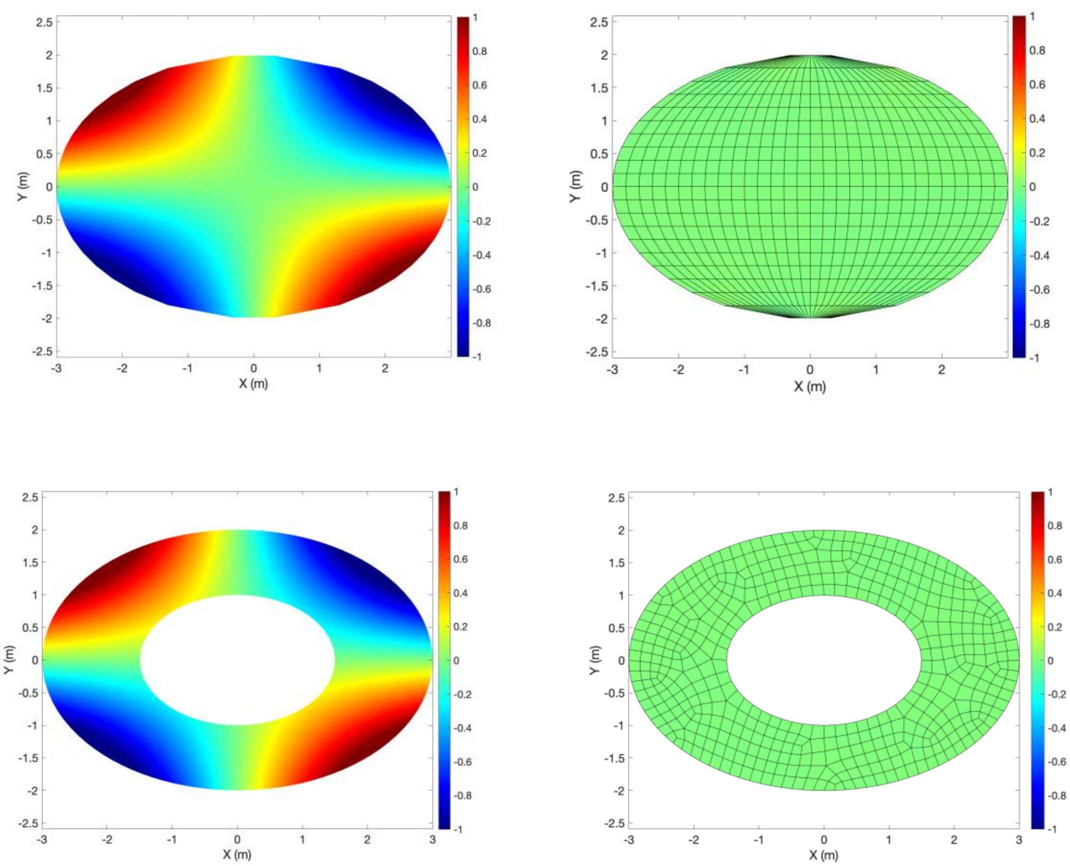

Figure 3-13 Summary of warping distribution of solid elliptic cross section (top) and cross section bounded by two confocal ellipses (bottom); homogenous isotropic (left) and functionally graded orthotropic (right) cross sections.

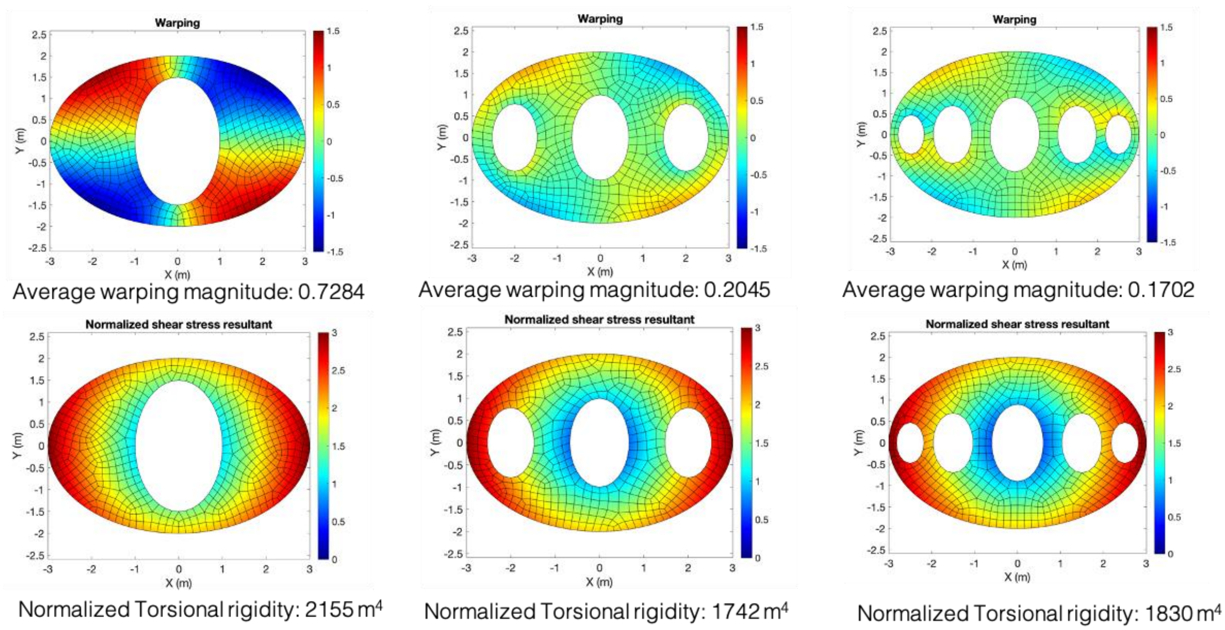

Figure 3-14 Warping (top) and normalized (bottom) shear stress resultant for porous elliptic cross section with 1, 3 and 5 porosities from left to right

Another approach to warping mitigation is through porosity grading. This is illustrated herein for elliptic cross sections with the same overall dimensions (major axis = 3, 1.5 m; minor axis = 2, 1 m), fixed porosity volume fraction, and increasing number of internal elliptical porosities of decreasing size with the aspect ratio of 2 arranged symmetrically about the minor axis. Figure 3-14 shows the *a*verage warping magnitude ($\sum|\psi_i|A_i/A$) and *n*ormalized shear stress ($\tau/\mu\theta$) distributions in the porous elliptic cross sections with 1, 3 and 5 porosities. These results indicate that porosity grading can be effective in reducing warping in materials subjected to torsion. Higher porosity in the warping-prone regions can act as a stress-relief mechanism and allow the cross section to deform more easily in the vicinity of those areas. This can result in a more uniform stress distribution throughout the material, reducing the likelihood of warping.

3.5.3 Horizontally laminated elliptical cross sections

It has been demonstrated in the literature that elliptical cross sections that are homogeneous and orthotropic with a certain orthotropy ratio of the shear moduli do not warp. An alternative, and perhaps more realistic, approach to tailoring the orthotropic shear modulus ratio is through laminated constructs. Postma (1955) developed an exact elasticity solution for the overall transversely isotropic properties of periodically layered structures consisting of alternating isotropic layers with different elastic moduli, with the direction of anisotropy orthogonal to the plane of alternating layers. For such laminations, exact expressions for the homogenized shear moduli in the $y - z$ and $x - z$ planes are obtained in the form,

$$
\begin{aligned}
G_{yz} &= (h_1 + h_2)\mu_1\mu_2/(h_1\mu_2 + h_2\mu_1) \\
G_{xz} &= (\mu_1 h_1 + \mu_2 h_2)/(h_1 + h_2)
\end{aligned}
\tag{3. 66}
$$

where μ_i are the shear moduli of the individual isotropic layers $i = 1, 2$, and h_i are the respective thicknesses. For equal layer thickness, and the ellipse aspect ratio $a/b = 2$, the isotropic layer ratio μ_1/μ_2 required to yield $G_{xz}/G_{yz} = 4$ that produces no warping at the homogenized level is around 14, which is not practical. Reducing the ellipse aspect ratio to $a/b = 1.5$ yields the homogenized shear modulus ratio $G_{xz}/G_{yz} = 2.25$ for no warping. This ratio, in turn, leads to the more realistic isotropic layer shear modulus ratio $\mu_1/\mu_2 = 6.854$.

A sequence of horizontally layered elliptical cross sections comprised of alternating isotropic layers with shear moduli that produce the homogenized shear modulus with the required ratio that eliminates warping has been constructed with progressively finer microstructures. Figure 3-15 illustrates the warping functions for three symmetrically laminated constructs comprised of 11, 31 and 61 layers. In contrast with homogeneous isotropic or orthotropic cross sections, warping occurs symmetrically about the major and minor axes of the laminated ellipses, producing an average value of zero in each quadrant of the elliptical cross sections. As the number of alternating stiff and soft layers increases for the same ellipse dimensions, the magnitude of local warping decreases accordingly. The elliptical cross section with the finest microstructure made up of 61 layers appears nearly flat relative to the coarsest layered ellipse comprised of 11 layers.

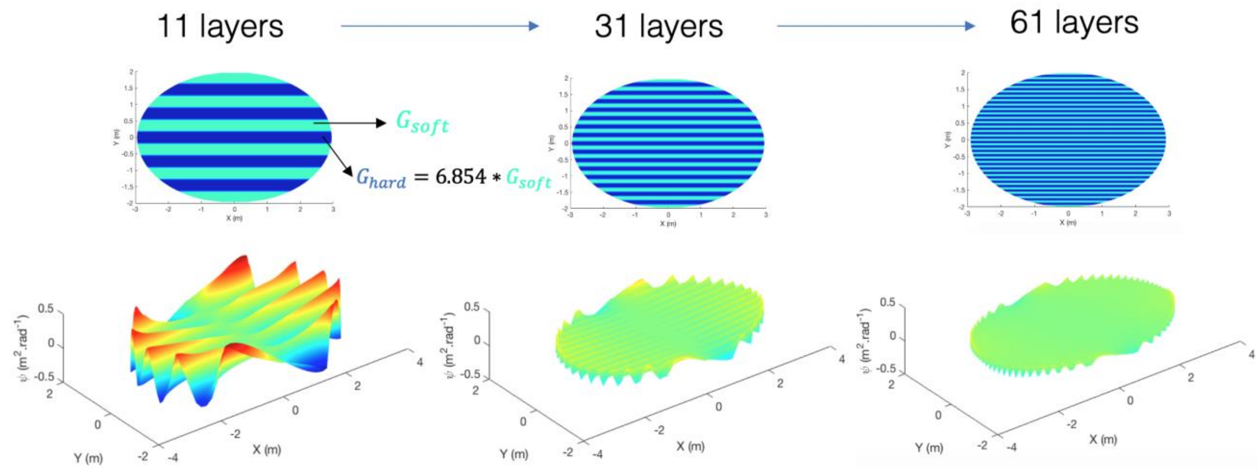

Figure 3-15 Warping functions of horizontally laminated elliptical cross sections with $a/b = 1.5$ and increasingly finer layered microstructures comprised of isotropic layers with the shear moduli ratio of 6.854

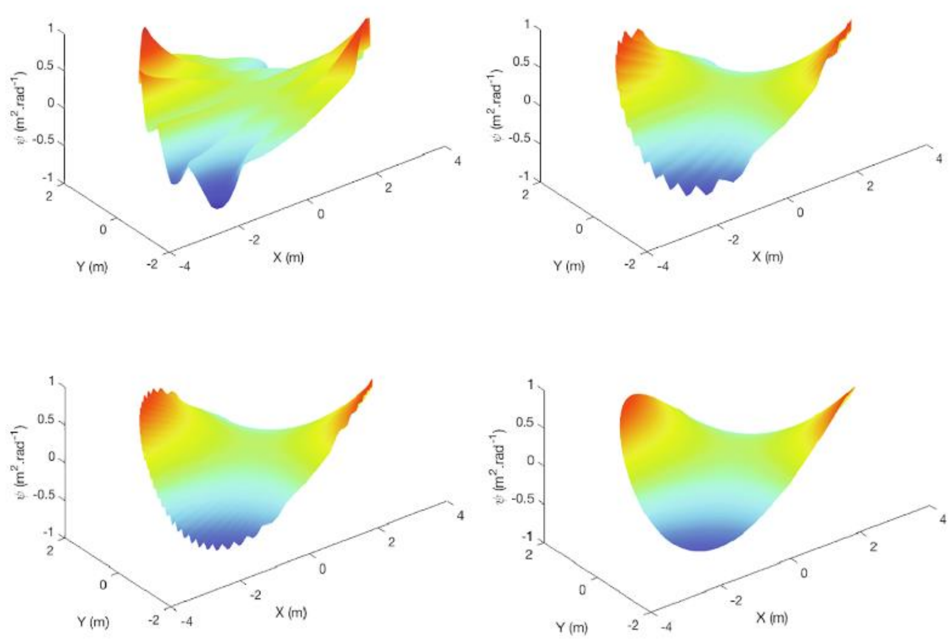

Figure 3-16 Warping functions of horizontally laminated elliptical cross sections with $a/b = 1.5$ and increasingly finer layered microstructures comprised of isotropic layers with the shear

moduli ratio $\mu_{stiff}/\mu_{soft} = 3.427$. Comparison with homogeneous cross section with equivalent orthotropic shear moduli obtained from the Postma elasticity-based model

When a different μ_1/μ_2 ratio is chosen, yielding a different homogenized shear modulus ratio, warping of the cross section approaches that obtained using the homogenized shear modulus ratio as the number of alternating layers increases. This is illustrated in Figure 3-16 for the isotropic layer shear modulus ratio $\mu_1/\mu_2 = 3.427$, or half of the preceding ratio, for the three symmetrically laminated configurations with increasingly finer microstructures. In this case, the homogenized shear modulus ratio obtained from the Postma model is $G_{xz}/G_{yz} = 1.43$, and the warping function for this ratio for a homogeneous and orthotropic cross section is included in Figure 3-16 for comparison. As observed, the warping in each quadrant of the finely layered elliptical cross section mimics that of the homogeneous ellipse.

The above results illustrate the FVM's capability to pursue novel approaches in the analysis of elliptical cross sections made up of homogeneous orthotropic materials with different shear modulus ratios which illustrate that no warping occurs with the proper choice of those ratios consistent with theoretical elasticity predictions reported in the literature. By laminating an elliptical cross section with alternating stiff and soft isotropic layers in a manner that mimics orthotropic shear moduli in the proper ratio at the homogenized level, warping can be practically eliminated with sufficient microstructural refinement. It is also shown that graded cross sections may produce the same result if the orthotropy ratio is preserved at every point of the cross section, consistent with the elasticity results as well.

3.5.4 Bamboo cross sections

Bamboo is a plant that has been used as a building material for centuries, and its unique cross-sectional shape has inspired structural designers to incorporate its principles into their work.

The bamboo cross section has two main features that make it an effective and efficient structural element. First, the hollow shape of the bamboo cross section reduces its weight without compromising its strength. For example, subjected to the wind load with twisting deformation, bamboo has its shear stress distributed mainly around the perimeter of the cross section to maximize the torsional rigidity. Second, the arrangement of the fibers in the bamboo cross section provides it with excellent resistance to bending and compression as fibers vary in size and are arranged in a radially graded pattern, with fibers becoming more crowded closer to the perimeter of the cross section. A cross section of bamboo culm showing this exact radial distribution of fibers through the thickness in Figure 3-17 has been provided by Silva (2006).

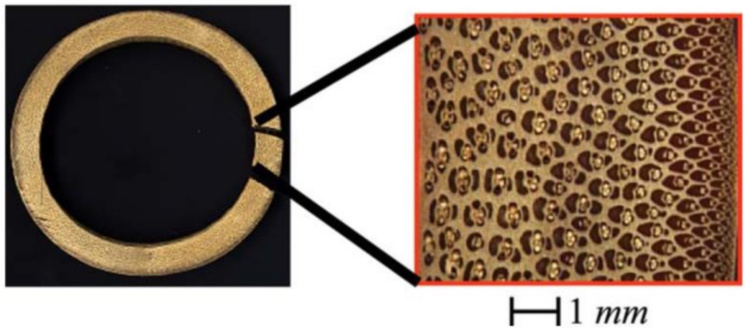

Figure 3-17 A cross section of bamboo culm with radial distribution of fibers through its thickness - Silva (2006).

By mimicking the cross-sectional shape of bamboo with its functionally graded microstructure that resists wind-induced torsional loads, structural designers can create typhoon-resistant structures that are lightweight, strong, and efficient. However, bamboo generally has very complicated microstructural shapes and material distribution for its fiber and matrix, and its culms are long with diaphragms which have complex structures as well. Nogata et al. (1995) used a combination of experimental testing and numerical simulations to study the properties of bamboo. By using the rule-of-mixture formula to estimate material properties of bamboo in its cross section, and experimental investigation of the radial variation of fiber volume fraction, Nogata et al. (1995) found that the properties of bamboo varied depending on the species and the location within the bamboo. Specifically, the rule-of-mixtures model based on the fiber and matrix with Young's moduli of 55 GPa and 2 GPa, respectively, yielded the homogenized Young's modulus variation throughout the cross section that was approximated by the equation $E(r) = 3.75e^{(2.2r/t)}$ as shown in Figure 3-18,

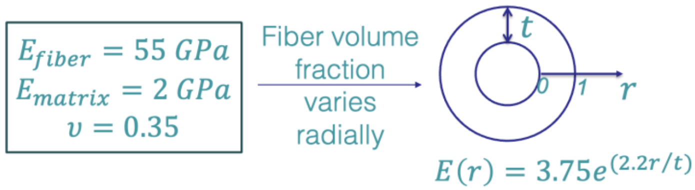

Figure 3-18 Homogenized Young's modulus variation throughout the bamboo cross section

Herein, comparison between the warping and shear stress resultant fields with continuous homogenization material properties and those following the actual radially varying fiber volume fraction is conducted for a bamboo slice with the inner radius of $0.028\ m$ and outer radius of $0.04\ m$. To save computational cost, a slice of the cross-sectional area was analyzed because of the bamboo cross section's symmetry about its centroid. This was accomplished by introducing periodic boundary conditions along the radial boundaries of the analyzed slice. The warping functions on the two straight edges of selected slice were set equal at each point along the radial direction, and the tractions were also set equal in magnitude but opposite in the z direction. The slice analysis only employs a portion of the whole region resulting in much quick computation while rendering the same local results as the analysis involving the entire cross-sectional area. The FVM analysis validates the results of warping absence in the bamboo cross section with continuously homogenized material properties, and linearly increasing shear stress in the radial direction (not shown). In contrast, the bamboo model based on the actual fiber and matrix distribution captures local microstructure-induced variations in the warping function and shear stress fields shown in Figure 3-19, confirming that the magnitude of the warping function is negligible.

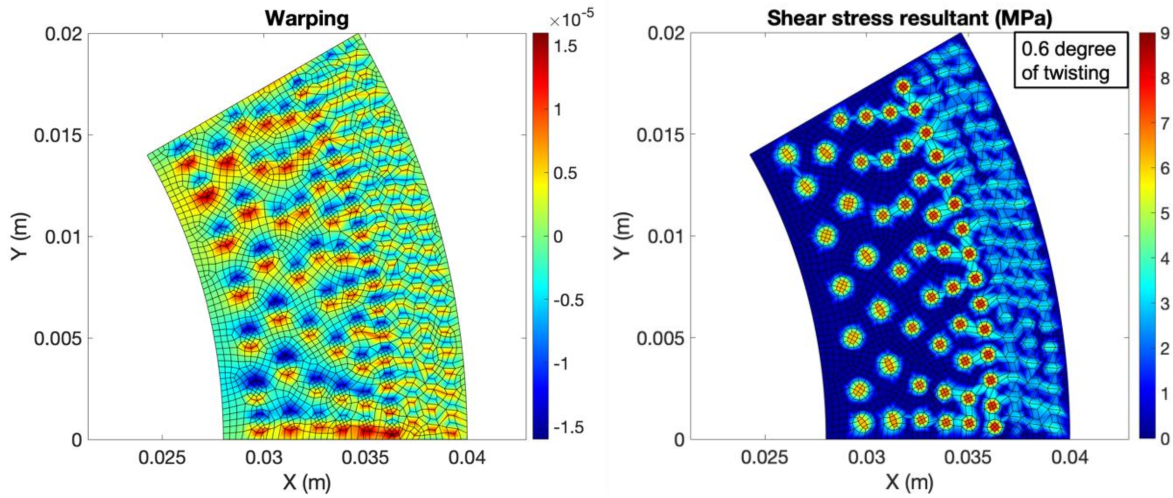

Figure 3-19 The distribution of warping function (left) and the shear stress resultant (right) of a 30-degree slice of a bamboo cross section

In contrast, for an applied angle of twist of 0.01 radians per unit length, the maximum shear stress resultant predicted by the FVM simulation based on the homogenized material properties is 7.03 MPa and that based on the actual fiber and matrix microstructure is 8.63 MPa. In addition, the torsional rigidity of the former model is 199.87 $GN.m^2$ while that of the latter is 246.96 $GN.m^2$. Both the maximum shear stress resultant and torsional rigidity are underestimated with the homogenized material properties, illustrating that the consideration of actual microstructural details versus homogenization is important in the torsional analysis of natural heterogeneous cross sections for conservative design purposes.

3.6 Summary

The finite-volume based approach to the solution of Saint Venant's torsion problems of bars and beams comprised of rectangular sections previously developed by the author has been extended to enable an analysis of arbitrary cross sections characterized by curved boundaries. This is accomplished by incorporating parametric mapping based on transfinite grid generation to enable discretization of the bar cross section by quadrilateral rather than rectangular subvolumes employed in the original version. The construction of the local stiffness matrix that relates the surface-averaged subvolume warping functions to the corresponding tractions is carried out in the reference plane such that the subvolume equilibrium in the physical plane is satisfied in a surface-averaged sense. This produces explicit expressions for the stiffness matrix elements that may be readily coded. Orthotropic subvolumes are intrinsic in the method’s construction so that bars with heterogeneous and composite microstructures may be analyzed. The convergence and accuracy of the parametric FVM are assessed and verified upon comparison with exact elasticity solutions for cross sections with convex and concave boundaries.

Examples involving structural applications of prismatic bars with curved boundaries illustrate the utility of the developed methodology. These include cross sections that resemble biological constructs with homogeneous and graded regions aimed at enhancing torsional rigidities, as well as homogeneous and graded elliptical cross sections with orthotropic shear moduli aimed at reducing and eliminating warping. Multi-phase and multi-porosity cross sections have also been analyzed. It was demonstrated that warping of solid cross sections can be mitigated through layering, and warping of porous cross sections may be mitigated through porosity grading. Finally, concluded from the torsional analysis of a bamboo’s functionally graded cross section, the result implies that consideration of actual microstructural details versus homogenization is important in mimicking the torsional response of natural heterogeneous cross sections.

Chapter 4

Torsion-Flexure Problems

4.1 Introduction

Beams are slender structures with longitudinal dimensions much longer than transverse ones. With the rapid development of composites technology, materials employed in beams can be tailored and assembled to achieve the required beam stiffness and strength. Composite beams are widely used in civil, mechanical and aerospace engineering for modeling bridge structures, construction elements, aircraft wings, wind turbine blades, and so on.

One technically important class of problems in the theory of elasticity concerns the study of elastic beams bounded by a cylindrical surface and by a pair of planes normal to the lateral surface with loading applied only on its end faces. When warping is not present, the two most common beam theories are the Euler-Bernoulli theory and the Timoshenko theory. Beyond the Euler-Bernoulli theory, the Timoshenko theory additionally allows transverse shear deformation. Many finite-element formulations have been developed using these two theories without including the effect of warping. Three-dimensional (3D) analysis of beams is capable of capturing the warping in the deformation of beams, but it is a cumbersome task requiring elaborate modeling and significant computational cost.

To simplify the modeling of 3D beams, the analysis is generally decomposed into a local cross section level and a global longitudinal axis level. A beam with homogeneous isotropic material properties subjected to specific resultant force and/or resultant moment will yield specific analytical solutions if it has a simple geometric cross section provided in some elasticity textbooks e.g., Love (1906) and Timoshenko (1951). Muskhelishvili (1953) outlined an elegant method for the solution of beam problems that accounts for the warping displacement in the axial direction of the beam. The complete problem of equilibrium of an elastic beam with a free lateral surface can be solved by utilizing the principle of superposition because it can be decomposed into four elementary problems: *extension*, *bending*, *torsion*, and *flexure*. This consists of making certain assumptions about the components of stress, strain, or displacement, yet leaving enough freedom in the quantities involved to satisfy the equilibrium and compatibility conditions. The extension of homogeneous isotropic beams by longitudinal forces has a straight-forward solution where the non-zero stress is the only normal stress in the direction of extension based on uniform stretch assumption. The stress in a bent beam that gives rise to the bending moment is a longitudinal stress varying linearly, assuming uniform curvature of the beam. With the only non-zero stress as the normal stress along the longitudinal direction involving the end moment and the moment of inertia, the pure bending problem has a closed-form solution for homogeneous isotropic beams of any cross-sectional shape. The in-plane displacements are explicitly expressed in the torsion problem from kinematics; therefore, the stresses are solved via Saint-Venant's semi-inverse method based on the equilibrium condition with no traction transversely on the beam but equal and opposite moments applied at both ends. The flexure problem can be modeled as a cantilever beam of the uniform cross section having one end ($z = 0$) fixed and the other end ($z = l$) loaded by some distribution of force $(W_x, W_y, 0)$ lying in the plane ($z = l$), Figure 4-1.

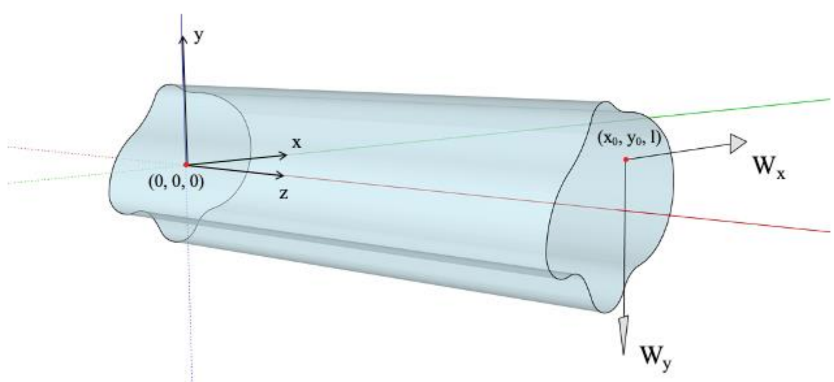

Figure 4-1 Prismatic bar problem under flexure with the z-axis taken along the central line of the beam while the x and y axes are any orthogonal axes intersecting at the centroid

The resultant force is assumed to act at the load point (x_0, y_0, l). The statically equivalent force is equal but opposite at fixed end if the beam is in equilibrium. The z axis is taken along the central line of the beam, while the x and y axes are any orthogonal axes intersecting at the centroid of the end $z = 0$. The lateral surface of the beam is free from external forces, and the body forces are assumed to vanish as well. The end-face forces usually produce both torsional and flexural coupling effects, therefore the flexure problem will be termed the "torsion-flexure" problem, consistent with the common terminology employed in structural engineering in the remainder of this chapter.

4.2 Literature review

Substantial effort has been made in the analysis of straight and prismatic beams subjected to end-face forces. Nonetheless, torsion-flexure problems have closed-form solutions only for specific cross section shapes made of linear homogeneous isotropic materials. Stevenson (1938) reduced the torsion-flexure problem to the determination of six canonical flexure functions, but a general process for obtaining these was lacking. Milne (1959) presented a general method based on the complex potential theory where the flexure function is mapped onto a unit circle in a manner that depends on a special formulation of the boundary conditions. Using conformal mapping, solutions to circular, cardioid, one-loop Bernoulli's lemniscate, and one-axis symmetric cross sections are obtained using this approach. Sokolnikoff (1956) explicitly demonstrated the general solution to flexure of cantilever beams by terminal loads, which applies to homogeneous isotropic beams of any uniform cross section. Using stress formulation, the flexure problem is reduced to the task of finding three harmonic functions involving the solution to two simpler problems: pure flexure problem and pure torsion problem. Stress-based solutions were provided to flexure problems of singly connected cross sections (e.g. circular and elliptical, rectangular, cardioid) as well as doubly-connected cross sections (e.g. circular pipes), including stress functions that yield solutions to elliptical, equilateral triangular and semicircular cross sections along with an interesting physical interpretation. Libenson (1947) used a similar method to obtain an approximate solution to this problem for a semi-circular tube of small thickness; Uflyand (1965) solved the problem of beams whose cross section is a circular segment in bipolar coordinates with the aid of Fourier integrals. Batra et al. (2005) used the method of Signorini's expansion to analyze the Saint-Venant problem for an isotropic and homogeneous second-order elastic prismatic bar in flexure.

FEM was first used by Mason and Herrmann (1968) in the solution of the torsion-flexure problem of isotropic beams of arbitrary cross sections following the Saint-Venant semi-inverse method. These semi-analytical methods have been extended to beams made of orthotropic materials by Tolf (1985), monoclinic materials by Woerndle (1981), and materials with rectilinear anisotropy by Kosmatka and Dong (1991). To achieve acceptable accuracy with the finite-element approach, a complicated cross section requires many elements. Moreover, finite-element based methods are limited by the shape of the elements that prevent elemental distortion, thereby introducing complications in the meshing process.

The power series approach, as one of the approximate techniques, was initially applied by Mindlin (1975) to the Saint-Venant's torsion problem using a double series expansion in powers of in-plane coordinates. A power series solution for the out-of-plane warping induced by torsion-flexure was obtained by Kosmatka (1993) to identify homogeneous isotropic section properties from torsion-flexure behavior. The power series coefficients were determined by FEM. The Ritz method was employed to aid in the numerical integration on the cross-sectional area, but this required many integration points because of the high order power series.

Friedman and Kosmatka (2000) employed a three-node isoparametric boundary element method (BEM) to improve efficiency and accuracy for homogeneous isotropic arbitrarily shaped cross sections. Petrolo and Casciaro (2004) derived stiffness matrices for beam elements with general homogeneous isotropic cross sections investigated by comparing different boundary element methods with FEM strategies. Gaspari and Aristodemo (2005) extended the BEM to orthotropic beams having polygonal cross sections. The Line Element-less Method (LEM) developed by Santoro (2011) was employed to provide approximate solutions to coupled torsion-flexure problems of orthotropic beams without the need for boundary discretization. Since the complex potential function is analytic in the whole cross-sectional area, LEM takes full advantage of the double-ended Laurent series involving harmonic polynomials, which can fully represent any analytic function in the complex domain.

The solutions mentioned above are not applicable in cases involving beam cross sections composed of heterogeneous materials. Solving flexure problems involving beams with heterogeneous anisotropic material properties remains a challenge because the basic assumptions employed in the solution approach based on Saint-Venant semi-inverse method are not satisfied. Nonetheless, some progress has been made in dealing with heterogeneous materials in terms of solving this general flexure problem analytically. Muskhelishvili (1953) analyzed the deformation of compound beams under end loads by adding boundary conditions at the interfaces of materials with different elastic properties but uniform Poisson's ratio. This approach was extended by Vekua and Rukhadze (1933) to include non-uniform Poisson's ratio. Lekhnitskii (1964) introduced radial isotropic property variation for circular cylinders and obtained a solution for materials with angular property variations. Rooney and Ferrari (1995) provided analytic solutions to the torsion and flexure of bars with heterogeneous shear modulus but under specific assumptions on the geometry and modulus.

The demand for accurate and efficient modeling and analysis of composite beams has led to the development of various more sophisticated theories. The finite-element based approach has been followed by relatively a few researchers. The work of Giavotto et al. (1983) laid the foundation for the linear finite-element cross-sectional analysis based on the anisotropic beam theory. They modeled the in-plane and the out-of-plane warping displacements for anisotropic and non-homogeneous materials. They also proposed the concept of far-from-end solutions to determine the cross-sectional uniform warping field while the end effects were represented through eigenmodes in the terminal zones. These eigenmodes are obtained by solving a homogeneous equation where an exponential decay is assumed along the beam axis. Yet, there was still a need for the development of transition elements that allows an efficient and accurate connection between different elements. Cesnik and Hodges (1997) introduced a new approach to finite-element analysis, known as Variational Asymptotic Beam Sectional analysis (VABS). This method uses a strain field to reduce the three-dimensional strain energy via the variational asymptotic method. The approach enables the analysis of thin-walled composite beams with both open and closed cross-sections. The strain energy is minimized by finding a sectional displacement field that satisfies the boundary conditions of the beam. Jung et al. (2002) refined VABS's displacement approximations systematically, providing a more accurate analysis of composite beams' behavior. They developed an efficient approach that involves refining the displacement approximation to achieve a more precise result. Yu et al. (2002) then validated VABS's accuracy and flexibility using finite-element tools. They compared VABS with other FEM and found that it provided an accurate solution with increased flexibility. Fatmi and Zenzri (2004) further simplified the numerical implementation of FEM for the exact elastic beam theory. The proposed numerical method uses three-dimensional finite elements and classical elasticity formulation, providing three-dimensional Saint Venant solutions for computing local effects. They demonstrated the efficiency and accuracy of the exact beam theory in the study of arbitrary elastic multi-material cross-sections, providing a more accurate solution to the behavior of beams under load. Their approach has the advantage of accurately predicting the behavior of beams under load with a lower computational cost compared to other methods.

FVM has been widely used in solving plane problems in structural mechanics and has gained popularity in solving torsion problems. However, there is a gap in the literature regarding the use of FVM in solving the torsion-flexure problem. This chapter aims to bridge this gap by providing a powerful alternative to the widely used variational techniques for this class of problems. The chapter focuses specifically on the development of a finite-volume based analysis of homogeneous orthotropic beams under end-face loading. This provides a valuable contribution to the field of structural mechanics and expands the scope of semi-analytical and numerical methods for the solution of torsion-flexure problems.

4.3 Torsion-Flexure Problems

Figure 4-1 illustrates the manner of applied loading characteristic of the torsion-flexure problem, which requires a statically equivalent force equal but opposite at the fixed end in order to satisfy overall beam equilibrium. The lateral surface of the beam is free from external forces, and the body forces are assumed to vanish simplifying the problem formulation. Though there is no applied or resultant moment M_z about the centroid of the cross section considered in the torsion-flexure problem, the deformation of the beam can involve both the flexure component and the additional torsion component when the statically equivalent force is not applied at a specific location on the free end face.

The local disturbances in the stress distribution near the end of the beam fixed rigidly to the wall will also be neglected following Saint-Venant's principle. If the bending force is inclined to the principal axes of the cross section of the beam, it can always be resolved into two components acting in the direction of the principal axes. Thus, bending in each of the two principal planes can be analyzed separately. The total stresses and displacement are then obtained using the principle of superposition.

Consider the case when the beam is homogeneous but orthotropic. Following the semi-inverse method of Saint-Venant involving assumptions on the stress fields as the starting point,

$$\sigma_{xx} = \sigma_{xy} = \sigma_{yy} = 0 \tag{4. 1}$$

the remaining stress fields σ_{zx}, σ_{zy} and σ_{zz} are then chosen such that the equations of equilibrium and compatibility, as well as the boundary conditions, are satisfied. The bending moment M_y that would be produced by the load W_x acting alone, in any cross section z unit distant from the fixed end, is $M_y = W_x(l - z)$. The stress distribution in this cross section is statically equivalent to the moment M_y and W_x. The normal stress in the direction of the beam's axis is then $\sigma_{zz} = -\frac{M_y}{I_{yy}}x$ due to the M_y bending moment. Similar conclusion is obtained when considering the axial stress due to the M_x bending moment produced by the force resultant W_x. Thus, in the presence of bending about the two transverse axes by both W_x and W_y, the normal stress along the longitudinal direction is assumed to be,

$$\sigma_{zz} = -E_{zz}(l - z)\left(K_x x + K_y y\right) \tag{4. 2}$$

where the constants K_x , K_y are determined from the conditions of cross-sectional force equilibrium.

$$\begin{gathered}\iint_A \sigma_{zx}\ dx\, dy = W_x \\ \iint_A \sigma_{zy}\, dx\, dy = W_y\end{gathered} \tag{4. 3}$$

Using the above assumptions on the stress field, the equations of equilibrium are reduced to,

$$\begin{gathered}\frac{\partial \sigma_{zx}}{\partial z} = 0 \to \sigma_{zx} = \sigma_{zx}(x, y) \\ \frac{\partial \sigma_{zy}}{\partial z} = 0 \to \sigma_{zy} = \sigma_{zy}(x, y) \\ \frac{\partial \sigma_{zx}}{\partial x} + \frac{\partial \sigma_{zy}}{\partial y} + E_{zz}\left(K_x x + K_y y\right) = 0\end{gathered} \tag{4. 4}$$

It follows from the first two of equilibrium equations that the shear stress components σ_{zx} and σ_{zy} have the same distributions in all transverse cross sections throughout the beam, while the third equation can be rearranged as

$$\frac{\partial}{\partial x}\left(\sigma_{zx}+\frac{1}{2}E_{zz}K_x x^2\right)+\frac{\partial}{\partial y}\left(\sigma_{zy}+\frac{1}{2}E_{zz}K_y y^2\right)=0 \tag{4. 5}$$

A potential function denoted by F is then introduced because the equation above has the components of the partial derivatives in terms of both x and y. The expressions in the parentheses are replaced by $\frac{\partial F}{\partial y}$ and $-\frac{\partial F}{\partial x}$ respectively, and the equation is identically satisfied.

$$\frac{\partial}{\partial x}\left(\frac{\partial F}{\partial y}\right)+\frac{\partial}{\partial y}\left(-\frac{\partial F}{\partial x}\right)=0 \tag{4. 6}$$

If the function F exists, the non-zero shear stresses are,

$$\begin{aligned}\sigma_{zx}&=\frac{\partial F}{\partial y}-\frac{1}{2}E_{zz}K_x x^2\\ \sigma_{zy}&=-\frac{\partial F}{\partial x}-\frac{1}{2}E_{zz}K_y y^2\end{aligned} \tag{4. 7}$$

Based on the constitutive equation for orthotropic materials, the strain components generated by the assumed stress fields are

$$\begin{aligned}\epsilon_{xx}&=-\frac{\nu_{zx}}{E_{zz}}\sigma_{zz}=\nu_{zx}(l-z)\left(K_x x+K_y y\right)\\ \epsilon_{yy}&=-\frac{\nu_{zy}}{E_{zz}}\sigma_{zz}=\nu_{zy}(l-z)\left(K_x x+K_y y\right)\\ \epsilon_{zz}&=\frac{1}{E_{zz}}\sigma_{zz}=-(l-z)\left(K_x x+K_y y\right)\\ \epsilon_{zy}&=\frac{1}{2G_{zy}}\sigma_{zy}=-\frac{1}{2G_{zy}}\frac{\partial F}{\partial x}-\frac{E_{zz}}{4G_{zy}}K_y y^2\\ \epsilon_{zx}&=\frac{1}{2G_{zx}}\sigma_{zx}=\frac{1}{2G_{zx}}\frac{\partial F}{\partial y}-\frac{E_{zz}}{4G_{zx}}K_x x^2\\ \epsilon_{xy}&=0\end{aligned} \tag{4. 8}$$

The condition to be satisfied by the function $F(x,y)$ can be determined from the strain compatibility equations. Substituting the shear stresses expressed in terms of the function F, the compatibility equations reduce to a set of two equations,

$$\frac{\partial}{\partial x}\left(\frac{1}{2G_{zy}}\frac{\partial^2 F}{\partial x^2}+\frac{1}{2G_{zx}}\frac{\partial^2 F}{\partial y^2}\right)=-\nu_{zx}K_y$$
$$\frac{\partial}{\partial y}\left(\frac{1}{2G_{zy}}\frac{\partial^2 F}{\partial x^2}+\frac{1}{2G_{zx}}\frac{\partial^2 F}{\partial y^2}\right)=\nu_{zy}K_x \tag{4. 9}$$

Integrating the above equations, and using the notation

$$\nabla'^2 F=\frac{1}{2G_{zy}}\frac{\partial^2 F}{\partial x^2}+\frac{1}{2G_{zx}}\frac{\partial^2 F}{\partial y^2} \tag{4. 10}$$

for the weighted Laplacian operator, one can obtain the following differential equation that governs the potential function F,

$$\nabla'^2 F=-\nu_{zx}K_y x+\nu_{zy}K_x y+C \tag{4. 11}$$

The partial derivative of the in-plane rotation component $\omega_{xy}=\frac{1}{2}\left(\frac{\partial v}{\partial x}-\frac{\partial u}{\partial y}\right)$ with respect to the axial coordinate, which produces local twist at a point (x,y) of the cross section, is then related to the strains ϵ_{zy} and ϵ_{zx},

$$\frac{\partial \omega_{xy}}{\partial z}=\frac{\partial \epsilon_{zy}}{\partial x}-\frac{\partial \epsilon_{zx}}{\partial y} \tag{4. 12}$$

This relationship is re-written in terms of the F function,

$$\frac{\partial \omega_{xy}}{\partial z}=\left(\frac{1}{2G_{zy}}\frac{\partial \sigma_{zy}}{\partial x}-\frac{1}{2G_{zx}}\frac{\partial \sigma_{zx}}{\partial y}\right)=-\nabla'^2 F \tag{4. 13}$$

or equivalently, using the previously obtained expression for $\nabla'^2 F$,

$$\frac{\partial \omega_{xy}}{\partial z}=\nu_{zx}K_y x-\nu_{zy}K_x y-C \tag{4. 14}$$

The constant C is determined in terms of the mean of the local twist θ over the entire cross section. Consequently, C must be equal to $-\theta$. Therefore,

$$\nabla^{2}F = -\nu_{zx}K_{y}x + \nu_{zy}K_{x}y - \theta \tag{4. 15}$$

The particular solution to the partial differential equation above is obtained as

$$F_{p}(x,y) = -\frac{\nu_{zx}G_{zy}}{3}K_{y}x^{3} + \frac{\nu_{zy}G_{zx}}{3}K_{x}y^{3} - \frac{\theta}{2}\left(G_{zy}x^{2} + G_{zx}y^{2}\right) \tag{4. 16}$$

and the homogeneous solution is $f(x,y)$, which is a weighted harmonic function satisfying,

$$\nabla'^{2}f = \frac{1}{2G_{zy}}\frac{\partial^{2}f}{\partial x^{2}} + \frac{1}{2G_{zx}}\frac{\partial^{2}f}{\partial y^{2}} = 0 \tag{4. 17}$$

Thus, the complete solution for F reads,

$$F(x,y) = f(x,y) - \frac{\nu_{zx}G_{zy}}{3}K_{y}x^{3} + \frac{\nu_{zy}G_{zx}}{3}K_{x}y^{3} - \frac{\theta}{2}\left(G_{zy}x^{2} + G_{zx}y^{2}\right) \tag{4. 18}$$

Further simplification is achieved by re-writing the stresses σ_{zx} and σ_{zy} in terms of the weighted conjugate $g(x,y)$ of $f(x,y)$, where $\frac{\partial g}{\partial x} = \frac{1}{G_{zx}}\frac{\partial f}{\partial y}$ and $\frac{\partial g}{\partial y} = -\frac{1}{G_{zy}}\frac{\partial f}{\partial x}$, that satisfies,

$$\nabla'^{2}g = \frac{1}{2G_{zy}}\frac{\partial^{2}g}{\partial x^{2}} + \frac{1}{2G_{zx}}\frac{\partial^{2}g}{\partial y^{2}} = 0 \tag{4. 19}$$

Using the weighted conjugate $g(x,y)$ the shear stresses are then expressed as,

$$\begin{aligned}
\sigma_{zx} &= G_{zx}\left(\frac{\partial g}{\partial x} - \theta y\right) + G_{zx}\nu_{zy}K_{x}y^{2} - K_{x}\frac{E_{zz}x^{2}}{2} \\
\sigma_{zy} &= G_{zy}\left(\frac{\partial g}{\partial y} + \theta x\right) + G_{zy}\nu_{zx}K_{y}x^{2} - K_{y}\frac{E_{zz}y^{2}}{2}
\end{aligned} \tag{4. 20}$$

Noting that the shear stress fields for the pure torsion problem for orthotropic materials are,

$$\begin{aligned}
\sigma_{zx} &= G_{zx}\theta\left(\frac{\partial \omega_{1}}{\partial x} - y\right) \\
\sigma_{zy} &= G_{zy}\theta\left(\frac{\partial \omega_{1}}{\partial y} + x\right)
\end{aligned} \tag{4. 21}$$

where ω_1 is the out-of-plane warping function from the pure torsion problem, the weighted conjugate function $g(x,y)$ may be expressed in terms of three weighted harmonic functions ω_1, ω_2, ω_3 ($\nabla'^2\omega_i = \frac{1}{2G_{zy}}\frac{\partial^2\omega_i}{\partial x^2} + \frac{1}{2G_{zx}}\frac{\partial^2\omega_i}{\partial y^2} = 0, i = 1,2,3$),

$$g(x,y) = \theta\omega_1 + K_x\omega_2 + K_y\omega_3 \tag{4. 22}$$

This leads to the shear stresses expressed in terms of these three functions as follows,

$$\sigma_{zx} = \theta G_{zx}\left(\frac{\partial\omega_1}{\partial x} - y\right) + K_x\left(G_{zx}\frac{\partial\omega_2}{\partial x} - \frac{E_{zz}x^2}{2} + G_{zx}\nu_{zy}y^2\right) + K_y G_{zx}\frac{\partial\omega_3}{\partial x} \tag{4. 23}$$

$$\sigma_{zy} = \theta G_{zy}\left(\frac{\partial\omega_1}{\partial y} + x\right) + K_y\left(G_{zy}\frac{\partial\omega_3}{\partial y} - \frac{E_{zz}y^2}{2} + G_{zy}\nu_{zx}x^2\right) + K_x G_{zy}\frac{\partial\omega_2}{\partial y} \tag{4. 24}$$

The above shear stresses must satisfy the traction-free boundary conditions on the lateral surface,

$$\sigma_{zx}\frac{dx}{dn} + \sigma_{zy}\frac{dy}{dn} = 0 \tag{4. 25}$$

Substituting the shear stress expressions into the equation above, one obtains,

$$\begin{gathered}
\theta\left(G_{zx}\frac{\partial\omega_1}{\partial x}\frac{dx}{dn} - G_{zx}y\frac{dx}{dn} + G_{zy}\frac{\partial\omega_1}{\partial y}\frac{dy}{dn} + G_{zy}x\frac{dy}{dn}\right) \\
+K_x\left(G_{zx}\frac{\partial\omega_2}{\partial x}\frac{dx}{dn} + G_{zy}\frac{\partial\omega_2}{\partial y}\frac{dy}{dn}\right) + K_x\left(\nu_{zy}G_{zx}y^2 - \frac{E_{zz}}{2}x^2\right)\frac{dx}{dn} \\
+K_y\left(G_{zx}\frac{\partial\omega_3}{\partial x}\frac{dx}{dn} + G_{zy}\frac{\partial\omega_2}{\partial y}\frac{dy}{dn}\right) + K_y\left(\nu_{zx}G_{zy}x^2 - \frac{E_{zz}}{2}y^2\right)\frac{dy}{dn} = 0
\end{gathered} \tag{4. 26}$$

Since the pure torsion contribution vanishes, the above equation is satisfied if the functions ω_2 and ω_3 are subject to the conditions,

$$G_{zx}\frac{\partial\omega_2}{\partial x}\frac{dx}{dn} + G_{zy}\frac{\partial\omega_2}{\partial y}\frac{dy}{dn} + \left(-\frac{E_{zz}}{2}x^2 + \nu_{zy}G_{zx}y^2\right)\frac{dx}{dn} = 0 \; on \; C \tag{4. 27}$$

$$G_{zx}\frac{\partial\omega_3}{\partial x}\frac{dx}{dn} + G_{zy}\frac{\partial\omega_3}{\partial y}\frac{dy}{dn} + \left(-\frac{E_{zz}}{2}y^2 + \nu_{zx}G_{zy}x^2\right)\frac{dy}{dn} = 0 \; on \; C \tag{4. 28}$$

The flexure problem is then reduced to the task of finding three harmonic potential functions subject to Neumann boundary conditions. The three weighted harmonic functions must satisfy the weighted Laplace's equation. Laplace's equation subject to Neumann boundary conditions must satisfy a compatibility condition for a solution to exist. A general boundary value problem involving Laplace's equation with Neumann boundary conditions is given by,

$$\nabla^2 \omega = 0 \ in \ A \tag{4. 29}$$

$$\frac{d\omega}{dn} = g \ on \ C \tag{4. 30}$$

Integrating the governing Laplace equation over the bar's cross section and applying the divergence theorem in conjunction with the boundary condition yields

$$\iint_A \nabla^2 \omega \, dA = \iint_A \nabla \cdot \nabla\omega \, dA = \int_C \frac{d\omega}{dn} \, ds = \int_C g \ ds = 0 \tag{4. 31}$$

In order to verify that the condition for the existence of a solution for this problem is fulfilled, application of the Green's theorem yields the result,

$$\begin{aligned} \int_C \left(G_{zx} \frac{\partial \omega_1}{\partial x} \frac{dx}{dn} + G_{zy} \frac{\partial \omega_1}{\partial y} \frac{dy}{dn} \right) ds = \int_C \left(G_{zx} y dy - G_{zy} x dx \right) = \iint_A (0-0) dx dy \\ \equiv 0 \end{aligned} \tag{4. 32}$$

$$\begin{aligned} \int_C \left(G_{zx} \frac{\partial \omega_2}{\partial x} \frac{dx}{dn} + G_{zy} \frac{\partial \omega_2}{\partial y} \frac{dy}{dn} \right) ds = \int_C \left(\frac{E_{zz}}{2} x^2 - \nu_{zy} G_{zx} y^2 \right) dy \\ = E_{zz} \iint_A x \ dx \, dy \equiv 0 \end{aligned} \tag{4. 33}$$

$$\begin{aligned} \int_C \left(G_{zx} \frac{\partial \omega_3}{\partial x} \frac{dx}{dn} + G_{zy} \frac{\partial \omega_3}{\partial y} \frac{dy}{dn} \right) ds = -\int_C \left(\frac{E_{zz}}{2} y^2 - \nu_{zx} G_{zy} x^2 \right) dx \\ = E_{zz} \iint_A y \ dx \, dy \equiv 0 \end{aligned} \tag{4. 34}$$

since the origin is at the centroid of the cross section.

In order to determine the constants K_x and K_y, it is necessary to recall the definition of the moments of inertia in the chosen coordinate system,

$$I_{xx} = \iint_A y^2 \, dx\, dy, \quad I_{yy} = \iint_A x^2 \, dx\, dy, \qquad I_{xy} = \iint_A xy \, dx\, dy \tag{4. 35}$$

Since the resultant of the stress σ_{zx} acting on the bar's cross section must equal W_x, applying the Green's theorem to the area integrals involving ω_2, ω_3, produces the expression for W_x,

$$W_x = K_x E_{zz} I_{yy} + K_y E_{zz} I_{xy} \tag{4. 36}$$

Similar to the component W_x of the applied load, one also obtains the expression for W_y,

$$W_y = K_y E_{zz} I_{xx} + K_x E_{zz} I_{xy} \tag{4. 37}$$

Solving the system of equation Eq. (4. 36) and Eq. (4. 37) yields the solution

$$\begin{cases} E_{zz} K_x = \dfrac{W_x I_{xx} - W_y I_{xy}}{I_{xx} I_{yy} - I_{xy}^2} \\ E_{zz} K_y = \dfrac{W_y I_{yy} - W_x I_{xy}}{I_{xx} I_{yy} - I_{xy}^2} \end{cases} \tag{4. 38}$$

The knowledge of the stress field enables the determination of the displacement field that generates it using the strain-displacement relations and the Hooke's law. In the absence of in-plane normal and shear stresses, $\sigma_{xx} = \sigma_{yy} = \sigma_{xy} = 0$, the constitutive equations become,

$$\begin{bmatrix} \epsilon_{xx} \\ \epsilon_{yy} \\ \epsilon_{zz} \\ \epsilon_{zy} \\ \epsilon_{zx} \\ \epsilon_{xy}(0) \end{bmatrix} = \begin{bmatrix} \dfrac{1}{E_{xx}} & -\dfrac{\nu_{yx}}{E_{yy}} & -\dfrac{\nu_{zx}}{E_{zz}} & 0 & 0 & 0 \\ -\dfrac{\nu_{xy}}{E_{xx}} & \dfrac{1}{E_{yy}} & -\dfrac{\nu_{zy}}{E_{zz}} & 0 & 0 & 0 \\ -\dfrac{\nu_{xz}}{E_{xx}} & -\dfrac{\nu_{yz}}{E_{yy}} & \dfrac{1}{E_{zz}} & 0 & 0 & 0 \\ 0 & 0 & 0 & \dfrac{1}{2G_{zy}} & 0 & 0 \\ 0 & 0 & 0 & 0 & \dfrac{1}{2G_{zx}} & 0 \\ 0 & 0 & 0 & 0 & 0 & \dfrac{1}{2G_{xy}} \end{bmatrix} \begin{bmatrix} \sigma_{xx}(0) \\ \sigma_{yy}(0) \\ \sigma_{zz} \\ \sigma_{zy} \\ \sigma_{zx} \\ \sigma_{xy}(0) \end{bmatrix} \tag{4. 39}$$

Writing the normal strains in terms of partial derivatives of the displacements, and using the above constitutive equations, yields,

$$\frac{\partial u}{\partial x} = \epsilon_{xx} = -\nu_{zx}(z - l)(K_x x + K_y y) \tag{4. 40}$$

$$\frac{\partial v}{\partial y} = \epsilon_{yy} = -\nu_{zy}(z - l)(K_x x + K_y y) \tag{4. 41}$$

$$\frac{\partial w}{\partial z} = \epsilon_{zz} = (z - l)(K_x x + K_y y) \tag{4. 42}$$

whose integrals yield expressions for the displacement components,

$$u = \nu_{zx}(l - z)\left(\frac{K_x x^2}{2} + K_y xy\right) + A(y, z) \tag{4. 43}$$

$$v = \nu_{zy}(l - z)\left(K_x xy + \frac{K_y y^2}{2}\right) + B(x, z) \tag{4. 44}$$

$$w = \left(\frac{z^2}{2} - lz\right)(K_x x + K_y y) + C(x, y) \tag{4. 45}$$

where the integration functions $A(y, z), B(x, z), C(y, z)$ need to be determined.

Since the in-plane shear strain is zero, i.e., $\epsilon_{xy} = 0$, the corresponding strain-displacement relation yields expressions for the functions $A(y, z), B(x, z)$ in terms of the additional integration functions $D_1(z), D_2(z)$ and a constant λ

$$A(y, z) = -\frac{1}{2}\nu_{zy}(l - z)K_x y^2 + D_1(z) - \lambda y \tag{4. 46}$$

$$B(x, z) = -\frac{1}{2}\nu_{zx}(l - z)K_y x^2 + D_2(z) + \lambda x \tag{4. 47}$$

In order to make the displacement applicable to pure torsion case, λ has to be equal to αz.

Using the strain-displacement relations for the out-of-plane shear strains, together with the corresponding shear stresses, yields the solution for the functions $D_1(z), D_2(z)$ and expressions for the partial derivatives of the function $C(x, y)$ with respect to x and y.

$$D_1(z) = \left(\frac{lz^2}{2} - \frac{z^3}{6}\right) K_x + c_1 \quad (4.48)$$

$$D_2(z) = \left(\frac{lz^2}{2} - \frac{z^3}{6}\right) K_y + c_2 \quad (4.49)$$

where c_1, c_2 are constants and

$$\frac{\partial C}{\partial x} = \nu_{zx}\left(\frac{K_x x^2}{2} + K_y xy\right) - \frac{\nu_{zy} K_x y^2}{2} + \frac{\sigma_{zx}}{G_{zx}} + \theta y \quad (4.50)$$

$$\frac{\partial C}{\partial y} = \nu_{zy}\left(K_x xy + \frac{K_y y^2}{2}\right) - \frac{\nu_{zx} K_y x^2}{2} + \frac{\sigma_{zy}}{G_{zy}} - \theta x \quad (4.51)$$

Once the function $C(x, y)$ is determined and the origin is fixed to produce zero displacements, the three displacement components are obtained in the form,

- $u(x,y,z) = -\theta yz + (l - z)\left(\nu_{zx}\frac{K_x x^2}{2} + \nu_{zx} K_y xy - \nu_{zy}\frac{K_x y^2}{2}\right) + K_x\left(\frac{l}{2} - \frac{z}{6}\right) z^2$ (4.52)
- $v(x,y,z) = \theta xz + (l - z)\left(\nu_{zy}\frac{K_y y^2}{2} + \nu_{zy} K_x xy - \nu_{zx}\frac{K_y x^2}{2}\right) + K_y\left(\frac{l}{2} - \frac{z}{6}\right) z^2$ (4.53)
- $w(x,y,z) = \theta\omega_1 + \left(\frac{z^2}{2} - lz\right)(K_x x + K_y y) + K_x\left(\omega_2 + \nu_{zx}\frac{x^3}{6} - \frac{E_{zz}x^3}{6G_{zx}} + \nu_{zy}\frac{xy^2}{2}\right) + K_y\left(\omega_3 + \nu_{zy}\frac{y^3}{6} - \frac{E_{zz}y^3}{6G_{zy}} + \nu_{zx}\frac{x^2 y}{2}\right)$ (4.54)

The stress expressions derived in this section for homogeneous orthotropic materials correctly reduce to those of homogeneous isotropic materials upon setting $G_{zx} = G_{zy} = \mu$ and $\nu_{zx} = \nu_{zy} = \nu$,

$$\sigma_{zx} = \mu\theta\left(\frac{\partial\omega_1}{\partial x} - y\right) + \mu K_x\left(\frac{\partial\omega_2}{\partial x} + \nu y^2 - \frac{Ex^2}{2\mu}\right) + \mu K_y\frac{\partial\omega_3}{\partial x} \quad (4.55)$$

$$\sigma_{zy} = \mu\theta\left(\frac{\partial\omega_1}{\partial y} + x\right) + \mu K_y\left(\frac{\partial\omega_3}{\partial y} + \nu x^2 - \frac{Ey^2}{2\mu}\right) + \mu K_x\frac{\partial\omega_2}{\partial y} \quad (4.56)$$

and the displacement in this section for homogeneous orthotropic materials reduce to

- $u(x,y,z) = \nu(l-z)\left(\frac{K_x x^2}{2} + K_y xy - \frac{K_x y^2}{2}\right) + K_x\left(\frac{l}{2} - \frac{z}{6}\right)z^2 - \theta yz$ (4. 57)

- $v(x,y,z) = \nu(l-z)\left(\frac{K_y y^2}{2} + K_x xy - \frac{K_y x^2}{2}\right) + K_y\left(\frac{l}{2} - \frac{z}{6}\right)z^2 + \theta xz$ (4. 58)

- $w(x,y,z) = \theta\omega_1 + \left(\frac{z^2}{2} - lz\right)\left(K_x x + K_y y\right) + K_x\left[\omega_2 + \frac{xy^2\nu}{2} - \frac{x^3(\nu+2)}{6}\right] + K_y\left[\omega_3 + \frac{x^2 y\nu}{2} - \frac{y^3(\nu+2)}{6}\right]$ (4. 59)

4.4 Finite Volume Method for Torsion-Flexure Problems

As observed in the preceding section, a solution to the torsion-flexure problem requires the determination of the three displacement-like functions ω_i. This section describes the finite-volume approach in the determination of these functions for flexural loading of arbitrarily shaped homogeneous cross sections. This motivates partitioning of isotropic or orthotropic cross sections into quadrilateral subvolumes that mimic the cross-section's shape. The quadrilateral subvolumes are the elementary units in the finite volume analysis wherein the local harmonic potential function fields (ω_1, ω_2, ω_3) are approximated using simple polynomial expressions. The employed polynomials satisfy Beltrami-Michelle compatibility equations, and the use of constitutive equations leads to the direct calculation of the local stress fields through simple differentiation. The use of simple polynomials precludes point-wise satisfaction of the potential functions ω_1, ω_2, ω_3, and traction component continuity across common faces of adjacent subvolumes. Hence a compromise is employed that involves the imposition of interfacial potential function and traction continuity in a surface-average sense. The equilibrium equations are satisfied in a surface-average sense as well. Hence the solution strategy employed in FVM follows the elasticity-based solution strategy, albeit in a surface-average as opposed to point-wise sense. Thus, it differs fundamentally from the variational-based solution strategies based on energy minimization. Whereas the subvolume equilibrium is always satisfied in a surface-average sense, the point-wise accuracy of the method increases with partition refinement.

The above overview of the method again clearly suggests that the finite volume method was originally developed as a semi-analytical tool for efficiently solving structural problems to avoid intricate mathematical derivations in the solution of torsion-flexure problems for homogenous cross sections with various boundary shapes.

The partitioning of the analyzed domain using (i) quadrilateral subvolumes to accommodate cross sections of arbitrary shapes is accomplished using parametric mapping of the reference square domain in the reference plane onto the actual quadrilateral subvolume in the physical plane. The three harmonic potential function field approximations are also made in the reference plane, and thus the FVM analysis, which entails the development of relations between potential functions and traction quantities is conducted in both planes. The establishment of these relations enables the construction of the local stiffness matrix for each quadrilateral subvolume in the physical plane that relates the surface-averaged potential functions to the corresponding tractions. The local stiffness matrix is constructed such that the quadrilateral subvolume's equilibrium is satisfied in the physical plane, and the assembly of all the local stiffness matrices ensures that traction and potential function continuity and prescribed boundary conditions are satisfied as well.

This section first describes the parametric mapping employed in the theory's construction, followed by subvolume discretization into quadrilateral partitions, displacement field construction, and the solution for these harmonic potential functions using the parametric FVM. Towards this end, local coordinate systems $(\bar{x},\bar{y})^{(i)}$ are set up at the subvolumes' centroids, where the coordinates $(x,y)^{(i)}$ of an arbitrary point within the subvolume (i) are referred in the global coordinate system. The global coordinates are employed in the parametric mapping described in the following subsection, whereas the local coordinates transferred in the reference system are employed in each subvolume's harmonic potential functions, strain, and stress field representation.

4.4.1 Parametric Mapping

The reference subvolume is a square in the $\eta - \xi$ plane bounded by $-1 \leq \eta \leq 1$, $1 \leq \xi \leq 1$. The vertices are numbered such that the first set of coordinates is at the lower left corner and the numbering convention increases in a counterclockwise fashion. The faces are numbered similarly such that the face F_p lies between the vertices $\left(\bar{x}_p,\bar{y}_p\right)^{(i)}$ and $\left(\bar{x}_{p+1},\bar{y}_{p+1}\right)^{(i)}$ with $p+1$ going to 1 when $p=4$. Thus, the components of the unit normal vector $\boldsymbol{n}_p^{(i)} = \left[n_x,n_y\right]_p^{(i)}$ to the face F_p in each subvolume (i) are given by

$$n_{x|_p} = \frac{\bar{y}_{p+1}^{(i)} - \bar{y}_p^{(i)}}{l_p}, \; n_{y|_p} = \frac{\bar{x}_{p+1}^{(i)} - \bar{x}_p^{(i)}}{l_p} \tag{4. 60}$$

where $l_p = \sqrt{\left(\bar{x}_{p+1}^{(i)} - \bar{x}_p^{(i)}\right)^2 + \left(\bar{y}_{p+1}^{(i)} - \bar{y}_p^{(i)}\right)^2}$. The mapping if the point (η, ξ) in the reference subvolume to the corresponding point $(\bar{x}, \bar{y})^{(i)}$ in the subvolume of the actual discretized cross section is given by Cavalcante et al. (2007).

$$\begin{aligned} \bar{x}^{(i)}(\eta, \xi) &= N_1(\eta, \xi)\bar{x}_1^{(i)} + N_2(\eta, \xi)\bar{x}_2^{(i)} + N_3(\eta, \xi)\bar{x}_3^{(i)} + N_4(\eta, \xi)\bar{x}_4^{(i)} \\ \bar{y}^{(i)}(\eta, \xi) &= N_1(\eta, \xi)\bar{y}_1^{(i)} + N_2(\eta, \xi)\bar{y}_2^{(i)} + N_3(\eta, \xi)\bar{y}_3^{(i)} + N_4(\eta, \xi)\bar{y}_4^{(i)} \end{aligned} \tag{4. 61}$$

where $N_1(\eta, \xi) = \frac{1}{4}(1 - \eta)(1 - \xi)$, $N_2(\eta, \xi) = \frac{1}{4}(1 + \eta)(1 - \xi)$, $N_3(\eta, \xi) = \frac{1}{4}(1 + \eta)(1 + \xi)$, $N_4(\eta, \xi) = \frac{1}{4}(1 - \eta)(1 + \xi)$.

The determination of the strains and stresses within quadrilateral subvolumes requires the relationship between first partial derivatives of the subvolume harmonic potential functions (general expression: ω) in the two planes $\eta - \xi$ and $x - y$. These are related through the Jacobian $\boldsymbol{J}$ and its inverse $\boldsymbol{J}^{-1}$,

$$\begin{bmatrix} \dfrac{\partial \omega}{\partial \eta} \\ \dfrac{\partial \omega}{\partial \xi} \end{bmatrix}^{(i)} = \boldsymbol{J} \begin{bmatrix} \dfrac{\partial \omega}{\partial x} \\ \dfrac{\partial \omega}{\partial y} \end{bmatrix}^{(i)} \leftrightarrow \begin{bmatrix} \dfrac{\partial \omega}{\partial x} \\ \dfrac{\partial \omega}{\partial y} \end{bmatrix}^{(i)} = \boldsymbol{J}^{-1} \begin{bmatrix} \dfrac{\partial \omega}{\partial \eta} \\ \dfrac{\partial \omega}{\partial \xi} \end{bmatrix}^{(i)} \tag{4. 62}$$

where the Jacobian $\boldsymbol{J}$ is obtained from the transformation equations in the form

$$\boldsymbol{J} = \begin{bmatrix} \dfrac{\partial \bar{x}^{(i)}}{\partial \eta} & \dfrac{\partial \bar{y}^{(i)}}{\partial \eta} \\ \dfrac{\partial \bar{x}^{(i)}}{\partial \xi} & \dfrac{\partial \bar{y}^{(i)}}{\partial \xi} \end{bmatrix} = \begin{bmatrix} A_1^{(i)} + A_2^{(i)}\xi & A_4^{(i)} + A_5^{(i)}\xi \\ A_3^{(i)} + A_2^{(i)}\eta & A_6^{(i)} + A_5^{(i)}\eta \end{bmatrix} \tag{4. 63}$$

with $A_1, \ldots, A_6$ are given in terms of the vertex coordinates $\left(\bar{x}_p, \bar{y}_p\right)^{(i)}$

$A_1^{(i)} = \frac{1}{4}(-\bar{x}_1 + \bar{x}_2 + \bar{x}_3 - \bar{x}_4)^{(i)}$, $A_2^{(i)} = \frac{1}{4}(\bar{x}_1 - \bar{x}_2 + \bar{x}_3 - \bar{x}_4)^{(i)}$

$A_3^{(i)} = \frac{1}{4}(-\bar{x}_1 - \bar{x}_2 + \bar{x}_3 + \bar{x}_4)^{(i)}$, $A_4^{(i)} = \frac{1}{4}(-\bar{y}_1 + \bar{y}_2 + \bar{y}_3 - \bar{y}_4)^{(i)}$

$A_5^{(i)} = \frac{1}{4}(\bar{y}_1 - y_2 + \bar{y}_3 - \bar{y}_4)^{(i)}$, $A_6^{(i)} = \frac{1}{4}(-\bar{y}_1 - y_2 + \bar{y}_3 + \bar{y}_4)^{(i)}$

For consistency with the surface-averaging framework of the finite-volume theory, the two sets of partial derivatives are connected through the volume-averaged Jacobian $\bar{\boldsymbol{J}}$,

$$\bar{\boldsymbol{J}} = \frac{1}{4}\int_{-1}^{+1}\int_{-1}^{+1}\boldsymbol{J}d\eta d\xi = \begin{bmatrix} A_1 & A_4 \\ A_3 & A_6 \end{bmatrix}^{(i)} \tag{4. 64}$$

with the inverse $\bar{\boldsymbol{J}}^{-1}$

$$\bar{\boldsymbol{J}}^{-1} = \frac{1}{|\bar{\boldsymbol{J}}|}\begin{bmatrix} A_6 & -A_4 \\ -A_3 & A_1 \end{bmatrix}^{(i)} = \frac{1}{A_1^{(i)}A_6^{(i)} - A_3^{(i)}A_4^{(i)}}\begin{bmatrix} A_6^{(i)} & -A_4^{(i)} \\ -A_3^{(i)} & A_1^{(i)} \end{bmatrix} \tag{4. 65}$$

In constructing the local stiffness matrix for each subvolume in terms of the surface-averaged displacements and tractions, $\boldsymbol{J}^{-1}$ is replaced by $\bar{\boldsymbol{J}}^{-1}$ in order to generate the elements of the stiffness matrix in closed form. This replacement avoids costly numerical integrations. For each subvolume (i),

$$\begin{gathered}
\begin{bmatrix} \dfrac{\partial\widehat{\omega}}{\partial x} \\ \dfrac{\partial\widehat{\omega}}{\partial y} \end{bmatrix}_{\xi=\mp1}^{(i)} = \bar{\boldsymbol{J}}^{-1(i)}\begin{bmatrix} \dfrac{\partial\widehat{\omega}}{\partial \eta} \\ \dfrac{\partial\widehat{\omega}}{\partial \xi} \end{bmatrix}_{\xi=\mp1}^{(i)} = \frac{1}{|\bar{\boldsymbol{J}}|^{(i)}}\begin{bmatrix} A_6 & -A_4 & 0 & \pm3A_4 \\ -A_3 & A_1 & 0 & \mp3A_1 \end{bmatrix}^{(i)}\begin{bmatrix} W_{\omega(10)} \\ W_{\omega(01)} \\ W_{\omega(20)} \\ W_{\omega(02)} \end{bmatrix}^{(i)} \\
\begin{bmatrix} \dfrac{\partial\widehat{\omega}}{\partial x} \\ \dfrac{\partial\widehat{\omega}}{\partial y} \end{bmatrix}_{\eta=\pm1}^{(i)} = \bar{\boldsymbol{J}}^{-1(i)}\begin{bmatrix} \dfrac{\partial\widehat{\omega}}{\partial \eta} \\ \dfrac{\partial\widehat{\omega}}{\partial \xi} \end{bmatrix}_{\eta=\pm1}^{(i)} = \frac{1}{|\bar{\boldsymbol{J}}|^{(i)}}\begin{bmatrix} A_6 & -A_4 & \pm3A_6 & 0 \\ -A_3 & A_1 & \mp3A_3 & 0 \end{bmatrix}^{(i)}\begin{bmatrix} W_{\omega(10)} \\ W_{\omega(01)} \\ W_{\omega(20)} \\ W_{\omega(02)} \end{bmatrix}^{(i)}
\end{gathered} \tag{4. 66}$$

In the above relations, $\omega(x, y)$ may be any of the selected field quantities.

The following concise vector notation is introduced in the sequel in the expressions above for notational convenience,

$\boldsymbol{a}_{1,3}^{(i)} = \frac{1}{|\bar{\boldsymbol{J}}|^{(i)}}[A_6 \quad -A_4 \quad 0 \quad \pm3A_4]^{(i)}$, $\boldsymbol{a}_{2,4}^{(i)} = \frac{1}{|\bar{\boldsymbol{J}}|^{(i)}}[A_6 \quad -A_4 \quad \pm3A_6 \quad 0]^{(i)}$,

$\boldsymbol{b}_{1,3}^{(i)} = \frac{1}{|\bar{\boldsymbol{J}}|^{(i)}}[-A_3 \quad A_1 \quad 0 \quad \mp3A_1]^{(i)}$, $\boldsymbol{b}_{2,4}^{(i)} = \frac{1}{|\bar{\boldsymbol{J}}|^{(i)}}[-A_3 \quad A_1 \quad \mp3A_3 \quad 0]^{(i)}$

and,

$$\boldsymbol{W}_{\omega}^{(i)} = \begin{bmatrix} W_{\omega(10)} \\ W_{\omega(01)} \\ W_{\omega(20)} \\ W_{\omega(02)} \end{bmatrix}^{(i)}$$

where $\boldsymbol{W}_{\omega}^{(i)}$ denotes the vector of coefficients in the second-order expansion of $\omega(x, y)$ as explained in detail in the following section.

4.4.2 Potential Function and Stress Fields

The three stress components have the following the elasticity-based forms,

$$\sigma_{zx} = \theta G_{zx}\left(\frac{\partial\omega_1}{\partial x} - y\right) + K_x\left(G_{zx}\frac{\partial\omega_2}{\partial x} - \frac{E_{zz}x^2}{2} + G_{zx}\nu_{zy}y^2\right) + K_y G_{zx}\frac{\partial\omega_3}{\partial x} \quad (4.\ 67)$$

$$\sigma_{zy} = \theta G_{zy}\left(\frac{\partial\omega_1}{\partial y} + x\right) + K_y\left(G_{zy}\frac{\partial\omega_3}{\partial y} - \frac{E_{zz}y^2}{2} + G_{zy}\nu_{zx}x^2\right) + K_x G_{zy}\frac{\partial\omega_2}{\partial y} \quad (4.\ 68)$$

$$\sigma_{zz} = -E_{zz}(l - z)\big(K_x x + K_y y\big) \quad (4.\ 69)$$

The three harmonic potential functions are approximated in each subvolume using a second-order expansion in the local coordinates as follows,

$$\begin{aligned}\omega_r^{(i)} = W_{\omega r(00)}^{(i)} + \eta W_{\omega r(01)}^{(i)} + \xi W_{\omega r(10)}^{(i)} + \frac{1}{2}(3\eta^2 - 1)W_{\omega r(20)}^{(i)} \\ + \frac{1}{2}(3\xi^2 - 1)W_{\omega r(02)}^{(i)}\end{aligned} \quad (4.\ 70)$$

where $r = 1, 2, 3$ and $W_{\omega r(mn)}^{(i)}$ are unknown coefficients subsequently redefined in terms of the surface-averaged warping functions along the four subvolume faces ($p = 1, 2, 3, 4$) following the subvolume faces order convention described in Chapter 2. The subvolumes may be occupied by (transversely) isotropic or orthotropic materials. The surface-averaged shear stress components in the two planes in each subvolume are given below after substituting the surface-averaged expressions in Eq. (4. 66):

$$\hat{\sigma}_{xz|p}^{(i)} = \theta G_{zx}\left(\frac{\partial\widehat{\omega_1}}{\partial x} - y\right) + K_x\left(G_{zx}\frac{\partial\widehat{\omega_2}}{\partial x} - \frac{E_{zz}x^2}{2} + G_{zx}\nu_{zy}y^2\right) + K_y G_{zx}\frac{\partial\widehat{\omega_3}}{\partial x}$$

$$\hat{\sigma}_{yz|p}^{(i)} = \theta G_{zy}\left(\frac{\partial\widehat{\omega_1}}{\partial y} + x\right) + K_y\left(G_{zy}\frac{\partial\widehat{\omega_3}}{\partial y} - \frac{E_{zz}y^2}{2} + G_{zy}\nu_{zx}x^2\right) + K_x G_{zy}\frac{\partial\widehat{\omega_2}}{\partial x} \tag{4. 71}$$

$$\hat{\sigma}_{zz|p}^{(i)} = -E_{zz}(l-z)\big(K_x\hat{x} + K_y\hat{y}\big)$$

4.4.3 Local Stiffness Matrix Construction

In order to reduce the number of unknown coefficients in the out-of-plane stress approximation when cross sections are discretized into a large number of subvolumes, the torsion-flexure problem is reformulated in terms of surface-averaged potential functions on the four faces of each subvolume as the primary solution variables. Then one constructs a local stiffness matrix for each subvolume by relating the surface-average potential functions to the corresponding surface-average tractions. We start by defining the surface-average potential functions,

$$\begin{aligned} \widehat{\omega}_r^{(i)}|_{1,3} &= \frac{1}{2}\int_{-1}^{1}\widehat{\omega}_r^{(i)}(\eta, \xi = \mp 1)\, d\eta = W_{r(00)}^{(i)} \mp W_{r(01)}^{(i)} + W_{r(02)}^{(i)} \\ \widehat{\omega}_r^{(i)}|_{2,4} &= \frac{1}{2}\int_{-1}^{1}\widehat{\omega}_r^{(i)}(\eta = \pm 1, \xi)\, d\xi = W_{r(00)}^{(i)} \mp W_{r(10)}^{(i)} + W_{r(20)}^{(i)} \end{aligned} \tag{4. 72}$$

where $r = 1, 2, 3$. Hence, the first and second-order coefficients $W_{r(mn)}^{(i)}$ may be expressed in terms of the surface-averaged potential functions and the zero-order coefficient $\boldsymbol{W}_{\boldsymbol{r}(\mathbf{00})}^{(\boldsymbol{\alpha},\boldsymbol{\beta})}$ where $r = 1, 2, 3$.

$$\boldsymbol{W}_r^{(i)} = \begin{bmatrix} W_{r(10)} \\ W_{r(01)} \\ W_{r(20)} \\ W_{r(02)} \end{bmatrix}^{(i)} = \frac{1}{2}\begin{bmatrix} 0 & 1 & 0 & -1 \\ -1 & 0 & 1 & 0 \\ 0 & 1 & 0 & 1 \\ 1 & 0 & 1 & 0 \end{bmatrix}\begin{bmatrix} \widehat{\omega}_{r|1} \\ \widehat{\omega}_{r|2} \\ \widehat{\omega}_{r|3} \\ \widehat{\omega}_{r|4} \end{bmatrix}^{(i)} - \begin{bmatrix} 0 \\ 0 \\ 1 \\ 1 \end{bmatrix} W_{r(00)}^{(i)} \tag{4. 73}$$

or

$$\boldsymbol{W}_r^{(i)} = \frac{1}{2}\boldsymbol{\alpha}\widehat{\boldsymbol{\omega}}_r^{(i)} - \boldsymbol{\beta} W_{r(00)}^{(i)}$$

Similarly, the corresponding surface-averaged interfacial tractions are defined as follows,

$$t_{z|1,3}^{(i)} = \frac{1}{2}\int_{-1}^{1} t_z^{(i)}(\eta, \xi = \mp 1)\ d\eta$$
$$t_{z|2,4}^{(i)} = \frac{1}{2}\int_{-1}^{1} t_z^{(i)}(\eta = \pm 1, \xi)\ d\xi \tag{4. 74}$$

where the traction vector associated with the face p characterized by the unit normal vector $\boldsymbol{n}_p$ is $t_{z|p}^{(i)} = \sigma_{oz}^{(i)} n_{o|p}^{(i)}\ (o = x, y, z)$. Hence the traction vector components on any of the four subvolume faces become, in terms of the three shear stress components,

$$\hat{t}_{z|p}^{(i)} = \left[\hat{\sigma}_{xz}^{(i)} n_x^{(i)} + \hat{\sigma}_{yz}^{(i)} n_y^{(i)} + \hat{\sigma}_{zz}^{(i)} n_z^{(i)}\right]_p \tag{4. 75}$$

which are expressed in terms of the corresponding surface-averaged shear strains for orthotropic materials,

$$\begin{aligned}
\hat{t}_{z|1,3}^{(i)} = & \left\{ G_{zx}\theta(\boldsymbol{a}_{1,3}^{(i)}\boldsymbol{W}_1^{(i)} - \frac{1}{2}\int_{-1}^{1} y|_{\eta,\xi=\mp 1}^{(i)}\ d\eta) \right. \\
& + K_x\left(G_{zx}\boldsymbol{a}_{1,3}^{(i)}\boldsymbol{W}_2^{(i)} - \frac{1}{2}\int_{-1}^{1}\left(\frac{E_{zz}x^2}{2} - G_{zx}\nu_{zy}y^2\right)_{\eta,\xi=\mp 1}^{(i)} d\eta\right) \\
& \left. + K_y G_{zx}\boldsymbol{a}_{1,3}^{(i)}\boldsymbol{W}_3^{(i)} \right\} n_{x|1,3}^{(i)} \\
& + \left\{ G_{zy}\theta(\boldsymbol{b}_{1,3}^{(i)}\boldsymbol{W}_1^{(i)} + \frac{1}{2}\int_{-1}^{1} x|_{\eta,\xi=\mp 1}^{(i)}\ d\eta) \right. \\
& + K_y\left(G_{zy}b_{1,3}^{(i)}\boldsymbol{W}_3^{(\alpha,\beta)} - \frac{1}{2}\int_{-1}^{1}\left(\frac{E_{zz}y^2}{2} - G_{zy}\nu_{zx}x^2\right)_{\eta,\xi=\mp 1}^{(i)} d\eta\right) \\
& \left. + K_x G_{zy}\boldsymbol{b}_{1,3}^{(\alpha,\beta)}\boldsymbol{W}_2^{(\alpha,\beta)} \right\} n_{y|1,3}^{(i)}
\end{aligned} \tag{4. 76}$$

$$
\begin{aligned}
\hat{t}_{z|2,4}^{(i)} = \Bigg\{ & G_{zx}\theta(\boldsymbol{a}_{\mathbf{2},4}^{(i)}\boldsymbol{W}_1^{(i)} - \frac{1}{2}\int_{-1}^{1} y|_{\eta=\pm1,\xi}^{(i)}\ d\xi) \\
& + K_x\left(G_{zx}\boldsymbol{a}_{2,4}^{(i)}\boldsymbol{W}_2^{(i)} - \frac{1}{2}\int_{-1}^{1}\left(\frac{E_{zz}x^2}{2} - G_{zx}\nu_{zy}y^2\right)_{\eta=\pm1,\xi}^{(i)} d\xi\right) \\
& + K_y G_{zx}\boldsymbol{a}_{1,3}^{(i)}\boldsymbol{W}_3^{(i)}\Bigg\} n_{x|2,4}^{(i)} \\
& + \Bigg\{ G_{zy}\theta(\boldsymbol{b}_{\mathbf{2},4}^{(i)}\boldsymbol{W}_1^{(i)} + \frac{1}{2}\int_{-1}^{1} x|_{\eta=\pm1,\xi}^{(i)}\ d\xi) \\
& + K_y\left(G_{zy}b_{2,4}^{(i)}\boldsymbol{W}_3^{(\alpha,\beta)} - \frac{1}{2}\int_{-1}^{1}\left(\frac{E_{zz}y^2}{2} - G_{zy}\nu_{zx}x^2\right)_{\eta=\pm1,\xi}^{(i)} d\xi\right) \\
& + K_x G_{zy}\boldsymbol{b}_{2,4}^{(\alpha,\beta)}\boldsymbol{W}_2^{(\alpha,\beta)}\Bigg\} n_{y|2,4}^{(i)}
\end{aligned}
\tag{4. 77}
$$

Since the traction is decomposed into three parts factorized by θ, K_x and K_y respectively, the traction decomposition can be illustrated as follows ($p = 1, 2, 3, 4$):

Torsion mode:

$$\hat{t}_{z|p}^{(T)(i)} = G_{zx}\theta\left(\boldsymbol{a}_p^{(i)}\boldsymbol{W}_1^{(i)} - I_{T2p}\right)n_{x|p}^{(i)} + G_{zy}\theta\left(\boldsymbol{b}_p^{(i)}\boldsymbol{W}_1^{(i)} + I_{T1p}\right)n_{y|p}^{(i)} \tag{4. 78}$$

Flexure mode (1):

$$\hat{t}_{z|p}^{(F1)(i)} = K_x\left(G_{zx}\boldsymbol{a}_p^{(i)}\boldsymbol{W}_2^{(i)} - I_{F1p}\right)n_{x|p}^{(i)} + K_x G_{zy}\boldsymbol{b}_p^{(i)}\boldsymbol{W}_2^{(i)} n_{y|p}^{(i)} \tag{4. 79}$$

Flexure mode (2):

$$\hat{t}_{z|p}^{(F2)(i)} = K_y G_{zx}\boldsymbol{a}_p^{(i)}\boldsymbol{W}_3^{(i)} n_{x|p}^{(i)} + K_y\left(G_{zy}\boldsymbol{b}_p^{(i)}\boldsymbol{W}_3^{(i)} - I_{F2p}\right)n_{y|p}^{(i)} \tag{4. 80}$$

where

$$I_{T11}^{(i)} = \frac{1}{2}\int_{-1}^{1} x|_{\eta,\xi=-1}^{(i)}\ d\eta = \frac{x_1 + x_2}{2}, I_{T21}^{(i)} = \frac{1}{2}\int_{-1}^{1} y|_{\eta,\xi=-1}^{(i)}\ d\eta = \frac{y_1 + y_2}{2}$$

$$I_{T12}^{(i)} = \frac{1}{2}\int_{-1}^{1} x|_{\eta=1,\xi}^{(i)}\ d\xi = \frac{x_2 + x_3}{2}, I_{T22}^{(i)} = \frac{1}{2}\int_{-1}^{1} y|_{\eta=1,\xi}^{(i)}\ d\xi = \frac{y_2 + y_3}{2}$$

$$I_{T13}^{(i)} = \frac{1}{2}\int_{-1}^{1} x|_{\eta,\xi=1}^{(i)}\ d\eta = \frac{x_3 + x_4}{2}, I_{T23}^{(i)} = \frac{1}{2}\int_{-1}^{1} y|_{\eta,\xi=1}^{(i)}\ d\eta = \frac{y_3 + y_4}{2}$$

$$I_{T14}^{(i)} = \frac{1}{2}\int_{-1}^{1} x|_{\eta=-1,\xi}^{(i)}\ d\xi = \frac{x_1 + x_4}{2}, I_{T24}^{(i)} = \frac{1}{2}\int_{-1}^{1} y|_{\eta=-1,\xi}^{(i)}\ d\xi = \frac{y_1 + y_4}{2}$$

$$I_{F11}^{(i)} = \frac{1}{2}\int_{-1}^{1} \left(\frac{E_{zz}x^2}{2} - G_{zx}\nu_{zy}y^2\right)_{\eta,\xi=-1}^{(i)} d\eta = \frac{E_{zz}}{8}(x_1 + x_2)^2 - \frac{G_{zx}\nu_{zy}}{4}(y_1 + y_2)^2 + \frac{E_{zz}}{24}(x_1 - x_2)^2 - \frac{G_{zx}\nu_{zy}}{12}(y_1 - y_2)^2$$

$$I_{F21}^{(i)} = \frac{1}{2}\int_{-1}^{1} \left(\frac{E_{zz}y^2}{2} - G_{zy}\nu_{zx}x^2\right)_{\eta,\xi=-1}^{(i)} d\eta = \frac{E_{zz}}{8}(y_1 + y_2)^2 - \frac{G_{zy}\nu_{zx}}{4}(x_1 + x_2)^2 + \frac{E_{zz}}{24}(y_1 - y_2)^2 - \frac{G_{zy}\nu_{zx}}{12}(x_1 - x_2)^2$$

$$I_{F12}^{(i)} = \frac{1}{2}\int_{-1}^{1} \left(\frac{E_{zz}x^2}{2} - G_{zx}\nu_{zy}y^2\right)_{\eta=1,\xi}^{(i)} d\xi = \frac{E_{zz}}{8}(x_2 + x_3)^2 - \frac{G_{zx}\nu_{zy}}{4}(y_2 + y_3)^2 + \frac{E_{zz}}{24}(x_2 - x_3)^2 - \frac{G_{zx}\nu_{zy}}{12}(y_2 - y_3)^2$$

$$I_{F22}^{(i)} = \frac{1}{2}\int_{-1}^{1} \left(\frac{E_{zz}y^2}{2} - G_{zy}\nu_{zx}x^2\right)_{\eta=1,\xi}^{(i)} d\xi = \frac{E_{zz}}{8}(y_2 + y_3)^2 - \frac{G_{zy}\nu_{zx}}{4}(x_2 + x_3)^2 + \frac{E_{zz}}{24}(y_2 - y_2)^3 - \frac{G_{zy}\nu_{zx}}{12}(x_2 - x_3)^2$$

$$I_{F13}^{(i)} = \frac{1}{2}\int_{-1}^{1} \left(\frac{E_{zz}x^2}{2} - G_{zx}\nu_{zy}y^2\right)_{\eta,\xi=1}^{(i)} d\eta = \frac{E_{zz}}{8}(x_3 + x_4)^2 - \frac{G_{zx}\nu_{zy}}{4}(y_3 + y_4)^2 + \frac{E_{zz}}{24}(x_3 - x_4)^2 - \frac{G_{zx}\nu_{zy}}{12}(y_3 - y_4)^2$$

$$I_{F23}^{(i)} = \frac{1}{2}\int_{-1}^{1} \left(\frac{E_{zz}y^2}{2} - G_{zy}\nu_{zx}x^2\right)_{\eta,\xi=1}^{(i)} d\eta = \frac{E_{zz}}{8}(y_3 + y_4)^2 - \frac{G_{zy}\nu_{zx}}{4}(x_3 + x_4)^2 + \frac{E_{zz}}{24}(y_3 - y_4)^2 - \frac{G_{zy}\nu_{zx}}{12}(x_3 - x_4)^2$$

$$I_{F14}^{(i)} = \frac{1}{2}\int_{-1}^{1} \left(\frac{E_{zz}x^2}{2} - G_{zx}\nu_{zy}y^2\right)_{\eta=-1,\xi}^{(i)} d\xi = \frac{E_{zz}}{8}(x_4 + x_1)^2 - \frac{G_{zx}\nu_{zy}}{4}(y_4 + y_1)^2 + \frac{E_{zz}}{24}(x_4 - x_1)^2 - \frac{G_{zx}\nu_{zy}}{12}(y_4 - y_1)^2$$

$$I_{F24}^{(i)} = \frac{1}{2}\int_{-1}^{1} \left(\frac{E_{zz}y^2}{2} - G_{zy}\nu_{zx}x^2\right)_{\eta=-1,\xi}^{(i)} d\xi = \frac{E_{zz}}{8}(y_4 + y_1)^2 - \frac{G_{zy}\nu_{zx}}{4}(x_4 + x_1)^2 + \frac{E_{zz}}{24}(y_4 - y_1)^3 - \frac{G_{zy}\nu_{zx}}{12}(x_4 - x_1)^2$$

The last step in the construction of the local stiffness matrix is to express the zero-order coefficients $W_{r(00)}^{(i)}$ in terms of the surface-averaged warping functions. This is achieved by satisfying the third equilibrium equation in the surface-averaged sense. The surface tractions associated with each face of the (i) subvolume are related to each other through the equilibrium equation satisfied in a volume-average sense. Using Gauss Theorem, the equilibrium equation is expressed in terms of surface-averaged traction components,

$$\oint_s \sigma_{jz}^{(T)(i)} n_j^{(i)} ds = \oint_s t_z^{(T)(i)}\ ds = \sum_{p=1}^{4} \hat{t}_{z|p}^{(T)(i)} l_p^{(i)} = 0 \tag{4. 81}$$

$$\oint_s \sigma_{jz}^{(F1)(i)} n_j^{(i)} ds = \oint_s t_z^{(F1)(i)}\ ds = \sum_{p=1}^{4} \hat{t}_{z|p}^{(F1)(i)} l_p^{(i)} = -\iint_{(i)} K_x E_{zz} x\ dx\ dy \tag{4. 82}$$

$$\oint_s \sigma_{jz}^{(F2)(i)} n_j^{(i)} ds = \oint_s t_z^{(F2)(i)}\ ds = \sum_{p=1}^{4} \hat{t}_{z|p}^{(F2)(i)} l_p^{(i)} = -\iint_{(i)} K_y E_{zz} y\, dx\, dy \tag{4. 83}$$

where s is the contour of subvolume (i) boundary.

Expanding the summation equations Eqs. (4. 81), (4. 82), (4. 83), for the surface-averaged tractions multiplied by the corresponding length over each subvolume contour, the following relations are obtained between the surface-averaged potential functions on each of the four subvolume faces and the zero-order coefficient $W_{r(00)}^{(i)}$, in terms of the surface-averaged potential functions for each mode,

Torsion mode:

$$W_{1(00)}^{(i)} = \frac{\boldsymbol{A}_h^{(i)} \boldsymbol{\alpha} \omega_1^{(i)}}{2A_h^{(i)} \boldsymbol{\beta}} \tag{4. 84}$$

where $\boldsymbol{A}_h^{(i)} = \sum_{p=1}^{4} G_{zx}\, l_p^{(i)} n_{x|p}^{(i)} \boldsymbol{a}_p^{(i)} + \sum_{p=1}^{4} G_{zy}\, l_p^{(i)} n_{y|p}^{(i)} \boldsymbol{b}_p^{(i)}$.

Flexure mode (1):

$$W_{2(00)}^{(i)} = \frac{\boldsymbol{A}_h^{(i)} \boldsymbol{\alpha} \omega_2^{(i)} - \lambda_1}{2A_h^{(i)} \boldsymbol{\beta}} \tag{4. 85}$$

where $\lambda_1 = \sum_{p=1}^{4} l_p^{(i)}\, I_{F1p}^{(i)} n_{x|p}^{(i)} - \iint_{(i)} E_{zz}\, x\, dx\, dy$.

Flexure mode (2):

$$W_{3(00)}^{(i)} = \frac{\boldsymbol{A}_h^{(i)} \boldsymbol{\alpha} \omega_3^{(i)} - \lambda_2}{2A_h^{(i)} \boldsymbol{\beta}} \tag{4. 86}$$

where $\lambda_2 = \sum_{p=1}^{4} l_p^{(i)}\, I_{F2p}^{(i)} n_{y|p}^{(i)} - \iint_{(i)} E_{zz}\, y\, dx\, dy$.

Substituting the first and second-order coefficient expressions Eq. (4. 73) into the surface-averaged traction components in the z direction acting on the four edges of the subvolume Eqs. (4. 78), (4. 79), (4. 80), the surface-averaged traction components are obtained solely in terms of the corresponding surface-averaged potential functions, related through the local stiffness matrix,

Torsion mode:

$$\begin{bmatrix} \hat{t}_{z|1}^{(T)} \\ \hat{t}_{z|1}^{(T)} \\ \hat{t}_{z|1}^{(T)} \\ \hat{t}_{z|1}^{(T)} \end{bmatrix}^{(i)} = \begin{bmatrix} L_{11} & L_{12} & L_{13} & L_{14} \\ L_{21} & L_{22} & L_{23} & L_{24} \\ L_{31} & L_{32} & L_{33} & L_{34} \\ L_{41} & L_{42} & L_{43} & L_{44} \end{bmatrix}^{(i)} \begin{bmatrix} \widehat{\omega}_{1|1} \\ \widehat{\omega}_{1|2} \\ \widehat{\omega}_{1|3} \\ \widehat{\omega}_{1|4} \end{bmatrix}^{(i)} + \begin{bmatrix} C_{T|1} \\ C_{T|2} \\ C_{T|3} \\ C_{T|4} \end{bmatrix}^{(i)} \tag{4. 87}$$

where $L_{p:} = \frac{\theta}{2}\left(G_{zx}\boldsymbol{a_p}n_{x|p} + G_{zy}\boldsymbol{b_p}n_{y|p}\right)\left(\boldsymbol{\alpha} - \frac{\boldsymbol{\beta}\boldsymbol{A_h}\boldsymbol{\alpha}}{\boldsymbol{A_h}\boldsymbol{\beta}}\right)$ **(**$\boldsymbol{L}_{p:}$ stands for the pth row vector in $[\boldsymbol{L}]$**)**

and $C_{T|p} = -G_{zx}\theta I_{T2p}n_{x|p} + G_{zy}\theta I_{T1p}n_{y|p}$.

Flexure mode (1):

$$\begin{bmatrix} \hat{t}_{z|1}^{(F1)} \\ \hat{t}_{z|1}^{(F1)} \\ \hat{t}_{z|1}^{(F1)} \\ \hat{t}_{z|1}^{(F1)} \end{bmatrix}^{(i)} = \begin{bmatrix} M_{11} & M_{12} & M_{13} & M_{14} \\ M_{21} & M_{22} & M_{23} & M_{24} \\ M_{31} & M_{32} & M_{33} & M_{34} \\ M_{41} & M_{42} & M_{43} & M_{44} \end{bmatrix}^{(i)} \begin{bmatrix} \widehat{\omega}_{2|1} \\ \widehat{\omega}_{2|2} \\ \widehat{\omega}_{2|3} \\ \widehat{\omega}_{2|4} \end{bmatrix}^{(i)} + \begin{bmatrix} C_{F1|1} \\ C_{F1|2} \\ C_{F1|3} \\ C_{F1|4} \end{bmatrix}^{(i)} \tag{4. 88}$$

where $M_{p:} = \frac{K_x}{2}\left(G_{zx}\boldsymbol{a_p}n_{x|p} + G_{zy}\boldsymbol{b_p}n_{y|p}\right)\left(\boldsymbol{\alpha} - \frac{\boldsymbol{\beta}\boldsymbol{A_h}\boldsymbol{\alpha}}{\boldsymbol{A_h}\boldsymbol{\beta}}\right)$ **(**$\boldsymbol{M}_{p:}$ stands for the pth row vector in $[\boldsymbol{M}]$**)**

and$C_{F1|p} = K_x(G_{zx}\boldsymbol{a_p}n_{x|p} + G_{zy}\boldsymbol{b_p}n_{y|p})\frac{\boldsymbol{\beta}\lambda_1}{\boldsymbol{A_h}\boldsymbol{\beta}} - K_x I_{T1p}n_{x|p}$.

Flexure mode (2):

$$\begin{bmatrix} \hat{t}_{z|1}^{(F2)} \\ \hat{t}_{z|2}^{(F2)} \\ \hat{t}_{z|3}^{(F2)} \\ \hat{t}_{z|4}^{(F2)} \end{bmatrix}^{(i)} = \begin{bmatrix} N_{11} & N_{12} & N_{13} & N_{14} \\ N_{21} & N_{22} & N_{23} & N_{24} \\ N_{31} & N_{32} & N_{33} & N_{34} \\ N_{41} & N_{42} & N_{43} & N_{44} \end{bmatrix}^{(i)} \begin{bmatrix} \widehat{\omega}_{3|1} \\ \widehat{\omega}_{3|2} \\ \widehat{\omega}_{3|3} \\ \widehat{\omega}_{3|4} \end{bmatrix}^{(i)} + \begin{bmatrix} C_{F2|1} \\ C_{F2|2} \\ C_{F2|3} \\ C_{F2|4} \end{bmatrix}^{(i)} \tag{4. 89}$$

where $\boldsymbol{N}_{p:} = \frac{K_y}{2}\left(G_{zx}\boldsymbol{a_p}n_{x|p} + G_{zy}\boldsymbol{b_p}n_{y|p}\right)\left(\boldsymbol{\alpha} - \frac{\boldsymbol{\beta}\boldsymbol{A_h}\boldsymbol{\alpha}}{\boldsymbol{A_h}\boldsymbol{\beta}}\right)$ **(**$\boldsymbol{N}_{p:}$ stands for the pth row vector in $[\boldsymbol{N}]$**)**

and $C_{F2|p} = K_y(G_{zx}\boldsymbol{a_p}n_{x|p} + G_{zy}\boldsymbol{b_p}n_{y|p})\frac{\boldsymbol{\beta}\lambda_2}{\boldsymbol{A_h}\boldsymbol{\beta}} - K_y I_{T2p}n_{y|p}$.

4.4.3 Global Stiffness Matrix Assembly

The solution for the unknown surface-averaged potential functions is obtained by constructing three systems of equations such that the interfacial potential function and traction continuity conditions are satisfied together with the traction boundary conditions. To maintain the order of the subvolume edges for a general unstructured mesh, each subvolume has four identical surface-averaged potential functions and tractions allocated in the system of equations. The system of equations for the solution of the unknown surface-averaged potential functions, which is comprised of potential function and traction continuity, boundary and constraint conditions, is called the global system.

Similar to the assembly process of the global system described in Chapter 3, the number of connected edges is denoted by N_{con} and the number of unconnected edges is denoted by N_{uncon} from the discretized grid. To solve each global system of equations for the surface-averaged potential functions, the global stiffness matrix is allocated $2N_{con} + N_{uncon}$ columns and $2N_{con} + N_{uncon} + 1$ rows. Each subvolume has four edges with the corresponding number of potential functions and contributes four equations to each global system. Each pair of two connected edges has the same surface-averaged potential functions and equal and opposite tractions, which results in $2N_{con}$ equations for traction and potential function continuity conditions, whereas the unconnected edges only need to satisfy the boundary conditions also in z directions, producing N_{uncon} equations. The breakdown of the $2N_{con} + N_{uncon} + 1$ rows in each global system is given below:

Displacement continuity condition equations

For a pair of connected edges from adjacent subvolumes, the potential function continuity conditions contribute one equation to each global stiffness matrix. p is the edge index from the first subvolume and p' is the edge index from the second subvolume.

$$\widehat{\omega}_p^{(i)} - \widehat{\omega}_{p'}^{(i')} = 0 \tag{4. 90}$$

Traction continuity condition equations

For a pair of connected edges from adjacent subvolumes, the traction continuity conditions contribute one equation each in the z direction to each global stiffness matrix. p is the edge index from the first subvolume and p' is the edge index from the second subvolume.

$$t_{z|p}^{(i)} + t_{z|p'}^{(i')} = 0 \tag{4. 91}$$

$t_{z|p}^{(i)}$ are expressed as linear combinations of surface-averaged displacements in each global system.

Boundary condition equations

For a pair of connected edges from adjacent subvolumes, the traction-free boundary conditions contribute one equation each in the z direction to the global stiffness matrix.

$$\hat{t}_{z|p}^{(i)} = 0 \tag{4. 92}$$

Constraint condition equations

Each global system of equations is singular with the rank of $2N_{con} + N_{uncon}$, thereby requiring an additional constraint that eliminates rigid body motion along the prismatic bar's axis. One approach is to constrain the potential function $\omega(x, y)$ by requiring that $\omega(x, y) = 0$ at the cross section's centroid where the in-plane displacements $u(x, y)$ and $v(x, y)$ vanish. This constraint cannot be employed, however, for hollow cross sections with the centroid located outside the cross section itself. A more general and rigorous fixation condition specifically for the torsion-flexure problem requires the integral of the potential function along the contour of the cross section to vanish,

$$\oint \omega(x, y) ds = \sum s_{(i,p)} \widehat{\omega}_{boundary|p}^{(i)} = 0 \tag{4. 93}$$

where the $s_{(i,p)}$ is the length of the p th edge in subvolume i. Solution of each above augmented global system of equations yields the unknown interfacial surface-averaged displacements which, in turn, yield the corresponding surface-averaged tractions as well as pointwise displacements, strains and stresses in each subvolume.

Solving the three global systems to obtain the three potential functions, one can evaluate the three displacement components in a surface-averaged sense from Eqs. (4. 52), (4. 53), (4. 54) for orthotropic materials or Eqs. (4. 57), (4. 58), (4. 59) for isotropic materials.

4.5 Verification and Assessment

The developed FVM has been verified by comparison with exact elasticity solutions of the flexure of isotropic homogeneous bars with circular, elliptic, and rectangular cross sections, shown in Figure 4-2, with Young's modulus E, Poisson's ratio υ and shear modulus μ. If the cross sections are subjected to the end loading $\left(P_x, P_y\right)$ that passes through the homogeneous bars' centroids, no torsion occurs and hence $\omega_1 = 0$. The following moduli are employed in the flexure analysis of the three cross sections: $E = 30{,}000\ ksi$ and $\nu = 0.3$, with G obtained from the relation $G = \frac{E}{2(1+\nu)}$ and loading by $P_y = 10\ kips$ applied vertically through the centroid.

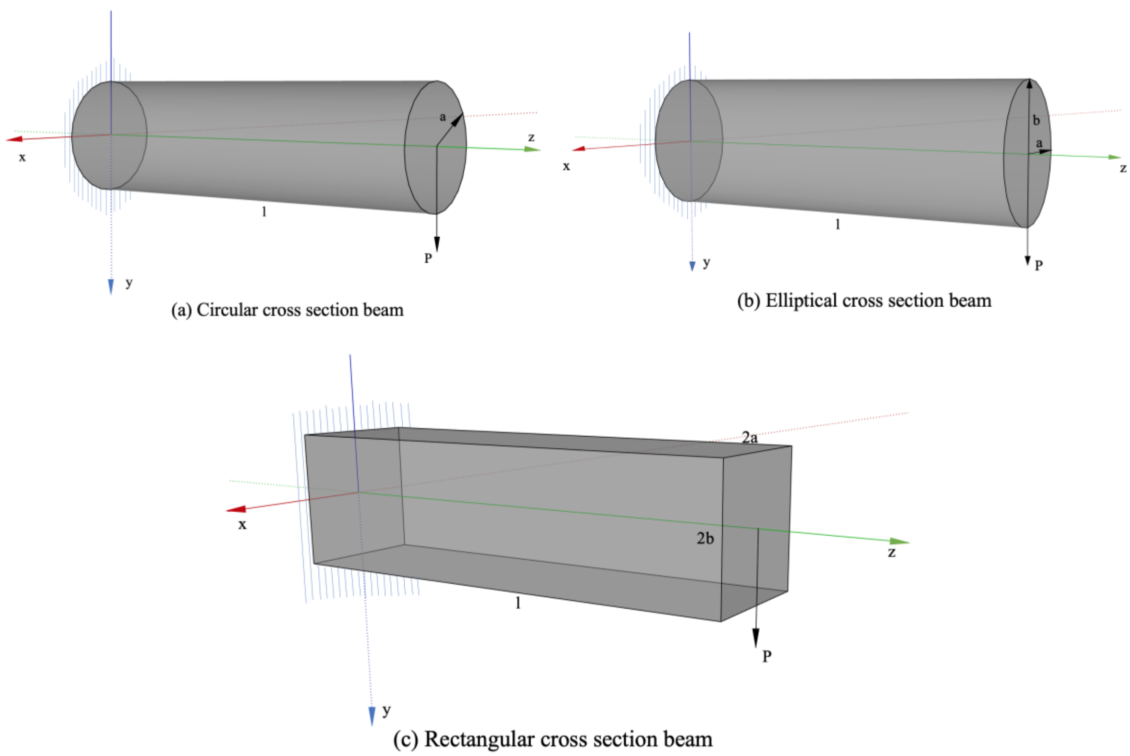

Figure 4-2 Circular (a), elliptic (b) and rectangular (c) cross section beams subjected to load P_y at the free end centroids.

Homogeneous Circular Beams

The boundary of the cross section of the circular bar shown in Figure 4-2 is given by $x^2 + y^2 = a^2$. The radius is taken to be $a = 2\ in$ and the length $l = 40\ in$ which produce the aspect ratio $l/(2a) = 10$. Solving this elasticity problem in the polar coordinate system with a vertical loading force of a magnitude of P applied at the free end by setting $P_y = P$, the two existing shear stresses are found to be,

$$\sigma_{zx} = -\frac{(1+2\nu)P}{\pi a^4(1+\nu)}xy \tag{4. 94}$$

$$\sigma_{zy} = \frac{(3+2\nu)P}{2\pi a^4(1+\nu)}\left(a^2 - y^2 - \frac{1-2\nu}{3+2\nu}x^2\right) \tag{4. 95}$$

with the normal axial stress,

$$\sigma_{zz} = -\frac{4P}{\pi a^4}(l-z)y \tag{4. 96}$$

The three stress distributions obtained from the elasticity solutions are illustrated in Figure 4-3 at $z = 20\ in$, or halfway along the bar's axis, with the corresponding distributions generated using the developed FVM shown in Figure 4-4. The full-field stress distributions generated by FVM are then compared with the corresponding elasticity results at the same locations. The differences between FVM and elasticity point-wise stress values calculated in the middle of each subvolume, and normalized by the maximum value of the elasticity results, are plotted in Figure 4-5, demonstrating excellent accuracy of FVM.

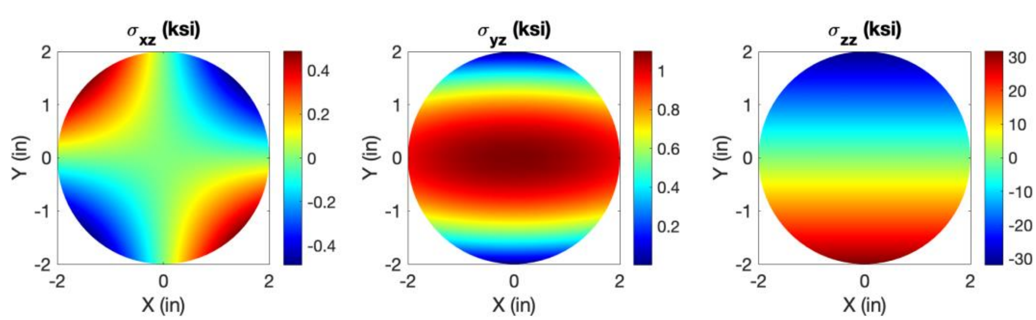

Figure 4-3 The distribution of stress for the circular beam at half-cut calculated by elasticity formulae with point load applied at the center of free end

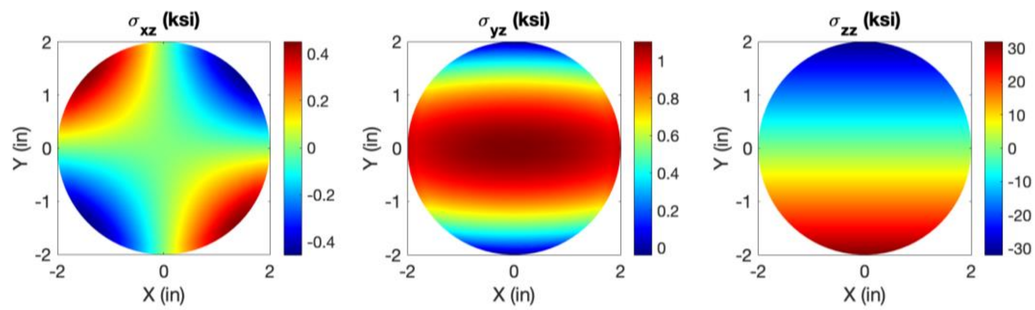

Figure 4-4 The distribution of stress for the circular beam at half-cut calculated by FVM (684 subvolumes) with point load applied at the center of free end

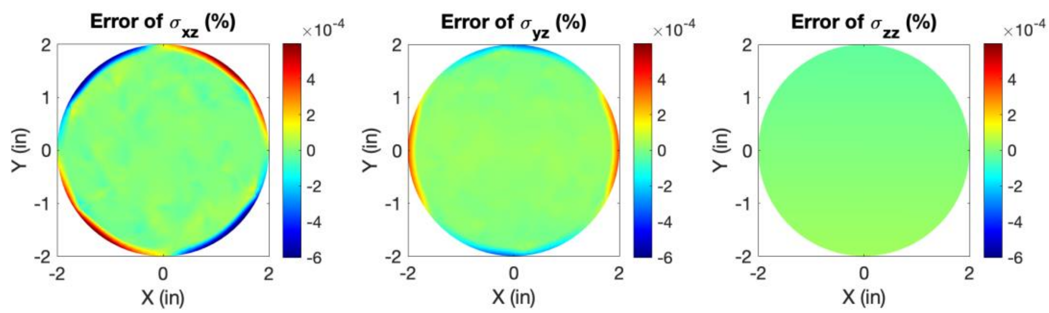

Figure 4-5 The difference of stress distribution for the circular beam at half-cut with point load applied at the center of free end between FVM and elasticity method

Homogeneous Elliptic Beams

Similarly, for a bar whose cross section is given by the equation $\frac{x^2}{a^2}+\frac{y^2}{b^2}=1$, the shear stresses obtained from the elasticity solution are obtained in the form given below with a vertical loading force of a magnitude of P applied at the free end by setting $P_y = P$,

$$\sigma_{zx} = -\frac{4P}{\pi b^3 a}\frac{(1+\nu)b^2+\nu a^2}{(1+\nu)(3b^3+a^2)xy} \tag{4. 97}$$

$$\sigma_{zy} = \frac{2P}{\pi b^3 a}\frac{2(1+\nu)b^2+a^2}{(1+\nu)(3b^3+a^2)}\left[b^2-y^2-\frac{(1-2\nu)b^2}{2(1+\nu)b^2+a^2}x^2\right] \tag{4. 98}$$

with the normal axial stress,

$$\sigma_{zz} = -\frac{4P}{\pi b^3 a}(l - z)y \tag{4. 99}$$

This solution reduces to the circular case if $a = b$. One can take $a = 1\ in$, $b = 2\ in$, and $l = 40\ in$ and generate full-field stress distributions at $z = 20\ m$ shown in Figure 4-6. The corresponding full-field stress distributions generated by FVM are illustrated in Figure 4-7 for comparison with the elasticity results at the same locations. The differences between FVM and elasticity results calculated in the middle of each subvolume, and normalized by the maximum value in the elasticity results, are plotted in Figure 4-8, again demonstrating FVM's excellent predictive capability.

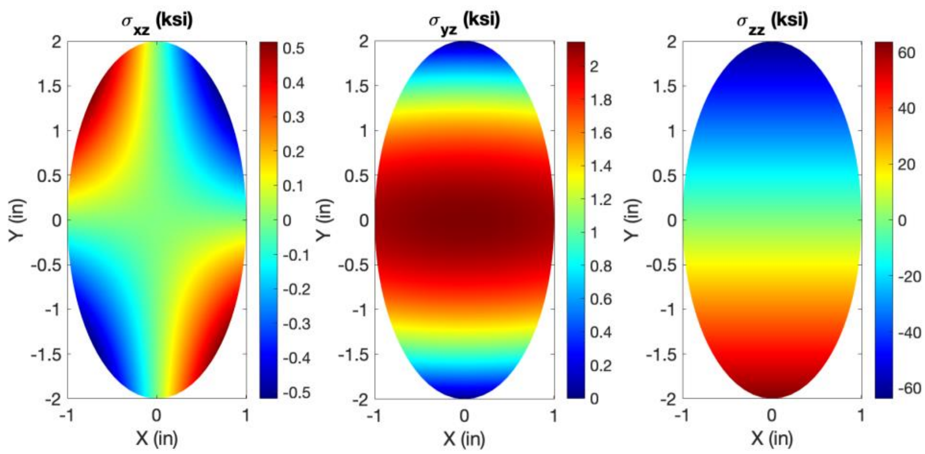

Figure 4-6 The distribution of stress for the elliptic beam at half-cut calculated by elasticity formulae with point load applied at the center of free end

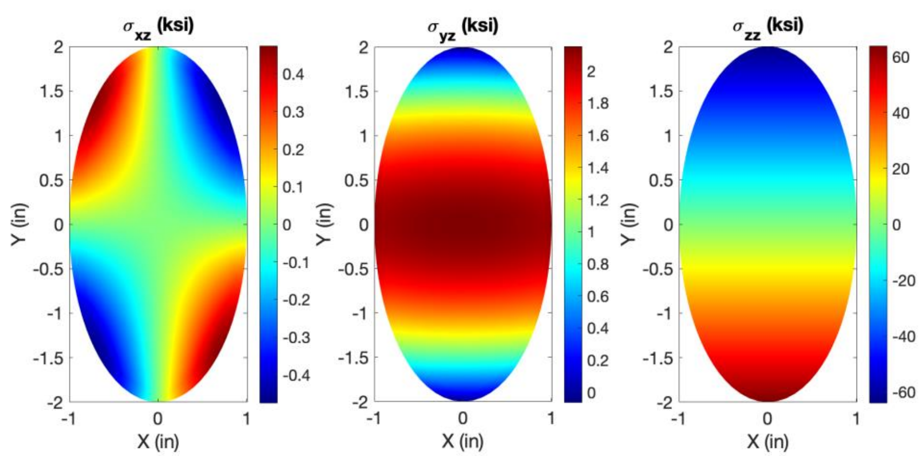

Figure 4-7 The distribution of stress for the elliptic beam at half-cut calculated by FVM (526 subvolumes) with point load applied at the center of free end

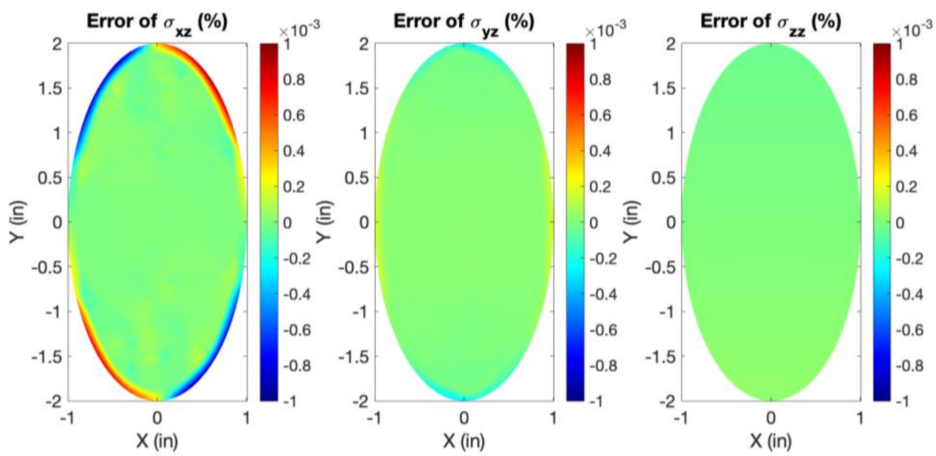

Figure 4-8 The difference of stress distribution for the elliptic beam at half-cut with point load applied at the center of free end between FVM and elasticity method

Homogeneous Rectangular Beams

The last comparison between elasticity and FVM results in this chapter is presented for a rectangular beam with $2a \times 2b$ cross section. The elasticity solution to this problem is obtained in the form of Fourier series for the out-of-plane shear stress components when the applied load is a vertical loading force of a magnitude of P applied at the free end, i.e., $P_y = P$.

$$\sigma_{xz} = \frac{2\nu a^2 P}{(1+\nu)\pi^2 I_{xx}} \sum_{n=1}^{\infty} \frac{(-1)^n}{n^2} \frac{sin\left(\frac{n\pi x}{a}\right) sinh\left(\frac{n\pi y}{a}\right)}{cosh\left(\frac{n\pi b}{a}\right)} \tag{4. 100}$$

$$\sigma_{yz} = \frac{P}{2I_{xx}}(b^2 - y^2) + \frac{\nu P}{6(1+\nu)I_{xx}}\left[3x^2 - a^2 - \frac{12a^2}{\pi^2}\sum_{n=1}^{\infty}\frac{(-1)^n}{n^2}\frac{cos\left(\frac{n\pi x}{a}\right) cosh\left(\frac{n\pi y}{a}\right)}{cosh\left(\frac{n\pi b}{a}\right)}\right] \tag{4. 101}$$

with the normal stress the same as before,

$$\sigma_{zz} = -\frac{P}{I_{xx}} y(l - z) \tag{4. 102}$$

where I_{xx} is the area moment of inertia of each cross section, $I_{xx} = \frac{(2b)^3(2a)}{12}$. The displacement components are obtained by integrating the strain-displacement equations in the form below upon fixing the centroid of left face of the beam,

$$u = \frac{\nu P y(l - z)x}{EI_{xx}} \tag{4. 103}$$

$$v = \frac{\nu P(l - z)(y^2 - x^2)}{2EI_{xx}} - \frac{P\left(l - \frac{z}{3}\right)z^2}{2EI_{xx}} \tag{4. 104}$$

$$w = \frac{Py\left(\frac{z^2}{2} - lz + \nu\frac{x^2}{2} + \nu\frac{y^2}{6} - \nu\frac{a^2}{3}\right)}{I_{xx}E} + \frac{P\left(b^2 y - \frac{y^3}{3}\right)}{2I_{xx}\mu} + \frac{2\nu a^2 P}{(1+\nu)\pi^2 I_{xx}\mu}\sum_{n=1}^{\infty}\frac{(-1)^{n+1}}{n^2}\frac{a\cos\left(\frac{n\pi x}{a}\right)\sinh\left(\frac{n\pi y}{a}\right)}{n\pi\cosh\left(\frac{n\pi b}{a}\right)} \tag{4. 105}$$

Using a 50-term series, distributions of shear stresses and displacements have been calculated for a rectangular beam with the dimensions $a = 1\ in$, $b = 2\ in$, and $l = 40\ in$ at $z = 20\ in$. The stress and displacement fields obtained from the elasticity solutions are illustrated in Figure 4-9 and Figure 4-10, respectively. The corresponding finite-volume results generated using a square grid with 512 subvolumes are shown in Figure 4-11 and Figure 4-12. The full-field stress and displacement fields generated by FVM may be then compared against those evaluated at the same locations by the elasticity expressions.

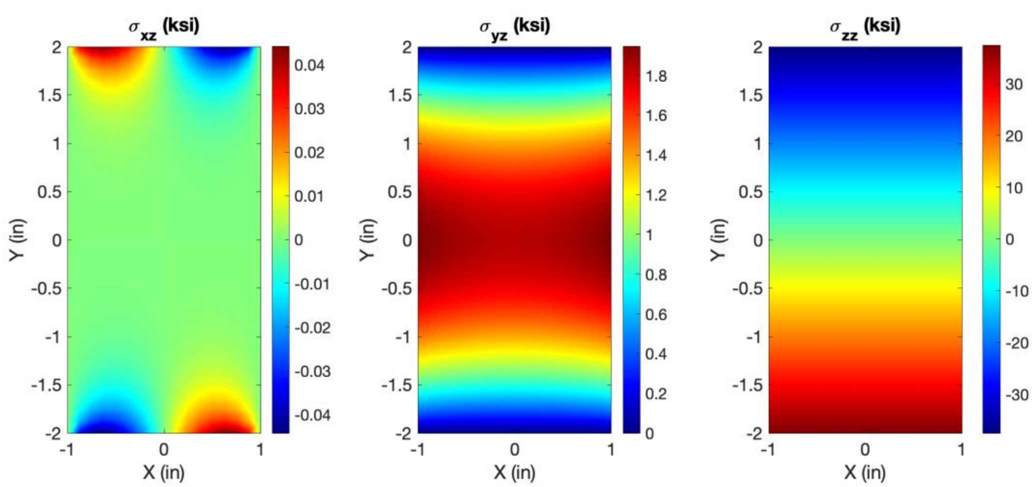

Figure 4-9 The distribution of stress for the rectangular beam at half-cut calculated by elasticity formulae with point load applied at the center of free end

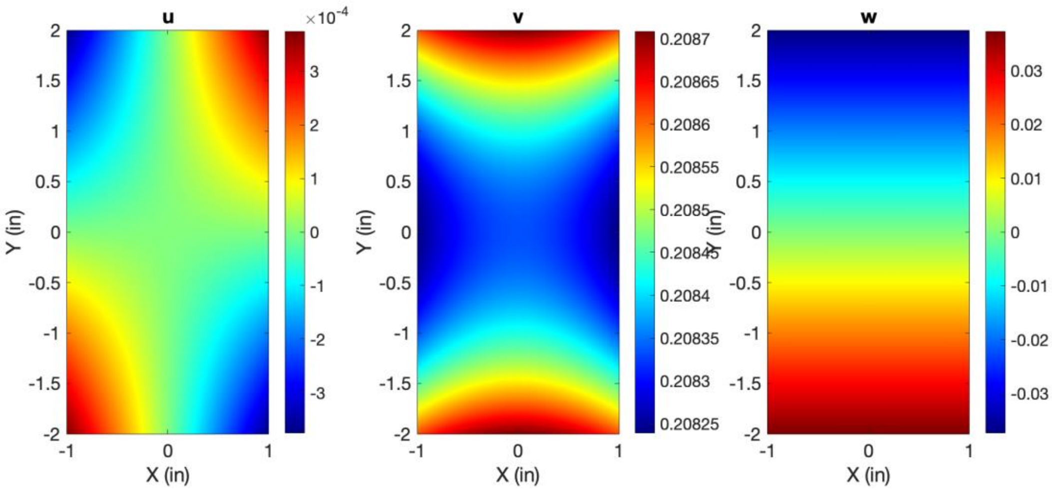

Figure 4-10 The distribution of displacement for the rectangular beam at half-cut calculated by elasticity formulae with point load applied at the center of free end

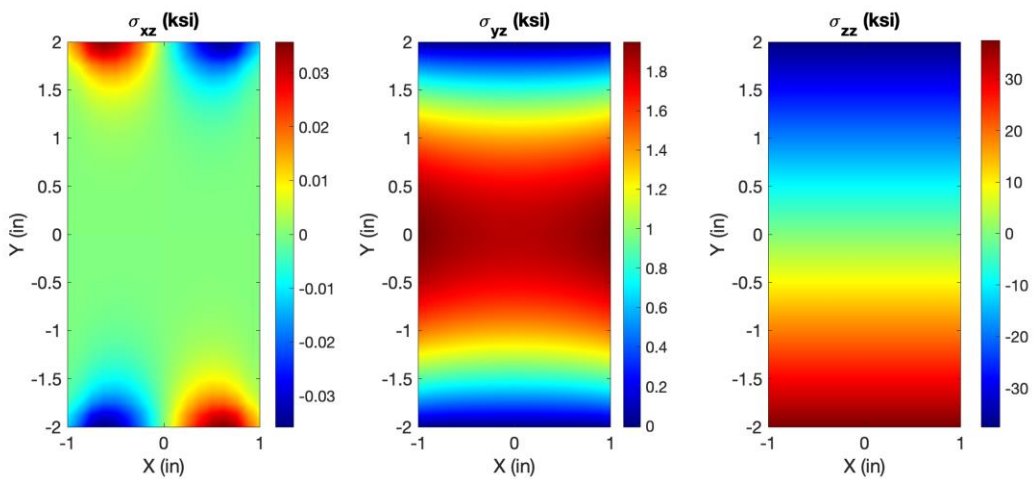

Figure 4-11 The distribution of stress for the rectangular beam at half-cut calculated by FVM with point load applied at the center of free end

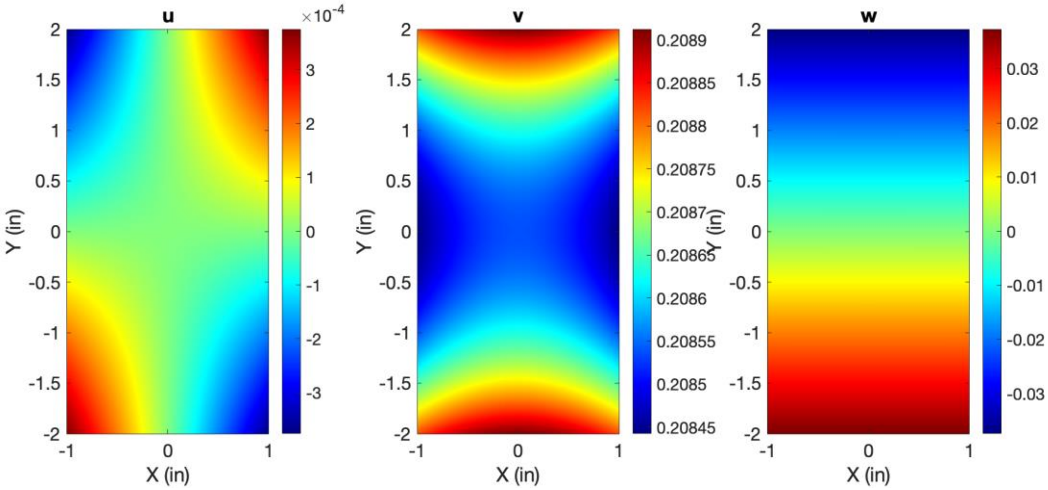

Figure 4-12 The distribution of displacement for the rectangular beam at half-cut calculated by FVM with point load applied at the center of free end

The differences in the point-wise stress and displacement values calculated in the middle of each subvolume, and normalized by the maximum value in the elasticity results, are plotted in Figure 4-13 and Figure 4-14, respectively. As observed, the differences in the displacement and stress fields are generally minimal, with σ_{xz} and w exhibiting greater deviations than the other stress or displacement components.

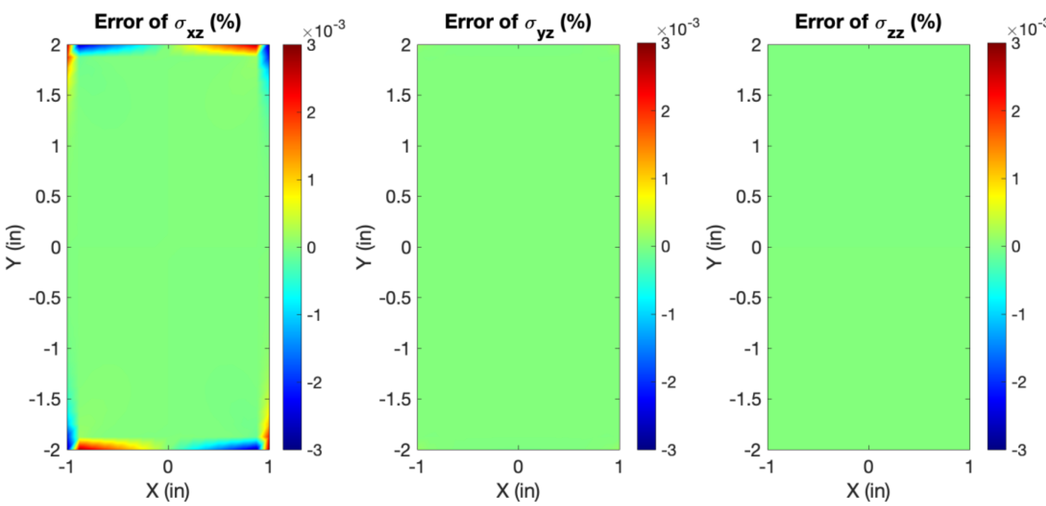

Figure 4-13 The difference of stress distribution for the rectangular beam at half-cut with point load applied at the center of free end between FVM and elasticity method

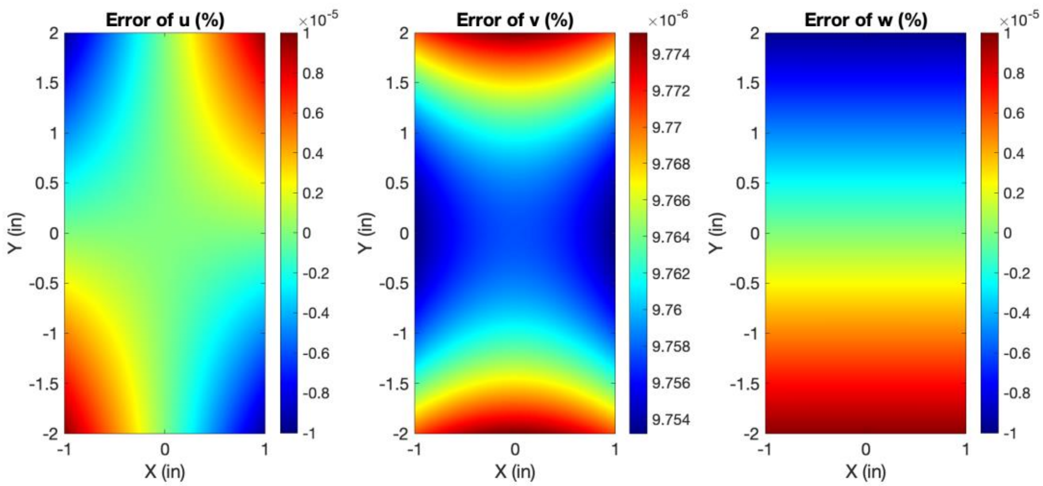

Figure 4-14 The difference of displacement distribution for the rectangular beam at half-cut with point load applied at the center of free end between FVM and elasticity method

4.6 Summary

The analysis of the elastic beam resulting from the intersection of a cylindrical surface with a pair of planes normal to the axis of the cylinder and loaded forces on its end face is a well-known problem in engineering. The Saint-Venant semi-inverse method provides a framework for assuming stress distributions that lead to solutions satisfying the equilibrium and compatibility conditions for this problem. The loading may involve pure bending, or a combination of bending and torsion typically known as torsion-flexure problems. In order to decouple the torsion-flexure problem into pure torsion and bending problems, a point must be found through which a prismatic bar, fixed at one end and loaded at the other, may be loaded to produce pure bending. This point is known as the shear center and plays a crucial role in designing cantilever beams. Chapter 5 will illustrate how the proposed FVM will be employed to determine the shear center location of beam cross sections of technological interest.

Analytical solutions have been developed for torsion-flexure problems, but they are limited to simple cross sections that are typically not of wide-ranging structural engineering interest. Beam cross sections that appear in structural designs are not easily amenable to analytical techniques and require either thin-wall approximations when applicable or numerical solutions. Of the several available numerical approaches, FEM has become the dominant solution technique for torsion-flexure problems because of its generality in handling structural components with arbitrary cross sections. In this chapter, FVM has been developed to formulate the solution of the full torsion-flexure problem as an alternative to the finite-element analysis. Validation of the FVM includes specialized comparison with pure bending results obtained by analytical methods for homogeneous beam problems. The full potential of the FVM will be further demonstrated through applications to structural engineering problems wherein shear center identification plays an important design role, critical analysis of errors involving thin-wall assumptions, and finally three-dimensional effects that arise due to fixity constraints in Chapter 6.

Chapter 5

Shear Center Determination

5.1 Introduction

One of the key tasks in structural engineering is the determination of the location of twist and shear centers in a structural member. The twist center and shear center are two crucial properties that play essential roles in the behavior and performance of a structural member, especially for the one subjected to both torsional and flexural loading. The twist center of a structural member is defined as the point about which the member twists or rotates when it is subjected to torsion. The location of the twist center depends on the member's cross-sectional geometry and material properties. The shear center of a structural member, on the other hand, is the point through which the applied flexural load can be transferred without inducing any torsional moments. The location of the shear center also depends on the member's cross-sectional geometry and material properties. Flexural loadings not applied through the shear center of a structural member may cause issues in stability and strength due to the induced twisting behavior.

Therefore, accurate determination of twist and shear centers is always very critical for the reliable design of structural systems as they may significantly affect the decision of the locations of external loadings applied on structural members. Accurately predicting these centers can be challenging; however, different methods have been proposed in the literature.

Several researchers have investigated the concept of twist and shear centers in structural engineering. In the 20th century, Timoshenko and Gere (1961) proposed a method for determining the location of the shear center of thin-walled open sections based on the principle of virtual work. A set of equations that determine the shear center location for sections with arbitrary shapes have been derived. Later, Chen and Atsuta (1972) proposed a method for determining the shear center location of doubly symmetric sections of arbitrary shapes. They introduced the concept of the auxiliary torsion constant, which could be used to determine the shear center location for sections with curved or asymmetrical shapes.

In recent years, there has been some progress in the determination of the shear center of structural systems. Researchers have proposed numerical methods and techniques to achieve more accurate and efficient determination of the shear center location. Friedman and Kosmatka (1998) employed the Boundary Element Method (BEM) to analyze the torsion and flexure behavior of a prismatic isotropic beam. Their study demonstrates the effectiveness of the BEM approach in accurately predicting stress and deformation of the beam as well as its shear center location, by developing a Fortran-based computer program for designing and optimizing beam structures. Dhadwal and Jung (2015) introduced a refined sectional analysis method to predict the shear center of nonhomogeneous anisotropic beams with nonuniform warping. Their proposed method, which exhibits good agreement with experimental data and accounts for material heterogeneity and warping, was applied to helicopter and wind turbine blade analysis. The refined sectional analysis method is a two-dimensional finite element method which offers an efficient alternative to the high-cost 3D finite element analysis.

This chapter aims to investigate the concept of the shear center in detail using the previously developed FVM, including its definition, determination, and practical applications. In particular, it will focus on the development of accurate and efficient methods for determining the location of shear centers for various types of long structural members by analyzing their cross-sectional behavior. In the previous chapter, FVM has been applied to the solution of torsion-flexure elasticity problems, which also includes the technologically important determination of the shear center of any structural member with arbitrarily shaped cross section. The FVM will be validated through numerical simulation tests in identifying the locations of shear centers, thereby contributing to the development of a more reliable and efficient design tool by providing data on shear centers of various structural systems subjected to torsional and flexural loading.

5.2 Twist Center

In Chapter 3, no assumptions were made regarding the location of the origin O of the cylindrical coordinate system or the orientation of the x and y axes. A different choice of the location of the axis of rotation parallel to the z axis may yield a different displacement solution, but not a different solution for stresses, see Sokolnikoff (1956). In a homogenous orthotropic material cross section, if the z' axis is chosen parallel to the z-axis which intersects the $x - y$ plane at some point (x_1, y_1), then the displacements will be,

$$u_1 = -\theta z(y - y_1) \tag{5. 1}$$

$$v_1 = \theta z(x - x_1) \tag{5. 2}$$

$$w_1 = \theta \psi_1(x, y) \tag{5. 3}$$

Calculating stresses that correspond to displacements above yields

$$\sigma_{zy} = G_{zy}\theta(\frac{\partial \psi_1}{\partial y} + x - x_1) \tag{5. 4}$$

$$\sigma_{zx} = G_{zx}\theta\left(\frac{\partial \psi_1}{\partial x} - y + y_1\right) \tag{5. 5}$$

$$\sigma_{xy} = \sigma_{xx} = \sigma_{yy} = \sigma_{zz} = 0 \tag{5. 6}$$

and the substitution of these values in the equations of equilibrium, Eq. (3. 5), shows that the function ψ_1 likewise satisfies the equation

$$G_{zx}\frac{\partial^2 \psi_1}{\partial x^2} + G_{zy}\frac{\partial^2 \psi_1}{\partial y^2} = 0 \tag{5. 7}$$

Moreover, the traction-free boundary condition demands that

$$G_{zx}(\frac{\partial \psi_1}{\partial x} + y_1)\frac{dx}{dn} + G_{zy}(\frac{\partial \psi_1}{\partial y} - x_1)\frac{dy}{dn} = G_{zx}y\frac{dx}{dn} - G_{zy}x\frac{dy}{dn} \tag{5. 8}$$

or

$$G_{zx}\frac{\partial \psi_1}{\partial x}\frac{dx}{dn} + G_{zy}\frac{\partial \psi_1}{\partial y}\frac{dy}{dn} + G_{zx}y_1\frac{dx}{dn} - G_{zy}x_1\frac{dy}{dn} = G_{zx}y\frac{dx}{dn} - G_{zy}x\frac{dy}{dn} \tag{5. 9}$$

The function $\psi_1 + y_1 x - x_1 y$ is weighted harmonic, and since it satisfies the same boundary condition as Eq. (3. 8), it follows from the uniqueness of the Neumann problem, Eq. (4. 32), that the two can differ only by a constant. Thus,

$$\psi_1 = \psi - y_1 x + x_1 y + const \tag{5. 10}$$

A simple calculation making use of Eqs. (5. 4), (5. 5), and (5. 6), shows that the system of stresses obtained by using the function ψ_1 is identical with that obtained by using the function ψ. It also indicates that the displacements in the two cases only differ by a rigid body motion. Therefore, the choice of the location of the rotating axis may be taken arbitrarily without altering stress fields in torsion problems, and we call the point about which the bar rotates the *twist center*.

Though the coordinate system can be set up with any origin yielding consistent stresses, one thing which needs additional attention is that the torsional analysis performed in Chapter 3 was always based on the rotation about the cross-section's centroid. The reason for locating the axis of rotation coincident with the centroid is to minimize the torsional rigidity apart from consideration of the warping effect. The smaller the torsional rigidity of a cross section, the greater its torsional deformation which typically is the focus of minimization. Equation (3. 13) exhibits a linear relationship between the torque M and the torsional rigidity D with the angle of twist per unit length θ as the proportionality constant. The torque M is produced by the shear stresses σ_{zy} and σ_{zx},

$$M = \iint_R \left(x\sigma_{zy} - y\sigma_{zx}\right) dxdy = \theta D = \theta \iint_R \left[G_{zy}x(\frac{\partial\psi_1}{\partial y} + x) - G_{zx}y\left(\frac{\partial\psi_1}{\partial x} - y\right)\right] dxdy \quad (5.\ 11)$$

Since the warping effect is usually not as significant as the rotational effect, the warping contribution to the torque may be neglected, yielding the reduced torque M',

$$M' = \theta D' = \theta \iint_R \left(G_{zy}x^2 + G_{zx}y^2\right) dxdy = \theta G_{zy}I_{xx} + \theta G_{zx}I_{yy} \quad (5.\ 12)$$

which is always at its minimum when the homogeneous bar is rotating about its centroid axis (I_{xx} and I_{yy} are also at their minimum) with a given angle of twist per unit length. For symmetric cross sections, the warping contribution to the torque sums to zero, so the torque equals the reduced torque, i.e., $M = M'$. Thus, the twist center of any symmetric cross section that minimizes torsional rigidity is exactly at its centroid.

For heterogeneous cross sections that are not symmetric, the twist center may be determined by minimizing the reduced torque ($M' = \iint_R (G_{zy}x^2 + G_{zx}y^2)dxdy$) where the shear moduli are included inside the integrals. In this way, the concept of the weighted moment of inertia would need to be considered. However, the twist center is again assumed to coincide with the centroid for heterogeneous cross sections also for convenience instead of optimizing M' based on the specific material distribution. This practice only affects the calculation of resultant torque (commonly just insignificant differences observed), and the stress results remain unchanged.

The torsion-flexure problem in Chapter 4 was separated into three boundary-value problems, two of which deal with flexure deformation and require an exact placement of the cross section in the coordinate system to ensure the existence of solutions. For flexure boundary-value problems of homogenous cross sections, the centroid of the cross section coincides with the coordinate system origin, which presents no issues as it happens to be its twist center to suit the torsion boundary value problems if there is any induced moment about the shear center. The torsion boundary-value problem reflects the pure torsion deformation, whose stress fields do not depend on the location of the twist center even if the cross section is heterogenous. The flexibility of selecting the twist center location, as discussed by Sokolnikoff (1956), validates the approach of splitting the stress expressions into three parts each with a distinct potential function in the stress formulation of the torsion-flexure problem in the same coordinate system, because any selection of twist center preserves stresses due to torsion and only requires rigid body translation in adjusting the torsional displacements based on the actual fixation condition in the overall torsion-flexure problem. Therefore, one may notice that the displacement component expressions in Eqs. (4. 52) – (4. 54) and (4. 57) – (4. 59) may be modified as a result of rigid body translation if the fixed point at the end of the beam does not coincide with the shear center or twist center.

In conclusion, the separation of the torsion-flexure problem into three modes allows to assign the twist center to any point without changing stress results. If the centroid happens to serve as the fixation point at the end of the beam, the twist center can be readily set to coincide with the centroid as well as the origin, and thus Eqs. (4. 52) – (4. 54) and (4. 57) – (4. 59) are still valid without any modification. The approach of solving the torsion-flexure problem with the centers chosen in the manner described above will be extended to the analysis of heterogenous bars with uniform Poisson's ratio in the following section, with their twist and shear centers verified to coincide with the centroids.

5.3 Torsion-Flexure of Heterogenous Bars with Uniform Poisson's Ratio

Chapter 4 describes the solution to the flexure problem of homogenous orthotropic and isotropic beams. In this section, that solution will be extended to composite bars with different materials but with a uniform Poisson's ratio. These composite bars consist of a number of homogenous, isotropic, cylindrical bodies. Each cross section can have parts with different Young's moduli E_j and shear moduli μ_j, yet the Poisson's ratio is the same over the entire area, which has the expression in each material region with the index j:

$$\mu_j = \frac{E_j}{2(1+\nu)} \tag{5. 13}$$

5.3.1 Weighted Centroid

The "weighted centroid" of the cross section can be understood as a special center which is obtained by associating various parts of the cross-section surface densities with the corresponding moduli of elasticity E_j; thus, if the origin of the coordinate system is placed at the weighted centroid, we have,

$$\iint_A Ex\, dxdy = \iint_A Ey\, dxdy = 0 \tag{5. 14}$$

The weighted centroid will now be defined as the moment of inertia, calculated under the same supposition with regard to the Young's moduli of the different parts of the cross-section in a piecewise sense. The weighted moment of inertia I_{yyE} about the y axis in the plane of the cross section is given by,

$$I_{yyE} = \iint_A Ex^2\, dxdy = \sum_j E_j\, I_{yyj} \tag{5. 15}$$

where j is the index of the enclosed parts with different Young's moduli and I_{yj} is the moment of inertia about the y axis. The weighted moment of inertia I_{xxE} about the x axis in the plane of the cross section is given in a similar manner,

$$I_{xxE} = \iint_A Ey^2\, dxdy = \sum_j E_j\, I_{xxj} \tag{5. 16}$$

Lastly, the weighted moment of inertia I_{xyE} in the plane of the cross section is given as

$$I_{xyE} = \iint_A Exy\, dxdy = \sum_j E_j\, I_{xyj} \tag{5. 17}$$

5.3.2 Modified Approach for Heterogeneous Regions

We follow the same manner of applied loading characteristic of the torsion-flexure problem as in Chapter 4, which requires a statically equivalent force equal but opposite at the fixed end in order to satisfy overall beam equilibrium. The lateral surface of the beam is free from external forces, and the body forces are assumed to vanish to simplify the problem formulation. However, this time the origin is placed at the weighted centroid of the left end of the beam, and the x and y axes are orthogonal to each other.

Now consider the case when the beam is heterogeneous with individual components isotropic. Following the semi-inverse method of Saint-Venant involving assumptions on the stress fields as the starting point,

$$\sigma_{xx} = \sigma_{xy} = \sigma_{yy} = 0 \tag{5. 18}$$

the remaining stress fields σ_{zx}, σ_{zy} and σ_{zz} are then chosen such that the equations of equilibrium and compatibility, as well as the boundary conditions, are satisfied. The bending moment M_y that would be produced by the load W_x acting alone, in any cross section z unit distant from the fixed end, is $M_y = W_x(l - z)$. The stress distribution in this cross section is statically equivalent to the moment M_y and W_x. The normal stress in the direction of the beam's axis is then $\sigma_{zz} = -\frac{M_y E_j}{I_{yyE}} x$ due to the M_y bending moment and different Young's moduli of longitudinal fibers or strips, $E_{zz}(x, y)$. A similar conclusion is obtained when considering the axial stress due to the M_x bending moment produced by the force resultant W_x. Thus, in the presence of bending about the two transverse axes by both W_x and W_y, the normal stress along the longitudinal direction is assumed to be,

$$\sigma_{zz} = -E_{zz}(x, y)(l - z)\big(K_x x + K_y y\big) \tag{5. 19}$$

The derivation follows Eqs. (4. 5) - (4. 31) except $E_{zz}(x, y)$ replaces constant E_{zz} for homogeneous materials. Upon verifying that the condition for the existence of a solution for this problem is fulfilled, application of the Green's theorem yields the result,

$$\begin{aligned}\sum_j \int_C \mu_j \left(\frac{\partial \omega_1}{\partial x}\frac{dx}{dn} + \frac{\partial \omega_1}{\partial y}\frac{dy}{dn}\right) ds &= \sum_j \int_C \mu_j (ydy - xdx) \\ &= \sum_j \mu_j \iint_A (0 - 0)dxdy \equiv 0\end{aligned} \tag{5. 20}$$

$$\begin{aligned}\sum_j \int_C \mu_j \left(\frac{\partial \omega_2}{\partial x}\frac{dx}{dn} + \frac{\partial \omega_2}{\partial y}\frac{dy}{dn}\right) ds &= \sum_j \int_C E_j \left[\frac{x^2}{2} - \frac{\nu y^2}{2(1+\nu)}\right] dy \\ &= \sum_j E_j \iint_A xdxdy \equiv 0\end{aligned} \tag{5. 21}$$

$$\begin{aligned}\sum_j \int_C \mu_j \left(\frac{\partial \omega_2}{\partial x}\frac{dx}{dn} + \frac{\partial \omega_2}{\partial y}\frac{dy}{dn}\right) ds &= -\sum_j \int_C E_j \left[\frac{y^2}{2} - \frac{\nu x^2}{2(1+\nu)}\right] dx \\ &= \sum_j E_j \iint_A ydxdy \equiv 0\end{aligned} \tag{5. 22}$$

since the origin is at the weighted centroid of the cross section.

The resultant of the stress σ_{zx} acting on the bar's cross section must equal W_x. Applying the Green's theorem to the area integrals involving ω_2, ω_3, produces the expression for W_x,

$$W_x = K_x I_{yyE} + K_y I_{xyE} \tag{5. 23}$$

Similar to the component W_x of the applied load, one also obtains the expression for W_y,

$$W_y = K_y I_{xxE} + K_x I_{xyE} \tag{5. 24}$$

Solving the system of equation Eq. (5. 23) and Eq. (5. 24) yields the solution,

$$\begin{cases} K_x = \dfrac{W_x I_{xxE} - W_y I_{xyE}}{I_{xxE} I_{yyE} - I_{xyE}^2} \\ K_y = \dfrac{W_y I_{yyE} - W_x I_{xyE}}{I_{xxE} I_{yyE} - I_{xyE}^2} \end{cases} \tag{5. 25}$$

Following the derivation of displacements for homogeneous cross sections, Eqs. (4. 39) - (4. 51) based on the fact that the x, y and z displacements of the origin are fully fixed, the expressions for displacements for piece-wise isotropic heterogeneous cross sections with constant Poisson's ratio are the same as those for homogeneous isotropic cross sections, Eqs. (4. 57) - (4. 59).

5.3.3 Flexure of Concentric Compound Bars

Muskhelishvili (1953) derived the solution for the flexure of a compound circular tube by a transverse force applied to one of its ends. The cross section of this tube consists of two concentric circular rings S_1 and S_2, the first of which surrounds that second one, as shown in Figure 5-1 below.

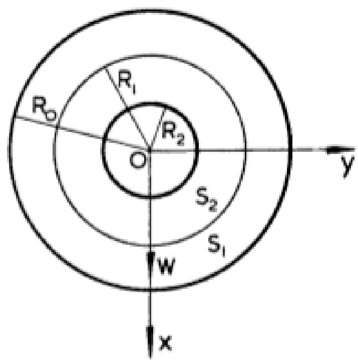

Figure 5-1 Compound circular tube made up with two homogeneous isotropic rings

The inner, middle and outer radii will be denoted by R_2, R_1, R_0, and Young's moduli corresponding to S_1 and S_2 by E_1 and E_2, respectively.

If the transverse force acts through the center of the circles in the positive direction of the x axis, then no torsion takes place as the shear center is at the origin (because the cross section is symmetric about x and y axes. Guided by the form of the stress and displacement expressions for the homogenous bar bending about y axis, the displacements of this flexure problem may be assumed to be satisfied by the following expressions,

$$u = -\theta yz + \frac{W_x}{I_{yyE}}\left[\frac{\nu}{2}(l-z)(x^2-y^2) + \frac{lz^2}{2} - \frac{z^3}{6}\right] \tag{5. 26}$$

$$v = \theta xz + \frac{W_x}{I_{yyE}}\nu(l-z)xy \tag{5. 27}$$

$$w = -\theta\psi - \frac{W_x}{I_{yyE}}\left[x\left(lz - \frac{z^2}{2}\right) + \chi + xy^2\right] \tag{5. 28}$$

where $\chi = \chi(x, y)$ represents some functions that can be found, denoted in regions S_1 and S_2 by χ_1 and χ_2, respectively).

Since the region is circular in the $x - y$ plane, let r and ϑ denote polar coordinates. The governing equation is the same as that of a single layer tube, which is,

$$\left[\frac{\nu x^2}{2} + \left(1 - \frac{\nu}{2}\right)y^2\right]\cos\vartheta + (2 + \nu)xy\sin\vartheta = -\frac{3}{4}r^2\cos 3\vartheta + (\frac{3}{4} + \frac{\nu}{2})\cos\vartheta \tag{5. 29}$$

and the boundary conditions are,

$$\text{for } r = R_0\text{: } \frac{\partial\chi_1}{\partial r} = (\frac{3}{4} + \frac{\nu}{2})R_0^2\cos\vartheta + \frac{3}{4}R_0^2\cos 3\vartheta \tag{5. 30}$$

$$\text{for } r = R_1\text{: } \begin{cases} \chi_1 = \chi_2 \\ E_1\frac{\partial\chi_1}{\partial r} - E_2\frac{\partial\chi_2}{\partial r} = (E_1 - E_1)[-(\frac{3}{4} + \frac{\nu}{2})R_1^2\cos\vartheta + \frac{3}{4}R_1^2\cos 3\vartheta] \end{cases} \tag{5. 31}$$

$$\text{for } r = R_2\text{: } \frac{\partial\chi_2}{\partial r} = -(\frac{3}{4} + \frac{\nu}{2})R_2^2\cos\vartheta + \frac{3}{4}R_2^2\cos 3\vartheta \tag{5. 32}$$

Expanding the harmonic functions χ_1 and χ_2 into series, and substituting in the preceding formulae which satisfy the solution for the hollow homogeneous circular cylinder, these functions are determined in the form,

$$\chi_1 = \left(a_1 r + \frac{a_1'}{r}\right)\cos\vartheta + \frac{r^3}{4}\cos 3\vartheta \qquad (R_1 \le r \le R_0) \tag{5. 33}$$

$$\chi_2 = \left(a_2 r + \frac{a_2'}{r}\right)\cos\vartheta + \frac{r^3}{4}\cos 3\vartheta \qquad (R_2 \le r \le R_1) \tag{5. 34}$$

Substituting these χ_1 and χ_2 expressions in the boundary conditions, all the constants may be obtained. They are listed below,

$$a_1 = -(\frac{3}{4} + \frac{\nu}{2})\frac{E_1(R_0^4 - R_1^4)(R_1^2 + R_2^2) + E_2(R_1^2 - R_2^2)[(R_1^2 + R_2^2)^2 + R_0^4 - R_2^4]}{E_1(R_1^2 + R_2^2)(R_0^2 - R_1^2) + E_2(R_0^2 + R_1^2)(R_1^2 - R_2^2)} \tag{5. 35}$$

$$a_2 = -\left(\frac{3}{4}+\frac{\nu}{2}\right)\frac{E_1(R_0^2-R_1^2)[(R_0^2+R_1^2)^2-R_0^4+R_2^4]+E_2(R_1^4-R_2^4)(R_0^2+R_1^2)}{E_1(R_1^2+R_2^2)(R_0^2-R_1^2)+E_2(R_0^2+R_1^2)(R_1^2-R_2^2)} \tag{5. 36}$$

$$a_1' = a_1R_0^2 + kR_0^4 \tag{5. 37}$$

$$a_2' = a_2R_2^2 + kR_2^4 \tag{5. 38}$$

These steps complete the solution of flexure of a compound two-layer concentric tube.

The developed FVM has been verified by comparison with the above exact elasticity solutions of the flexure of composite bars made of two isotropic materials, with the ratio of Young's modulus of 2, i.e., $E_1{:}E_2 = 2$. If the cross sections are subjected to the end loading $(P_x, 0)$ that passes through the bars' centroids, no torsion occurs and hence $\omega_1 = 0$ and $\omega_2 = 0$. The following moduli are employed in the flexure analysis of the three cross sections: $E_1 = 20{,}000\ ksi$, $E_1 = 10{,}000\ ksi$, and $\nu = 0.3$, with the shear moduli G obtained from the relation $G_j = \frac{E_j}{2(1+\nu)}$ and loading by $P_x = 10\ kips$ applied horizontally through the centroid along the positive direction of the x axis.

To solve the flexure problem for this concentric tube numerically via FVM, 6552 subvolumes are employed with the meshing pattern shown in Figure 5-2, where the inner layer as well as the vicinity of material interface has much higher meshing density than the outer layer.

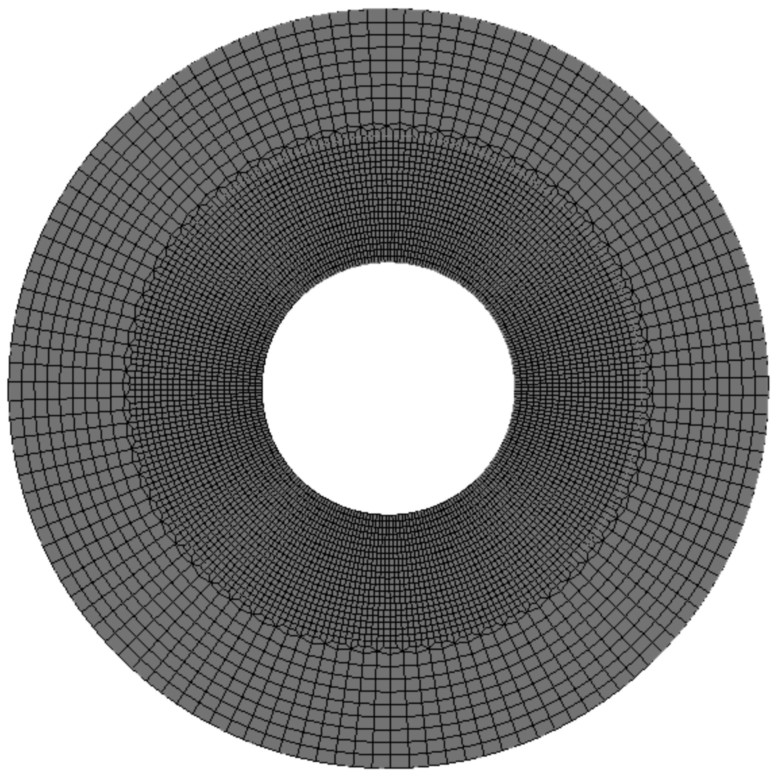

Figure 5-2 Meshing discretization of a concentric tube

The in-plane displacement u, v and w expressed in Eqs. (5. 26), (5. 27), and (5. 28) from Muskhelishvili's analytical approach as well as FVM are shown in Figure 5-3, Figure 5-4, and Figure 5-5.

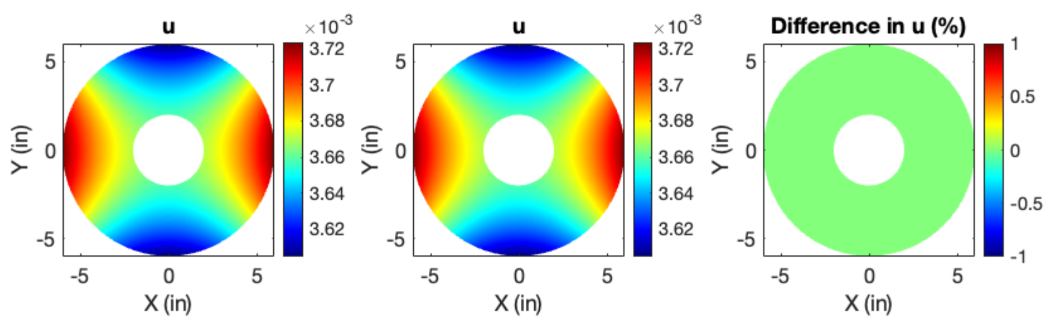

Figure 5-3 u displacement field in the compound concentric tube (left: FVM solution; middle: analytical solution; right: difference in percentage)

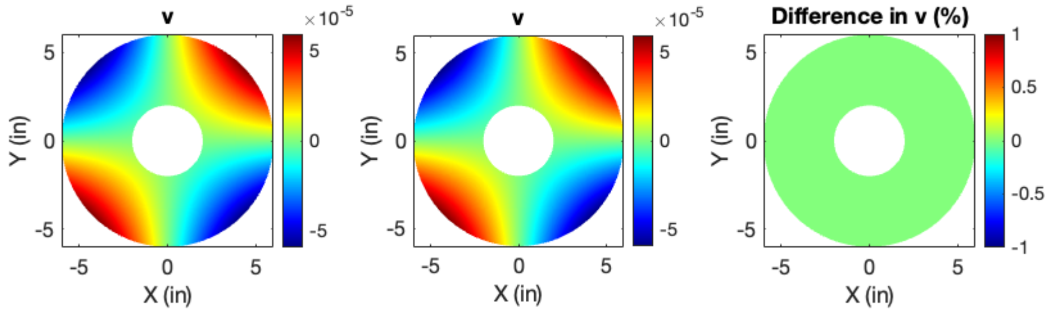

Figure 5-4 *v* displacement field in the compound concentric tube (left: FVM solution; middle: analytical solution; right: difference in percentage)

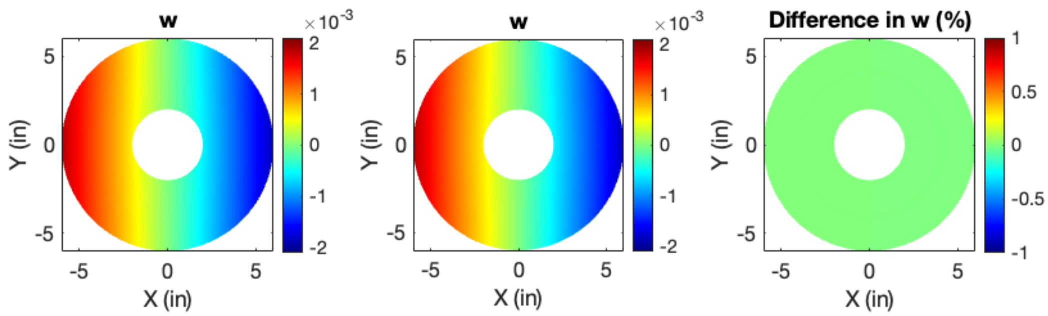

Figure 5-5 *w* displacement field in the compound concentric tube (left: FVM solution; middle: analytical solution; right: difference in percentage)

All three displacement components exhibit very small differences between FVM and analytical solutions, as shown in the third (rightmost) sub-figure in each subsequent set, which is normalized by the maximum value from the analytical solutions.

Substituting χ_1 and χ_2 from Eqs. (5. 33) and (5. 34) respectively to χ in the following stress component expressions, one can compute the stress field analytically for both material regions.

$$\sigma_{zx} = \mu_j\theta\left(\frac{\partial\omega_1}{\partial x} - y\right) - \frac{W_xE_j}{2I_{yyE}(1+\nu)}\left[\frac{\partial\chi}{\partial x} + \frac{\nu}{2}x^2 + \left(1 - \frac{\nu}{2}\right)y^2\right] \tag{5. 39}$$

$$\sigma_{zy} = \mu_j\theta\left(\frac{\partial\omega_1}{\partial y} + x\right) - \frac{W_xE_j}{2I_{yyE}(1+\nu)}\left[\frac{\partial\chi}{\partial y} + (2+\nu)xy\right] \tag{5. 40}$$

$$\sigma_{zz} = -\frac{W_xE_j}{I_{yyE}}(l-z)x \tag{5. 41}$$

The FVM solution also renders the stress field results. Therefore, shear stresses σ_{xz} and σ_{yz}, as well as the normal stress or so-called the bending stress σ_{zz}, obtained from FVM and analytical solutions can also be compared. In general, all of the stress components exhibit small differences between FVM and analytical solutions, as shown Figure 5-6, Figure 5-7, and Figure 5-8. The difference for each stress component is also normalized by the maximum value from the analytical solutions.

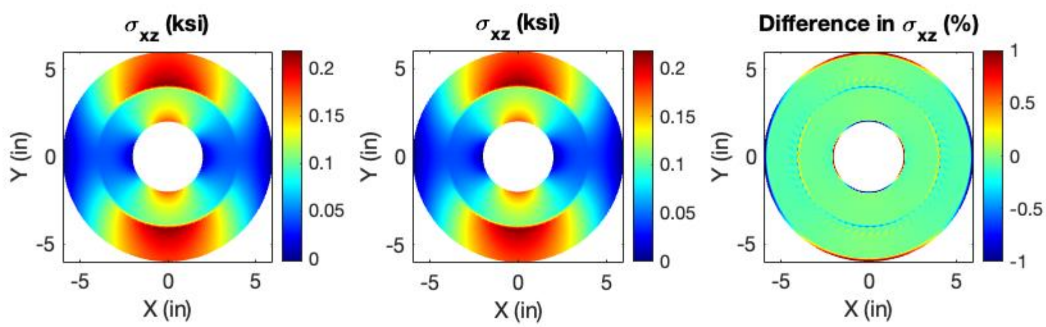

Figure 5-6 Stress fields in the compound concentric tube (left: FVM solution; middle: analytical solution; right: difference in percentage)

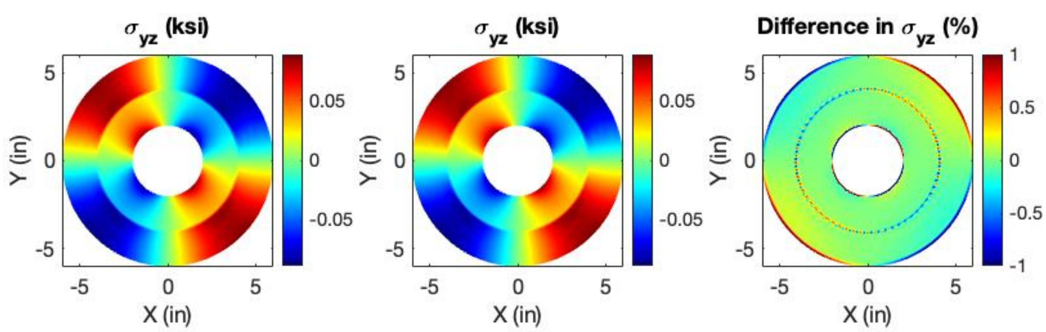

Figure 5-7 Stress fields in the compound concentric tube (left: FVM solution; middle: analytical solution; right: difference in percentage)

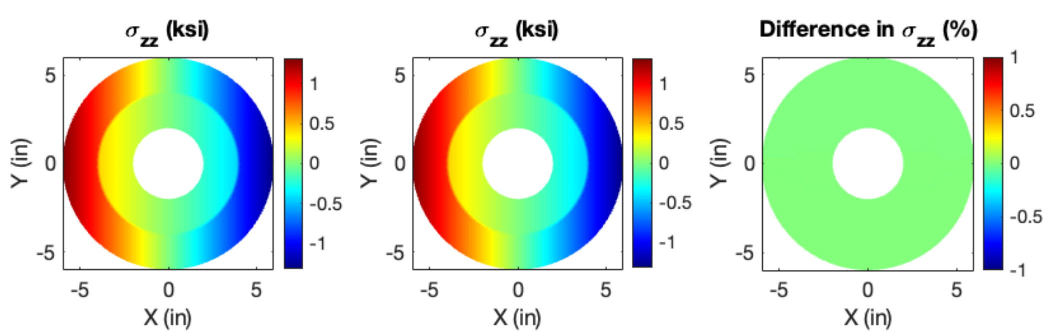

Figure 5-8 Stress fields in the compound concentric tube (left: FVM solution; middle: analytical solution; right: difference in percentage)

The difference between FVM and analytical solution for the bending stress σ_{zz} is consistently small over the entire cross section. While the differences between FVM solutions and analytical solutions for the shear stress σ_{xz} and σ_{yz} are also small in most regions, greater differences occur at the material interfaces and the inner radius faces. These differences may be further reduced through selective mesh refinement in the outer layer region.

5.4 Shear Center Determination

The derived expressions for shear stresses suggest a resolution of the general flexure problem into the following simpler problems: pure flexure problem with zero local twist and pure torsion problem due to a twisting moment. To bend a beam without twisting, the plane of loads must contain the axis of bending; that is the plane of loads must pass through the shear center of every cross section of the beam. *Shear center* is identified as the location in each cross section where the applied load cannot produce any local twist. Shear center is also known as the center of flexure in some books. It is a point in a beam or structure where the application of a transverse load does not cause any twisting or torsion. In other words, it is the point on a beam where the bending and twisting due to transverse loads are separated, and only the bending moment acts.

The determination of shear centers of structural components plays a key role in their design, and accurate determination of the shear center location is crucial for practical application of beams. Kosmatka and Dong (1991) presented a Saint-Venant semi-inverse based Ritz method predicting the location of shear center for homogeneous anisotropic beams. Yu et al. (2002) used the shear coupling stiffness coefficients from the stiffness matrix in the finite-element cross-sectional analysis VABS to predict the shear center location for beams of arbitrary cross-section geometry with specific material distribution.

The concept of a shear center is particularly important for thin-walled structures like beams, plates, and shells. In such structures, shear forces and bending moments are coupled, and the location of the shear center affects the distribution of stresses and deformations. For example, in an airplane wing, the location of the shear center affects the stability of the aircraft during flight. If the shear center is not located at the desired position, the wing may twist under load, causing loss of stability. The shear center is also critical in designing of thin-walled structures subject to torsion, such as hollow drive shafts, where the location of the shear center determines the amount of torque that can be transmitted without causing excessive deformation or failure. Conventionally, the concept of shear flow is employed with proper structural mechanics assumptions for estimating the shear center based on equilibrium considerations. However, in this section, the determination of the shear center will take advantage of the separation of deformation modes in the torsion-flexure problem.

5.4.1 Shear Center for Homogeneous Cross Sections

For a homogeneous beam with a cross section that possesses two axes of symmetry or anti-symmetry, the shear center lies at the intersection of the two axes, whereas in the case of a single plane of symmetry the shear center lies along its axis. Without the local twist ($\theta = 0$), the shear stress components come solely from flexural deformation modes. The resultant moment caused by these shear stresses equals the twisting moment generated by the end resultant forces W_x and W_y,

$$\iint_A (x\sigma_{zy} - y\sigma_{zx})\, dxdy = x_s W_y - y_s W_x \tag{5. 42}$$

So, for homogeneous orthotropic beams, the shear center location is (x_s, y_s), where

$$x_s = J\left(I_{yy}S_2 - I_{xy}S_1\right) \tag{5. 43}$$

$$y_s = J\left(I_{xy}S_2 - I_{xx}S_1\right) \tag{5. 44}$$

and

$$S_1 = \iint_A \left[G_{zy}x\frac{\partial \omega_2}{\partial y} - G_{zx}y\frac{\partial \omega_2}{\partial x} + \frac{E_{zz}}{2}x^2y - G_{zx}\nu_{zy}y^3\right] dx\, dy \tag{5. 45}$$

$$S_2 = \iint_A \left[G_{zy}x\frac{\partial \omega_3}{\partial y} - G_{zx}y\frac{\partial \omega_3}{\partial x} - \frac{E_{zz}}{2}xy^2 + G_{zy}\nu_{zx}x^3\right] dx\, dy \tag{5. 46}$$

$$J = \frac{1}{E_{zz}\left(I_{xx}I_{yy} - I_{xy}^2\right)} \tag{5. 47}$$

$$I_{xx} = \iint_A y^2 \, dx\, dy, I_{yy} = \iint_A x^2 \, dx\, dy, I_{xy} = \iint_A x\, y\, dx\, dy \tag{5. 48}$$

The shear center locations calculated in this section for homogeneous orthotropic materials also reduce to those of homogeneous isotropic materials upon setting $G_{zx} = G_{zy} = \mu$ and $\nu_{zx} = \nu_{zy} = \nu$,

$$S_1 = \iint_A \mu \left[x \frac{\partial \omega_2}{\partial y} - y \frac{\partial \omega_2}{\partial x} + (1+\nu)x^2 y - \nu y^3 \right] dx\, dy \tag{5. 49}$$

$$S_2 = \iint_A \mu \left[x \frac{\partial \omega_3}{\partial y} - y \frac{\partial \omega_3}{\partial x} - (1+\nu)x y^2 + \nu x^3 \right] dx\, dy \tag{5. 50}$$

$$J = \frac{1}{E\left(I_{xx} I_{yy} - I_{xy}^2\right)} \tag{5. 51}$$

$$I_{xx} = \iint_A y^2 \, dx\, dy, I_{yy} = \iint_A x^2 \, dx\, dy, I_{xy} = \iint_A x\, y\, dx\, dy \tag{5. 52}$$

For cross sections with two planes of symmetry, the shear center lies at the intersection of the **two** planes, whereas in the case of a single plane of symmetry the shear center lies along the plane of symmetry. The shear center of an arbitrary homogeneous isotropic or orthotropic cross section may be precisely determined using Eqs. (5. 43) and (5. 44) once the functions ω_2 and ω_3 due to flexure loading are obtained from the developed finite-volume solution strategy. These equations apply to any homogeneous cross section, including open and closed cross sections with thin or thick walls.

Homogeneous Equilateral Triangular Beams

The torsion-flexure problem was previously treated as a boundary-value problem with the introduction of the potential function $F(x, y)$ from which the out-of-plane shear stresses were derived to satisfy the third equilibrium equation, see Eq. (4. 5) or (4. 6) in Chapter 4. The function $F(x, y)$ can be determined by satisfying the Beltrami-Michell equations, Eq. (4. 9). Sokolnikoff (1956) presented another solution approach for the torsion-flexure problem with a new stress function $T(x, y) = F(x, y) - \int R(x)dx - \int S(y)dy$, where the functions $R(x)$ and $S(y)$ are chosen such that the stress expressions with respect to $T(x, y)$ satisfy either a simple boundary condition or a simple differential equation, e.g. $R(x) = -\frac{1}{2}EK_y y^2$ and $S(y) = \frac{1}{2}EK_x x^2$ on the boundary. The introduction of the additional functions $R(x)$ and $S(y)$ enables satisfaction of a constant T value along the boundary contour ($\frac{dT}{ds} = 0$ on C), which is analogous to the deflection of a stretched elastic membrane. This step simplifies the solution process by reducing the number of boundary conditions that need to be satisfied, and leads to a more efficient solution method for the torsion-flexure problem. As one of the results, the location of the shear center can also be related to the function $T(x, y)$ from the stress components in Eq. (5. 42) by substituting $R(x)$ with $-\frac{1}{2}EK_y y^2$ and $S(y)$ with $\frac{1}{2}EK_x x^2$.

$$x_s W_y - y_s W_x = 2\iint_A T(x,y)dxdy - \frac{1}{3}E\left(K_y\int_C xy^3dx + K_x\int_C x^3ydy\right) \tag{5. 53}$$

The coordinates (x_s, y_s) of the shear center are then found by comparing the coefficients of W_x and W_y. For the special case of bending by a load W_x along the x axis (one of the principal axes), the y coordinate of the shear center becomes

$$y_s = -\frac{2}{W_x}\iint_A T(x,y)dxdy + \frac{1}{3I_{yy}}\int_C x^3ydy \tag{5. 54}$$

For the case of a W_x-loaded beam whose cross section is an equilateral triangle, the stress function $T(x, y)$ could be used to solve the torsion-flexure problem. The boundary of an equilateral triangular section with a side length of $2\sqrt{3}a$ can be written as

$$(y-a)\left(x+\frac{2a+y}{\sqrt{3}}\right)\left(x-\frac{2a+y}{\sqrt{3}}\right) = 0 \tag{5. 55}$$

where the origin is taken at the centroid of the cross section shown in Figure 5-9.

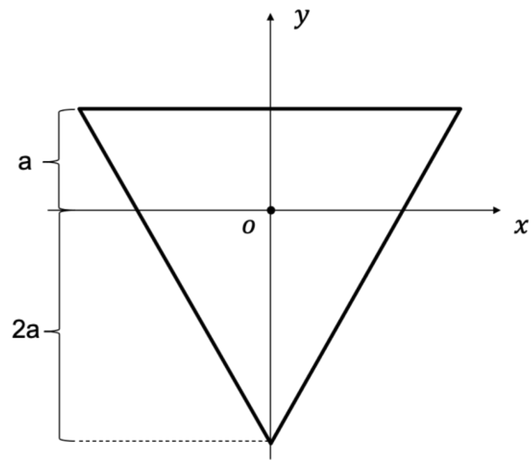

Figure 5-9 The configuration of an equilateral triangular cross section

Straight-forward calculations for several components in Eq. (5. 53) give

$$I_{yy} = \frac{3\sqrt{3}a^4}{2} \tag{5. 56}$$

$$\iint_A T(x,y)dxdy = \frac{3\sqrt{3}W_x a^5}{10 I_{yy}} = \frac{aW_x}{5} \tag{5. 57}$$

$$\int_C x^3 y dy = 2\int_0^{a\sqrt{3}} x^3(\sqrt{3}x - 2a)\sqrt{3}\,dx = \frac{9\sqrt{3}a^5}{5} \tag{5. 58}$$

and thus they yield y coordinate of the shear center as zero by substituting into Eq. (5. 54). Since the equilateral triangle is symmetric about the y axis, the shear center lies on the symmetric y axis. Therefore, its shear center is exactly at the origin in the coordinate system, which is also the centroid for this equilateral triangle.

To assess the accuracy of FVM in predicting the shear center location, a sequence of equilateral triangles of the same dimensions with continuously refined meshes was employed to demonstrate solution convergence with the number of subvolumes, which is illustrated in Figure 5-10. The side length of the equilateral triangle is $3\sqrt{3}$ inches, which is used to normalize the difference in the y coordinate of the shear center between the FVM and analytical solutions. The FVM error against the exact analytical solution decreases roughly exponentially with increasing number of subvolumes employed in the FVM analysis.

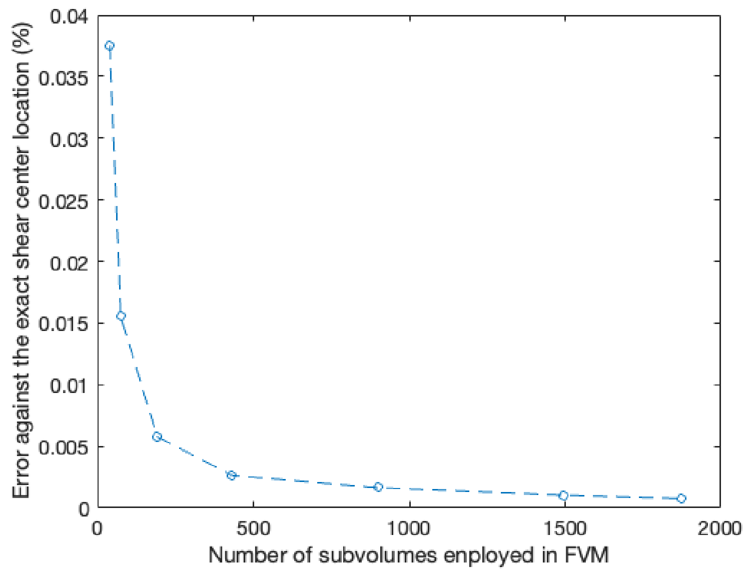

Figure 5-10 The convergence of FVM error in determining the location of an equilateral triangular cross section

Homogeneous Semi-circular Beams

As observed in the previous example, the shear center location of a homogeneous beam with an equilateral triangle coincides with its centroid. As a further illustration of the usefulness of the function $T(x, y)$, the solution of the torsion-flexure problem for a semicircular beam shown in Figure 5-11 becomes available, which highlights the case where the shear center and its centroid are not at the same location.

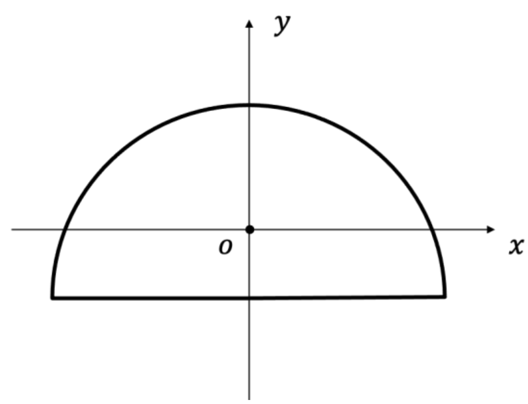

Figure 5-11 The configuration of a semi-circular cross section

If the load is only applied along the x axis direction and the origin O of the coordinate system is chosen at the centroid of each cross section of the semicircular beam, the function $T(x, y)$

satisfies its governing differential equation and vanishes on its boundary. The solution of this problem is given by the uniformly and absolutely convergent series for $T(x, y)$ expressed in the polar coordinate system (r, θ) set up at the middle point of its bottom diameter. The solution for $T(r, \theta)$ is represented by an infinite series below,

$$T(r,\theta) = Ar^3 \cos\theta + Br^2(1 + \cos 2\theta) + \sum_{n=0}^{\infty} A_{2n+1} r^{2n+1} \cos(2n+1)\theta \qquad (5.\ 59)$$

where,

$$A = \frac{1}{8}\frac{W_x}{I_{yy}}\frac{1+2\nu}{1+\nu} \qquad (5.\ 60)$$

$$B = -\frac{1}{4}\left[\frac{W_x}{I_{yy}}\frac{\nu}{1+\nu}\left(y + \frac{4a}{3\pi}\right) + 2\mu a\right] \qquad (5.\ 61)$$

$$\begin{cases} A_1 = -\dfrac{16a}{3\pi}B - a^2 A, \\ A_{2m+1} = \dfrac{a^{-2m-1}16a^2(-1)^m B}{\pi(2m+1)[(2m+1)^2-4]}, \qquad m = 1, 2, 3, \ldots \end{cases} \qquad (5.\ 62)$$

Thus, by substituting Eq. (5. 59) into Eq. (5. 53), the shear center lies on the y axis due to its symmetry, and the y coordinate may be expressed in the following approximate form

$$y_s = \frac{8a}{15(1+\upsilon)\pi}\left[3 + \upsilon\left(\frac{40}{\pi^2} - 1\right)\right] + \frac{4a}{3\pi} \qquad (5.\ 63)$$

To assess the accuracy of FVM in predicting the shear center location, a sequence of continuously refined meshes of a semi-circle was used to demonstrate the solution convergence with the number of subvolumes, Figure 5-12.

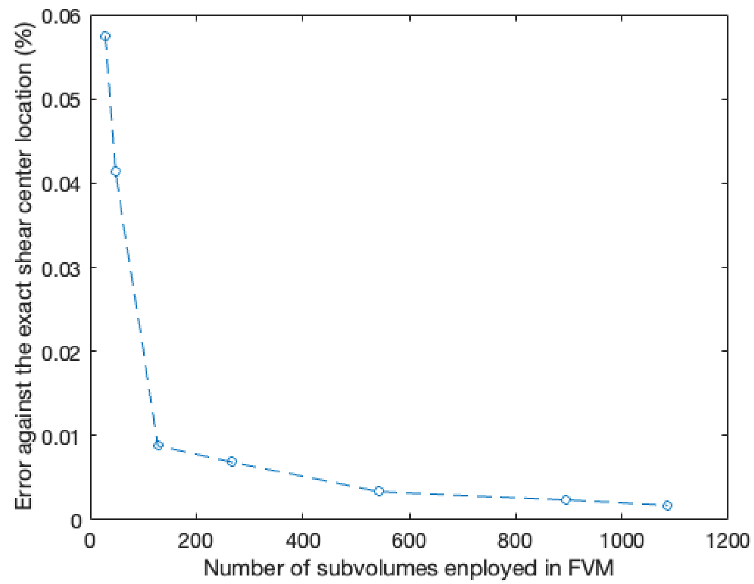

Figure 5-12 The convergence of FVM error in determining the location of a semi-circular cross section

The diameter of the semi-circle is 2 inches, which is used to normalize the difference in the y coordinate of the shear center between the FVM and analytical solutions. The FVM error relative to the exact analytical solution also decreases roughly exponentially as more subvolumes are employed in the FVM analysis.

Thin-walled Cross Section Family

For thin-walled structures, the so-called thin-wall assumption employed in structural engineering enables the derivation of closed-form expressions for the shear center of many cross sections of structural components used in the construction industry. This assumption states that the shear flow is uniform if the wall is thin enough compared to the length of the web or flanges for a homogeneous isotropic beam. The average shear stress at each point in the beam's cross section is thus assumed to have a direction tangent to the wall. Shear centers of typical structural components are provided in standard advanced mechanics books that are used for design purposes, cf. Boresi et al. (1985). Five typical cross sections are shown in Figure 5-13, and the formulae for their shear centers given in terms of the eccentricity ratios are provided for each cross section (A - E) in the following.

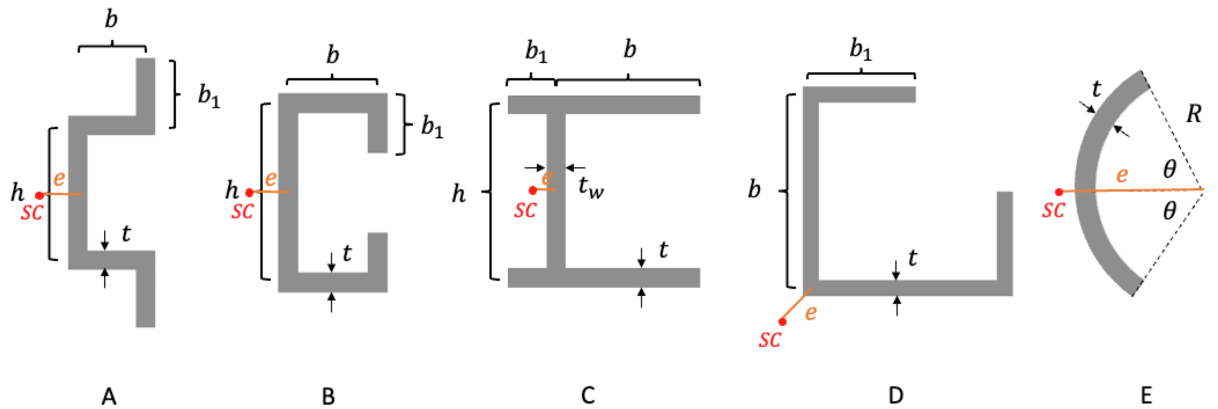

Figure 5-13 Thin-walled cross section profile (A - E)

One may notice the absence of wall thickness in the formulae for some thin-walled cross sections. This is because the thin-wall assumption is only valid when the thickness is much smaller than the overall dimension of the cross section.

Cross section A:

$$\frac{e}{b}=\frac{1+\frac{2b_1}{b}\left(1-\frac{4b_1^2}{3h^2}\right)}{2+\frac{h}{3b}+\frac{2b_1}{b}\left(1+\frac{2b_1}{h}+\frac{4b_1^2}{3h^2}\right)} \tag{5. 64}$$

Cross section B:

$$\frac{e}{b}=\frac{1+\frac{2b_1}{b}\left(1-\frac{4b_1^2}{3h^2}\right)}{2+\frac{h}{3b}+\frac{2b_1}{b}\left(1-\frac{2b_1}{h}+\frac{4b_1^2}{3h^2}\right)} \tag{5. 65}$$

Cross section C:

$$\frac{e}{b}=\frac{1-\frac{1-b_1^2}{b}}{2+\frac{2b_1}{b}+\frac{t_w h}{3t_f b}} \tag{5. 66}$$

Cross section D:

$$\frac{e}{b}=\frac{\frac{b_1}{\sqrt{2}b^2}\left(3-\frac{b_1}{b}\right)}{1+\frac{3b_1}{b}-\frac{3b_1^2}{b^2}+\frac{b_1^3}{b^3}} \tag{5. 67}$$

Cross section E:

$$\frac{e}{R}=\frac{2(sin\theta-\theta cos\theta)}{\theta-sin\theta cos\theta} \tag{5. 68}$$

The above formulae are assessed by comparison with the results of finite-volume based calculations to determine their limits of applicability. Towards this end, the five cross sections with increasingly thicker walls are analyzed to establish the wall thickness dimensions for which the thin-wall assumption produces unacceptably large errors. In the following analysis, the parameters or the dimensions of those five cross sections are listed below for reference (unit: inch):

Cross section A: $b_1 = 1, b = 1, h = 2$

Cross section B: $b_1 = 1, b = 1, h = 4$

Cross section C: $b_1 = 0.5, b = 1, h = 4, t = t_w$

Cross section D: $b_1 = 1, b = 2$

Cross section E: $R = 2, \theta = \pi/2$

Plots of eccentricity differences versus wall thickness normalized by a fixed dimension have been generated for each cross section using regular (left) and log-log (right) scales. They are shown in Figure 5-14 – Figure 5-18 for the five cross sections.

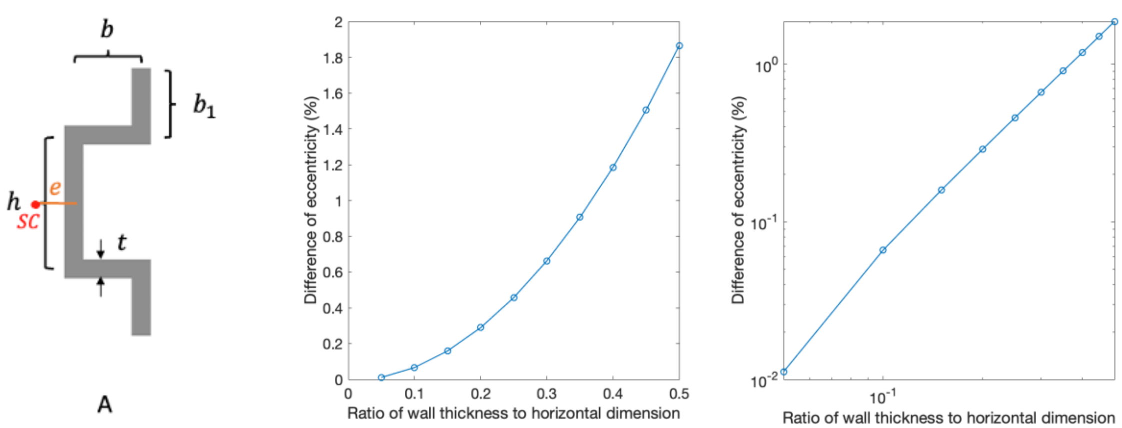

Figure 5-14 The normalized error of the eccentricity for cross section A and that in log-log scale

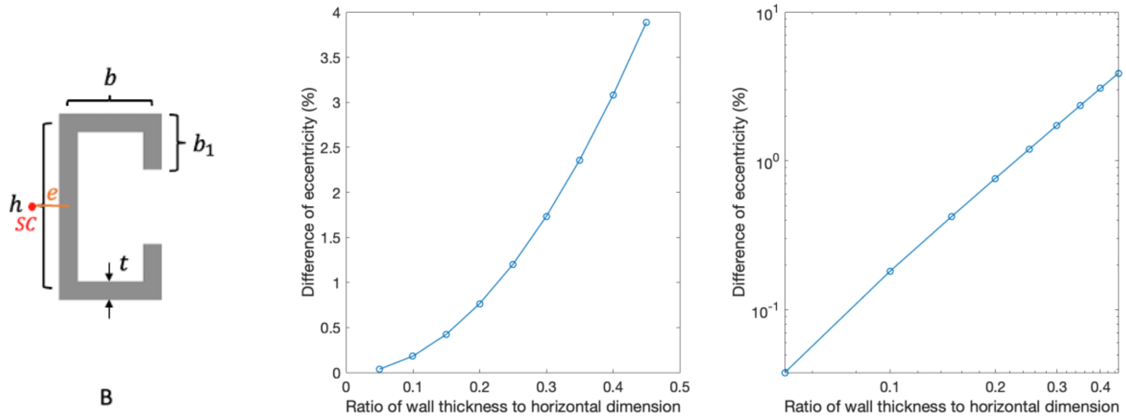

Figure 5-15 The normalized error of the eccentricity for cross section B and that in log-log scale

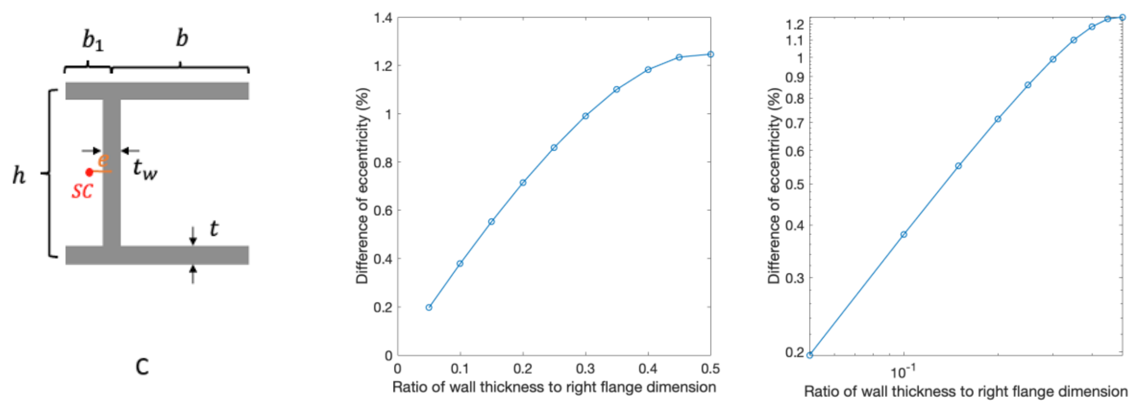

Figure 5-16 The normalized error of the eccentricity for cross section C and that in log-log scale

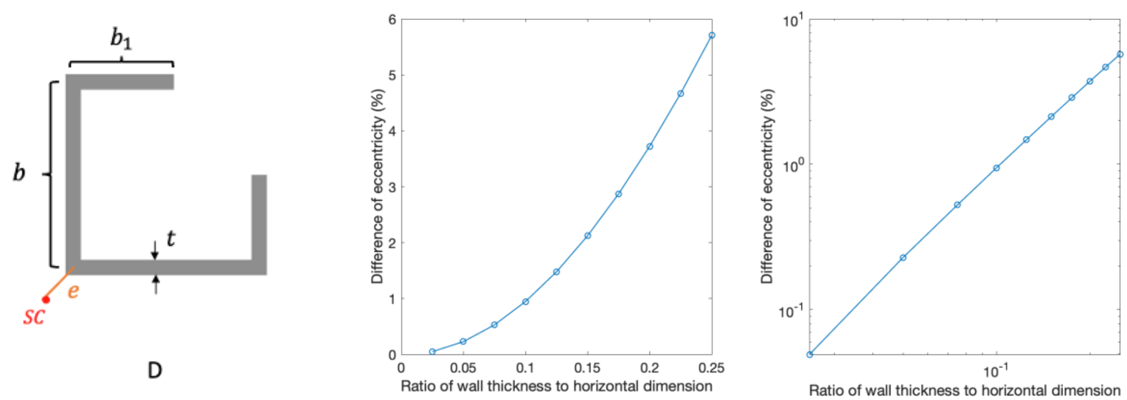

Figure 5-17 The normalized error of the eccentricity for cross section D and that in log-log scale

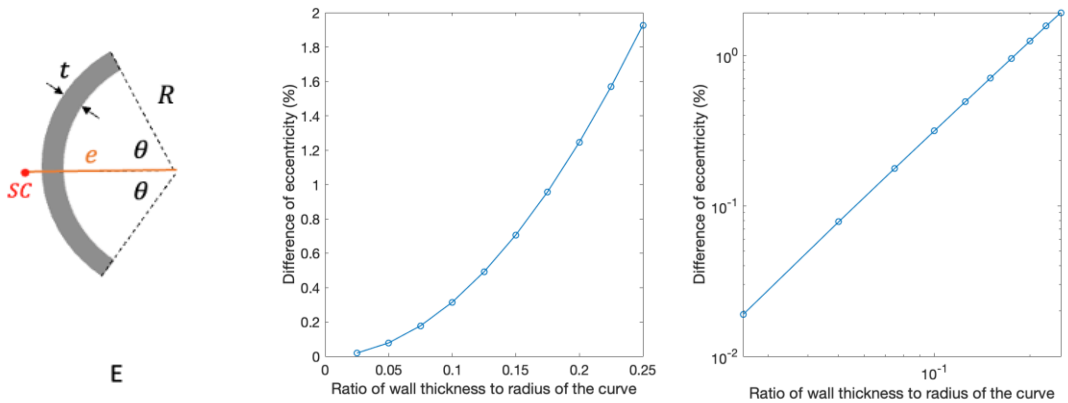

E

Figure 5-18 The normalized error of the eccentricity for cross section E ($\theta = \pi/4$) and that in log-log scale

For all these five types of thin-walled cross sections, the difference in eccentricity between the FVM-predicted and the estimated one based on the thin-wall assumption increases as the wall becomes thicker. The relationship between the difference in eccentricity versus the wall thickness ratio exhibits concave upward curves except for the unsymmetric I-beam cross section (cross section C). However, all these types of cross sections exhibit an approximately linear relationship between the eccentricity difference versus the wall thickness ratio in the log-log scale. This assessment provides a detailed and insightful answer to the question of how thin the structure should be for the thin-walled formulae to be applicable in structural design. Finding the shear center location accurately is of importance for some thin-walled structural elements because the torsion effects due to the eccentrically applied forces may be devastating.

5.4.2 Shear Center for Heterogeneous Cross Sections

In composite structures, the shear center may not be located at the centroid of the cross-section due to the different material properties of the constituent layers or regions. For heterogeneous cross-sections, the computation of the shear center becomes even more complicated than homogenous ones due to the variation of material properties across the cross-section. Various analytical and numerical methods have been developed to determine the shear center of such cross-sections. Merely following the scheme of separating deformation modes and assuming the absence of σ_{xx}, σ_{yy} and σ_{xy} over the entire homogeneous cross section, the shear center locations identified in a cross section made of heterogeneous isotropic materials require the following components for Eq. (5. 42),

$$S_1 = \sum_j \mu_j \iint_A \left[x \frac{\partial \omega_2}{\partial y} - y \frac{\partial \omega_2}{\partial x} + (1+\nu)x^2 y - \nu y^3 \right] dx\, dy \tag{5. 69}$$

$$S_2 = \sum_j \mu_j \iint_A \left[x \frac{\partial \omega_3}{\partial y} - y \frac{\partial \omega_3}{\partial x} - (1+\nu)x y^2 + \nu x^3 \right] dx\, dy \tag{5. 70}$$

$$J = \frac{1}{\left(I_{xxE} I_{yyE} - I_{xyE}^2\right)} \tag{5. 71}$$

if the heterogeneous isotropic cross section has a uniform Poisson's ratio. This has been verified in the case of flexure of concentric compound bars in Section 5.3.3 by FVM predicting the location of the shear center extremely close to the centroid. However, one must always keep in mind that the solution to the flexure of concentric compound bars in Section 5.3.3 follows the Saint-Venant semi-inverse method assumptions, which requires the absence of all in-plane stresses. Therefore, unlike torsion of the heterogenous cross section which initiates from the displacement formulation, the in-plane stresses induced by flexure may not always properly guarantee their absence between material interfaces in heterogeneous cross sections.

Structural components subjected to combined torsion-flexure loading are employed with increasing frequency in aerospace and civil engineering applications, including composite rotor blades and pultruded I, T and channel beams, amongst others. Cross sections of such structural elements may be laminated with homogeneous layers possessing different isotropic moduli yet exhibiting overall homogenized orthotropic moduli, such as in the previous example of an elliptical cross section subjected to pure torsion (Chapter Section 3. 5: Horizontally laminated elliptical cross sections), or I or T beams constructed of differently-oriented composite plies characteristic of pultruded elements. We have shown that an elliptical cross section laminated with alternating plies of two different elastic moduli could be treated as a homogeneous cross section possessing equivalent homogenized moduli G_{xz} and G_{yz} with sufficient microstructural refinement.

The same approach could be employed to analyze composite cross sections made up of different laminations with isotropic or transversely isotropic composite plies. We note that the outlined semi-inverse solution strategy for the combined torsion-flexure problem is based on the assumption that the in-plane normal and shear stresses σ_{xx}, σ_{yy} and σ_{xy} are zeroes over the entire plane. This is no longer true for laminated cross sections subjected to flexure loading. Nonetheless, the layer microstructure may be replaced by an equivalent homogeneous one with orthotropic homogenized elastic moduli under certain circumstances. This is the approach employed in the proposed combined torsion-flexure analysis of composite structural components. In the case of laminations involving isotropic layers, the Postma model will be employed to determine equivalent homogenized moduli. In the case of cross sections laminated with differently oriented composite plies, symmetrically laminated cross sections will be considered for which the concept of homogenized laminate moduli applies in the absence of bending-stretching coupling. Hence the lamination plate theory will be employed to determine the equivalent laminate moduli from the laminate extensional stiffness matrix. This approach will be assessed and validated upon comparison with the results of the three-dimensional finite-element analysis of the combined torsion-flexure problem for homogenous and heterogenous beams in the next chapter. Upon validation, structural elements with laminated cross sections that are employed in the construction industry will be analyzed to determine shear center and effective torsional and flexural stiffness. The assessment will address the question of the extent of microstructural refinement required for the overall torsion-flexural response based on the equivalent homogenized moduli to approach the response of an actual heterogeneous cross section.

5.5 Summary

When a long cylindrical beam is subjected to loadings at one end, if those loads can be considered as being applied at its shear center in the form of a resultant force, the beam would experience no twisting and its deformation would be dominated by pure flexure. To identify the shear center for a homogenous cross section, the torsion-flexure problem can be decomposed into three deformation modes. This decomposition approach has been programmed using FVM and validated through convergence studies using equilateral triangular and semi-circular cross sections. The assessment of this decomposition methodology will be conducted against the 3D FEM simulation in Chapter 6. In addition, this decomposition approach will further be assessed in different cross sections along the beam's span at various distances from the ends. The so-far validated FVM method can also be employed to assess the thin-walled structure assumptions commonly used in structural engineering practice for thin-walled cylindrical members. To determine the flexure and shear center for heterogeneous beams, the solution for homogeneous beams can be extended in a piecewise integral manner. However, the proposed semi-inverse solution strategy for the torsion-flexure problem is based on the assumption that may be violated at material interfaces. Therefore, replacing the equivalent heterogeneous beam with homogenized elastic moduli could be an alternative approach to the analysis of composite structural components with combined torsion and flexure loadings.

Chapter 6

Flexure Response of Beams: FVM vs 3D FEM Comparison

6.1 Introduction

When analyzing a long and slender beam that is primarily designed to resist loads through bending and shearing, the beam theory is used to examine its behavior under different loading conditions. The behavior of beams can be analyzed using various beam theory models, which are based on certain assumptions about their geometries, material properties, loading conditions, and boundary conditions. The most commonly used theoretical models are the *Euler-Bernoulli beam theory* and the *Timoshenko beam theory*.

The Euler-Bernoulli beam theory, also known as the classical beam theory, assumes that a beam is a one-dimensional homogeneous linearly elastic isotropic object, and that the deformation of the beam is only caused by bending. It neglects the effects of shear deformation, axial deformation, as well as rotary inertia. This theory provides a simple and elegant way to analyze the behavior of slender beams that are relatively long and thin (usually with aspect ratio more than 10). The Timoshenko beam theory, on the other hand, is still limited to homogeneous linearly elastic isotropic material beam, yet it takes into account the effects of shear deformation and rotary inertia, which are neglected in the Euler-Bernoulli beam theory. The Timoshenko beam theory is more appropriate for beams that are relatively short and thick, or for beams that are subjected to significant shear stresses. Both of these beam theories provide handy tools for analyzing the behavior of beams, and can be used to estimate the deflections, stresses, and reactions of a beam under various loading conditions. Accurate prediction of the behavior of beams under different end loading conditions plays an important role in designing cantilever beams or supported girders. Although the Timoshenko beam theory takes into account various factors like bending, shearing, axial deformation and even rotation of cross-sections, it does not incorporate torsional deformation into its formulation.

When addressing the problem of torsion-flexure as a fundamental problem in structural engineering, analysis taking into consideration the displacement and stress distribution across each cross section of the beam is always required. However, traditional beam theories may not provide the level of detail required as they only consider the beam as a whole, rather than the specific geometry of each cross section. Finding a solution to this challenge can prove difficult without the help of comprehensive three-dimensional structural analysis, but a thorough cross-sectional analysis can lead to a rapid and accurate understanding of the beam deformation problem where the loadings and constraints are applied at the ends. Barretta (2014) developed an exact solution for Saint-Venant's beams under flexure by relating the torsion-flexure to Kirchoff plates. A semi-analytical finite-element approach was used for analyzing the torsion-flexure response of beams by Dong et al. (2001) and Kosmatka et al. (2001). A quasi-3D FEM with a low computational cost is presented for coupled bending and torsional-warping analysis of thin-walled beams by Lezgy-Nazargah et al. (2021) through conversion of the 3D problem into separated 2D cross-sectional and 1D modeling. However, fully three-dimensional beam modeling using FEM is computationally intensive and time-consuming, which makes it challenging to use in the design of real-world structures. As an alternative to 3D FEM, FVM has been proposed herein as a computationally efficient approach for beam modeling with end loads and constraints for those cross section away from the ends. Its capability of accurately analyzing either the pure torsion or pure flexure structural responses and predicting the shear center of beams has been demonstrated in Chapters 3, 4 and 5, respectively. Nonetheless, the application of FVM is still at an early stage and requires more validation through comparison with the combined torsion-flexure responses obtained from established methods like 3D FEM which the analytical solutions are not competent of generating.

The FVM is a semi-analytical approach that takes into account both the flexure and torsion effects on any specific beam cross section incorporated with the Saint-Venant's semi-inverse method, making it a computationally efficient approach compared to 3D FEM. Therefore, this chapter starts with the review of previous studies that have investigated the accuracy of the pure flexure response of homogenous isotropic beams against analytical solutions. This chapter then focuses on the comparison of the torsion-flexure response of beams obtained using the 3D FEM and FVM when both of the flexure and torsion modes exist. The potential of FVM as an alternative to FEM is additionally highlighted, and the need for further research to validate its application to a broader range of beams including thin-walled structures emphasized. The aim of this chapter is to contribute to the field of structural engineering by providing a comparison of the accuracy and efficiency of FVM designed for torsion-flexure problem versus 3D FEM in predicting the torsion-flexure response of homogenous isotropic beams.

6.2 Three-dimensional Finite Element Analysis (ANSYS)

ANSYS is a widely used software for fluid, thermal and structural analysis and simulation in engineering. It provides a range of tools and capabilities for modeling and analyzing structures. In this chapter, ANSYS static structure tool is implemented for modeling of cantilever beams using Solid-186 elements to validate the FVM in solving torsion-flexure problems. Solid-186 elements are higher order 3D 20-node elements that exhibit quadratic displacement behavior. This type of element is defined by 20 nodes each having three degrees of freedom (translation in x, y and z directions) shown in Figure 6-1. The default form of Solid-186, "homogeneous structural solid" is set, as all the analyzed beams in this chapter are homogeneous isotropic.

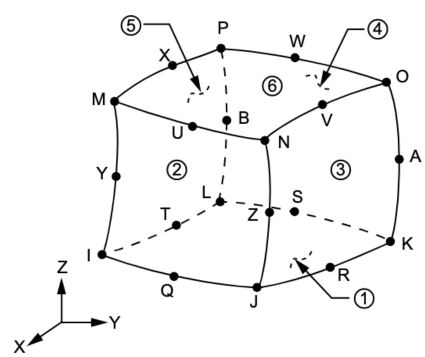

Figure 6-1 Solid 186 Homogeneous structural solid element illustration

The full integration method is applied to each Solid-186 element, and all its integration points are used to evaluate the stiffness matrix for accurate element stiffness matrix components. By using the full integration method, the stress distribution within the element is evaluated exactly at each integration point using displacements, which leads to more accurate stress predictions. This is especially helpful for elements with irregular geometries or where stress concentrations may occur. Each Solid-186 element has a 60×60 stiffness matrix which is significantly larger than those employed in FVM analysis whose size is 4×4 for basic deformation mode, as the basic quadrilateral unit in FVM (known as "subvolume") relates four surface-averaged traction and displacement components in the longitudinal direction. To balance this intrinsic difference between the settings of elements in 3D FEM and subvolumes in FVM in order to compare results at levels as close as possible, the nodal values of 20 nodes in each Solid-186 together with those on the centers of six surfaces plus the entire body (27 nodal values in total) are exported from each element in 3D FEM. These nodal quantities are re-generated in FVM by employing a similar but finer meshing grid with four times of the total number of elements in each cross section, through splitting of each Solid-186 element into eight subvolumes with each taking over one the vertices of the Solid-186 element. For any cross section, nodal values exported from 3D FEM analysis and FVM analysis are point-to-point compared at the vertices of each subvolume, and the results in the remaining cross-sectional area are obtained by linear interpolation.

Generating a finite mesh in ANSYS is an important task as well since its quality affects the results of both 3D FEM and FVM. The elemental or subvolume shapes implemented can also greatly impact the behavior of the model as well as the stresses and displacements. Meshing with quadrilateral shape units is necessary for successful implementations of the FVM based on the same cross-sectional meshing grid, as FVM is currently capable of dealing with four-side units. Since the cross-sectional area of each analyzed beam in this chapter is simple, the default meshing methods "automatic method control" in ANSYS is selected, which attempts to sweep a hexahedral mesh for solid models prior to turning to the tetrahedron method. A sweeping mesh generates a mesh on one surface of a body and sweeps along the length of the body up to another surface. As a result, the mesh pattern is identical along the length of the body, which ensures consistent cross-sectional mesh through the longitudinal direction for 3D FEM and FVM analysis. Using this meshing scheme, each meshed unit cubic with uniform size length of 0.1 inch is generated.

The structural model in ANSYS is the cantilever cylindrical beam with one face fully attached to a rigid surface (known as "fixed support" face). Different types of loading conditions may be applied to the other end face of the cylindrical beam which will be discussed in the next section in detail. The structural models for the cantilever cylindrical beams are solved in "Mechanical APDL" under linear elastic analysis. The solution information contains the distribution of three stress components $(\sigma_{xz}, \sigma_{yz}, \sigma_{zz})$ and three displacement components (u, v, w)

on specific cross sections. Upon completion of generating the solution, stress components $(\sigma_{xz}, \sigma_{yz}, \sigma_{zz})$ and displacement components (u, v, w) are exported to corresponding six datasets with each row in any of those datasets containing the information of a node's properties. Those datasets do not only specify the nodal quantities for $\sigma_{xz}, \sigma_{yz}, \sigma_{zz}, u, v, w$, but also provide sufficient data for setting up the meshing grid of FVM analysis, since each row processes information about the nodal index, nodal coordinates, as well as the index of the element that the node belongs to.

6.3 Performance Comparison in Cross Sections Away from the Ends

The cross-sectional performance of beams is a critical factor in structural engineering design. The Saint Venant's principle states that the behavior of any cross section of a beam only depends on the away-from-end forces and/or moments in the resultant sense as long as the cross section is not close to them. For the torsion-flexure problem of any cantilever beam, the majority of the beam cross sections are away from the ends, thus three cross sections at each quarter of the beam length (25%, 50%, 75%) will be selected first and then analyzed for the validation of the Saint Venant's semi-inverse approach, which is intrinsic to the FVM approach. The cross section at 50% of the beam length is the furthest one to either end, and the cross sections at 25% and 75% of the beam length are also checked in case of any unexpected significant variation exists in the interval.

Solutions of the torsion-flexure problem by 3D FEM and FVM are compared in this section for each of the cases in the sequel, with the analytical solution also included for the rectangular cross section with the end subjected to either a transverse force or a twisting moment, i.e., the rectangular beam either deforms by pure bending about one specific direction or by pure twisting about its centroid (also serving as the shear center for the rectangle). If the free end of a rectangular beam were subjected to a resultant force not directed through the shear center, no analytical solution would be available without decomposing the loading into two flexure force components and a torque about the centroid and treating the entire problem as three separate sub-problems. Since comparisons are conducted in a point-to-point fashion, 3D FEM and FVM will be verified with the analytical solution if it is available, and the error is normalized by the maximum value among all the nodal values in the analytical solution. This error is evaluated for any quantity of interest Q_k at every refined mesh grid point (node i) when there is an analytical solution available.

$$Error\ of\ FVM\ @\ node\ i = \frac{Q_{ki}^{FVM} - Q_{ki}^{analytical}}{\max(Q_{k1}^{analytical}, Q_{k2}^{analytical}, \ldots, Q_{km}^{analytical})} \quad (6.\ 72)$$

$$Error\ of\ 3D\ FEM\ @\ node\ i = \frac{Q_{ki}^{3D\ FEM} - Q_{ki}^{analytical}}{\max(Q_{k1}^{analytical}, Q_{k2}^{analytical}, \ldots, Q_{km}^{analytical})} \quad (6.\ 73)$$

If an analytical solution is not available because of complex geometries of the cross sections or complicated loading conditions, comparison between FVM and 3D FEM predictions will solely employ the normalized difference using the maximum value among all the nodal values obtained from the rectangular mesh grid points in the 3D FEM simulations. This error or difference is evaluated for any quantity of interest Q_k at every refined mesh grid point (node i) only when these is no analytical solution available.

$$Error\ of\ FVM\ @\ node\ i = \frac{Q_{ki}^{FVM} - Q_{ki}^{3D\ FEM}}{\max(Q_{k1}^{3D\ FEM}, Q_{k2}^{3D\ FEM}, \ldots, Q_{km}^{3D\ FEM})} \quad (6.\ 74)$$

A rectangular beam with 2 inches (width) × 4 inches (height) cross section and the length of 40 inches is taken from Section 4.5 for more detailed comparisons. If the longitudinal coordinate z starts from the fixed end face along the beam, the z coordinates for 25%, 50%, 75% of the beam length are $z = 10, 20, 30$ inches respectively denoted cross sections A, B and C. The following moduli are employed uniformly in the homogenous isotropic beam analysis: Young's modulus $E = 30{,}000\ ksi$, and Poisson's ratio $\nu = 0.3$, with the shear modulus obtained from the relation $G = \frac{E}{2(1+\nu)} = 11{,}538\ ksi$.

6.3.1 Pure Flexure of Beams

<u>Flexure about one principal direction (one flexure mode in FVM):</u>

The performance comparison of the three methods (FVM, 3D FEM, analytical) is based on the flexure response of beams about the principal y axis produced by the resultant force $F_y = 10\ kips$ located in the center of the free end illustrated in Figure 6-2.

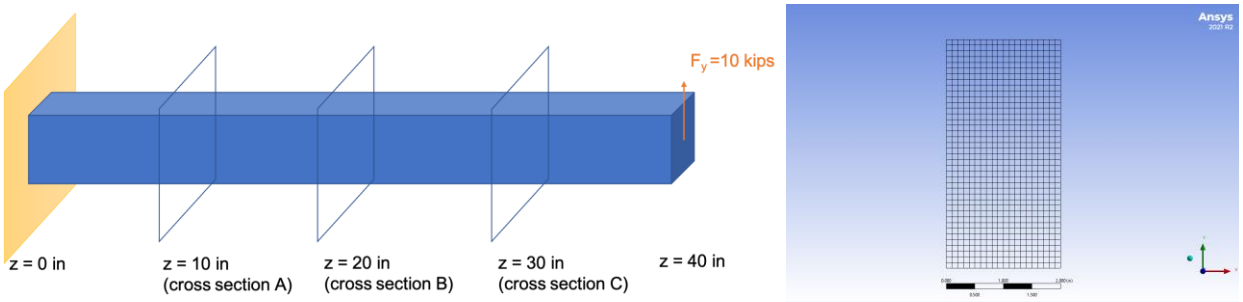

Figure 6-2 Homogeneous isotropic rectangular cantilever beam with vertical loading at the end (left) and the ANSYS mesh of each cross section with 800 elements (right)

For this loading condition, the shear stress σ_{xz} distributions exhibit little difference in the cross sections A, B, C shown in Figure 6-3:

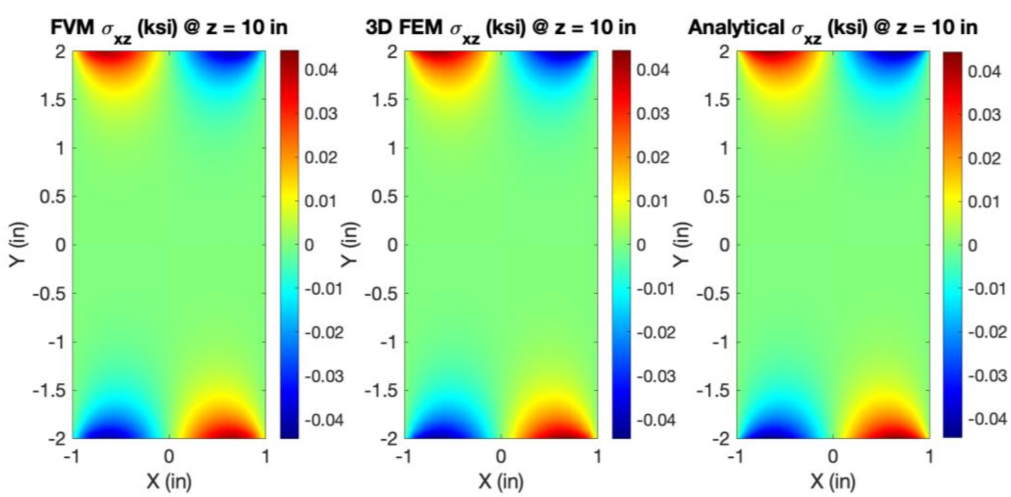

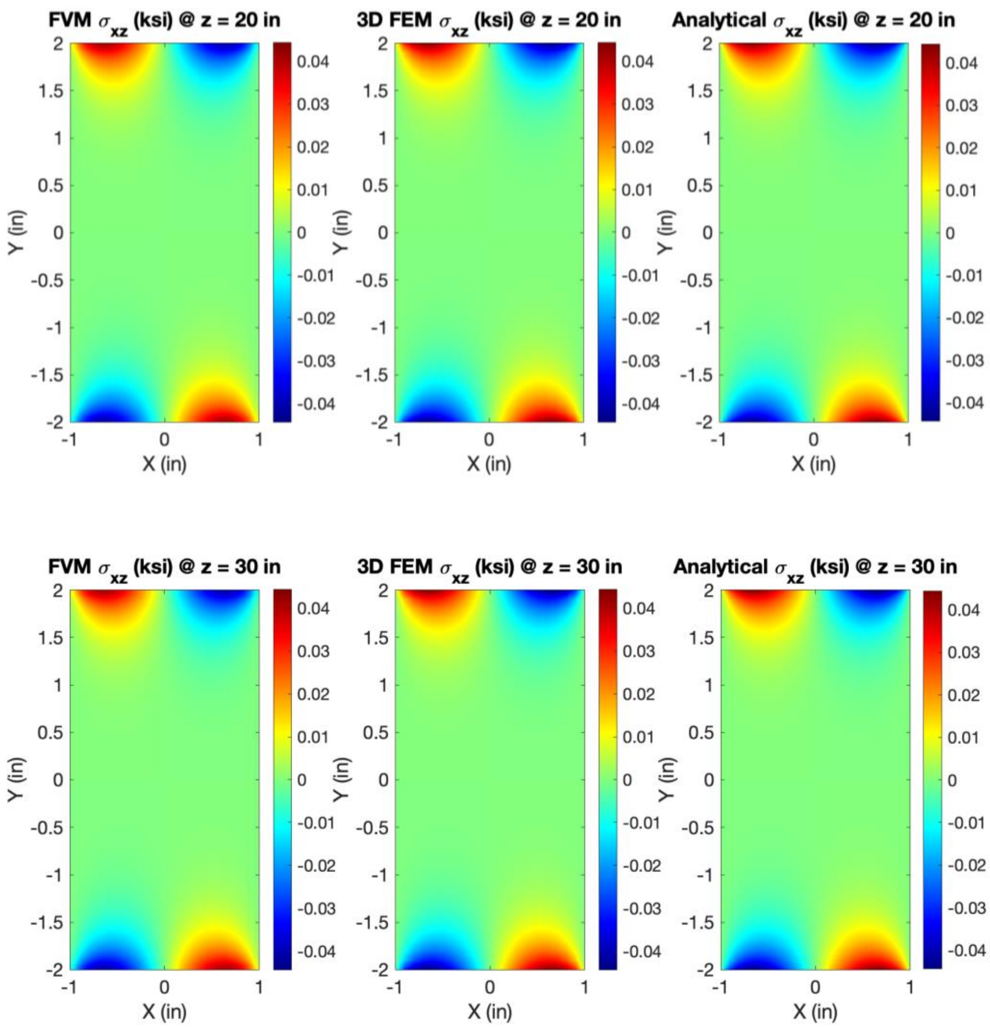

Figure 6-3 Shear stress σ_{xz} distribution for the rectangular beam with $F_y = 10\ kips$

The errors of FVM and 3D FEM with respect to the analytical solutions are generally unnoticeable for σ_{xz}, except around the boundary in FVM results, as shown in Figure 6-4:

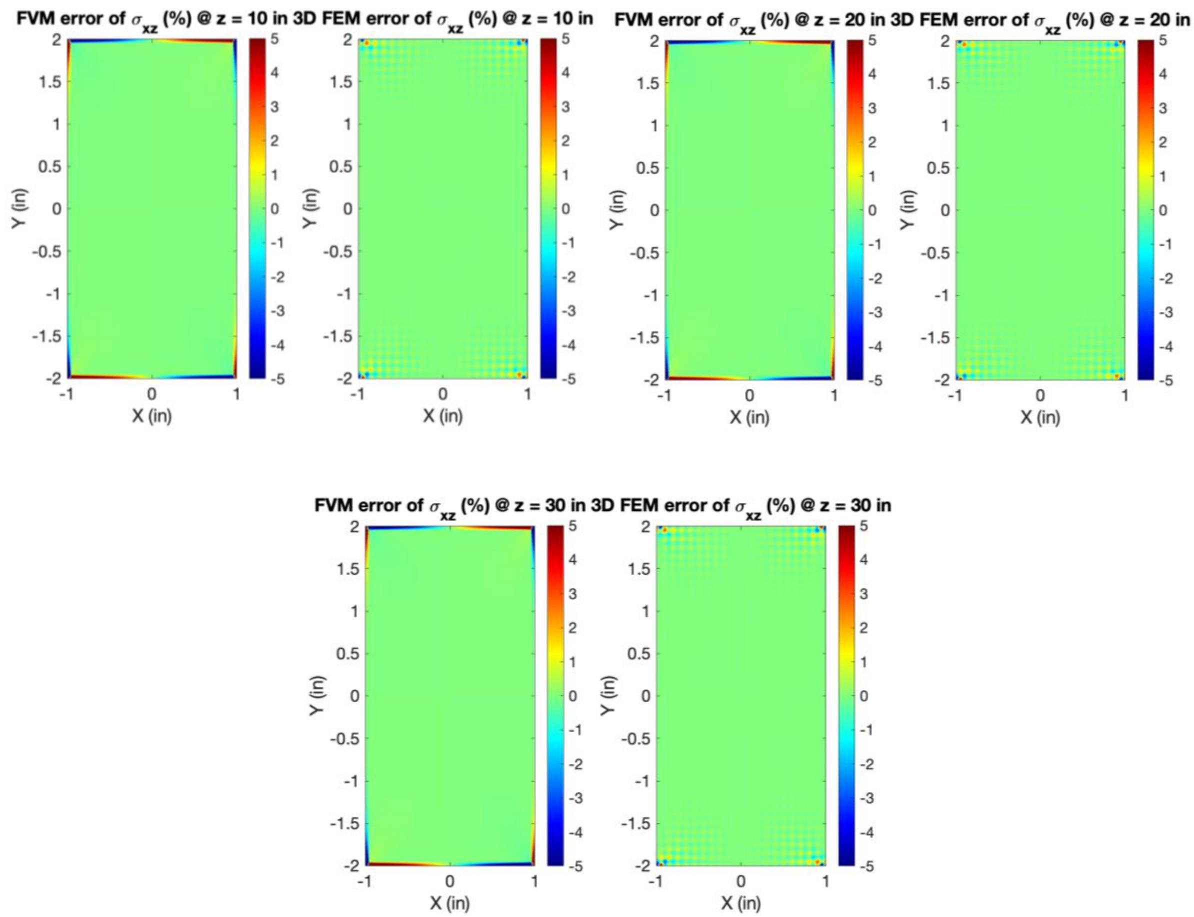

Figure 6-4 Shear stress σ_{xz} distribution error for the rectangular beam with $F_y = 10\ kips$

The shear stress σ_{yz} distributons also exhibit little difference in the cross sections A, B, C which are shown in Figure 6-5:

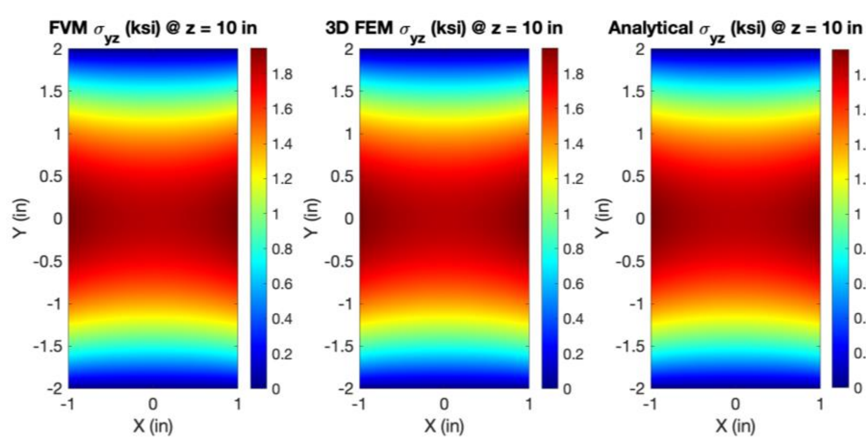

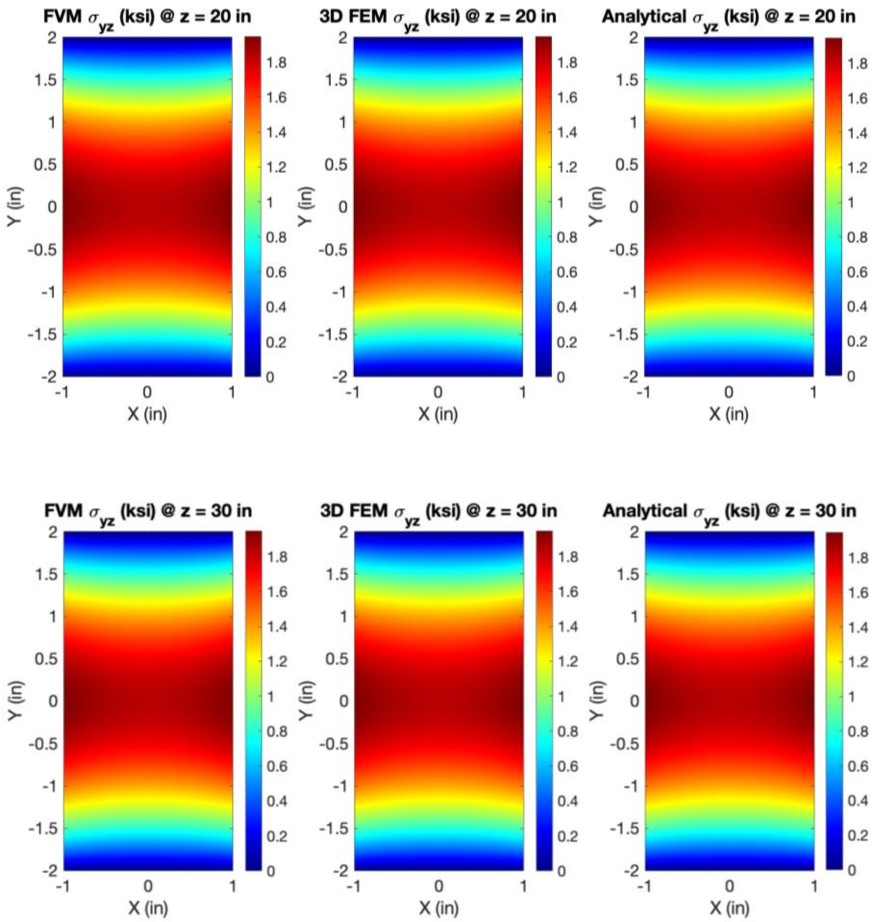

Figure 6-5 Shear stress σ_{yz} distribution for the rectangular beam with $F_y = 10\ kips$

The errors in FVM and 3D FEM results with respect to the analytical solution are also very small for σ_{yz}, as shown in Figure 6-6:

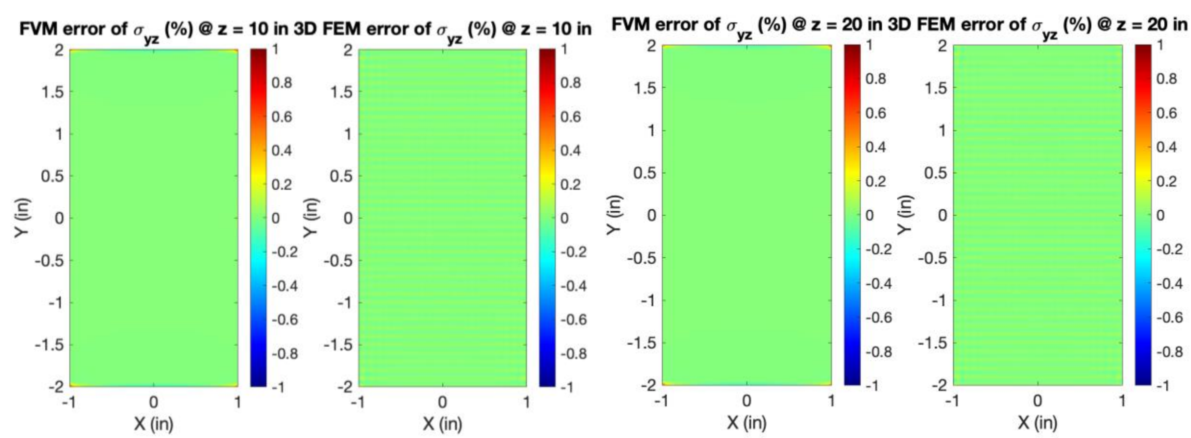

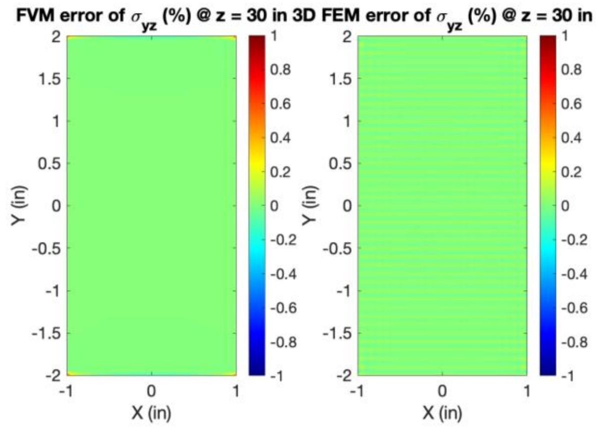

Figure 6-6 Shear stress σ_{yz} distribution error for the rectangular beam with $F_y = 10\ kips$

The normal stress σ_{zz} distributions in the cross sections A, B, C are plotted using different scales due to their decreasing magnitude away from the fixed end, however, the variation along the vertical direction is similar in the three cross sections shown in Figure 6-7.

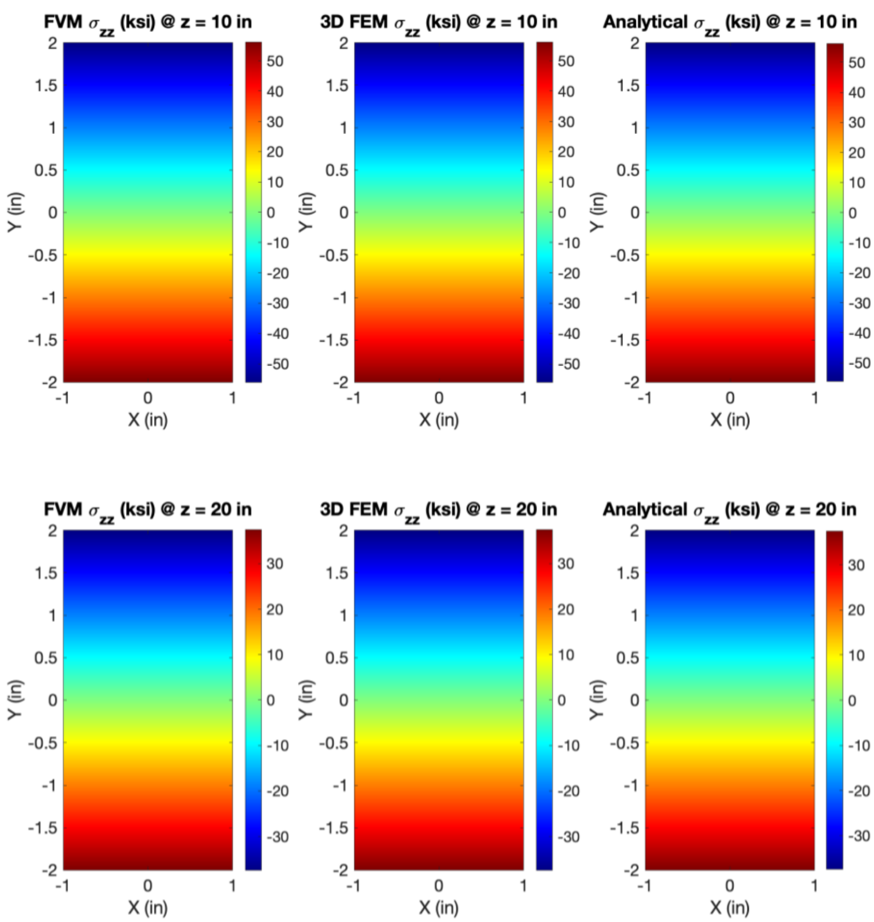

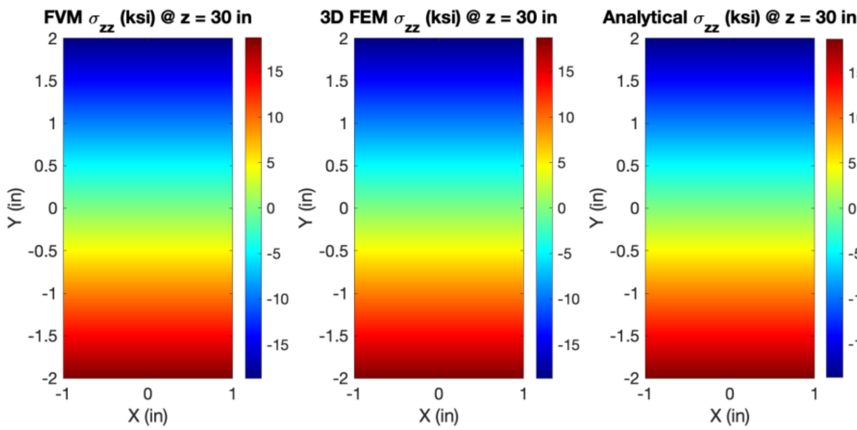

Figure 6-7 Normal stress σ_{zz} distribution for the rectangular beam with $F_y = 10\ kips$

The errors in FVM and 3D FEM results with respect to the analytical solutions are also trivial for σ_{zz}, as shown in Figure 6-8:

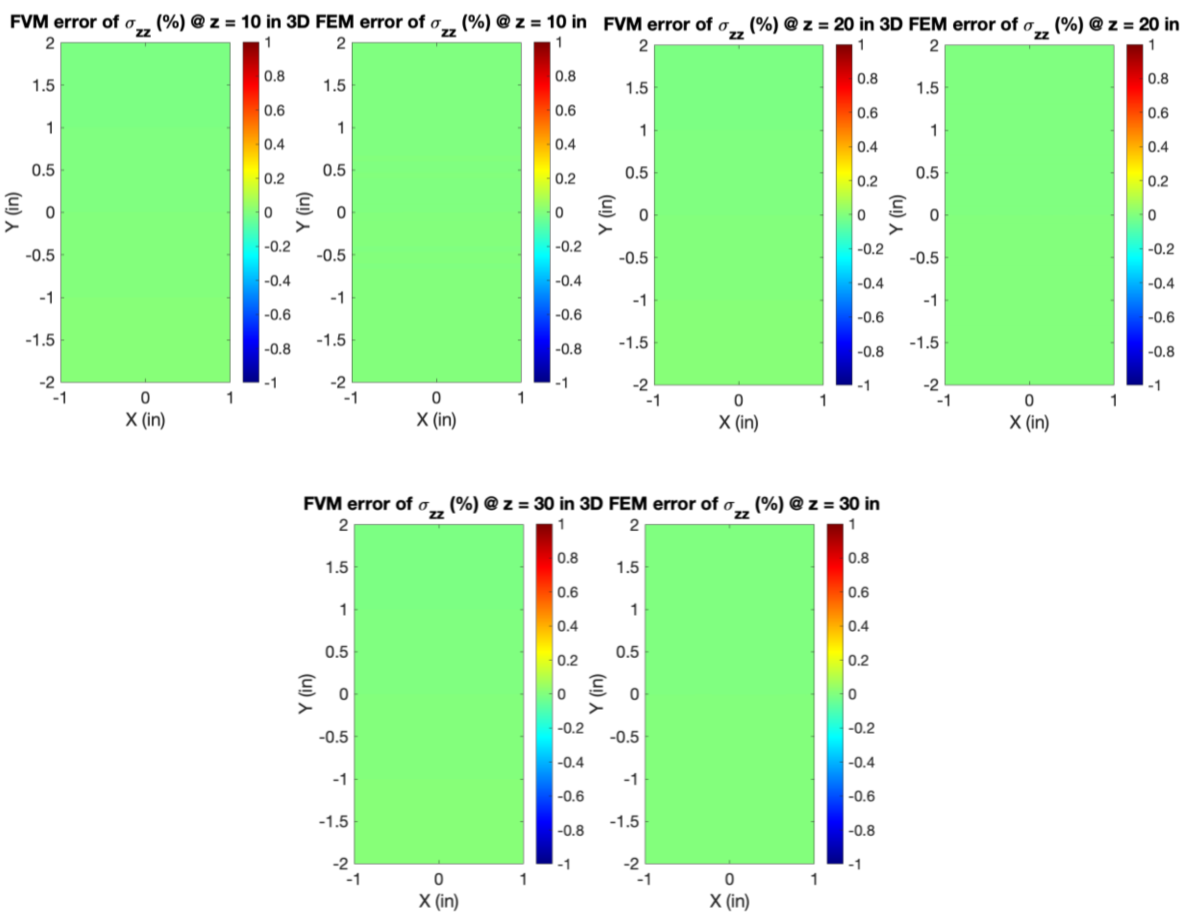

Figure 6-8 Normal stress σ_{zz} distribution error for the rectangular beam with $F_y = 10\ kips$

The x displacement component u has close distribution at cross section A, B, C shown in Figure 6-9:

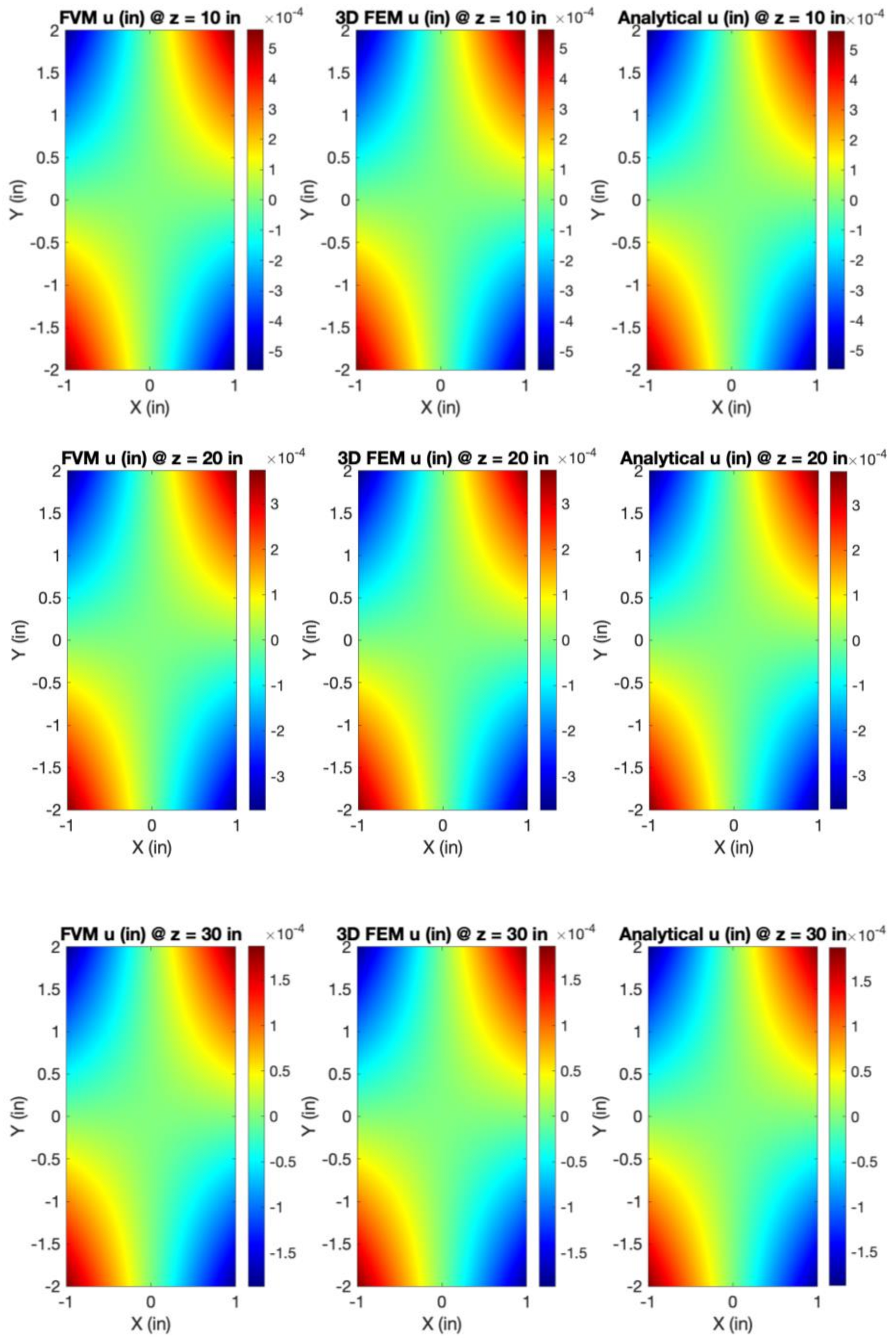

Figure 6-9 Displacement u distribution for the rectangular beam with $F_y = 10\ kips$

The errors in FVM and 3D FEM results with respect to the analytical solutions are insignificant for u, as shown in Figure 6-10:

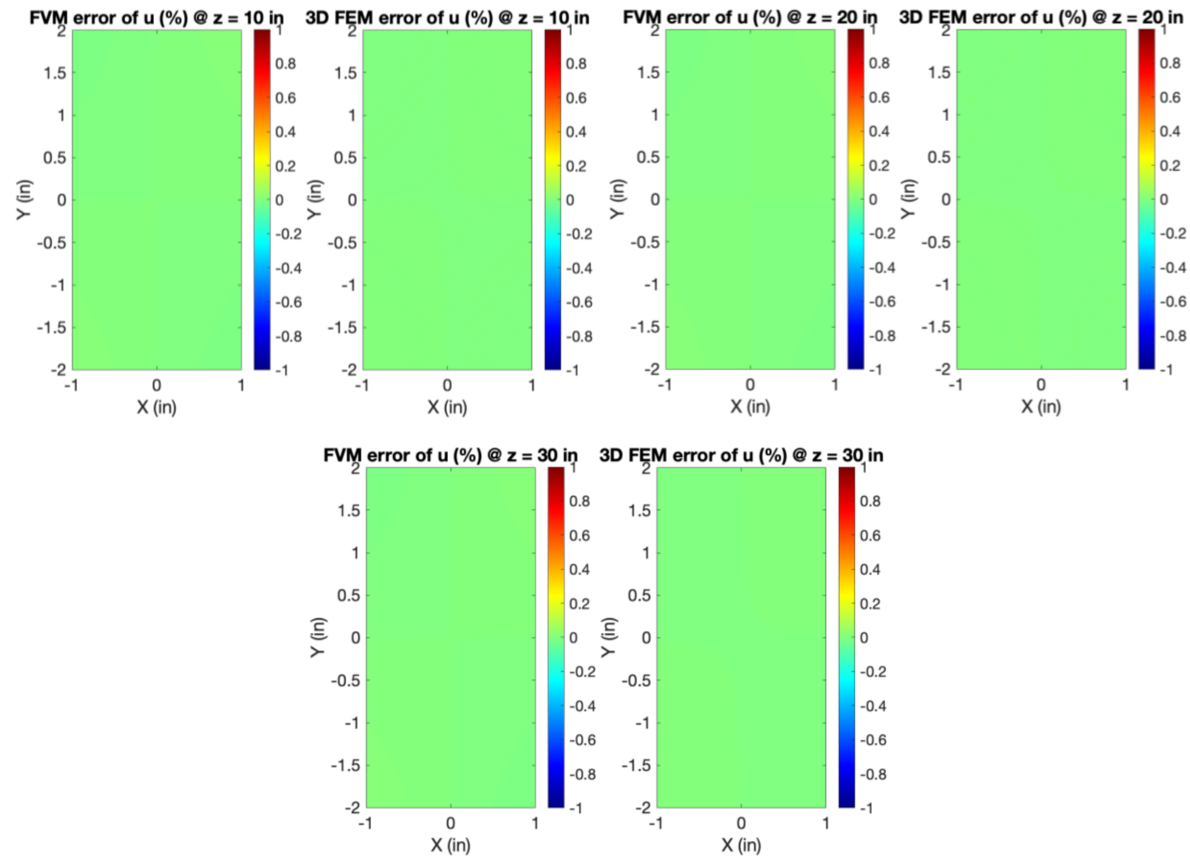

Figure 6-10 Displacement u distribution error for the rectangular beam with $F_y = 10\ kips$

The y displacement component v has similar distributions in the cross sections A, B, C which is shown in Figure 6-11.

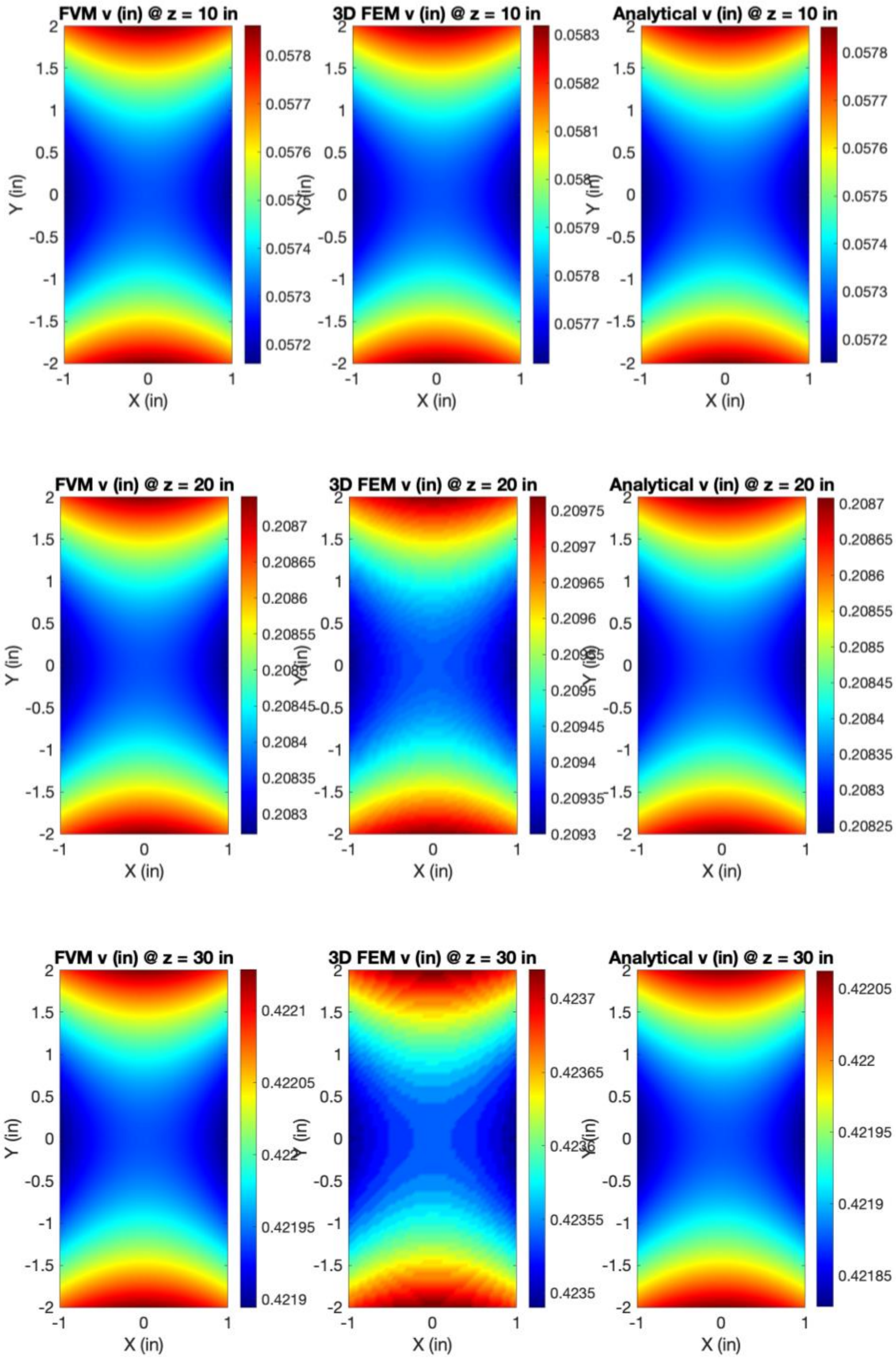

Figure 6-11 Displacement v distribution for the rectangular beam with $F_y = 10\ kips$

One can easily observe that the 3D FEM does not have smooth pattern for cross sections closer to the free end (those with larger deflection) while FVM and analytical solutions do. It appears that 3D FEM has lower resolution than FVM for a comparable number of nodes relative to the number of subvolume surfaces in FVM analysis in some cross sections.

The errors in FVM and 3D FEM results with respect to the analytical solutions are small and uniform in terms of v over each cross section, and the errors in v decrease as the cross section moves away from the fixed end shown in Figure 6-12.

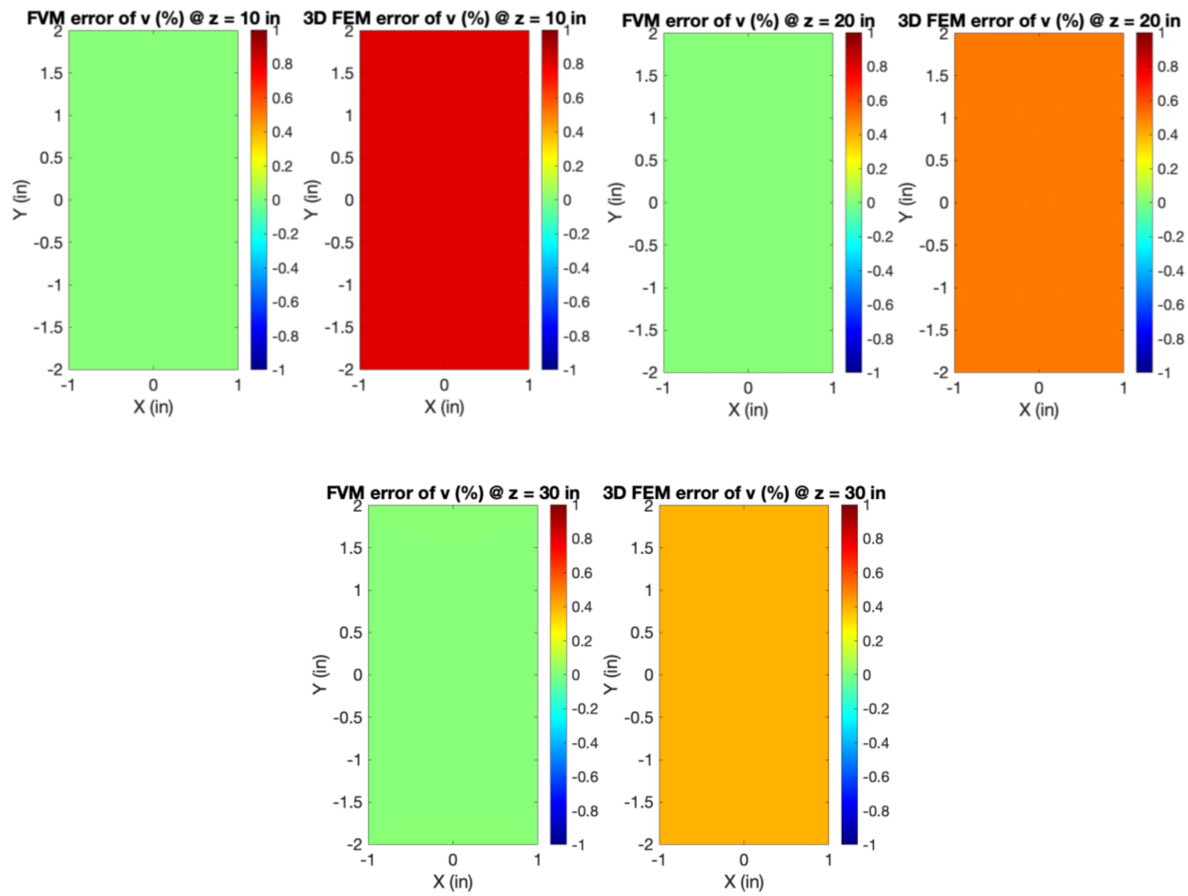

Figure 6-12 Displacement v distribution error for the rectangular beam with $F_y = 10\ kips$

The z displacement component w distributions are plotted in different scales in the cross sections A, B, C due to increasing magnitudes away from the fixed end, however, the variation along the vertical direction is still similar in the three cross sections shown in Figure 6-13:

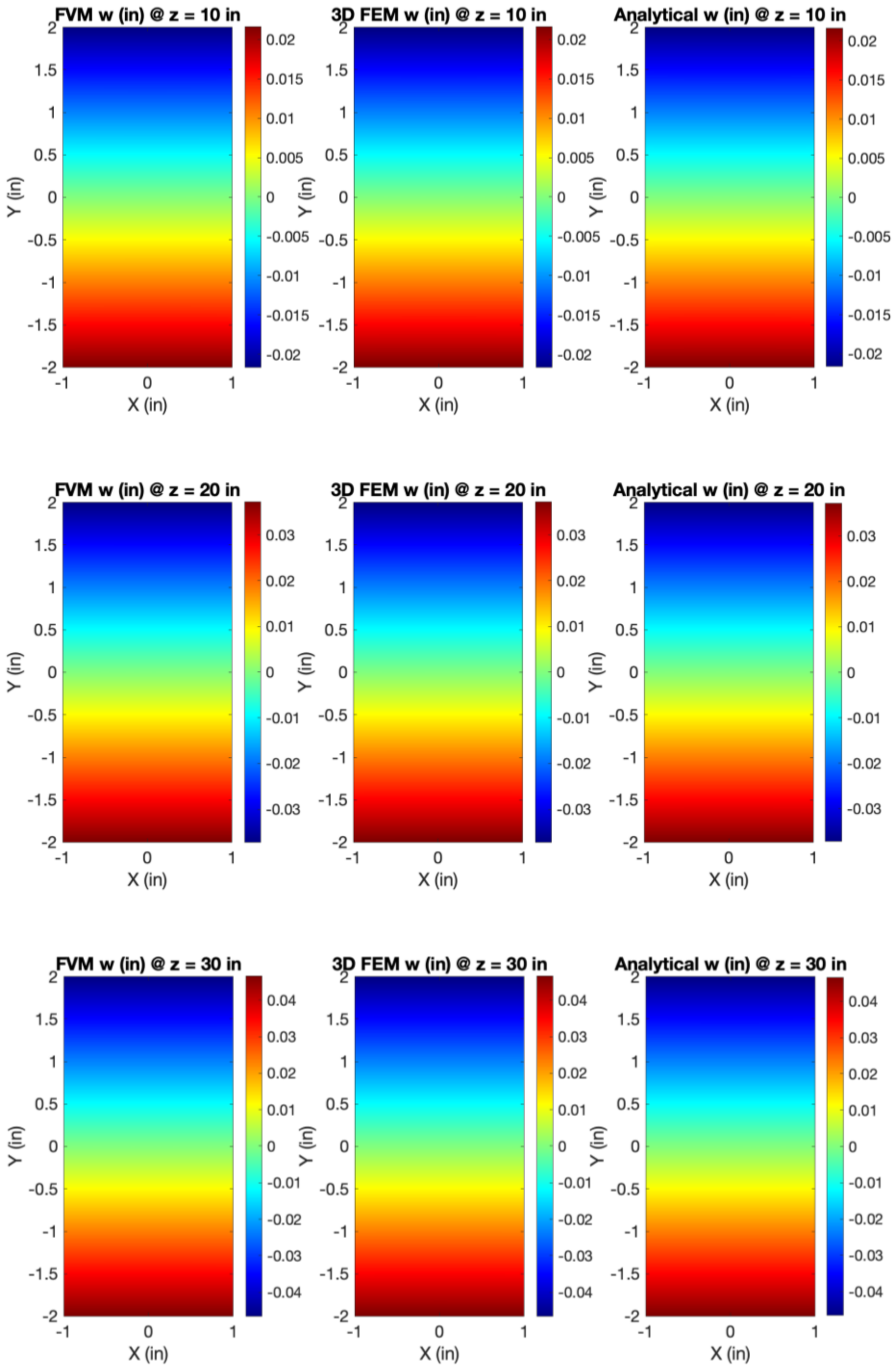

Figure 6-13 Displacement w distribution for the rectangular beam with $F_y = 10\ kips$

The errors in FVM and 3D FEM results with respect to the analytical solutions are small for w, and the errors in w decrease as the cross section moves away from the fixed end shown in Figure 6-14.

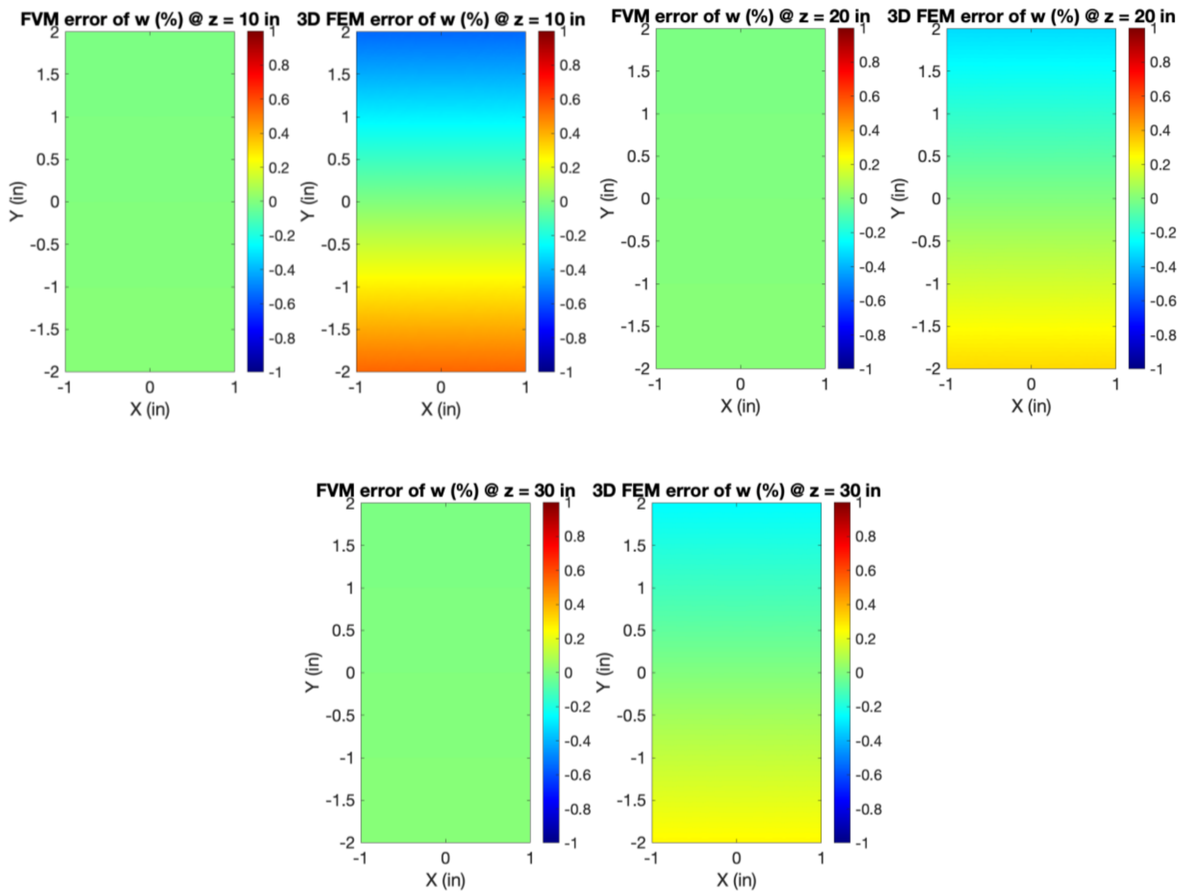

Figure 6-14 Displacement w distribution error for the rectangular beam with $F_y = 10\ kips$

In summary, for the rectangular beam loaded with only $F_y = 10\ kips$ at the center of free end, the shear stresses σ_{xz} and σ_{yz} as well as the displacements u and v exhibit very similar magnitudes and distributions in the cross sections A, B, and C, while the normal stress σ_{zz} and displacement w have similar distributions but different magnitudes corresponding to the assumptions in the elasticity solution. All the errors in FVM or 3D FEM results relative to the analytical solution are relatively small. Though 3D FEM has a slightly smaller average and maximum error than FVM over the entire rectangular cross sections A, B and C in stress fields, FVM outperforms 3D FEM in predicting the displacements. For this validation case, all stresses and displacements except the normal longitudinal stress and displacement exhibit close performance in the cross sections A, B, C. Therefore, only stress and displacement fields in the middle cross section B, serving as the representative of any cross section away from the beam ends, will be illustrated in the following cases for conciseness.

6.3.2 Pure Torsion of Beams

<u>Torsion about longitudinal direction (only torsion mode in FVM):</u>

The performance comparison of the three methods (FVM, 3D FEM, analytical) is based on the torsional response of beams along the z direction produced by the resultant twisting moment $M_z = 30\ kips.in$ about the center of the free end illustrated in Figure 6-15.

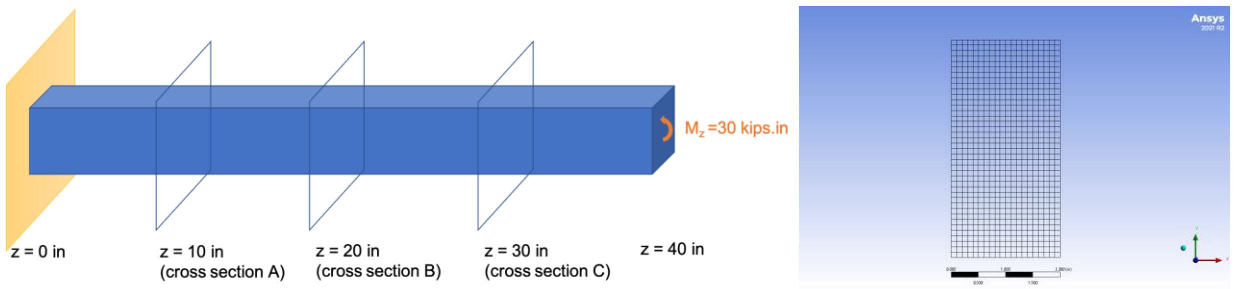

Figure 6-15 Homogeneous isotropic rectangular cantilever beam with a moment in the end plane (left) and the ANSYS mesh of each cross section with 800 elements (right*)*

The normal stress is everywhere zero in the solutions of the three methods, while the shear stresses σ_{xz} and σ_{yz} have distributions in the cross section B shown in Figure 6-16.

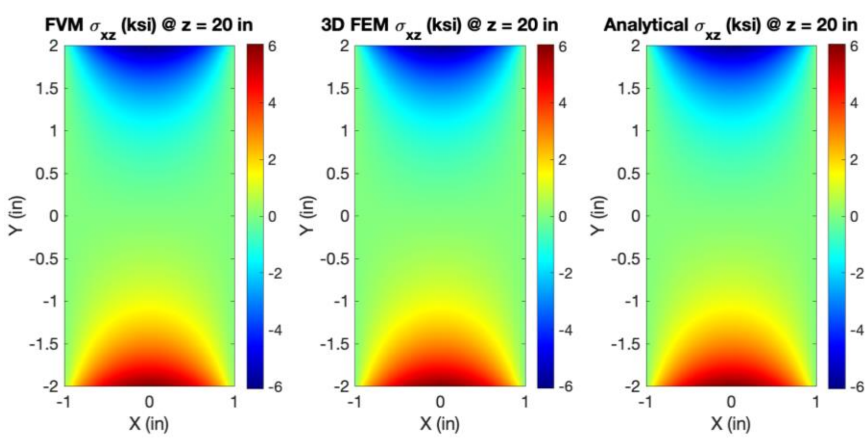

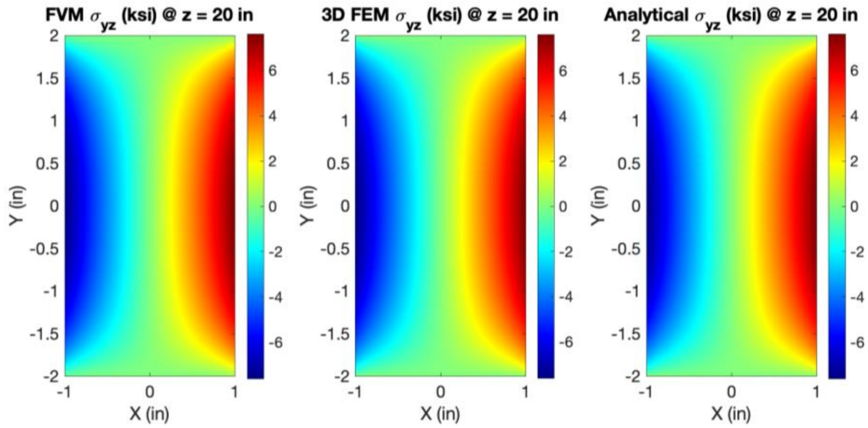

Figure 6-16 Shear stresses σ_{xz} (top) and σ_{yz} (bottom) distribution for the rectangular beam with $M_z = 30\ kips.in$

The errors in FVM and 3D FEM results with respect to the analytical solutions are very small throughout most of the cross section for σ_{yz}, as shown in Figure 6-17.

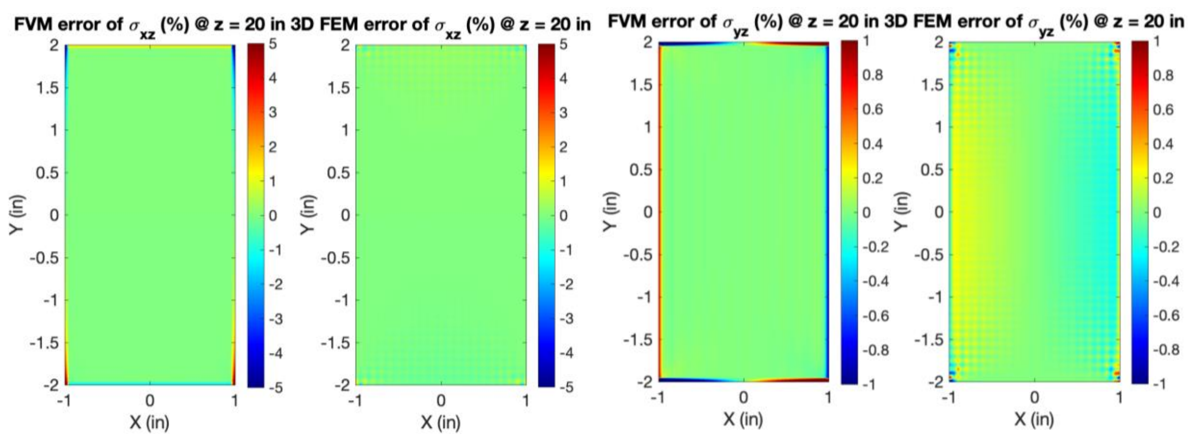

Figure 6-17 Shear stresses σ_{xz} (left two) and σ_{yz} (right two) distribution errors for the rectangular beam with $M_z = 30\ kips.in$

The errors in FVM results are noticeable along the boundary, and the errors for σ_{xz} are slightly larger than σ_{yz} for both FVM and 3D FEM solutions.

Each of the x, y, z displacement components u, v, w predicted by the three methods have very similar distributions in the cross sections A, B, C, with the distribution in the cross section B selected for conciseness. The x, y displacement components u, v increase linearly with the distance from the fixed end, however the distribution pattern is not affected by the cross section location and hence only displacements in the cross section B are shown in Figure 6-18:

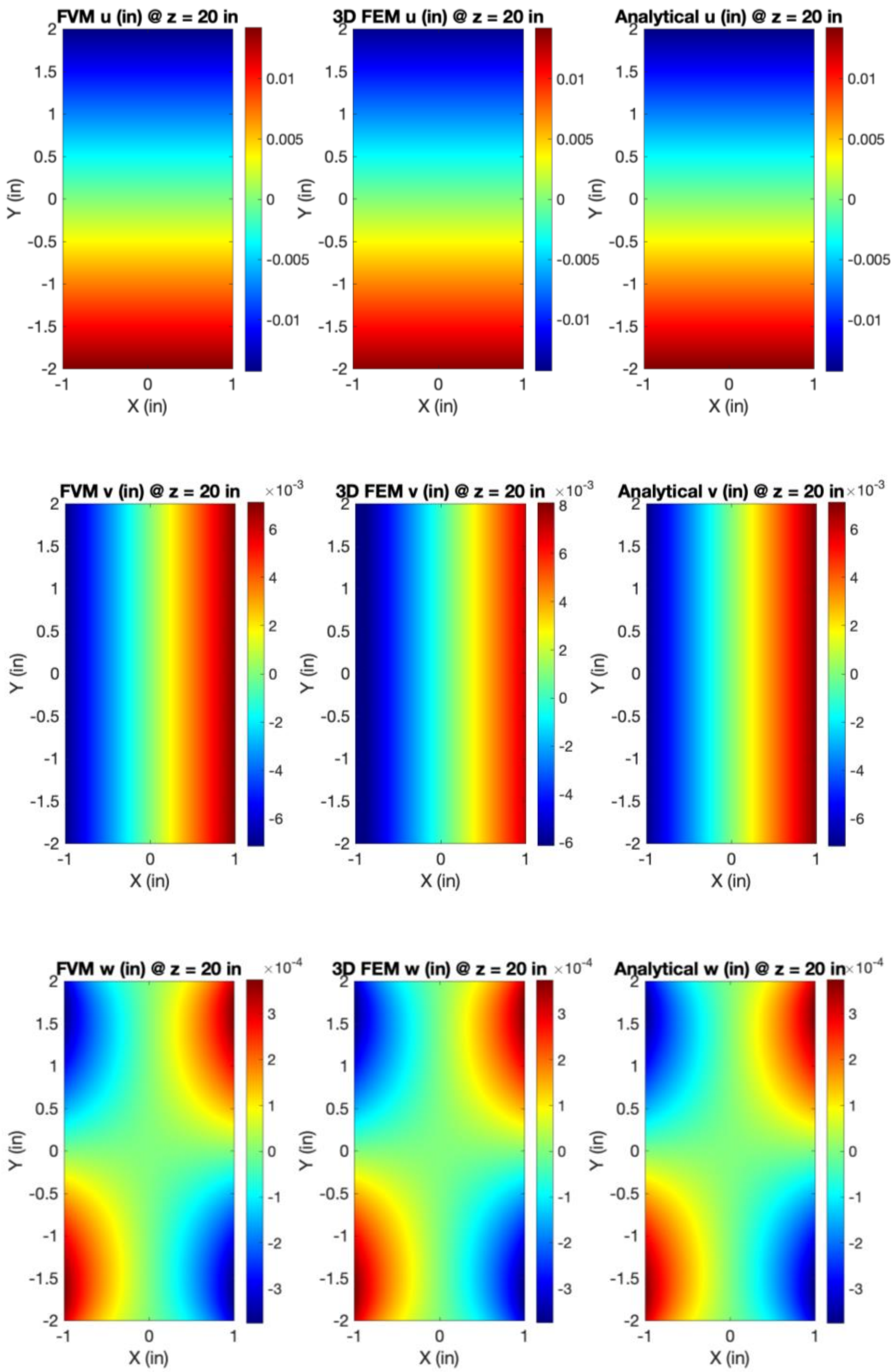

Figure 6-18 Displacements u, v, w distribution for the rectangular beam with $M_z = 30\ kips.in$

The errors in 3D FEM results with respect to the analytical solutions are within 5% for u and v, and are within 1% for w shown in Figure 6-19. FVM solutions do exhibit any noticeable difference relative to the analytical solutions.

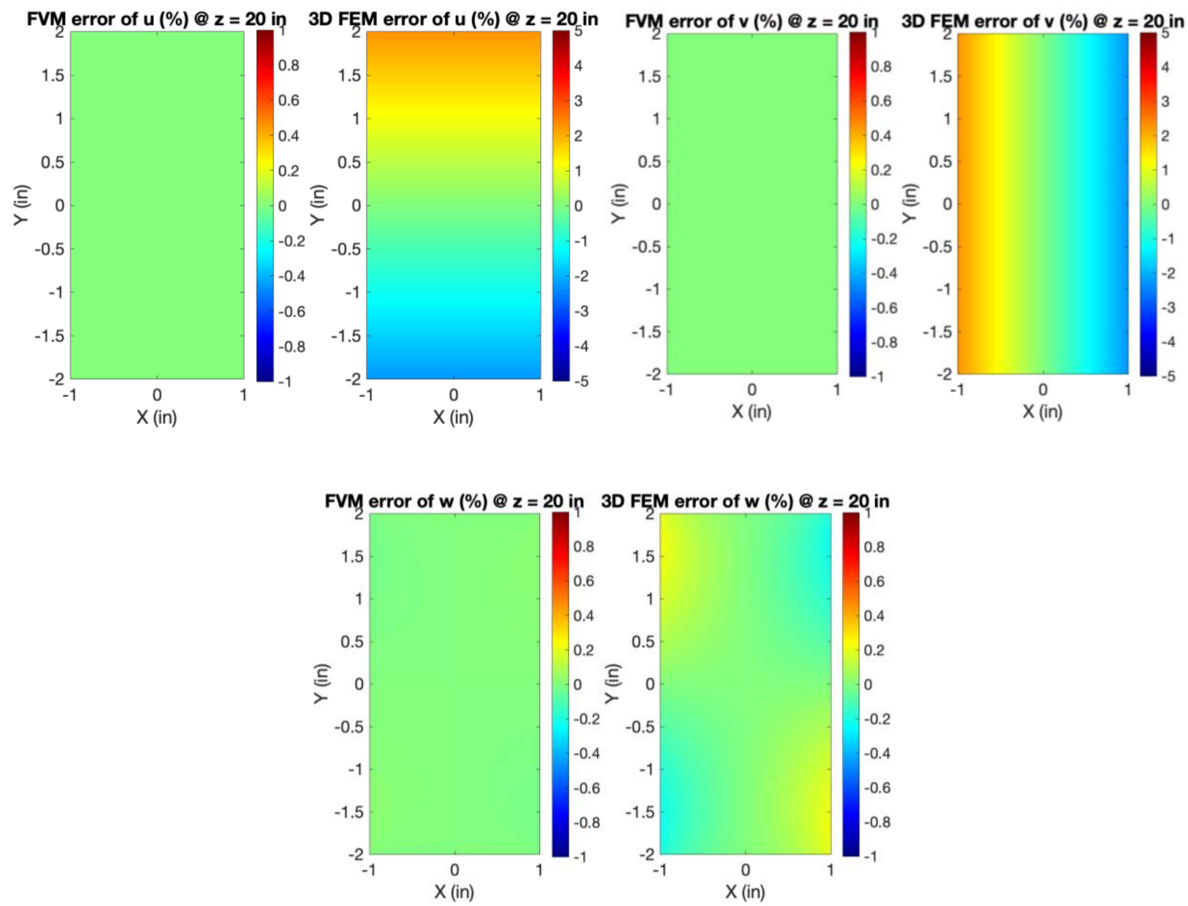

Figure 6-19 Displacements u, v, w distribution errors for the rectangular beam with $M_z = 30\ kips.in$

In summary, for the rectangular beam loaded by only $M_z = 30\ kips.in$ about the center of free end, the shear stresses σ_{xz} and σ_{yz} as well as the displacement w exhibit very similar magnitudes and distributions in the cross sections A, B, and C, while the displacement u and v have similar distributions but different magnitudes according to the assumptions employed in the elasticity solutions. All the errors in FVM or 3D FEM results relative to the analytical solution are relatively small. Though 3D FEM has slightly smaller average and maximum errors than FVM over the entire rectangular cross sections A, B and C in the stress fields, FVM outperforms 3D FEM in predicting the displacements.

6.3.2 Torsion-Flexure of Beams

The numerical methods employed in previous cases could be validated with the analytical approach because of the specific applied loading. For general torsion-flexure problem when more than one deformation mode appears, or problems involving complex beam geometry shape are encountered, no analytical solution is available. Therefore, FVM will only be compared with 3D FEM for mutual verification. A rectangular beam and a C-shape channel beam with an end force applied at the corner, as well as a C-shape channel beam with an end force applied at its shear center will be analyzed in the sequel.

Torsion-flexure about any of principal direction (torsion mode and one flexure mode in FVM):

The performance comparison of the two methods (FVM, 3D FEM) is based on the torsion-flexure response of beams that experience bending about a principal direction as well as rotation produced by the resultant force component $F_x = 10\ kips$ and a twisting moment $M_z = 10\ kips.in$ about the centroid illustrated in Figure 6-20. This is an equivalent treatment of a force situated at the corner of the free end face of the rectangular beam. Unlike the previous cases where the beam either bends about just one principal axis or rotates about the center line, the beam in this case deforms both by twisting and bending due to the eccentric load.

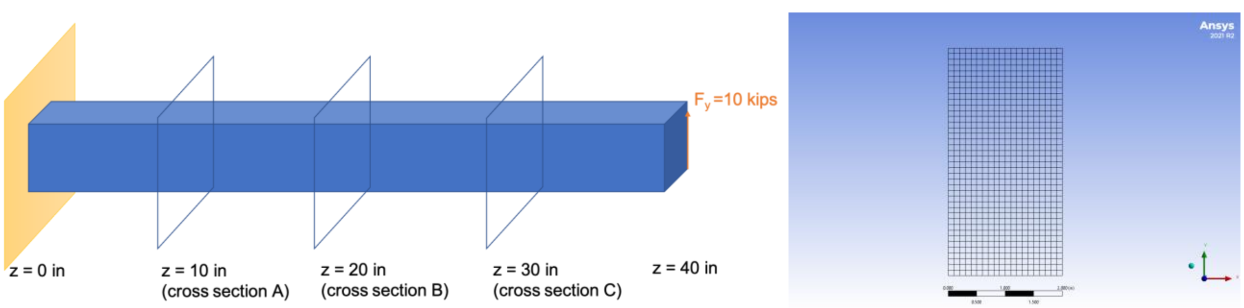

Figure 6-20 Homogeneous isotropic rectangular cantilever beam with a force at the corner (left) and the ANSYS mesh of each cross section with 800 elements (right)

The stresses σ_{xz}, σ_{yz} and σ_{zz} have distributions in the middle cross section B shown in Figure 6-21.

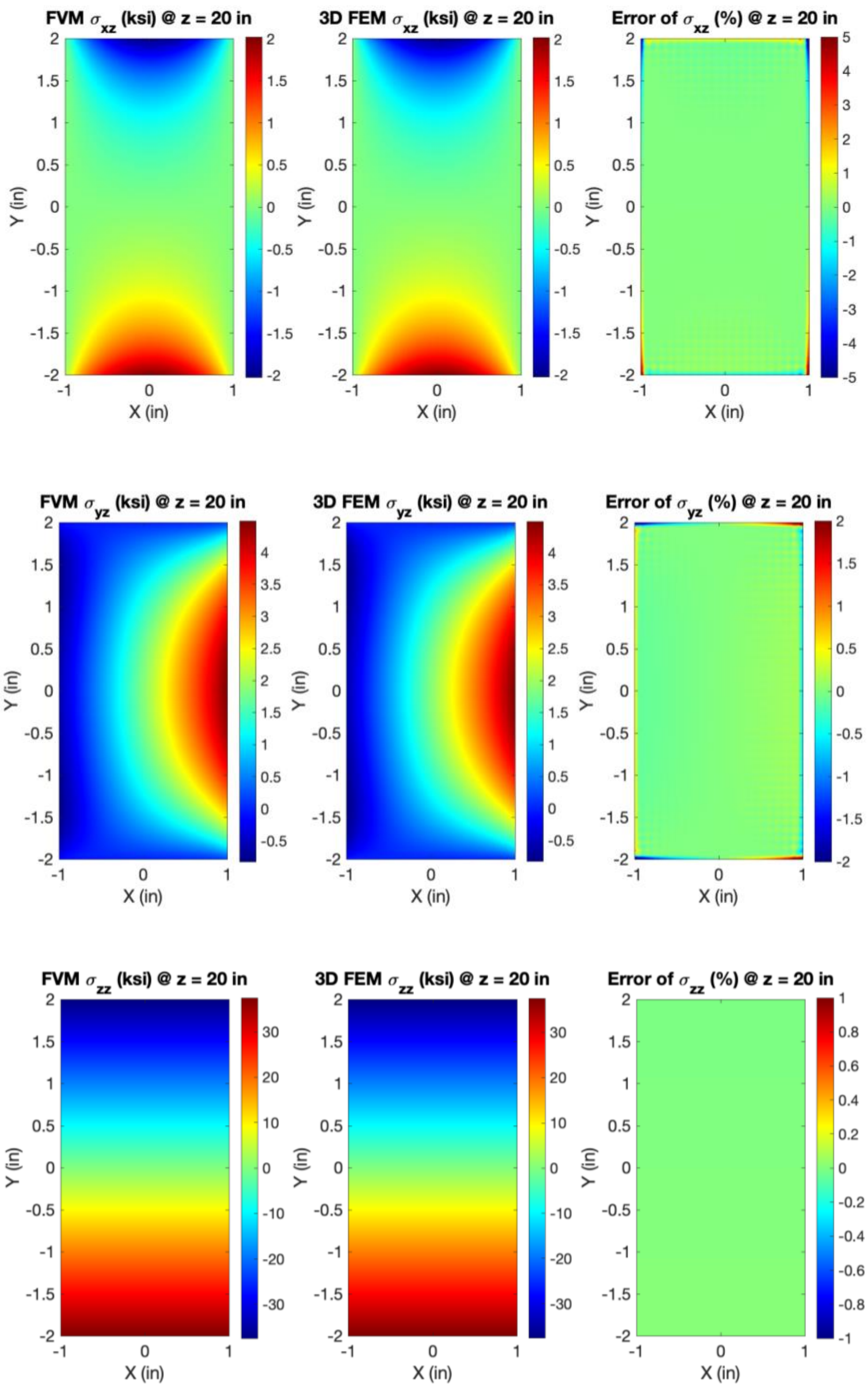

Figure 6-21 Stresses $\sigma_{xz},\ \sigma_{yz},\ \sigma_{zz}$ distribution errors for the rectangular beam with $F_y = 10\ kips\ at\ the\ corner$

Differences in the two shear stress components σ_{xz} and σ_{yz} are limited to very small regions along the right and left, and upper and lower, boundaries of the cross section and vanish within.

The displacements u, v and w have distributions in the middle cross section B also shown in Figure 6-22.

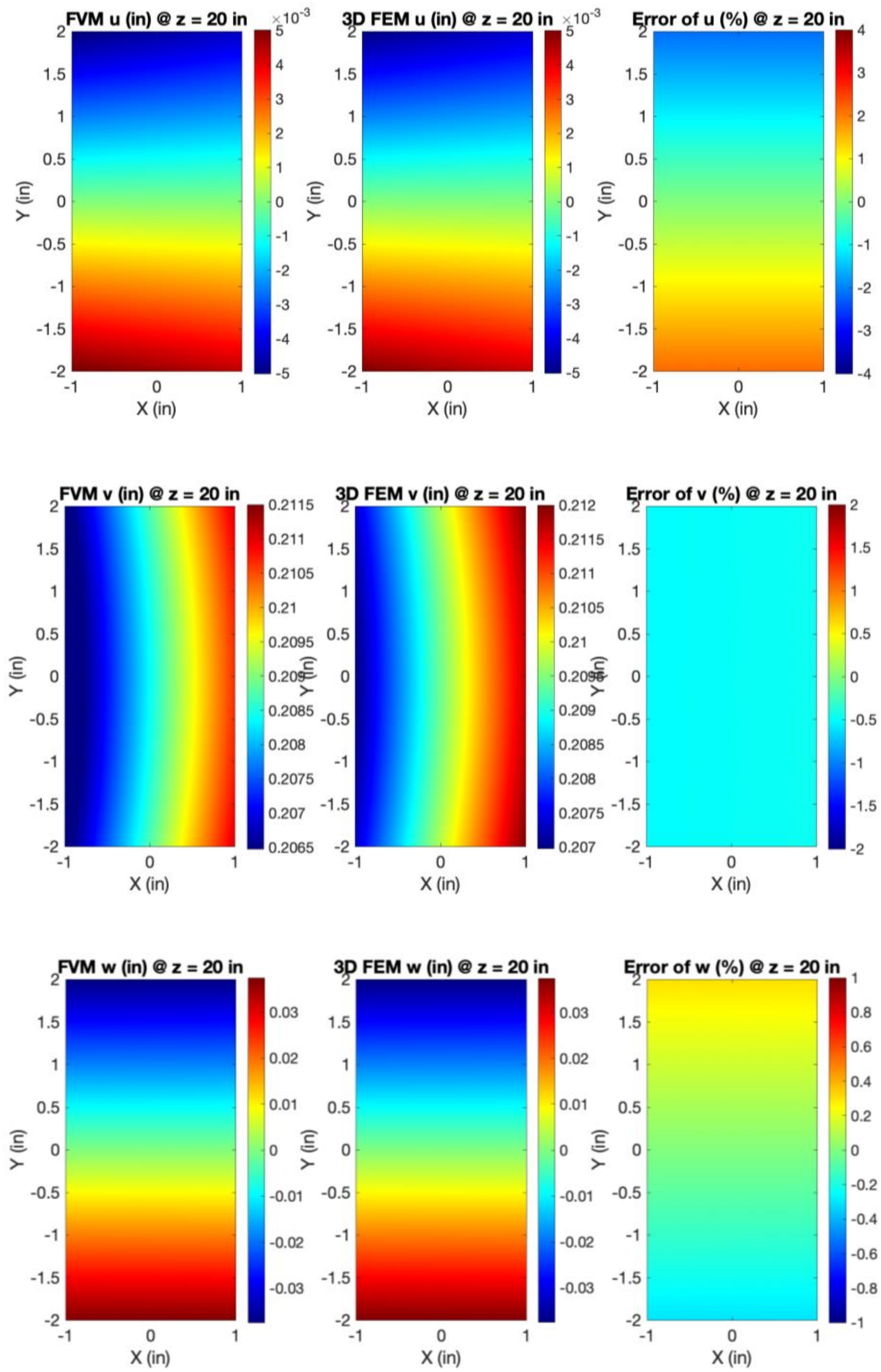

Figure 6-22 Displacements $u,\ v,\ w$ distribution errors for the rectangular beam with $F_y = 10\ kips\ at\ the\ corner$

Differences in the u displacement distributions are observed along the vertical direction, whereas the v displacement has a consistent error of about 0.5% over the entire cross section B. Differences in the w displacement distributions are also observed along the vertical direction, albeit to a much smaller extent than those of u.

Torsion-flexure for C-shape channel beam (one flexure mode in FVM):

The performance comparison of the two methods (FVM, 3D FEM) is based on the torsion-flexure response of beams about a principal direction produced by the resultant force component $F_y = 10\ kips$ located in the shear center of the free end illustrated in Figure 6-23. As the force is directed through the shear center, the beam only bends only about the x axis without twisting.

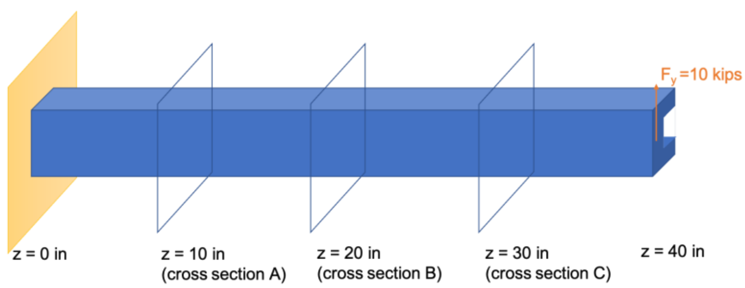

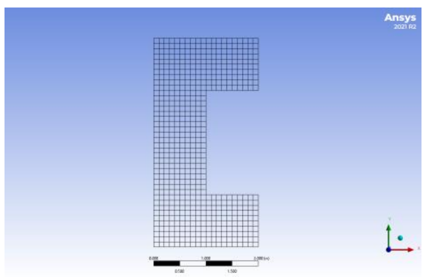

Figure 6-23 Homogeneous isotropic C-shape channel cantilever beam with a force at the shear center (left) and the ANSYS mesh of each cross section with 600 elements (right)

The shear center, where F_y resides, is computed by FVM based on the geometry of the cross section using the approach described in Chapter 5. All the stresses σ_{xz}, σ_{yz} and σ_{zz} have close distributions in the middle cross section B shown in Figure 6-24.

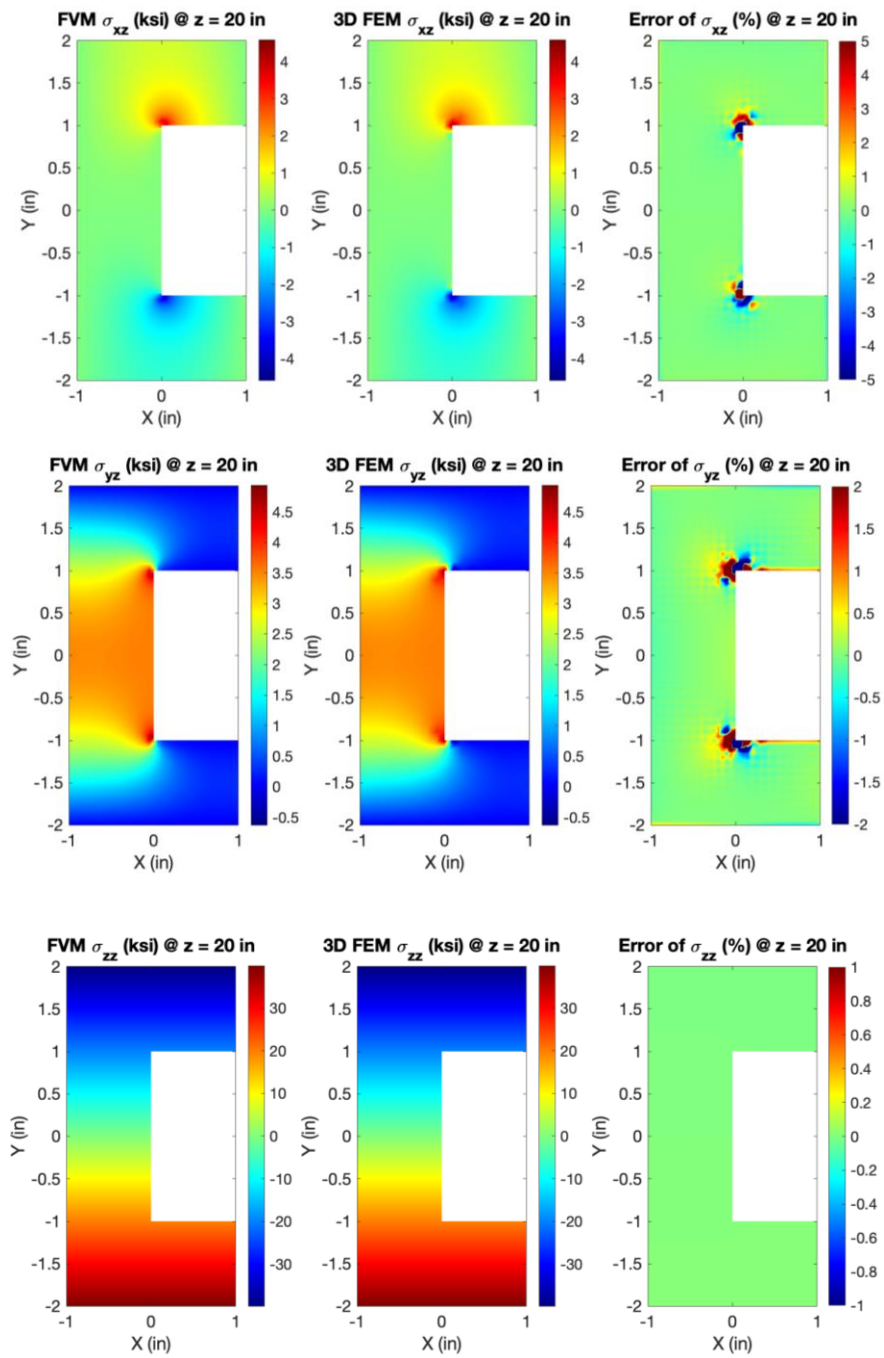

Figure 6-24 Stresses σ_{xz}, σ_{yz}, σ_{zz} distribution errors for the C-shape channel beam with $F_y = 10\ kips$ at the shear center

Major differences are observed concentrating at the re-entrant corners of the C-shape cross section for σ_{xz} and σ_{yz}. The field plots for the displacements u, v, w are not shown here for conciseness as FVM and 3D FEM generate close results. However, it is worth noting that the horizontal displacement varies from -0.0006 to 0.0006 inch in both FVM and 3D FEM predictions, indicating absence of twisting movement in the C-shape channel beam for loading applied through its shear center.

Torsion-flexure for C-shape channel beam (torsion mode and one flexure mode in FVM):

The performance comparison of the two methods (FVM, 3D FEM) is based on the torsion-flexure response of beams experiencing bending about a principal direction as well as rotation both produced by the resultant force component $F_y = 10\ kips$ located at the corner of the free end illustrated in Figure 6-25, which generates an additional moment about the shear center.

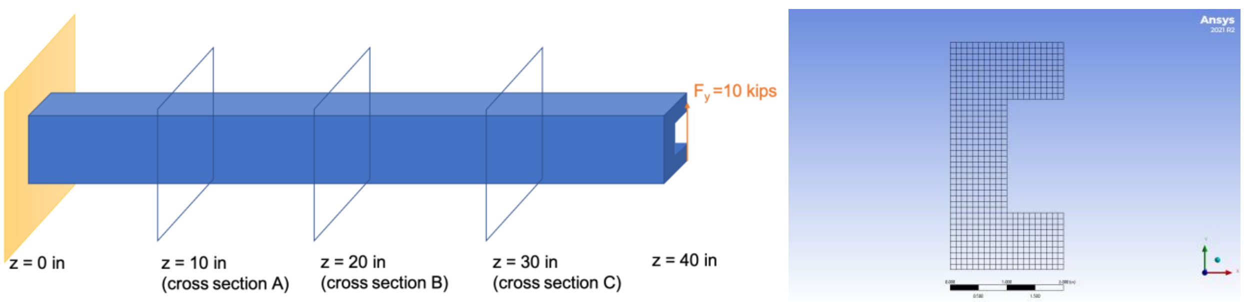

Figure 6-25 Homogeneous isotropic C-shape channel cantilever beam with a force at the corner (left) and the ANSYS mesh of each cross section with 600 elements (right)

The stresses σ_{xz}, σ_{yz} and σ_{zz} have close distributions in the middle cross section B shown in Figure 6-26:

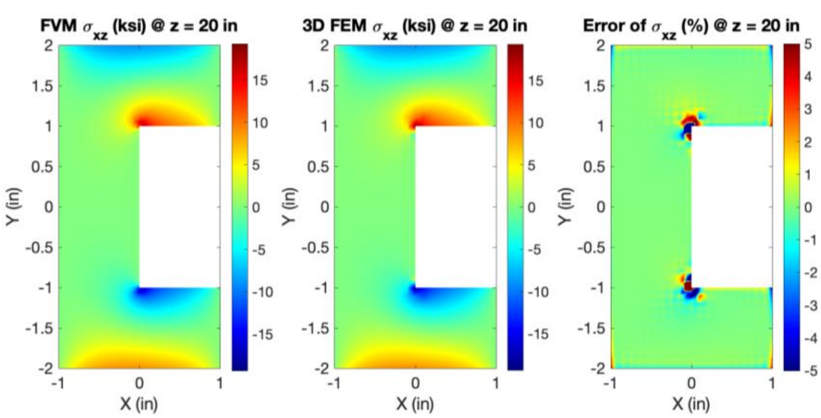

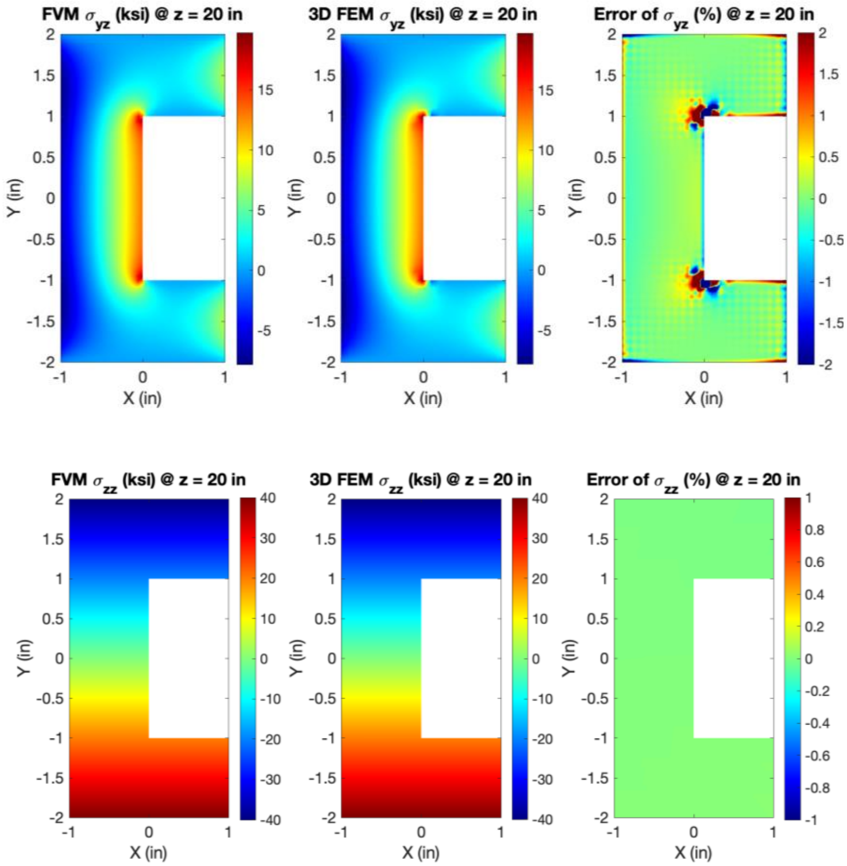

Figure 6-26 Stresses σ_{xz}, σ_{yz}, σ_{zz} distribution errors for the C-shape channel beam with $F_y = 10\ kips$ at the corner

The shear stresses σ_{xz} and σ_{yz} become more intense as torsion greatly contributes to shear deformation, while the normal stress σ_{zz} remains unchanged from the previous case. Major differences still concentrate at the re-entrant corners of the C-shape cross section for σ_{xz} and σ_{yz}.

6.4 Variation of Cross-Sectional Performance Along the Longitudinal Axis

The torsion-flexure problem involves analysis of deformation and stress distributions in a structural member subjected to both torsional and flexural loads. Understanding the behavior of structural members under these loads is critical for designing safe and efficient structures. One of the key assumptions behind the solution of the torsion-flexure problem is the Saint-Venant's principle, which states that the actual boundary conditions and their statical equivalent will produce the same stress field at a sufficient distance from the boundary. This principle allows engineers to simplify the analysis of complex structures by focusing on a smaller region rather than analyzing the entire structure.

To validate the Saint-Venant's principle, cross section analysis at different distances from the end of the structural member can be conducted using numerical methods such as the proposed FVM and 3D FEM. Both methods provide detailed information about the stress distribution and deformation within the structural member, allowing one to compare the results with the Saint-Venant's principle. This section aims to perform a comprehensive validation of the Saint-Venant's principle by analyzing the torsion-flexure problem using FVM and 3D FEM on multiple cross sections along the beam's span. The stress distribution and deformation in the structural member at different distances from the end will be investigated to determine how far from the fixed end the Saint-Venant's principle becomes valid. This section may have significant implications in designing more efficient and safer structures and providing insights into design limitations near the ends of a beam.

Torsion-flexure for rectangular beam (torsion mode and both flexure modes in FVM):

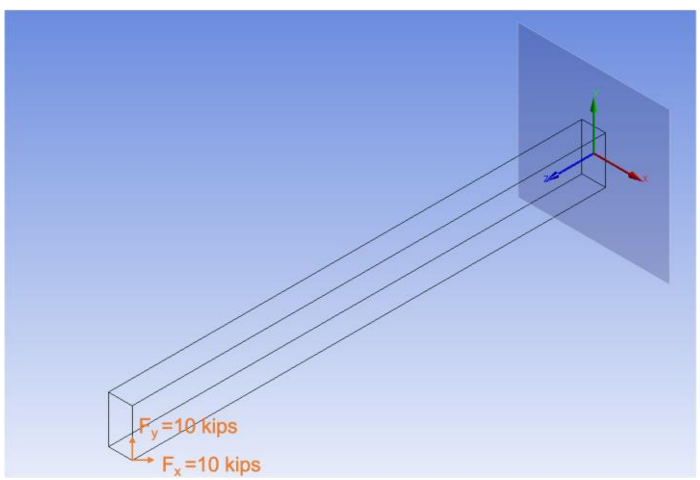

Figure 6-27 Homogeneous isotropic rectangular cantilever beam with combined forces at the corner

The meshing rectangular units in both 3D FEM and FVM are uniform 0.05×0.05 inch, and the cross section has the dimension of 2×4 inches. The average errors for quantities of interest among all the vertices of the meshing units are plotted versus the longitudinal coordinates of each cross section in Figure 6-28.

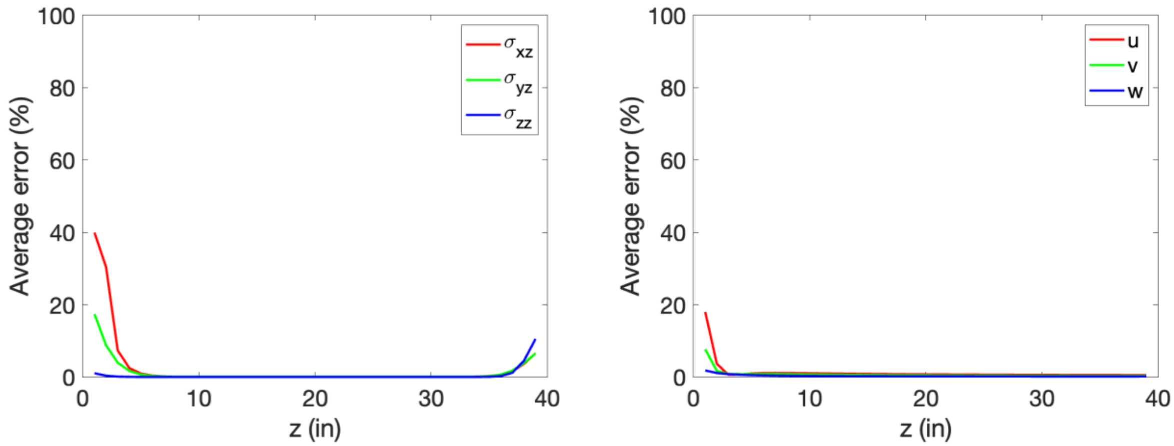

Figure 6-28 The error variation of stresses and displacements along the length of a homogeneous isotropic rectangular cantilever beam with combined forces at the corner

The stresses σ_{xz}, σ_{yz}, and σ_{zz} all have less than 0.05% averaged errors in interior cross sections ranging from $z = 6$ to $z = 35$ inches. In the immediate vicinity of the fixed end or the end where load is applied, the FVM shear stress predictions differ substantially from the 3D FEM results, with the differences vanishing at distances approximately one and a half times the beam height as expected from the Saint Venant's principle. In contrast, the averaged errors in the displacements u, v and w are much smaller than the shear stress errors and decrease at a faster rate with increasing distance from the fixed end. Beyond $z = 3$ inches from the fixed end the averaged errors in the displacements are below 1.2%.

Torsion-flexure for I shape beam (torsion mode and both flexure modes in FVM):

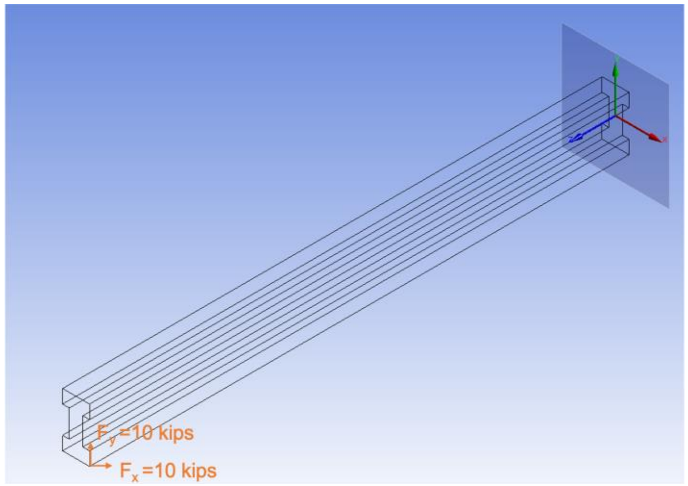

Figure 6-29 Homogeneous isotropic I-shape cantilever beam with combined forces at the corner

With the same meshing unit size as previous (uniformly 0.05×0.05 inch), this I-shape beam cross section has the overall dimension of 2×4 inches. Both the web and flanges are 1 inch thick. The average errors for quantities of interest among all the vertices of the meshing units are plotted versus the longitudinal coordinates of each cross section in Figure 6-30.

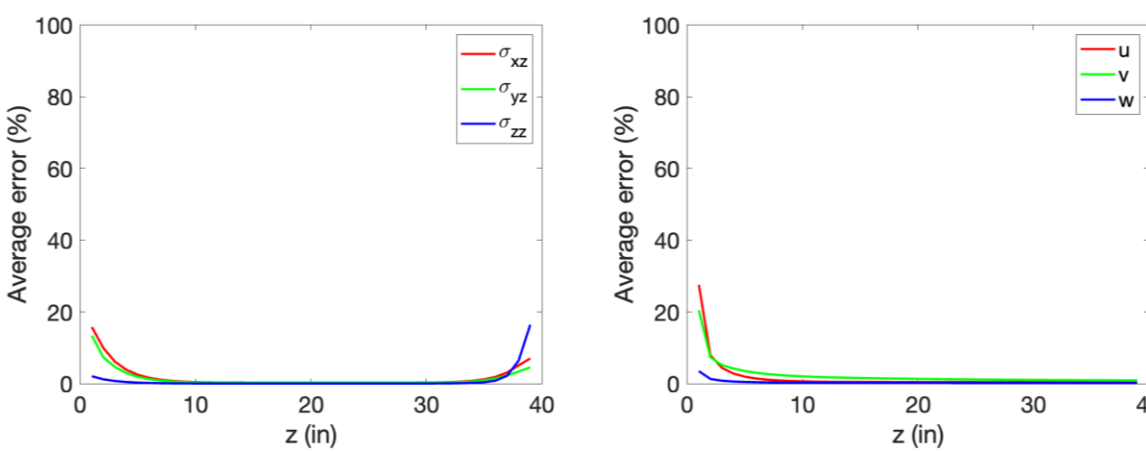

Figure 6-30 The error variation of stresses and displacements along the length of a homogeneous isotropic I-shape cantilever beam with combined forces at the corner

The stresses σ_{xz}, σ_{yz}, and σ_{zz} all have less than 1% averaged errors in cross sections ranging from $z = 7$ to $z = 35$ inches, which indicates error attenuation similar to that of the rectangular beam. This points to the importance of the overall cross section dimensions rather than cross sectional details as one would expect from Saint Venant's principle. Apparently, the cross-sectional geometry influences the magnitude of the differences at the fixation point, producing smaller errors for the I beam relative to the rectangular beam. The averaged errors in the displacements u, v and w die down as the cross-section's distance increases from the fixed end to the free end, with all the averaged displacement errors below 2% beyond $z = 10$ inches.

Torsion-flexure for C-shape beam (torsion mode and both flexure modes in FVM):

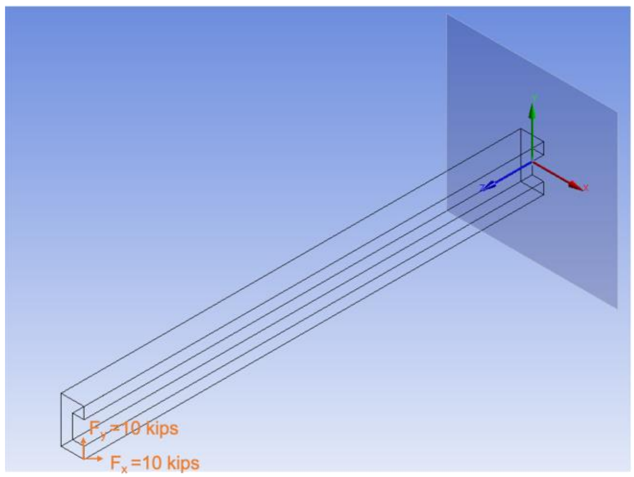

Figure 6-31 Homogeneous isotropic C-shape cantilever beam with combined forces at the corner

With the same meshing unit size as previous (uniformly 0.05×0.05 inch), this C-shape channel beam cross section has the overall dimension of 2×4 inches. Both its web and flanges are 1 inch thick. The average errors among all the vertices of the meshing units are plotted versus the longitudinal coordinates of each cross section in Figure 6-32.

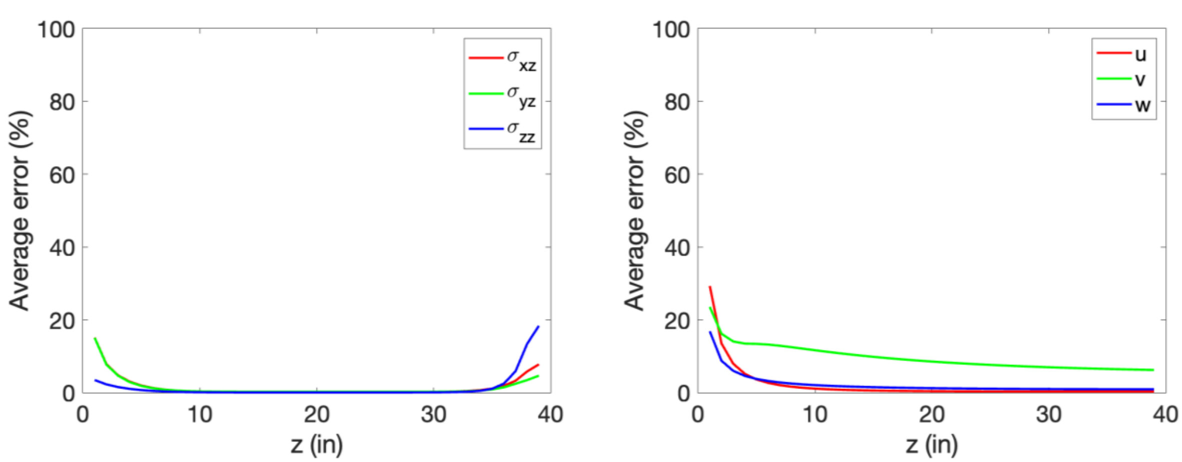

Figure 6-32 The error variation of stresses and displacements along the length of a homogeneous isotropic C-shape channel cantilever beam with combined forces at the corner

The stresses σ_{xz}, σ_{yz}, and σ_{zz} all have less than 1% averaged errors in cross sections ranging from $z = 6$ to $z = 34$ inches, which again confirms the error attenuation rate similar to those observed for the rectangular and I-shape beams, further supporting the validity of Saint Venant's principle in structural engineering applications. The averaged errors of displacements u, v and w decrease as the cross section moves from the fixed end to the free end as predicted. The averaged errors of the u and w displacements are below 2% beyond $z = 10$ inches, while the averaged errors of the v displacements are above 6.2% for all the cross sections analyzed.

6.5 Summary

Two structural modeling approaches are compared for torsion-flexure of beams: 3D FEM and FVM. The FEM approach is a well-established numerical method for analyzing the torsion-flexure response of structures. The FVM is a relatively new and emerging approach that exhibits the potential to address certain limitations of 3D FEM. FVM offers improved computational efficiency, demonstrating a speed advantage of five to six times faster compared to 3D FEM. Moreover, FVM outperforms 3D FEM in displacement field predictions, albeit at the expense of small degradation in the stress fields, under pure flexure of a rectangular cross section. The comparison of the two methods' performance in torsion-flexure can contribute to the field of structural engineering by providing reliable insights into the strengths and weaknesses of different numerical methods for analyzing the torsion-flexure response of beams. The results of this chapter also demonstrate the suitability of FVM modeling approaches for different types of beam problems and their future applications in the design of real-world structures. The Saint Venant's principle is verified in solving the torsion-flexure problem which validates the FVM's capability in analyzing cross sections away from the ends where the manner of applying boundary conditions matters.

This chapter helps bridge the gap between the existing numerical approaches, such as 3D FEM and FVM as well as the analytical approaches, thereby broadening the scope of beam modeling approaches available to engineers. Ultimately, this study could aid in the design and development of safer and more efficient structures in various fields of engineering.

Chapter 7

Summary and Conclusions

7.1 Summary of Accomplishments

The theory of elasticity provides a mathematical framework for studying elastic deformation and stress distribution of solid materials subjected to external loads. When applied to general three-dimensional deformation problems, the theory of elasticity can become complex and computationally intensive. Reducing a three-dimensional problem in elasticity to a quasi-three-dimensional one greatly simplifies the analysis by making assumptions for a body or structure under specific considerations. Therefore, categories of elasticity problems are made based on geometry and the manner of boundary condition application that gives rise to specific functional forms of displacements, strains and stresses arising within the elastic body or structure. This dissertation develops two novel implementations of finite-volume based solutions for three technically important classes of problems in the theory of elasticity: *plane problems, torsion problems* and *flexure problems*. Plane problems form a large category applicable to solid materials subjected to loads that act only in the plane of the structure. Plane condition assumptions help establish two-dimensional models for analyzing the behaviors of plates, shells or thick structures under different loading conditions. By understanding the stresses and strains in structures under plane loading conditions, structural engineers are able to design structures that are optimized to withstand different types of force and displacement loadings. The other technically important class of problems in the theory of elasticity concerns the study of prismatic bars of arbitrary cross section bounded by a cylindrical surface and by a pair of planes normal to the traction-free surface with loadings applied only on its end faces. When the applied loading produces twisting only, this class of problems is called torsion and often treated as a separate class of problems. The complete problem of equilibrium of an elastic bar can be solved by utilizing the principle of superposition because loading applied to the end faces can be decomposed into four elementary loadings that produce: extension, bending, torsion, and flexure. Analyzing the behavior of beams under these four fundamental modes of deformation provides structural engineers with insights into the design of beam-like structures that can resist these loads with greater efficiency and safety.

Numerical methods in mechanics based on variational principles can provide solutions to the above classes of elasticity problems even for which analytical solutions do not exist. An attractive alternative to the solution of those problems is offered by the finite-volume method (FVM) which has gained popularity because of its explicit form and ability to deal with composite structures. The FVM specifically suited to the above classes of elasticity problems was developed by leveraging the classical finite-volume direct averaging micromechanics (FVDAM), Bansal and Pindera (2003, 2005).

In the context of plane problems, plane stress, plane strain and generalized plane strain conditions have been formulated within the parametric finite-volume framework for numerical solution implementation. Moreover, FVM has been extended to accommodate the analysis of structural components composed of orthotropic and monoclinic materials. The FVM solution for plane problems has been verified using elasticity solutions for rectangular cantilever beams subjected to bending loads under plane strain and plane stress conditions, and subsequently employed to investigate technologically significant problems of multi-layered beams and heterogenous beams with inclusions and porosities under transverse bending loads. The generated solutions were subsequently used to address questions regarding the applicability of homogenization when analyzing the response of multilayered beam or plate-like structures, as well as simulated response of composite beams under generalized plane strain. The FVM has also been applied to assist in the shear characterization of advanced unidirectional composites in off-axis tension tests and Iosipescu shear tests, and to evaluate analysis errors in these two common test methods employed for the determination of the axial shear modulus.

As one fundamental deformation problem, the Saint Venant's torsion of bars comprised of rectangular orthotropic sections previously developed by the author has been extended to enable analysis of arbitrary cross sections characterized by curved boundaries in a similar parametric manner as in the FVM solution of plane problems. A comprehensive assessment and verification of the convergence and accuracy of the parametric finite-volume method was first presented by comparing it with elasticity solutions for cross sections with both convex and concave boundaries.

The FVM was subsequently applied to various structural applications of prismatic bars with curved boundaries, including star-shaped cross sections with homogeneous and graded regions designed to enhance torsional rigidities, and elliptical cross sections with orthotropic shear moduli designed to reduce and eliminate warping. The analysis also included multi-phase and multi-porosity cross sections. The results demonstrate that warping of solid cross sections can be mitigated through layering, and warping of porous cross sections may be mitigated through porosity grading. Additionally, torsional analysis of natural materials highlights the importance of considering actual microstructural details in the torsional response of natural heterogeneous cross sections, as demonstrated by the analysis of a bamboo's functionally graded cross section. The developed FVM and its findings provide valuable insights for the torsional design and analysis of a wide range of complex structural systems.

Flexure is another basic but non-trivial deformation mode as the flexure response of beams can produce significant shear stresses which are often overshadowed by larger magnitudes of bending stresses. The Saint-Venant's semi-inverse method provides a framework for this class of problems based on assumed stress distributions that lead to solutions satisfying conditions of equilibrium and compatibility rather than assumed in-plane displacements based on kinematics in the torsion problem formulation. Analytical solutions have been developed for flexure problems, but they are limited to simple homogenous cross sections that are typically not of wide-ranging structural engineering interest. Beam cross sections that appear in structural designs are not easily amenable to analytical techniques and require either structural approximations or numerical solutions. FVM then has been developed to formulate the solution of the flexure problem as an alternative to FEM. Validation of the accuracy of FVM includes specialized comparison with pure bending results obtained by analytical methods for homogeneous circular, elliptic and rectangular beam problems.

Flexure without twisting only occurs when a cylindrical beam is subjected to loadings at one end whose resultant passes through the beam's shear center. Once the shear center is identified for a beam's cross section, the torsion-flexure problem can be decomposed into three deformation modes: two flexure modes in the two principal in-plane direction and the torsion mode about the longitudinal direction. The determination of the shear center as well as the decomposition approach for composite beams with uniform Poisson's ratios has been programmed using FVM and validated through convergence studies using equilateral triangular and semi-circular cross sections. FVM was also employed to assess the thin-wall structure assumptions commonly used in structural engineering practice for thin-walled cylindrical members. To check the programmed approach to determine the shear center via FVM, as well as to examine the flexure response of heterogeneous beams, a two-phase concentric beam was analyzed and the FVM predictions compared with the analytical solution, demonstrating high agreement.

A comprehensive assessment of the decomposition methodology intrinsic to FVM is conducted against the 3D FEM simulation. FVM approach demonstrated its potential in overcoming some of the limitations of 3D FEM, such as increased computational efficiency. Moreover, FVM outperformed 3D FEM in displacement field predictions, albeit at the expense of small degradation in the stress fields, under pure flexure of a rectangular cross section. The comparison of the two methods' performance in torsion-flexure of various beams contributes to the field of structural engineering by providing reliable insights into the strengths and weaknesses of different numerical methods for analyzing the torsion-flexure response of beams. The decomposition approach of the torsion-flexure behavior into separate deformation modes has been successfully assessed in rectangular, I-shape and C-shape cross sections along the beam's span at various distances from the ends. Hence, Saint Venant's principle was verified in solving the torsion-flexure problem which validated FVM's capability in analyzing cross sections away from the ends where the manner of applying boundary conditions matters. The gap between the existing numerical approaches, such as 3D FEM and FVM as well as the analytical approaches was filled, and the scope of beam modeling approaches available to engineers was broadened with more design confidence.

This dissertation demonstrated the application of the finite-volume method developed at the University of Virginia during the past twenty years to structural engineering problems involving torsion, flexure and plane problems of elasticity theory, thereby building a bridge between the two fields that are often treated separately. This involves the extension of the finite-volume theory to enable solutions to the three classes of elasticity problems, and subsequent application to the solution of specific problems of importance in the design of structural engineering components as well as advanced material testing. Traditional and emerging structural components were considered, including components made up of laminated cross sections, and cross sections reinforced or weakened by cylindrical inclusions or cavities. Application to the testing of orthotropic and monoclinic materials was also provided through appropriate extension of the finite-volume theory to accommodate orthotropic and monoclinic materials.

The completed work fills the gap between structural engineering and mechanics on the one hand and elasticity theory formulation and limited solutions of the related problems when they cannot be treated using the analytical approach. It also provides a powerful alternative to the widespread use of variational techniques for the considered classes of structural engineering problems. Ultimately, this dissertation has the potential to aid in the design and development of safer and more efficient structures in various fields of engineering from the accurate analysis conducted by FVM.

7.2 Summary of Contributions

While the finite-volume theory has been used extensively in the solution of plane problems with isotropic materials, including contact and crack problems, there appear to be no reported results that address the use of the FVM in the solution of plane problems with materials more complicated than orthotropic, such as monoclinic materials with a single plane of material symmetry. Materials with monoclinic elastic moduli in the coordinate system in which analysis is conducted are obtained by rotating a unidirectional composite through an angle about the out-of-plane axis. Multi-directional laminated plates made up of a number of such plies are employed in numerous structural engineering applications, including the aircraft industry. Off-axis plies are also employed in the determination of the axial shear modulus of advanced unidirectional composites based on the off-axis tension test because of its simplicity. The extended finite-volume theory enables re-examination of the effects of various parameters on the accuracy of the results obtained from this test method.

Selected problems involving laminated constructs with rectangular cross sections within the plane strain elasticity framework are also revisited in the context of microstructural effects introduced by the individual layers. Explicit treatment of such microstructures based on the finite-element method is challenging due to the need for extensive discretization when the elastic moduli contrast between the layers is large in the presence of large number of layers. Such problems are illustrated to be readily solved using the finite-volume method.

The major contributions of this dissertation include the extension of the finite-volume theory to the Saint-Venant's torsion problem involving arbitrarily shaped cross sections enabled by newly implemented parametric mapping, and the implementation of stress-based formulation of the general torsion-flexure problem based on the Saint-Venant's semi-inverse method as well. The parametric mapping capability is implemented within any structured or non-structured mesh framework. This is complemented by a novel incorporation of arbitrary discretization capability and the corresponding assembly algorithm for the global system of equations that enables efficient modeling of cross sections reinforced or weakened by inclusions or porosities, illustrated through examples from the traditional industry and natural plant world.

In addition, there is a need for a series of accurate, efficient and easy-to-use computational tools that automatically generate results and provide quick answers to the pure torsion problems or even the more general torsion-flexure problems in the analysis and design of structural elements. One of the byproducts of this dissertation research is a computer program that enables pure torsion analysis of homogeneous and composite structures with the output given in terms of displacement, strain, and stress fields, as well as the torsion rigidity, based on solid elasticity foundations. Figure 7-1 shows a screenshot of a developed GUI for the torsional analysis of typical structural engineering beams. The cross sections include rectangular, I, T, channel and box beams, and will be expanded to a wide range of beams used in aerospace engineering. A practicing engineer will choose a specific cross section, define the dimensions, specify either isotropic or orthotropic moduli and load locations to generate the torsional response.

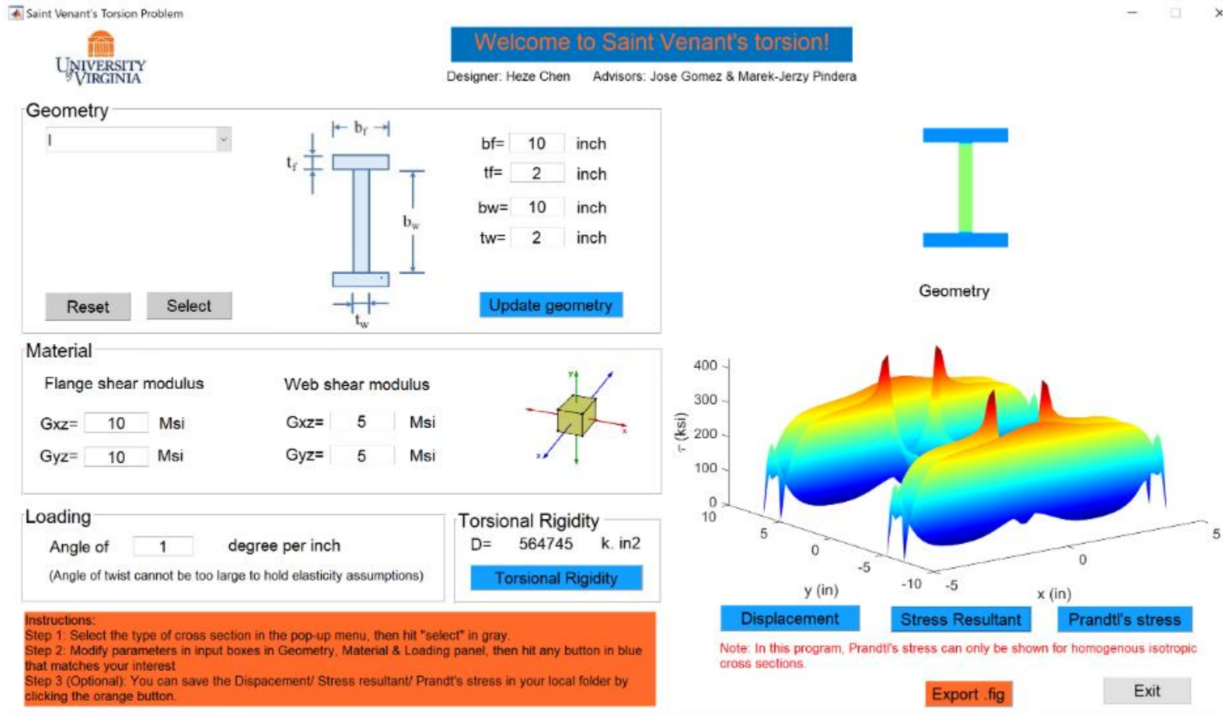

Figure 7-1 MATLAB GUI screenshot: solving the torsion problem for an I-beam

At present, this may only be achieved by a detailed finite-element analysis based on a variational principle that requires detailed meshing, as well as substantial training on using commercially available software. A series of MATLAB-based or Python-based computational tools executed through user-friendly graphical user interfaces based on the developed finite-volume solution strategy will democratize structural engineering analysis in this area, increasing accessibility, and accelerating the development of novel structural designs.

7.3 Present Limitations and Future Work

The construction of the FVM-based solutions of plane problems, torsion problems and torsion-flexure problems was based on certain elasticity assumptions which can limit the range of applications in structural engineering. Despite this constraint, FVM exhibits potential to overcome some of the limitations of FEM for torsion and torsion-flexure analyses, such as the requirement of sufficiently fine mesh in the vicinity of material changes. However, FVM is currently limited to certain types of stress or displacement field assumptions and boundary conditions and requires further research to be applied to a broader range of beam problems, e.g., the torsion-flexure of composite beams with isotropic or more complex material properties.

The reduction of a three-dimensional torsion-flexure problem to three two-dimensional ones in the spirit of computational efficiency comes at the cost of sacrificing the possibility of obtaining results generated from full three-dimensional modeling in the immediate vicinity of fixation points and/or load application. The results in Chapter 6 confirm the error attenuation for the three types of beams away from the beam ends, supporting the validity of Saint Venant's principle in structural engineering applications. While the FVM has been shown to be effective in analyzing problems (plane problems, torsion problems, and torsion-flexure problems) in two-dimensional domains, many engineering applications involve structures with complex 3D geometries. Therefore, a natural extension of the completed FVM framework for the above classes of problems work would be to extend it to three-dimensional elasticity problems.

One of the potential applications of the three-dimensional finite-volume method (3D FVM) includes the analysis of composite materials with complex microstructures. The ability to accurately predict the mechanical response of such materials is critical for their design and optimization in the industry that needs high-accuracy results. This could include analysis of laminates with curved or twisted fibers, as well as incorporation of voids and inclusions into the model. The 3D FVM with periodic boundary conditions has been formulated and tested by Chen et al. (2016, 2018) with cubic subvolumes and parametric hexahedron subvolumes. The 3D FVM could also possibly involve the challenging use of unstructured meshes, adaptive subvolume geometry, and even higher-order theory for three-dimensional finite-volume schemes, and more importantly, its compatibility to deal with structural boundary conditions in modeling real 3D structural problems.

References

Aboudi, J., Pindera, M.-J., & Arnold, S. M. (1999). Higher-order theory for functionally graded materials. Composites Part B: Engineering, 30(8), 777-832.

Aboudi, J., Pindera, M.-J., & Arnold, S. M. (2003). Higher-order theory for periodic multiphase materials with inelastic phases. International Journal of Plasticity, 19(6), 805-847.

Bansal, Y., & Pindera, M.-J. (2003). Efficient reformulation of the thermoelastic higher-order theory for functionally graded materials. Journal of Thermal Stresses, 26(11-12), 1055-1092.

Bansal, Y., & Pindera, M.-J. (2005). A second look at the higher-order theory for periodic multiphase materials. J. Appl. Mech., 72(2), 177-195.

Bansal, Y., & Pindera, M.-J. (2006). Finite-volume direct averaging micromechanics of heterogeneous materials with elastic–plastic phases. International Journal of Plasticity, 22(5), 775-825.

Barretta, R. (2014). Analogies between Kirchhoff plates and Saint-Venant beams under flexure. Acta Mechanica, 225(7), 2075-2083.

Birman, V., & Byrd, L. W. (2007). Modeling and analysis of functionally graded materials and structures.

Boresi, A. P., & Schmidt, R. (1985). Sidebottom. Advanced mechanics of materials, 4.

Bufler, H. (1971). Theory of elasticity of a multilayered medium. Journal of Elasticity, 1(2), 125-143.

Buryachenko, V. (2007). Micromechanics of heterogeneous materials. Springer Science & Business Media.

Cardiff, P., & Demirdžić, I. (2021). Thirty years of the finite volume method for solid mechanics. Archives of Computational Methods in Engineering, 28(5), 3721-3780.

Cavalcante, M. A., & Marques, S. P. (2014). Homogenization of periodic materials with viscoelastic phases using the generalized FVDAM theory. Computational Materials Science, 87, 43-53.

Cavalcante, M. A., & Pindera, M. -J. (2016). Generalized FVDAM theory for elastic–plastic periodic materials. International Journal of Plasticity, 77, 90-117.

Cavalcante, M. A., Marques, S. P., & Pindera, M. J. (2008). Computational aspects of the parametric finite-volume theory for functionally graded materials. Computational Materials Science, 44(2), 422-438.

Cavalcante, M. A., Marques, S. P., & Pindera, M.-J. (2007). Parametric formulation of the finite-volume theory for functionally graded materials—part I: analysis.

Cavalcante, M. A., Marques, S. P., & Pindera, M.-J. (2007). Parametric formulation of the finite-volume theory for functionally graded materials—Part II: numerical results.

Cavalcante, M. A., Pindera, M.-J., & Khatam, H. (2012). Finite-volume micromechanics of periodic materials: past, present and future. Composites Part B: Engineering, 43(6), 2521-2543.

Charalambakis, N., & Murat, F. (2006). Homogenization of stratified thermoviscoplastic materials. Quarterly of applied mathematics, 64(2), 359-399.

Chatzigeorgiou, G., Charalambakis, N., & Murat, F. (2008). Homogenization problems of a hollow cylinder made of elastic materials with discontinuous properties. International Journal of Solids and Structures, 45(18-19), 5165-5180.

Chen, H., Gomez, J., & Pindera, M.-J. (2020). Saint Venant's torsion of homogeneous and composite bars by the finite volume method. Composite Structures, 242, 112128.

Chen, H., Gomez, J., & Pindera, M.-J. (2021). Parametric finite-volume method for Saint Venant's torsion of arbitrarily shaped cross sections. Composite Structures, 256, 113052.

Chen, T. (2004). A homogeneous elliptical shaft may not warp under torsion. Acta Mechanica, 169(1-4), 221-224.

Chen, T., & Wei, C.-J. (2005). Saint-Venant torsion of anisotropic shafts: theoretical frameworks, extremal bounds and affine transformations. Quarterly Journal of Mechanics and Applied Mathematics, 58(2), 269-287.

Chen, Q., Chen, X., Zhai, Z., & Yang, Z. (2016). A new and general formulation of three-dimensional finite-volume micromechanics for particulate reinforced composites with viscoplastic phases. Composites Part B: Engineering, 85, 216-232.

Chen, Q., Wang, G., & Chen, X. (2018). Three-dimensional parametric finite-volume homogenization of periodic materials with multi-scale structural applications. International Journal of Applied Mechanics, 10(04), 1850045.

Darılmaz, K., Orakdöğen, E., & Girgin, K. (2018). Saint-Venant torsion of arbitrarily shaped orthotropic composite or FGM sections by a hybrid finite element approach. Acta Mechanica, 229, 1387-1398.

Dong, S., Kosmatka, J., & Lin, H. (2001). On Saint-Venant's problem for an inhomogeneous, anisotropic cylinder—Part I: Methodology for Saint-Venant solutions. J. Appl. Mech., 68(3), 376-381.

Ecsedi, I. (2004). Elliptic cross section without warping under torsion. Mechanics Research Communications, 31(2), 147-150.

Galerkin, B. G. (1915). Series solution of some problems of elastic equilibrium of rods and plates. Vestnik inzhenerov i tekhnikov, 19(7), 897-908.

Gattu, M., Khatam, H., Drago, A. S., & Pindera, M.-J. (2008). Parametric finite-volume micromechanics of uniaxial continuously-reinforced periodic materials with elastic phases. Journal of Engineering Materials and Technology, 130(3).

Gordon, W. J., & Hall, C. A. (1973). Transfinite element methods: blending-function interpolation over arbitrary curved element domains. Numerische Mathematik, 21(2), 109-129.

Gordon, W. J., & Thiel, L. C. (1982). Transfinite mappings and their application to grid generation. Applied Mathematics and Computation, 10, 171-233.

He, J., Chiang, M. Y., McDonough, W., & Hunston, D. L. (2002). Experimental and theoretical evaluations of the Iosipescu shear test for hybrid fiber composites. International SAMPE Symposium and Exhibition,

Hellinger, E. (1907). Die allgemeinen ansätze der mechanik der kontinua. Springer.

Horgan, C., & Chan, A. (1999). The pressurized hollow cylinder or disk problem for functionally graded isotropic linearly elastic materials. Journal of Elasticity, 55, 43-59.

Horgan, C. O. (2007). On the torsion of functionally graded anisotropic linearly elastic bars. IMA Journal of Applied Mathematics, 72(5), 556-562.

Hu, H.-C. (1955). On some variational principles in the theory of elasticity and plasticity. Sci. Sin., 4, 33-54.

Jung, S. N., Dhadwal, M. K., Kim, Y. W., Kim, J. H., & Riemenschneider, J. (2015). Cross-sectional constants of composite blades using computed tomography technique and finite element analysis. Composite Structures, 129, 132-142.

Khatam, H., & Pindera, M.-J. (2009). Parametric finite-volume micromechanics of periodic materials with elastoplastic phases. International Journal of Plasticity, 25(7), 1386-1411.

Khatam, H., & Pindera, M.-J. (2009). Thermo-elastic moduli of periodic multilayers with wavy architectures. Composites Part B: Engineering, 40(1), 50-64.

Kolosov, G. (1909). On the Application of the Theory of Functions of a Complex Variable to a Plane problem in the Mathematical Theory of Elasticity. Yur'ev.

Kosmatka, J., Lin, H., & Dong, S. (2001). On saint-venant's problem for an inhomogeneous, anisotropic cylinder—part ii: Cross-sectional properties. J. Appl. Mech., 68(3), 382-391.

Lekhnitskii, S. G., Fern, P., Brandstatter, J. J., & Dill, E. (1964). Theory of elasticity of an anisotropic elastic body. Physics Today, 17(1), 84.

LeVeque, R. J. (2002). Finite volume methods for hyperbolic problems (Vol. 31). Cambridge university press.

Lezgy-Nazargah, M., Vidal, P., & Polit, O. (2021). A quasi-3D finite element model for the analysis of thin-walled beams under axial–flexural–torsional loads. Thin-Walled Structures, 164, 107811.

Muskhelishvili, N. I. (1953). Some basic problems of the mathematical theory of elasticity (Vol. 15). Noordhoff Groningen.

Nogata, F., & Takahashi, H. (1995). Intelligent functionally graded material: bamboo. Composites Engineering, 5(7), 743-751.

Pagano, N. J., & Halpin, J. (1968). Influence of end constraint in the testing of anisotropic bodies. Journal of Composite Materials, 2(1), 18-31.

Paulino, G., Fannjiang, A., & Chan, Y.-S. (2003). Gradient elasticity theory for mode III fracture in functionally graded materials—part I: crack perpendicular to the material gradation. J. Appl. Mech., 70(4), 531-542.

Pindera, M.-J. (1991). Local/global stiffness matrix formulation for composite materials and structures. Composites Engineering, 1(2), 69-83.

Pindera, M.-J. (1991). Local/global stiffness matrix formulation for anisotropic multilayered structures. Advanced Composites Materials in Civil Engineering Structures,

Pindera, M.-J., Choksi, G., Hidde, J. S., & Herakovich, C. T. (1987). A methodology for accurate shear characterization of unidirectional composites. Journal of Composite Materials, 21(12), 1164-1184.

Pindera, M.-J., & Herakovich, C. (1986). Shear characterization of unidirectional composites with the off-axis tension test. Experimental Mechanics, 26, 103-112.

Postma, G. (1955). Wave propagation in a stratified medium. Geophysics, 20(4), 780-806.

Rayleigh, J. W. S. B. (1896). The theory of sound (Vol. 2). Macmillan.

Reissner, E. (1950). On a variational theorem in elasticity. Journal of Mathematics and Physics, 29(1-4), 90-95.

Reissner, E. (1965). A note on variational principles in elasticity. International Journal of Solids and Structures, 1(1), 93-95.

Reissner, E. (1985). On mixed variational formulations in finite elasticity. Acta Mechanica, 56(3-4), 117-125.

Ritz, W. (1909). Über eine neue Methode zur Lösung gewisser Variationsprobleme der mathematischen Physik.

Rooney, F. J., & Ferrari, M. (1995). Torsion and flexure of inhomogeneous elements. Composites Engineering, 5(7), 901-911.

Rukhadze, A., & Vekua, I. y. N. (1933). Sur la torsion d'un cylindre armé d'une tige. Izvestiya Rossiiskoi Akademii Nauk. Seriya Matematicheskaya(3), 373-386.

Sadd, M. H. (2009). Elasticity: theory, applications, and numerics. Academic Press.

Santoro, R. (2011). Solution of De Saint Venant flexure-torsion problem for orthotropic beam via LEM (Line Element-less Method). European Journal of Mechanics-A/Solids, 30(6), 924-939.

Silva, E. C. N., Walters, M. C., & Paulino, G. H. (2006). Modeling bamboo as a functionally graded material: lessons for the analysis of affordable materials. Journal of Materials Science, 41, 6991-7004.

Sokolnikoff, I. S., & Specht, R. D. (1956). Mathematical theory of elasticity (Vol. 83). McGraw-Hill New York.

Stevenson, A. (1938). Flexure with shear and associated torsion in prisms of uni-axial and asymmetric cross-sections. Philosophical Transactions of the Royal Society of London. Series A, Mathematical and Physical Sciences, 237(776), 161-229.

Suquet, P. (1987). Elements of homogenization for inelastic solid mechanics. Homogenization techniques for composite media.

Timoshenko, S., & Goodier, J. N. (1951). Theory of Elasticity: By S. Timoshenko and JN Goodier. McGraw-Hill.

Timoshenko, S. P., & Gere, J. M. (2009). Theory of elastic stability. Courier Corporation.

Ting, T. C.-t., & Ting, T. C.-t. (1996). Anisotropic elasticity: theory and applications. Oxford University Press on Demand.

Tolf, G. (1985). Saint-Venant bending of an orthotropic beam. Composite Structures, 4(1), 1-14.

Uflyand, Y. S. (1965). SURVEY OF ARTICLES ON THE APPLICATIONS OF INTEGRAL TRANSFORMS IN THE THEORY OF ELASTICITY.

Ugural, A. C., & Fenster, S. K. (2003). Advanced strength and applied elasticity. Pearson education.

Várady Filho, C. A., & Cavalcante, M. A. (2023). Evaluation of macroscopic yield surfaces of periodic porous microstructures employing transformation field analysis and high order finite element method. Materials Today Communications, 34, 105462.

Versteeg, H. K., & Malalasekera, W. (2007). An introduction to computational fluid dynamics: the finite volume method. Pearson education.

Worndle, R. (1981). CALCULATION OF THE CROSS SECTION PROPERTIES AND THE SHEAR STRESSES OF COi'lPOS ITE ROTOR BLADES.

Yu, W., Volovoi, V. V., Hodges, D. H., & Hong, X. (2002). Validation of the variational asymptotic beam sectional analysis. AIAA journal, 40(10), 2105-2112.

Zhong, Y., Bansal, Y., & Pindera, M.-J. (2004). Efficient reformulation of the thermal higher-order theory for FGMs with locally variable conductivity. International Journal of Computational Engineering Science, 5(04), 795-831.

Appendix

I. Reduced compliance matrix for monoclinic materials ($x-y$ plane symmetry) under plane stress condition

For an orthotropic material whose principal material coordinate system $1-2-3$ is aligned with $x-y-z$ coordinate system, the plane stress problem is derived from the constitutive equation for the in-plane stress and strain. Based on those plane stress restrictions, the reduced stiffness matrix for an orthotropic material is

$$[\boldsymbol{Q}]=\begin{bmatrix} \frac{E_{11}}{1-\nu_{12}V_{21}} & \frac{\nu_{21}E_{11}}{1-\nu_{12}\nu_{21}} & 0 \\ \frac{\nu_{21}E_{11}}{1-\nu_{12}\nu_{21}} & \frac{E_{22}}{1-\nu_{12}\nu_{21}} & 0 \\ 0 & 0 & G_{12} \end{bmatrix}$$

A specific type of monoclinic material comes from the rotation by angle θ about the z axis, has the compliance matrix of the following:

$$[\overline{\boldsymbol{C}}]=\begin{bmatrix} m^2 & n^2 & -2mn \\ n^2 & m^2 & 2mn \\ mn & -mn & m^2-n^2 \end{bmatrix}^{-1}[\boldsymbol{Q}]\begin{bmatrix} m^2 & n^2 & -mn \\ n^2 & m^2 & mn \\ 2mn & -2mn & m^2-n^2 \end{bmatrix}$$

where $m=\cos\theta$, $n=\sin\theta$, which satisfied

$$\begin{bmatrix} \sigma_{xx} \\ \sigma_{yy} \\ \sigma_{xy} \end{bmatrix}=[\overline{\boldsymbol{C}}]\begin{bmatrix} \epsilon_{xx} \\ \epsilon_{yy} \\ \gamma_{xy} \end{bmatrix}=\begin{bmatrix} \boxed{\bar{C}_{11}} & \boxed{\bar{C}_{12}} & \boxed{\bar{C}_{16}} \\ \boxed{\bar{C}_{12}} & \boxed{\bar{C}_{22}} & \boxed{\bar{C}_{26}} \\ \boxed{\bar{C}_{16}} & \boxed{\bar{C}_{26}} & \boxed{\bar{C}_{66}} \end{bmatrix}\begin{bmatrix} \epsilon_{xx} \\ \epsilon_{yy} \\ \gamma_{xy} \end{bmatrix}$$

II. Reduced compliance matrix for monoclinic materials ($x-y$ plane symmetry) under plane strain condition

For an orthotropic material whose principal material coordinate system $1-2-3$ is aligned with $x-y-z$ coordinate system, the plane strain problem is derived from the constitutive equation for the in-plane stress and strain. The compliance matrix for an orthotropic material is

$$
[\underline{\boldsymbol{S}}] = \begin{bmatrix}
\frac{1}{E_{11}} & -\frac{\upsilon_{21}}{E_{22}} & -\frac{\upsilon_{21}}{E_{22}} & 0 & 0 & 0 \\
-\frac{\upsilon_{12}}{E_{11}} & \frac{1}{E_{22}} & \frac{\upsilon_{23}}{E_{22}} & 0 & 0 & 0 \\
-\frac{\upsilon_{12}}{E_{11}} & -\frac{\upsilon_{23}}{E_{22}} & \frac{1}{E_{22}} & 0 & 0 & 0 \\
0 & 0 & 0 & \frac{1+\upsilon_{23}}{2E_{22}} & 0 & 0 \\
0 & 0 & 0 & 0 & \frac{1}{G_{12}} & 0 \\
0 & 0 & 0 & 0 & 0 & \frac{1}{G_{12}}
\end{bmatrix}
$$

A specific type of monoclinic material comes from the rotation by angle θ about the z axis, has the compliance matrix of the following:

$$
[\underline{\bar{\boldsymbol{S}}}] = \begin{bmatrix}
m^2 & n^2 & 0 & 0 & 0 & mn \\
n^2 & m^2 & 0 & 0 & 0 & -mn \\
0 & 0 & 1 & 0 & 0 & 0 \\
0 & 0 & 0 & m & -n & 0 \\
0 & 0 & 0 & n & m & 0 \\
-2mn & 2mn & 0 & 0 & 0 & m^2-n^2
\end{bmatrix}^{-1}
[\underline{\boldsymbol{S}}]
\begin{bmatrix}
m^2 & n^2 & 0 & 0 & 0 & 2mn \\
n^2 & m^2 & 0 & 0 & 0 & -2mn \\
0 & 0 & 1 & 0 & 0 & 0 \\
0 & 0 & 0 & m & -n & 0 \\
0 & 0 & 0 & n & m & 0 \\
-mn & mn & 0 & 0 & 0 & m^2-n^2
\end{bmatrix}
$$

where $m = \cos\theta$, $n = \sin\theta$, which satisfied

$$
\begin{bmatrix} \sigma_{xx} \\ \sigma_{yy} \\ \sigma_{zz} \\ \sigma_{yz} \\ \sigma_{xz} \\ \sigma_{xy} \end{bmatrix}
= [\underline{\bar{\boldsymbol{S}}}]^{-\mathbf{1}}
\begin{bmatrix} \epsilon_{xx} \\ \epsilon_{yy} \\ \epsilon_{zz} \\ \epsilon_{yz} \\ \epsilon_{xz} \\ \epsilon_{xy} \end{bmatrix}
= \begin{bmatrix}
\boxed{C_{11}} & \boxed{C_{12}} & C_{13} & C_{14} & C_{15} & \boxed{C_{16}} \\
\boxed{C_{12}} & \boxed{C_{22}} & C_{23} & C_{24} & C_{25} & \boxed{C_{26}} \\
C_{13} & C_{23} & C_{33} & C_{34} & C_{35} & C_{36} \\
C_{14} & C_{24} & C_{34} & C_{44} & C_{45} & C_{46} \\
C_{15} & C_{25} & C_{35} & C_{45} & C_{55} & C_{56} \\
\boxed{C_{16}} & \boxed{C_{26}} & C_{36} & C_{46} & C_{56} & \boxed{C_{66}}
\end{bmatrix}
\begin{bmatrix} \epsilon_{xx} \\ \epsilon_{yy} \\ \epsilon_{zz} \\ \epsilon_{yz} \\ \epsilon_{xz} \\ \epsilon_{xy} \end{bmatrix}
$$

III. Stiffness matrix components in plane stress problem

When $r = 1, 3, 5, 7$ which corresponds to $p = 1, 2, 3, 4$, half of components of the stiffness matrix in FVM solving for the plane stress problem are listed below:

$$k_{r1} = \left(\bar{C}_{11}^{(i)} n_{x|p}^{(i)} + \bar{C}_{16}^{(i)} n_{y|p}^{(i)}\right) \boldsymbol{a}_p^{(i)} \mathcal{E}_{(:,1)}^{(i)} + \left(\bar{Q}_{12}^{(i)} n_{x|p}^{(i)} + \bar{C}_{26}^{(i)} n_{y|p}^{(i)}\right) \boldsymbol{b}_p^{(i)} \mathcal{H}_{(:,1)}^{(i)} + \left(\bar{C}_{16}^{(i)} n_{x|p}^{(i)} + \bar{C}_{66}^{(i)} n_{y|p}^{(i)}\right) (\boldsymbol{b}_p^{(i)} \mathcal{E}_{(:,1)}^{(i)} + \boldsymbol{a}_p^{(i)} \mathcal{H}_{(:,1)}^{(i)}),$$

$$k_{r2} = \left(\bar{C}_{11}^{(i)} n_{x|p}^{(i)} + \bar{C}_{16}^{(i)} n_{y|p}^{(i)}\right) \boldsymbol{a}_p^{(i)} \mathcal{F}_{(:,1)}^{(i)} + \left(\bar{Q}_{12}^{(i)} n_{x|p}^{(i)} + \bar{C}_{26}^{(i)} n_{y|p}^{(i)}\right) \boldsymbol{b}_p^{(i)} \mathcal{G}_{(:,1)}^{(i)} + \left(\bar{C}_{16}^{(i)} n_{x|p}^{(i)} + \bar{C}_{66}^{(i)} n_{y|p}^{(i)}\right) (\boldsymbol{b}_p^{(i)} \mathcal{F}_{(:,1)}^{(i)} + \boldsymbol{a}_p^{(i)} \mathcal{G}_{(:,1)}^{(i)}),$$

$$k_{r3} = \left(\bar{C}_{11}^{(i)} n_{x|p}^{(i)} + \bar{C}_{16}^{(i)} n_{y|p}^{(i)}\right) \boldsymbol{a}_p^{(i)} \mathcal{E}_{(:,2)}^{(i)} + \left(\bar{Q}_{12}^{(i)} n_{x|p}^{(i)} + \bar{C}_{26}^{(i)} n_{y|p}^{(i)}\right) \boldsymbol{b}_p^{(i)} \mathcal{H}_{(:,2)}^{(i)} + \left(\bar{C}_{16}^{(i)} n_{x|p}^{(i)} + \bar{C}_{66}^{(i)} n_{y|p}^{(i)}\right) (\boldsymbol{b}_p^{(i)} \mathcal{E}_{(:,2)}^{(i)} + \boldsymbol{a}_p^{(i)} \mathcal{H}_{(:,2)}^{(i)}),$$

$$k_{r4} = \left(\bar{C}_{11}^{(i)} n_{x|p}^{(i)} + \bar{C}_{16}^{(i)} n_{y|p}^{(i)}\right) \boldsymbol{a}_p^{(i)} \mathcal{F}_{(:,2)}^{(i)} + \left(\bar{Q}_{12}^{(i)} n_{x|p}^{(i)} + \bar{C}_{26}^{(i)} n_{y|p}^{(i)}\right) \boldsymbol{b}_p^{(i)} \mathcal{G}_{(:,2)}^{(i)} + \left(\bar{C}_{16}^{(i)} n_{x|p}^{(i)} + \bar{C}_{66}^{(i)} n_{y|p}^{(i)}\right) (\boldsymbol{b}_p^{(i)} \mathcal{F}_{(:,2)}^{(i)} + \boldsymbol{a}_p^{(i)} \mathcal{G}_{(:,2)}^{(i)}),$$

$$k_{r5} = \left(\bar{C}_{11}^{(i)} n_{x|p}^{(i)} + \bar{C}_{16}^{(i)} n_{y|p}^{(i)}\right) \boldsymbol{a}_p^{(i)} \mathcal{E}_{(:,3)}^{(i)} + \left(\bar{Q}_{12}^{(i)} n_{x|p}^{(i)} + \bar{C}_{26}^{(i)} n_{y|p}^{(i)}\right) \boldsymbol{b}_p^{(i)} \mathcal{H}_{(:,3)}^{(i)} + \left(\bar{C}_{16}^{(i)} n_{x|p}^{(i)} + \bar{C}_{66}^{(i)} n_{y|p}^{(i)}\right) (\boldsymbol{b}_p^{(i)} \mathcal{E}_{(:,3)}^{(i)} + \boldsymbol{a}_p^{(i)} \mathcal{H}_{(:,3)}^{(i)}),$$

$$k_{r6} = \left(\bar{C}_{11}^{(i)} n_{x|p}^{(i)} + \bar{C}_{16}^{(i)} n_{y|p}^{(i)}\right) \boldsymbol{a}_p^{(i)} \mathcal{F}_{(:,3)}^{(i)} + \left(\bar{Q}_{12}^{(i)} n_{x|p}^{(i)} + \bar{C}_{26}^{(i)} n_{y|p}^{(i)}\right) \boldsymbol{b}_p^{(i)} \mathcal{G}_{(:,3)}^{(i)} + \left(\bar{C}_{16}^{(i)} n_{x|p}^{(i)} + \bar{C}_{66}^{(i)} n_{y|p}^{(i)}\right) (\boldsymbol{b}_p^{(i)} \mathcal{F}_{(:,3)}^{(i)} + \boldsymbol{a}_p^{(i)} \mathcal{G}_{(:,3)}^{(i)}),$$

$$k_{r7} = \left(\bar{C}_{11}^{(i)} n_{x|p}^{(i)} + \bar{C}_{16}^{(i)} n_{y|p}^{(i)}\right) \boldsymbol{a}_p^{(i)} \mathcal{E}_{(:,4)}^{(i)} + \left(\bar{Q}_{12}^{(i)} n_{x|p}^{(i)} + \bar{C}_{26}^{(i)} n_{y|p}^{(i)}\right) \boldsymbol{b}_p^{(i)} \mathcal{H}_{(:,4)}^{(i)} + \left(\bar{C}_{16}^{(i)} n_{x|p}^{(i)} + \bar{C}_{66}^{(i)} n_{y|p}^{(i)}\right) (\boldsymbol{b}_p^{(i)} \mathcal{E}_{(:,4)}^{(i)} + \boldsymbol{a}_p^{(i)} \mathcal{H}_{(:,4)}^{(i)}),$$

$$k_{p8} = \left(\bar{C}_{11}^{(i)} n_{x|p}^{(i)} + \bar{C}_{16}^{(i)} n_{y|p}^{(i)}\right) \boldsymbol{a}_p^{(i)} \mathcal{F}_{(:,4)}^{(i)} + \left(\bar{Q}_{12}^{(i)} n_{x|p}^{(i)} + \bar{C}_{26}^{(i)} n_{y|p}^{(i)}\right) \boldsymbol{b}_p^{(i)} \mathcal{G}_{(:,4)}^{(i)} + \left(\bar{C}_{16}^{(i)} n_{x|p}^{(i)} + \bar{C}_{66}^{(i)} n_{y|p}^{(i)}\right) (\boldsymbol{b}_p^{(i)} \mathcal{F}_{(:,4)}^{(i)} + \boldsymbol{a}_p^{(i)} \mathcal{G}_{(:,4)}^{(i)}),$$

$$k_r^{ezz} = 0$$

When $r = 2, 4, 6, 8$ which corresponds to $p = 1, 2, 3, 4$, the rest half of components of the stiffness matrix in FVM solving for the plane stress problem are listed below:

$$k_{r1} = \left(\bar{C}_{16}^{(i)} n_{x|p}^{(i)} + \bar{C}_{12}^{(i)} n_{y|p}^{(i)}\right) \boldsymbol{a}_p^{(i)} \mathcal{E}_{(:,1)}^{(i)} + \left(\bar{C}_{26}^{(i)} n_{x|p}^{(i)} + \bar{C}_{22}^{(i)} n_{y|p}^{(i)}\right) \boldsymbol{b}_p^{(i)} \mathcal{H}_{(:,1)}^{(i)} + \left(\bar{C}_{66}^{(i)} n_{x|p}^{(i)} + \bar{C}_{26}^{(i)} n_{y|p}^{(i)}\right) (\boldsymbol{b}_p^{(i)} \mathcal{E}_{(:,1)}^{(i)} + \boldsymbol{a}_p^{(i)} \mathcal{H}_{(:,1)}^{(i)}),$$

$$k_{r2} = \left(\bar{C}_{16}^{(i)} n_{x|p}^{(i)} + \bar{C}_{12}^{(i)} n_{y|p}^{(i)}\right) \boldsymbol{a}_p^{(i)} \mathcal{F}_{(:,1)}^{(i)} + \left(\bar{C}_{26}^{(i)} n_{x|p}^{(i)} + \bar{C}_{22}^{(i)} n_{y|p}^{(i)}\right) \boldsymbol{b}_p^{(i)} \mathcal{G}_{(:,1)}^{(i)} + \left(\bar{C}_{66}^{(i)} n_{x|p}^{(i)} + \bar{C}_{26}^{(i)} n_{y|p}^{(i)}\right) (\boldsymbol{b}_p^{(i)} \mathcal{F}_{(:,1)}^{(i)} + \boldsymbol{a}_p^{(i)} \mathcal{G}_{(:,1)}^{(i)}),$$

$$k_{r3} = \left(\bar{C}_{16}^{(i)} n_{x|p}^{(i)} + \bar{C}_{12}^{(i)} n_{y|p}^{(i)}\right) \boldsymbol{a}_p^{(i)} \mathcal{E}_{(:,2)}^{(i)} + \left(\bar{C}_{26}^{(i)} n_{x|p}^{(i)} + \bar{C}_{22}^{(i)} n_{y|p}^{(i)}\right) \boldsymbol{b}_p^{(i)} \mathcal{H}_{(:,2)}^{(i)} + \left(\bar{C}_{66}^{(i)} n_{x|p}^{(i)} + \bar{C}_{26}^{(i)} n_{y|p}^{(i)}\right) (\boldsymbol{b}_p^{(i)} \mathcal{E}_{(:,2)}^{(i)} + \boldsymbol{a}_p^{(i)} \mathcal{H}_{(:,2)}^{(i)})$$

$$k_{r4} = \left(\bar{C}_{16}^{(i)} n_{x|p}^{(i)} + \bar{C}_{12}^{(i)} n_{y|p}^{(i)}\right) \boldsymbol{a}_p^{(i)} \mathcal{F}_{(:,2)}^{(i)} + \left(\bar{C}_{26}^{(i)} n_{x|p}^{(i)} + \bar{C}_{22}^{(i)} n_{y|p}^{(i)}\right) \boldsymbol{b}_p^{(i)} \mathcal{G}_{(:,2)}^{(i)} + \left(\bar{C}_{66}^{(i)} n_{x|p}^{(i)} + \bar{C}_{26}^{(i)} n_{y|p}^{(i)}\right) (\boldsymbol{b}_p^{(i)} \mathcal{F}_{(:,2)}^{(i)} + \boldsymbol{a}_p^{(i)} \mathcal{G}_{(:,2)}^{(i)}),$$

$$k_{r5} = \left(\bar{C}_{16}^{(i)} n_{x|p}^{(i)} + \bar{C}_{12}^{(i)} n_{y|p}^{(i)}\right) \boldsymbol{a}_p^{(i)} \mathcal{E}_{(:,3)}^{(i)} + \left(\bar{C}_{26}^{(i)} n_{x|p}^{(i)} + \bar{C}_{22}^{(i)} n_{y|p}^{(i)}\right) \boldsymbol{b}_p^{(i)} \mathcal{H}_{(:,3)}^{(i)} + \left(\bar{C}_{66}^{(i)} n_{x|p}^{(i)} + \bar{C}_{26}^{(i)} n_{y|p}^{(i)}\right) (\boldsymbol{b}_p^{(i)} \mathcal{E}_{(:,3)}^{(i)} + \boldsymbol{a}_p^{(i)} \mathcal{H}_{(:,3)}^{(i)}),$$

$$k_{r6} = \left(\bar{C}_{16}^{(i)} n_{x|p}^{(i)} + \bar{C}_{12}^{(i)} n_{y|p}^{(i)}\right) \boldsymbol{a}_p^{(i)} \mathcal{F}_{(:,3)}^{(i)} + \left(\bar{C}_{26}^{(i)} n_{x|p}^{(i)} + \bar{C}_{22}^{(i)} n_{y|p}^{(i)}\right) \boldsymbol{b}_p^{(i)} \mathcal{G}_{(:,3)}^{(i)} + \left(\bar{C}_{66}^{(i)} n_{x|p}^{(i)} + \bar{C}_{26}^{(i)} n_{y|p}^{(i)}\right) (\boldsymbol{b}_p^{(i)} \mathcal{F}_{(:,3)}^{(i)} + \boldsymbol{a}_p^{(i)} \mathcal{G}_{(:,3)}^{(i)}),$$

$$k_{r7} = \left(\bar{C}_{16}^{(i)} n_{x|p}^{(i)} + \bar{C}_{12}^{(i)} n_{y|p}^{(i)}\right) \boldsymbol{a}_p^{(i)} \mathcal{E}_{(:,4)}^{(i)} + \left(\bar{C}_{26}^{(i)} n_{x|p}^{(i)} + \bar{C}_{22}^{(i)} n_{y|p}^{(i)}\right) \boldsymbol{b}_p^{(i)} \mathcal{H}_{(:,4)}^{(i)} + \left(\bar{C}_{66}^{(i)} n_{x|p}^{(i)} + \bar{C}_{26}^{(i)} n_{y|p}^{(i)}\right) (\boldsymbol{b}_p^{(i)} \mathcal{E}_{(:,4)}^{(i)} + \boldsymbol{a}_p^{(i)} \mathcal{H}_{(:,4)}^{(i)}),$$

$$k_{r8} = \left(\bar{C}_{16}^{(i)} n_{x|p}^{(i)} + \bar{C}_{12}^{(i)} n_{y|p}^{(i)}\right) \boldsymbol{a}_p^{(i)} \mathcal{F}_{(:,4)}^{(i)} + \left(\bar{C}_{26}^{(i)} n_{x|p}^{(i)} + \bar{C}_{22}^{(i)} n_{y|p}^{(i)}\right) \boldsymbol{b}_p^{(i)} \mathcal{G}_{(:,4)}^{(i)} + \left(\bar{C}_{66}^{(i)} n_{x|p}^{(i)} + \bar{C}_{26}^{(i)} n_{y|p}^{(i)}\right) (\boldsymbol{b}_p^{(i)} \mathcal{F}_{(:,4)}^{(i)} + \boldsymbol{a}_p^{(i)} \mathcal{G}_{(:,4)}^{(i)}),$$

$$k_r^{ezz} = 0$$

IV. Stiffness matrix components in plane strain problem and generalized plane strain

When $r = 1, 3, 5, 7$ which corresponds to $p = 1, 2, 3, 4$, half of components of the stiffness matrix in FVM solving for the plane strain problem are listed below:

$$k_{r1} = \left(C_{11}^{(i)} n_{x|p}^{(i)} + C_{16}^{(i)} n_{y|p}^{(i)}\right) \boldsymbol{a}_p^{(i)} \mathcal{E}_{(:,1)}^{(i)} + \left(C_{12}^{(i)} n_{x|p}^{(i)} + C_{26}^{(i)} n_{y|p}^{(i)}\right) \boldsymbol{b}_p^{(i)} \mathcal{H}_{(:,1)}^{(i)} + \left(C_{16}^{(i)} n_{x|p}^{(i)} + C_{66}^{(i)} n_{y|p}^{(i)}\right) (\boldsymbol{b}_p^{(i)} \mathcal{E}_{(:,1)}^{(i)} + \boldsymbol{a}_p^{(i)} \mathcal{H}_{(:,1)}^{(i)}),$$

$$k_{r2} = \left(C_{11}^{(i)} n_{x|p}^{(i)} + C_{16}^{(i)} n_{y|p}^{(i)}\right) \boldsymbol{a}_p^{(i)} \mathcal{F}_{(:,1)}^{(i)} + \left(C_{12}^{(i)} n_{x|p}^{(i)} + C_{26}^{(i)} n_{y|p}^{(i)}\right) \boldsymbol{b}_p^{(i)} \mathcal{G}_{(:,1)}^{(i)} + \left(C_{16}^{(i)} n_{x|p}^{(i)} + \bar{C}_{66}^{(i)} n_{y|p}^{(i)}\right) (\boldsymbol{b}_p^{(i)} \mathcal{F}_{(:,1)}^{(i)} + \boldsymbol{a}_p^{(i)} \mathcal{G}_{(:,1)}^{(i)}),$$

$$k_{r3} = \left(C_{11}^{(i)} n_{x|p}^{(i)} + C_{16}^{(i)} n_{y|p}^{(i)}\right) \boldsymbol{a}_p^{(i)} \mathcal{E}_{(:,2)}^{(i)} + \left(C_{12}^{(i)} n_{x|p}^{(i)} + C_{26}^{(i)} n_{y|p}^{(i)}\right) \boldsymbol{b}_p^{(i)} \mathcal{H}_{(:,2)}^{(i)} + \left(C_{16}^{(i)} n_{x|p}^{(i)} + C_{66}^{(i)} n_{y|p}^{(i)}\right) (\boldsymbol{b}_p^{(i)} \mathcal{E}_{(:,2)}^{(i)} + \boldsymbol{a}_p^{(i)} \mathcal{H}_{(:,2)}^{(i)}),$$

$$k_{r4} = \left(C_{11}^{(i)} n_{x|p}^{(i)} + C_{16}^{(i)} n_{y|p}^{(i)}\right) \boldsymbol{a}_p^{(i)} \mathcal{F}_{(:,2)}^{(i)} + \left(C_{12}^{(i)} n_{x|p}^{(i)} + C_{26}^{(i)} n_{y|p}^{(i)}\right) \boldsymbol{b}_p^{(i)} \mathcal{G}_{(:,2)}^{(i)} + \left(C_{16}^{(i)} n_{x|p}^{(i)} + C_{66}^{(i)} n_{y|p}^{(i)}\right) (\boldsymbol{b}_p^{(i)} \mathcal{F}_{(:,2)}^{(i)} + \boldsymbol{a}_p^{(i)} \mathcal{G}_{(:,2)}^{(i)}),$$

$$k_{r5} = \left(C_{11}^{(i)} n_{x|p}^{(i)} + C_{16}^{(i)} n_{y|p}^{(i)}\right) \boldsymbol{a}_p^{(i)} \mathcal{E}_{(:,3)}^{(i)} + \left(C_{12}^{(i)} n_{x|p}^{(i)} + C_{26}^{(i)} n_{y|p}^{(i)}\right) \boldsymbol{b}_p^{(i)} \mathcal{H}_{(:,3)}^{(i)} + \left(C_{16}^{(i)} n_{x|p}^{(i)} + C_{66}^{(i)} n_{y|p}^{(i)}\right) (\boldsymbol{b}_p^{(i)} \mathcal{E}_{(:,3)}^{(i)} + \boldsymbol{a}_p^{(i)} \mathcal{H}_{(:,3)}^{(i)}),$$

$$k_{r6} = \left(C_{11}^{(i)} n_{x|p}^{(i)} + C_{16}^{(i)} n_{y|p}^{(i)}\right) \boldsymbol{a}_p^{(i)} \mathcal{F}_{(:,3)}^{(i)} + \left(C_{12}^{(i)} n_{x|p}^{(i)} + C_{26}^{(i)} n_{y|p}^{(i)}\right) \boldsymbol{b}_p^{(i)} \mathcal{G}_{(:,3)}^{(i)} + \left(C_{16}^{(i)} n_{x|p}^{(i)} + C_{66}^{(i)} n_{y|p}^{(i)}\right) (\boldsymbol{b}_p^{(i)} \mathcal{F}_{(:,3)}^{(i)} + \boldsymbol{a}_p^{(i)} \mathcal{G}_{(:,3)}^{(i)}),$$

$$k_{r7} = \left(C_{11}^{(i)} n_{x|p}^{(i)} + C_{16}^{(i)} n_{y|p}^{(i)}\right) \boldsymbol{a}_p^{(i)} \mathcal{E}_{(:,4)}^{(i)} + \left(C_{12}^{(i)} n_{x|p}^{(i)} + C_{26}^{(i)} n_{y|p}^{(i)}\right) \boldsymbol{b}_p^{(i)} \mathcal{H}_{(:,4)}^{(i)} + \left(C_{16}^{(i)} n_{x|p}^{(i)} + C_{66}^{(i)} n_{y|p}^{(i)}\right) (\boldsymbol{b}_p^{(i)} \mathcal{E}_{(:,4)}^{(i)} + \boldsymbol{a}_p^{(i)} \mathcal{H}_{(:,4)}^{(i)}),$$

$$k_{r8} = \left(C_{11}^{(i)} n_{x|p}^{(i)} + C_{16}^{(i)} n_{y|p}^{(i)}\right) \boldsymbol{a}_p^{(i)} \mathcal{F}_{(:,4)}^{(i)} + \left(C_{12}^{(i)} n_{x|p}^{(i)} + C_{26}^{(i)} n_{y|p}^{(i)}\right) \boldsymbol{b}_p^{(i)} \mathcal{G}_{(:,4)}^{(i)} + \left(C_{16}^{(i)} n_{x|p}^{(i)} + C_{66}^{(i)} n_{y|p}^{(i)}\right) (\boldsymbol{b}_p^{(i)} \mathcal{F}_{(:,4)}^{(i)} + \boldsymbol{a}_p^{(i)} \mathcal{G}_{(:,4)}^{(i)}),$$

$$k_r^{ezz} = [(C_{11}^{(i)} n_{x|p}^{(i)} + C_{16}^{(i)} n_{y|p}^{(i)}) \boldsymbol{a}_p^{(i)} \vec{\mathrm{C}}_{\mathcal{EF}} + (C_{12}^{(i)} n_{x|p}^{(i)} + C_{26}^{(i)} n_{y|p}^{(i)}) \boldsymbol{b}_p^{(i)} \vec{\mathrm{C}}_{\mathcal{GH}} + (C_{13} n_{x|p}^{(i)} + C_{36}^{(i)} n_{y|p}^{(i)}) + \left(C_{16}^{(i)} n_{x|p}^{(i)} + C_{66}^{(i)} n_{y|p}^{(i)}\right) (\boldsymbol{b}_p^{(i)} \vec{\mathrm{C}}_{\mathcal{EF}} + \boldsymbol{a}_p^{(i)} \vec{\mathrm{C}}_{\mathcal{GH}})] \bar{\epsilon}_{zz}$$

When $r = 2, 4, 6, 8$ which corresponds to $p = 1, 2, 3, 4$, the rest half of components of the stiffness matrix in FVM solving for the plane strain problem are listed below:

$$k_{r1} = \left(C_{16}^{(i)} n_{x|p}^{(i)} + C_{12}^{(i)} n_{y|p}^{(i)}\right) \boldsymbol{a}_p^{(i)} \mathcal{E}_{(:,1)}^{(i)} + \left(C_{26}^{(i)} n_{x|p}^{(i)} + C_{22}^{(i)} n_{y|p}^{(i)}\right) \boldsymbol{b}_p^{(i)} \mathcal{H}_{(:,1)}^{(i)} + \left(C_{66}^{(i)} n_{x|p}^{(i)} + C_{26}^{(i)} n_{y|p}^{(i)}\right) (\boldsymbol{b}_p^{(i)} \mathcal{E}_{(:,1)}^{(i)} + \boldsymbol{a}_p^{(i)} \mathcal{H}_{(:,1)}^{(i)}),$$

$$k_{r2} = \left(C_{16}^{(i)} n_{x|p}^{(i)} + C_{12}^{(i)} n_{y|p}^{(i)}\right) \boldsymbol{a}_p^{(i)} \mathcal{F}_{(:,1)}^{(i)} + \left(C_{26}^{(i)} n_{x|p}^{(i)} + C_{22}^{(i)} n_{y|p}^{(i)}\right) \boldsymbol{b}_p^{(i)} \mathcal{G}_{(:,1)}^{(i)} + \left(C_{66}^{(i)} n_{x|p}^{(i)} + C_{26}^{(i)} n_{y|p}^{(i)}\right) (\boldsymbol{b}_p^{(i)} \mathcal{F}_{(:,1)}^{(i)} + \boldsymbol{a}_p^{(i)} \mathcal{G}_{(:,1)}^{(i)}),$$

$$k_{r3} = \left(C_{16}^{(i)} n_{x|p}^{(i)} + C_{12}^{(i)} n_{y|p}^{(i)}\right) \boldsymbol{a}_p^{(i)} \mathcal{E}_{(:,2)}^{(i)} + \left(C_{26}^{(i)} n_{x|p}^{(i)} + C_{22}^{(i)} n_{y|p}^{(i)}\right) \boldsymbol{b}_p^{(i)} \mathcal{H}_{(:,2)}^{(i)} + \left(C_{66}^{(i)} n_{x|p}^{(i)} + C_{26}^{(i)} n_{y|p}^{(i)}\right) (\boldsymbol{b}_p^{(i)} \mathcal{E}_{(:,2)}^{(i)} + \boldsymbol{a}_p^{(i)} \mathcal{H}_{(:,2)}^{(i)}),$$

$$k_{r4} = \left(C_{16}^{(i)} n_{x|p}^{(i)} + C_{12}^{(i)} n_{y|p}^{(i)}\right) \boldsymbol{a}_p^{(i)} \mathcal{F}_{(:,2)}^{(i)} + \left(C_{26}^{(i)} n_{x|p}^{(i)} + C_{22}^{(i)} n_{y|p}^{(i)}\right) \boldsymbol{b}_p^{(i)} \mathcal{G}_{(:,2)}^{(i)} + \left(C_{66}^{(i)} n_{x|p}^{(i)} + C_{26}^{(i)} n_{y|p}^{(i)}\right) (\boldsymbol{b}_p^{(i)} \mathcal{F}_{(:,2)}^{(i)} + \boldsymbol{a}_p^{(i)} \mathcal{G}_{(:,2)}^{(i)}),$$

$$k_{r5} = \left(C_{16}^{(i)} n_{x|p}^{(i)} + C_{12}^{(i)} n_{y|p}^{(i)}\right) \boldsymbol{a}_p^{(i)} \mathcal{E}_{(:,3)}^{(i)} + \left(C_{26}^{(i)} n_{x|p}^{(i)} + C_{22}^{(i)} n_{y|p}^{(i)}\right) \boldsymbol{b}_p^{(i)} \mathcal{H}_{(:,3)}^{(i)} + \left(C_{66}^{(i)} n_{x|p}^{(i)} + C_{26}^{(i)} n_{y|p}^{(i)}\right) (\boldsymbol{b}_p^{(i)} \mathcal{E}_{(:,3)}^{(i)} + \boldsymbol{a}_p^{(i)} \mathcal{H}_{(:,3)}^{(i)}),$$

$$k_{r6} = \left(C_{16}^{(i)} n_{x|p}^{(i)} + C_{12}^{(i)} n_{y|p}^{(i)}\right) \boldsymbol{a}_p^{(i)} \mathcal{F}_{(:,3)}^{(i)} + \left(C_{26}^{(i)} n_{x|p}^{(i)} + C_{22}^{(i)} n_{y|p}^{(i)}\right) \boldsymbol{b}_p^{(i)} \mathcal{G}_{(:,3)}^{(i)} + \left(C_{66}^{(i)} n_{x|p}^{(i)} + C_{26}^{(i)} n_{y|p}^{(i)}\right) (\boldsymbol{b}_p^{(i)} \mathcal{F}_{(:,3)}^{(i)} + \boldsymbol{a}_p^{(i)} \mathcal{G}_{(:,3)}^{(i)}),$$

$$k_{r7} = \left(C_{16}^{(i)} n_{x|p}^{(i)} + C_{12}^{(i)} n_{y|p}^{(i)}\right) \boldsymbol{a}_p^{(i)} \mathcal{E}_{(:,4)}^{(i)} + \left(C_{26}^{(i)} n_{x|p}^{(i)} + C_{22}^{(i)} n_{y|p}^{(i)}\right) \boldsymbol{b}_p^{(i)} \mathcal{H}_{(:,4)}^{(i)} + \left(C_{66}^{(i)} n_{x|p}^{(i)} + C_{26}^{(i)} n_{y|p}^{(i)}\right) (\boldsymbol{b}_p^{(i)} \mathcal{E}_{(:,4)}^{(i)} + \boldsymbol{a}_p^{(i)} \mathcal{H}_{(:,4)}^{(i)}),$$

$$k_{r8} = \left(C_{16}^{(i)} n_{x|p}^{(i)} + C_{12}^{(i)} n_{y|p}^{(i)}\right) \boldsymbol{a}_p^{(i)} \mathcal{F}_{(:,4)}^{(i)} + \left(C_{26}^{(i)} n_{x|p}^{(i)} + C_{22}^{(i)} n_{y|p}^{(i)}\right) \boldsymbol{b}_p^{(i)} \mathcal{G}_{(:,4)}^{(i)} + \left(C_{66}^{(i)} n_{x|p}^{(i)} + C_{26}^{(i)} n_{y|p}^{(i)}\right) (\boldsymbol{b}_p^{(i)} \mathcal{F}_{(:,4)}^{(i)} + \boldsymbol{a}_p^{(i)} \mathcal{G}_{(:,4)}^{(i)}),$$

$$\begin{aligned} k_r^{ezz} = [(&C_{16}^{(i)} n_{x|p}^{(i)} + C_{12}^{(i)} n_{y|p}^{(i)}) \boldsymbol{a}_p^{(i)} \vec{\mathrm{C}}_{\mathcal{E}\mathcal{F}} + (C_{26}^{(i)} n_{x|p}^{(i)} + C_{22}^{(i)} n_{y|p}^{(i)}) \boldsymbol{b}_p^{(i)} \vec{\mathrm{C}}_{\mathcal{G}\mathcal{H}} + (C_{36} n_{x|p}^{(i)} + C_{23}^{(i)} n_{y|p}^{(i)}) + \left(C_{66}^{(i)} n_{x|p}^{(i)} + C_{26}^{(i)} n_{y|p}^{(i)}\right) (\boldsymbol{b}_p^{(i)} \vec{\mathrm{C}}_{\mathcal{E}\mathcal{F}} \\ &+ \boldsymbol{a}_p^{(i)} \vec{\mathrm{C}}_{\mathcal{G}\mathcal{H}})] \bar{\epsilon}_{zz} \end{aligned}$$